ABSTRACT

Title of Document: TECTONICS OF ICY SATELLITES DRIVEN BY MELTING AND CRYSTALLIZATION OF WATER BODIES INSIDE THEIR ICE SHELLS

Stephanie Ann Johnston, Doctor of Philosophy, 2015

Directed By: Associate Professor Laurent Montési, Department of Geology

Enceladus and Europa are icy satellites that currently support bodies of liquid water in the outer solar system Additionally, they show signs of being geologically active. Developing numerical models informed by observations of these icy satellites allows for the development of additional constraints and an improved understanding of the tectonics and evolution of icy satellites.

The formation mechanisms for both chaos and ridges on Europa are thought to involve water as albedo changes observed in association with them imply the deposition of salt-rich water near these features. Ridges are the most ubiquitous feature on Europa and are described as central troughs flanked by two raised edifices, range in height from tens to hundreds of meters. Europan ridges can extend hundreds of km continuously along strike but are only about 2 km across. A model of a crystallizing dike–like water intrusion is able to match the overall morphology of

ridges, and is consistent the long continuous strike. However, the intrusion of a large volume of water is required to match the most common heights of the ridges.

Chaos on Europa is defined as a large area of disrupted ice that contain blocks of pre-existing material separated by a hummocky matrix. A proposed mechanism for the formation of Chaos is that a region of heterogeneous ice within the shell is melted and then recrystallizes. Comparing the model results with the geology of Thera Macula, a region where it has been proposed that Chaos is currently forming, suggests that additional processes may be needed to fully understand the development of Chaos.

Water-rich plumes erupt from the south pole of Enceladus, suggesting the presence of a pressurized water reservoir. If a pressurized sea is located beneath the south polar terrain, its geometry and size in the ice shell would contribute to the stress state in the ice shell. The geometry and location of such an ocean, as well as the boundary conditions and thickness of an ice shell have important implications for the faulting and tectonic deformation anticipated at the surface.

TECTONICS OF ICY SATELLITES DRIVEN BY MELTING AND CRYSTALLIZATION OF WATER BODIES INSIDE THEIR ICE SHELLS.

By

Stephanie Ann Johnston

Dissertation submitted to the Faculty of the Graduate School of the
University of Maryland, College Park, in partial fulfillment
of the requirements for the degree of
Doctor of Philosophy
2015

Advisory Committee:

Associate Professor Laurent Montési, Chair
Professor Michael Brown
Assistant Professor Vedran Lekic
Assistant Professor Derrick Lampkin
Dr. Lori Glaze (NASA-GSFC)
Professor Jessica Sunshine (Dean's Representative)

Foreword

A portion of the research presented in this dissertation was previously published as a peer-reviewed journal article. I made substantial contributions to the relevant aspects of the jointly authored work included in this dissertation. Following is a summary of the contributions made by each author for the published chapter.

Chapter 2

S.A. Johnston and L.G.J. Montesi. (2014). Formation of ridges on Europa above crystallizing water bodies inside the ice shell. Icarus, 237, 190-201

I developed the model, reviewed model results, and wrote the first draft of the manuscript. Dr. Montési assisted in the interpretation of the final results and provided edits and assisted with figures in the manuscript.

Acknowledgements

First and foremost, I would like to thank Laurent Montési for his support, guidance and patience during my graduate school career. His encouragement and willingness to allow me to pursue a wide range of scientific opportunities has enriched my graduate school experience. I have greatly enjoyed many frank discussions with him regarding the philosophy of science and research careers. I am also incredibly grateful to Lori Glaze for her unwavering support, remarkable insights and her mentorship.

This project was funded by NASA Grant NNX10AG41G and the Geology Department through a teaching fellowship. Funding for the presentation of my research was awarded by the Earth System Science Interdisciplinary Committee.

I am also thankful for the administrative and technical support from Dorothy Brown, Todd Karwoski, Susanne Martin, Michelle Montero, Sandy Romeo and Nicole (Siyu) Shan.

I am thankful for the support of many graduate students in particular: Minjin Baek, Hailong Bai, Caitlyn Brown, Jodi Gaeman, Laura Hebert, Kevin Miller, Miriam and Nick Sharp, Lisa Walsh, Galen Wallaert, Jesse Wimert, and Christopher Yakymchuk. I also want to acknowledge the friendship and laughter from Justin DeSha-Overcash. I want to thank my Parents who have supported and believed in me in all I do; Maeghan Davis, for her unending encouragement, support, and late night conversations about the meaning of life and research; David Kruckvich for his

emotional support, encouragement and willingness to put up with an absent minded scientist.

And finally I would like to thank my sister, Michelle Lock, without whom I never would have discovered a love for science, space and the unknown. Thank you for showing such an interest in my research, for allowing me to ramble on about my scientific interests and for lending me your spark when I needed it. Without your unwavering love and support, this would not have been possible.

Table of Contents

List of Tables

List of Figures

Chapter 1 : Introduction to Icy Satellite Tectonics

1.1 Solar System Exploration

The study of planetary bodies in our solar system provides a valuable opportunity to evaluate our understanding of geological processes. Icy satellites are moons with surfaces composed predominantly of ice that reside in the outer solar system. They offer a unique opportunity to fine-tune our understanding of both rocky and icy geologic activity while also allowing us to evaluate the astrobiological potential of the outer solar system. Our ability to obtain detailed observations of icy satellites is hindered by their absence in the inner solar system, forcing observations to either be made from afar or the designing of a planetary exploration mission. While the appearance of icy satellites is distinct from that of rocky planets, the formation of the geologic features is governed by the same chemical, physical, and geologic principles as features on the terrestrial planets and their natural moons. They have an abundance of one of the elements thought to be critical to the existence of life, liquid water, providing a potential to support life (Reynolds et al., 1983; Chyba and Phillips, 2002). Because of the unique insight and potential for improving our understanding of the workings of the solar system, the National Aeronautics and Space Administration (NASA), recognizing the valuable insight that these satellites can provide, has flown several missions to explore and return observation data from icy satellites. Of key importance to this work are the Voyager Missions, Galileo, and Cassini-Huygens.

1.1.1 Voyager Missions

The first missions to explore the outer solar system were the Voyager missions launched in 1977. These missions were designed to be a grand tour of the solar system and provide humankind with some of the first flyby images of the planetary bodies in the outer solar system (Kohlhase and Penzo, 1977). Voyager 2 flew by Jupiter, Saturn, Uranus and Neptune, returning the images of not only the planets themselves but also their orbiting satellites. The data returned to Earth included the first detailed images of icy satellites. Because the mission was design to provide an overview of the solar system rather than a detailed study of specific planetary bodies, many images received were of large swatches of planetary surfaces but at low resolution. Despite the lack of detail, the Voyager missions paved the way for future orbital missions designed to conduct more detailed studies of outer solar system objects.

1.1.2 Galileo Mission

Galileo was a two-phase mission launched in 1989 and arrived at the Jovian system in 1995. The first phase included launching a probe into Jupiter's atmosphere to gather data about the atmospheric conditions. The second phase was an orbital tour of Io, Callisto, Ganymede and Europa to study the surfaces of these satellites. The orbiter mission included several different experiments (Table 1.1) which provided a significant portion of the data for this research. Galileo completed a total of 35 orbits, eleven of which targeted Europa (National Aeronautics and Space Administration, 2003). The images returned from Galileo's Solid-State Imager (SSI) were higher resolution than those from Voyager and allowed for a more detailed study of the 40

Experiment	Objectives
Dust Detector (DDS)	Measure particles' mass, velocity, and charge
Energetic Particles Detector (EPD)	Measure high-energy electrons, protons, and heavy ions in and around Jovian magnetosphere and study processes affecting these populations
Extreme Ultraviolet Spectrometer (EUV)	Investigate S, O ion emissions of the Io torus, and atomic and molecular H auroral and airglow emissions of Jupiter
Heavy Ion Counter (HIC)	Monitor the fluxes and composition of energetic heavy ions in the inner Jovian magnetosphere, and high energy solar particles in the outer magnetosphere, characterize the ionizing radiation
Magnetrometer (MAG)	Monitor magnetic field for strength and changes
Near-Infrared Mapping Spectrometer (NIMS)	Observe Jupiter and its satellites in the infrared to study satellite surface composition, Jovian atmospheric composition and temperature
Photopolarimeter Radiometer (PPR)	Determine distribution and character of atmospheric particles; compare flux of thermal radiation to incoming solar levels
Plasma Dectector (PLS)	Assess composition, energy, and three- dimensional distribution of low- energy electrons and ions
Plasma Wave (PWS)	Detect electromagnetic waves and analyze wave-particle interactions
Radio Science (RS): Celestial Mechanics	Determine mass of Jupiter and its satellites (uses radio system and high-gain antenna)
Radio Science (RS): Propagation	Measure atmospheric structure and objects' radii (uses radio system and high-gain antenna)
Solid-State Imaging (SSI)	Map Galilean satellites at roughly 1-km resolution, and monitor atmospheric circulation over 20 months while in orbit around planet
Ultraviolet Spectrometer (UVS)	Measure gases and aerosols in Jovian atmosphere

Table 1.1. Experiments onboard Galileo Orbiter and their mission objectives from (Johnson et al., 1992). Of particular interest to this proposal are the Solid-State Imaging (SSI), Near-Infrared Mapping Spectrometer (NIMS) and Magnetrometer (MAG).

percent of Europa's surface that was imaged. Galileo's Near-Infrared Mapping Spectrometer (NIMS) mapped the chemical composition of the surface of the icy satellites targeted. NASA's end of mission briefing (2003) highlights a few of the major scientific discoveries associated with Galileo. Of interest to this thesis are: (1) possible existence of a global ocean on Europa, and (2) evidence that Europa, Ganymede and Callisto have a liquid-saltwater layer. Additional scientific discoveries have been made since, through the continued analysis of data from Galileo.

1.1.3 Cassini-Huygen Mission

The Cassini-Huygens spacecraft was launched in 1997 to study Saturn's system in much the same way that Galileo studied Jupiter's. It arrived in the Saturnian system in 2004 where the Huygens probe separated from the orbiter and made its way to Titan, where it descended to the surface, and transmitted data via the Cassini orbiter. The Cassini spacecraft carried with it several instruments (Table 1.2) of key importance to this work. Including the Imaging Science Subsystem (ISS), Visible and Infrared Mapping Spectrometer (VIMS), and Cosmic Dust Analyzer (CDA),which are of key importance to this work as they provides insight to the appearance of the surface and presence of a jets of brine originating from the south polar terrain (Hansen et al., 2006).

Experiment	Objectives
Cassini Plasma Spectrometer (CAPS)	In situ study of plasma within and near Saturn's magnetic field
Cosmic Dust Analyzer (CDA)	In situ study of ice and dust grains in the Saturn system
Compositie Infrared Spectrometer (CIRS)	Temperature and composition of surfaces, atmospheres, and rings within the Saturn system
Ion and Neutral Mass Spectrometer (INMS)	In situ compositions of neutral and charged particles within the Saturn magnetosphere
Imaging Science Subsystem (ISS)	Multispectral imaging of Saturn, Titan, rings, and the icy satellites to observe their properties
Dual Technique Magnetrometer (MAG)	Saturn magnetosphere
Magnetospheric Imaging Instrument (MIMI)	Global magnetospheric imaging and in situ measurements of Saturn's magnetosphere and solar wind interactions
Cassini Radar (RADAR)	Radar imaging, altimetry, and passive radiometry of Titan's surface
Radio and Plasma Wave Science (RPWS)	Measure the electric and magnetic fields and electron density and temperature in the interplanetary medium and within the Saturn magnetosphere
Radio Science Subsystem (RSS)	Study of atmospheric and ring structure, gravity fields, and gravitational waves
Ultraviolet Imaging Spectrograph (UVIS)	Spectra and low resolution imaging of atmospheres and rings for structure, chemistry, and composition
Visible and Infrared Mapping Spectrometer (VIMS)	Spectral mapping to study composition and structure of surfaces, atmospheres, and rings

Table 1.2. Experiments onboard *Cassini* Orbiter and their mission objectives (Matson et al., 2002). Of particular interest to this proposal are the Imaging Science Subsystem (ISS) and Visible and Infrared Mapping Spectrometer (VIMS).

1.2 Synthesizing Mission Data

This dissertation utilizes data from the Voyager, Galileo, Cassini-Huygen missions to motivate numerical models of the potential formation mechanism of tectonic features on Europa and Enceladus. Both icy satellites have ample evidence that liquid water may play an important role in their tectonic processes. The work for this dissertation focuses specifically on the geologic setting and formation of Europan ridges and chaos, as well as the south polar terrain of Enceladus. All of the features examined show indications that cryovolcanic or cryomagmatic processes are involved in their formation. This allows my model results to provide constraints on the potential volume and location of liquid water on icy satellites. Observations and data from volcanic and magmatic processes on Earth informed the development of the models. Conversely I hope that the model results may be able to inform our understanding of volcanic and magmatic processes on Earth.

It is important to understand the tectonic setting for each of the features modeled, as well as their appearance. The next two sections provide a brief overview of Europa and Enceladus.

1.3 Europan Tectonics

Europa is the smallest of the Galilean satellites with a radius of 3,100 km, slightly less than the Moon. It has an average density of 3.01 $g/m^3$and is composed of an iron core, rocky mantle, and a global ocean beneath an icy shell (Anderson et al., 1998). Estimates of ice shell thickness range from 1 to 30 km (Cassen and Reynolds,

1979; Pappalardo et al., 1998; Collins et al., 2000; Figueredo and Greeley, 2004) with the whole of the cryosphere (ice and liquid water) ~100 km (Kivelson et al., 1997, 2000).

Europa has no atmosphere and surface temperatures range from 80 to 130 K, conditions that make common hexagonal (Ih) and amorphous ice the most likely forms of ice. Amorphous ice forms from both the rapid quenching of water at below ~110 K, and by the modification of crystalline ice by radiation bombardment (Hobbs, 1974; Leto et al., 1996). Based on NIMS data, the top ~1 mm of Europa is composed of predominantly amorphous ice (Hansen and McCord, 2004), though the majority of the ice shell is thought to consist of Ih ice based on phase diagrams. With a maximum shell thickness estimated at 30 km (~35 MPa), no other ice phase transition is expected within the shell.

The observation of a time varying induced magnetic field (via MAG) suggests the presence of salts in the global ocean (Kivelson et al., 1997). Additional evidence for a briny ocean comes from evidence for near surface salts (McCord et al., 1998; Sohl et al., 2010) and the modeled conductivity of the subsurface ocean (Schilling et al., 2007, 2008).

Impurities within the ice shell may impact the strength of ice (Hiraoka et al., 2008; Schulson and Duval, 2009) as well as the relative density of both water and ice. Porosity of the ice is also poorly constrained and has the potential to impact the rheological properties of the ice shell.

Based on cratering estimates, Europa's surface is thought to be only 30-70 Myr old (Zahnle et al., 2003). While geologically young, Europa's surface displays a wide range of geologic features. Of key interest to this work are ridges and chaos.

1.3.1 Ridges

Europa's most widespread features are ridges. Based on images from *Voyager* and *Galileo,* previous workers (Head et al., 1999; Greeley et al., 2000) have differentiated between several ridge morphologies, including single ridges, double ridges, complex ridges, which are nearly linear in map view, and cycloidal ridges, which have characteristic arcuate segments. Although these features are unique to themselves at a smaller scale they also have similar morphologies. The most ubiquitous ridges have a central trough flanked by two raised edifices (Kattenhorn and Hurford, 2007), called a double ridge. Double ridges are commonly long linear features that can extend 1000s of km and consist of two peaks separated by a central trough. The trough can be narrow or wide. Double ridges have an average height of a few hundred meters and width less than 5 km. Single ridges are also observed on Europa; these structures are ridges that appear to lack the central trough. Complex ridges display a range of morphologies including anastomosing or near-parallel ridges, ridges flanked by narrow troughs and ridges with a modified summital trough, featuring a flat floor or an irregular ridge (Johnston and Montési, 2014). Along-strike transitions are also observed (Johnston and Montési, 2014).

Chapter 2 evaluates if a crystallizing water body within the Europan ice shell has the ability to reproduce the overall appearance and properties of ridges on Europa.

In it I also evaluate the geometry and volume of the water body needed to obtain results consistent with Europan ridges.

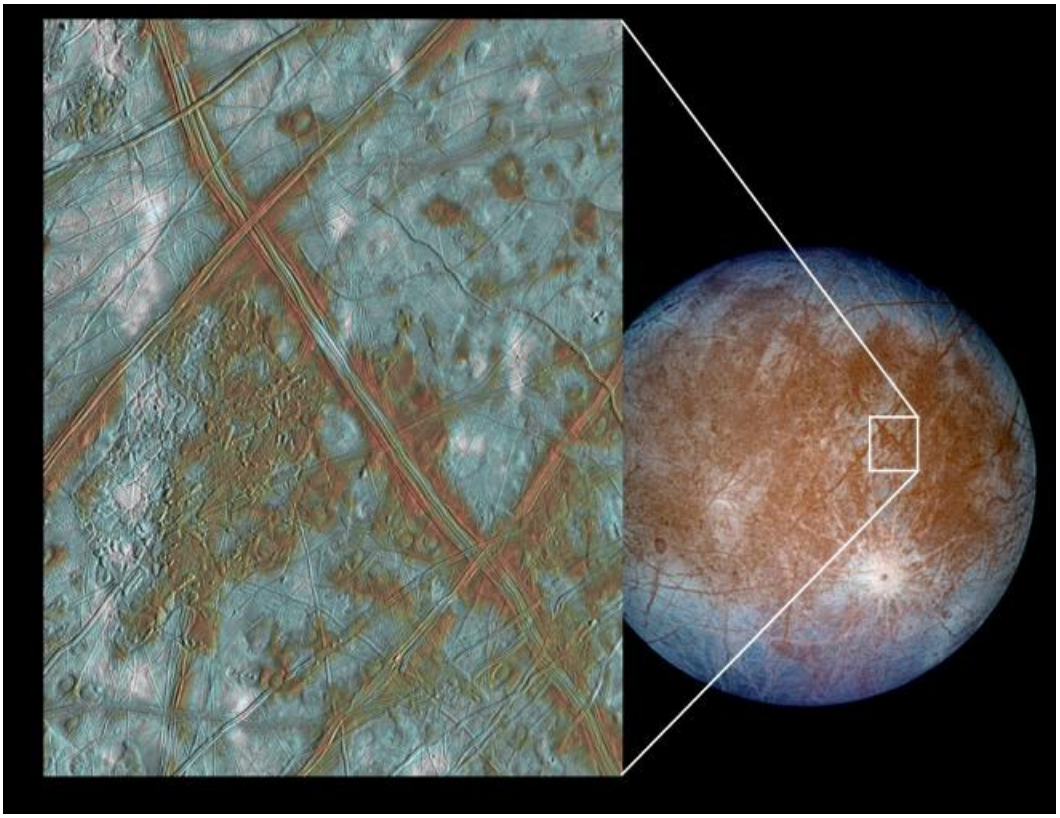

Figure 1.1. Conamara Chaos is shown in false color on the left. Color variations indication differences in surface composition with red indicating non-ice material and bright light blue indicating ice. NASA's photojournal image PIA03002 courtesy of University of Arizona.

1.3.2 Chaos

Chaos on Europa can be defined as regions of disrupted ice that contains blocks of preexisting material separated by a hummocky matrix. The identification, classification and subdivision of chaos is still debated (Greenberg et al., 1999; Schenk and Pappalardo, 2004; Collins and Nimmo, 2009). While Conamara Chaos (Figure1.1) is the iconic definition of chaos, the classification of other smaller features such as domes, pits, and lenticulae (Figure 1.2) are debated. Thera Macula is one such feature that has a similar appearance, and that has been argued to be chaos in the process of forming (Schmidt et al., 2011). Conamara Chaos, Thera Macula and other chaos are often associated with changes in albedo, suggesting that the composition of the ice could play a role in their formation.

Chapter 3 focuses on evaluating the ability of the formation mechanism proposed by Schmidt et al. (2011) for Thera Macula and other chaos. I model the stresses and strain resulting from the proposed formation mechanism and compare them with the present day appearance of Thera Macula.

1.4 Enceladus Tectonics

Enceladus is a small icy satellite of Saturn with a radius of ~ 252 km, and average density of 1.6 g cm^{-3}. It has one of the brightest surfaces in the solar system, consistent with fresh snow or ice (Smith et al., 1986; Verbiscer et al., 2005). Even highly deformed older terrain exhibit high albedo, suggesting that the entire surface is blanketed by fresh material (Buratti, 1988). The surface appears to have a

Figure 1.2. Domes, pits and lenticulae (dark pits) on the Europa. NASA's photojournal image PIA03878.

considerable range in age, with some regions estimated to be less than 200 million years old (Kargel and Pozio, 1996) and others potentially dating back to the age of the solar system (Spencer et al., 2006). This range in surface age has been interpreted to mean that Enceladus has undergone episodic resurfacing (O'Neill and Nimmo, 2010).

1.4.1 South Polar Terrain

The south polar terrain (SPT) is a heavily tectonized, geologically young region (Figure 1.3) surrounded by compressional folding belts hundreds of meters above the adjacent topography (Porco et al., 2006). The SPT is stratigraphically complex, including cross-cutting fracture patterns. Tiger stripes are geologically and morphologically distinct cracks that are ~130 km in length and quasi parallel through the SPT. They are ~2 km across with 100 m high flanking ridges. The tiger stripes also have an albedo ~10 percent brighter than the planetary average.

Tiger stripes are the source of eruptive water plumes (Hansen et al., 2006; Porco et al., 2006, 2014) and thermal anomalies (Spencer et al., 2006). The observation of water-rich plumes erupting from this region suggests a body of water lies beneath the SPT. Based on the global topography (Collins and Goodman, 2007) of Enceladus and numerical modeling (Tobie et al., 2008) a regional sea confined to the south pole has been suggested. However the fracture patterns observed suggest non-synchronous rotation which requires the decoupling of the ice shell from the rocky interior, most likely made possible by a global ocean (Patthoff and Kattenhorn, 2011). The ability to differentiate between the global and regional ocean on

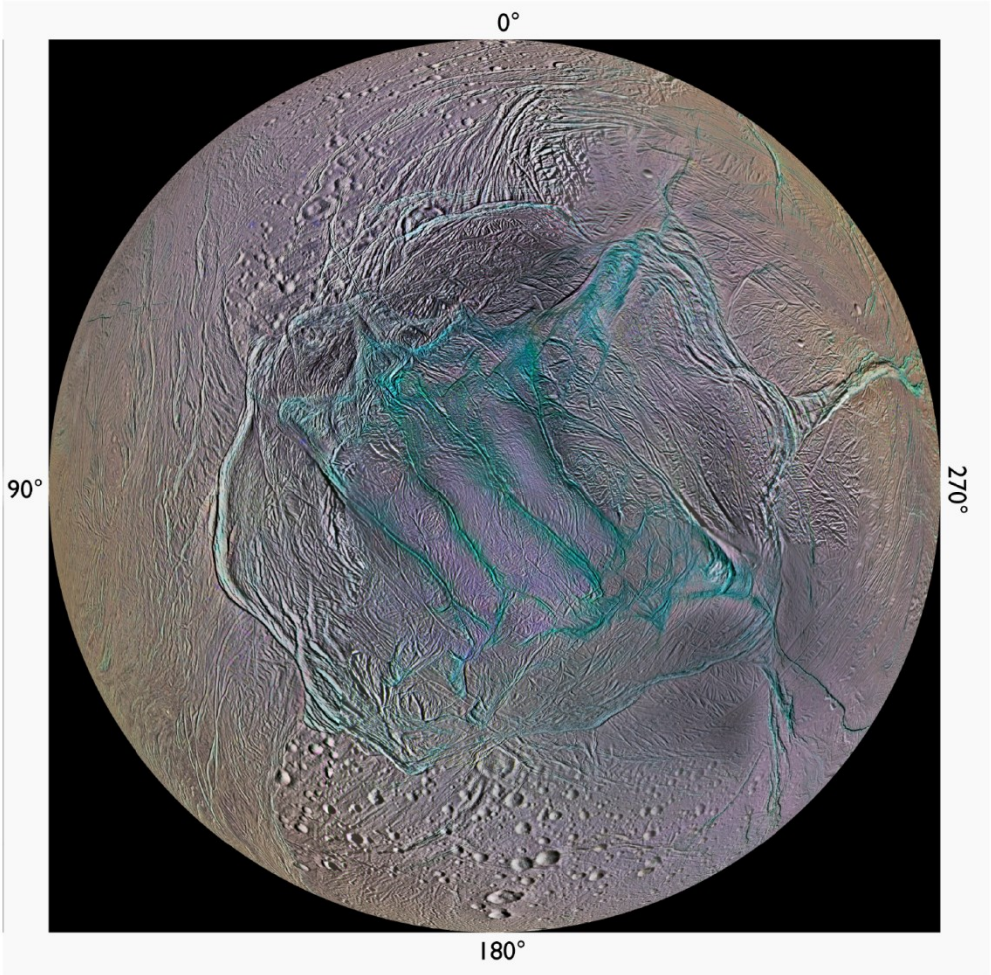

Figure 1.3. Enhanced color map of the south pole of Enceladus. NASA's photojournal image PIA18435.

Enceladus will have important implications for the thermal history and astrobiological potential of the icy satellite.

In chapter 4, I report the magnitude and pattern of stresses predicted by a model of a pressurized ocean beneath the south pole of Enceladus. I evaluate several model configurations, varying the ocean geometry, ice shell thickness, and basal boundary condition (bonded or partially decoupled). The model results are then compared with the present day appearance of the surface of Enceladus.

1.5 Outline of Dissertation

This dissertation is composed of five chapters, of which Chapters 2 through 4 are standalone manuscripts. Chapter 2 has been published in Icarus, a peer reviewed journal, . Chapter 3 and 4 will also be submitted for publication in a peer-reviewed journal. Chapter 5 is a summary of the work presented in this dissertation, and a discussion of the implications and possible future research.

Chapter 2 : Formation of ridges on Europa above crystallizing water bodies inside the ice shell

2.1 Abstract

Jupiter's second Galilean satellite, Europa, is a Moon-sized body with an icy shell and global ocean approximately 100 km thick surrounding a rocky interior. Its surface displays extensive tectonic activity in a geologically recent past. Europa's most ubiquitous surface features, double ridges, have a central trough flanked by two raised edifices. Double ridges can extend hundreds of kilometers and appear genetically related to cracks formed in the Europan ice shell. The origin of the raised flanks has been the center of much debate and many models have been proposed. There are also ridges without a central trough, single ridges. These ridges are far less common than their double ridge counterparts. However, there are locations where along-strike changes in ridge type appear to occur. We explore an elastic model in which the ridges form in response to crystallization of a liquid water intrusion. In our model, liquid water fills tension cracks that open in the Europan crust in response to tidal stress or perhaps overpressure of a subsurface ocean. The crack would be long and essentially continuous, similar to dikes on Earth, explaining the remarkable continuity and lack of segmentation of Europan ridges. The freezing of the water would cause a volume expansion, compressing and buckling the adjacent crust. We find that the geometry of the intruding water body controls the shape of the resulting ridges, with single ridges forming above sill-like intrusions and double ridges above dike-like intrusions. In order to match the ridge heights observed for double ridges,

approximately 1.5 km^2 of water would need to be intruded at a shallow depth in the ice shell, potentially over the course of multiple events. Deeper intrusions result in a broader, lower amplitude ridge than shallow intrusions.

2.2 Introduction

The most ubiquitous features on Europa are double ridges, which consist of a central trough flanked by two raised edifices (Head et al., 1999; Greeley et al., 2000; Kattenhorn and Hurford, 2007). They are most often long linear features that extend hundreds of kilometers. However, there are also cycloidal ridges that have curved segments joined by together by cusps. Understanding the formation process of ridges can provide constraints on the structure of the ice crust and with it the thermal evolution of the satellite. We show that the morphology of double ridges can be explained by the deformation of the ice crust of Europa over a crystallizing water-filled crack.

Below we summarize ridge morphology and the various models proposed for the origin of ridges. We also motivate the consideration of this model by reviewing the evidence for water bodies inside the crust of Europa. Then we describe the setup of our models and the relation between the geometry of the crystallizing water body and surface features.

2.3 Water in the Europan ice shell

The presence of a time varying induced magnetic field around Europa (Kivelson et al., 1997) suggests that the ~100 km thick global H_2O layer of Europa (Anderson et al., 1998) is composed of a briny global ocean covered with an ice shell estimated to be between 1 and 30 km thick (Cassen and Reynolds, 1979; Pappalardo et al., 1998; Collins et al., 2000; Figueredo and Greeley, 2004). It is the presence of this ocean that, among other things, makes Europa such an important planetary body to understand, as liquid water is believed to be necessary to support life (e.g., Reynolds et al., 1987; Chyba and Phillips, 2002). An abundance of liquid water also creates a unique geologic setting, especially for magmatic and volcanic processes.

Albedo changes and a reddish coloration, observed in images from Voyager and Galileo missions, are associated with many surface features including ridges, lenticulae, chaos terrain and bands (e.g., Greeley et al., 1998). A change in surface properties suggests a change in surface composition from relatively pure water ice. The precise composition of the impurities that create the red coloration is not known, however. Observations from the Near Infrared Mapping Spectrometer (NIMS) onboard Galileo are compatible with hydrated salts such as magnesium and sodium sulfates (McCord et al., 1998, 1999; Kargel et al., 2000; Prieto-Ballesteros et al., 2005). The reddish coloration on the shell is rarely related to undisrupted regions of ice with relatively no observable features, suggesting that the mechanism(s) responsible for transporting or concentrating the impurities at the surface may also play a role in the formation of the features. McCord et al. (1998) suggests that impurities may be carried by water or slush making its way to the surface. During the

crystallization of salt water, brine rejection often observed on Earth causes the ice to contain significantly less impurities than the water from which is crystallized from (e.g. Lake and Lewis, 1970). A similar process active during the freezing of the ice shell on Europa would result in highly concentrated brine that, when it finally crystallizes at the surface, would produce the compositional heterogeneities observed on Europa.

Manga and Wang (2007) determined that cracks can form from a pressurized ocean beneath the shell. As Europa cools and its shell thickens, it would freeze downward. Since water expands when it freezes this would create a force that acts on the surface of the global ocean to pressurize it. Water is mostly incompressible causing it to exert a restoring force back on the base of the ice shell, creating cracks when the strength of the ice is exceeded. Manga and Wang (2007) showed that stress gradients in the shell cause these cracks to penetrate through the entire shell. Water can rise inside the crack to a level of equilibrium inside the shell, which, in the absence of ocean overpressure, would be approximately 90% of the shell thickness. Ocean overpressure pushes water slightly higher than this level but is not sufficient to push water to the surface, causing eruptions (Manga and Wang, 2007). Moreover, ocean overpressure would diminish if water was free to be expelled to the surface, negating any long term effect of ocean pressurization. Nevertheless, cracks would provide a pathway for water to move into the ice shell. Heterogeneities within the ice can further facilitate lateral and vertical movement of water within the ice shell, by depressing the melting temperature of pure ice. Heterogeneities are common in the

Earth's crust and are observed in sea ice on Earth (Kusunoki, 1955); while the settings differ, heterogeneities may still be possible in ice on Europa.

The clearest evidence of cracks at the surface of Europa is in the form of long, continuous fractures that take on a cycloidal trajectory. The depth to which cracks extend may be debated (Hoppa et al., 1999; Lee et al., 2005), but their abundance is irrefutable. Pressurized water near a crack may be injected into it, following the pre-existing trajectory of that crack. Depending on the stress conditions near an intrusion and the extent of pressurization of the reservoir injecting water into the cracks, freezing has the ability to aid in the perpetuation of a crack. The models described below presuppose the presence of a liquid water body inside the ice shell. Determining the source and migration of this water body is beyond the scope of this model. Instead, the observed correlation between ridges and albedo changes provides motivation to investigate the formation of ridge-like features above a confined crystallization of body of water.

2.4 Morphology of double ridges and proposed formation models

Coulter (2009) and Coulter et al. (2009) describe the characteristic dimensions of ridges on Europa. Ridge height ranges from tens of meters to 400 m and ridge width is usually less than 3 km. A maximum ratio of ridge height to width was observed, suggesting that ridges cannot be wide and tall. However, a few ridges have widths just over 4 km but a relief not exceeding 400 m. The outer sides of double ridges have slopes measured to be less than 28˚, implying that ridges are not formed principally by surface processes such as mass wasting.

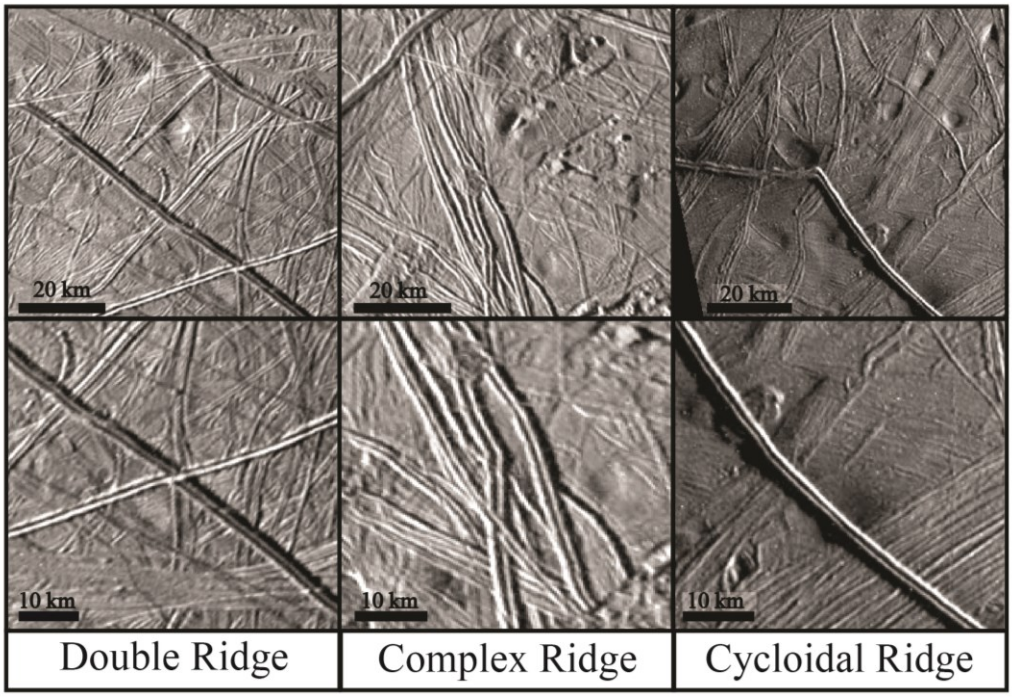

Figure 2.1. Types of ridges on Europa. Images of a single ridge (left), a complex ridge (middle) and a cycloid ridge (right) are show at low and high magnification on top at the bottom. Galileo SSI images 17E0092, 17E0002, and 15E0090. High magnification morphologies are remarkably similar in spite of the difference planforms of these features as a whole.

Previous workers (Head et al., 1999; Greeley et al., 2000) have differentiated between several ridge types, including single ridges, double ridges, complex ridges and cycloidal ridges. All of these ridges are nearly linear in map view, with the exception of cycloidal ridges, which have characteristic arcuate segments joined together by cusps (Figure 2.1). Although each of these ridge types is clearly distinguishable from the others at regional scale, ridge morphology is remarkably similar for all these ridge types when viewed at a scale of a only a few km (Figure 2.1).

Cycloidal ridges have double ridge morphology (Figure 2.1) but appear as linked arcuate segments rather than continuous, linear features. The formation of cycloids is often considered separate from ridges because this unique trajectory is well predicted by models of crack propagation in a rotating diurnal stress field (Hoppa et al., 1999; Hurford et al., 2007a, 2007b; Rhoden et al., 2010, 2012). However, the fine scale morphology of cycloidal ridges is similar to that of linear ridges. Cycloids also can transition along strike to quasi-linear trajectories, similar to double ridges. Therefore, any model that proposes to explain ridge morphology must also be applicable to cycloids.

Complex ridges are often composed of several ridges that run parallel or anastomose to one another. It has been suggested that these features are formed by the successive build-up of double ridges (Figueredo and Greeley, 2004). It is not hard to imagine that complex ridges are gradually formed by several ridge building events because the individual morphology of these ridge pairs is remarkably similar to double ridges (Figure 2.1). Figure 2.2 shows some ridge morphologies, indicated by

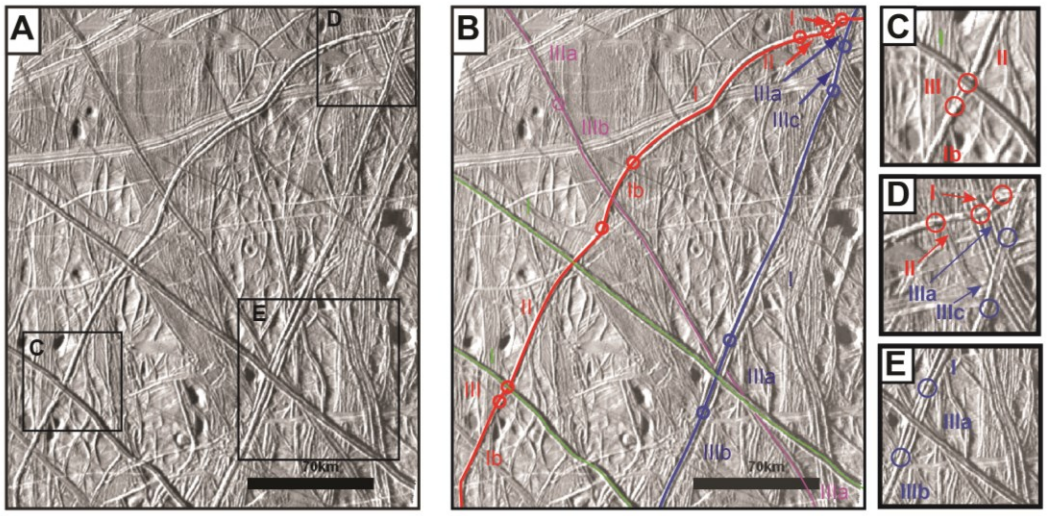

Figure 2.2. Along strike changes in morphology. (A) Galileo SSI image mosaic of Europa's surface centered at 77˚W, 45˚S with (B) interpretation and (C–E) close-ups. Five major ridges are identified in the image. The type of morphology and transitions (circles) are marked. I: Double ridge with variant IB as a ridge with narrow summital trough; II: single ridge; III: complex ridge with variants IIIa (subparallel ridges), IIIb (trough-flanked ridge), IIIc (ridge with flat-floored trough), IIId (ridge with modified trough).

roman numerals, and along strike transitions, indicated by circles. Boxes C, D and E illustrate the fine scale morphology changes of ridges from boxes A and B. There are double ridges (I) with narrow summital troughs (Ib); single ridges (II) and complex ridge (III) with variants. The range of morphologies for complex ridges extends beyond parallel and anastomosing, to ridges flanked by narrow troughs (IIIb) and ridges with a modified summital trough, which could be expressed as subparallel ridges (IIIa) or a flat floor (IIIc), possibly hummocky. These modified troughs may indicate that volcanic processes play a central role in ridge development (Fagents, 2003).

Along-strike transitions between different ridge morphologies and cracks are not uncommon. Figure 2.2 shows some of the transitions identified and indicated by circles in a region centered at 77˚W, 45˚S. The similarities in small-scale ridge morphologies (Figure 2.1) and along strike transitions between ridge types (Figure 2.2) motivates us to look for a unifying process that can be active in the formation of all the ridge types described.

Single ridges are also observed on Europa. Figueredo and Greeley (2004) observed that single ridges are usually associated with chaotic terrain and suggests they may be a part of the formation mechanism for chaotic terrain. The fact that these ridges cut across chaotic terrain and are often slightly more sinuous than double ridges in their trajectory (Figueredo and Greeley, 2004) supports their distinct classification. However, single ridges are also found outside of chaos terrain (Figure 2.2). Also, we cannot rule out that single ridges may be double ridges that are just below the resolution of the images so that the central trough cannot be recognized. If

they are not single ridges they must be double ridges with narrower troughs, indicating some change in morphology and near surface conditions. In the absence of higher resolution images we assume that these are indeed single ridges.

Many models of ridge formation have been proposed including tidal working, cryovolcanism, and shear heating. Greenberg et al. (1998) proposed that diurnal tides caused a pre-existing crack to open and fill with water, then close and squeeze water and partially frozen ice onto the surface. This model has only been applied to the formation of double and complex ridges, leaving single and cycloidal ridges unexplained. It is also unclear if it would be able to explain the full range of ridge heights observed. Moreover, flow morphologies are rarely observed along ridge flanks (Head et al., 1999).

Kadel et al.'s (1998) cryovolcanic model calls for the eruption of material from a fissure that builds up levees, which form the double ridges. While levees are present at volcanic fissures on Earth (e.g. Thordarson and Self, 1993), we do not yet know if erupted water at Europa would behave similarly. Levees can form on the edge of flowing lava rivers, but it is clear from cross-cutting relations between double ridges or individual strands of complex ridges that double ridges are not strongly influenced by pre-existing topography (Figure 2.1). Levees are separated by a flat-floored channel rather than a narrow trough, limiting their analogy with Europan double ridges. Levees can also form at fissure eruption sites. One of the largest volcanic fissure systems on Earth, Laki, extends 27 km and features levees. Individual fissures are not continuous along its entire length and instead include regions devoid of these volcanic levees, splatter cones, and lava flows originating

from the levees (Thordarson and Self, 1993). Although splatter may be difficult to observe in the low gravity, low pressure environment of Europa, we would expect to observe significant variability along the strike of ridges if they were formed along a fissure eruption site. Therefore, a purely cryovolcanic process appears unlikely as the origin of ridge flanks.

Shear heating (Gaidos and Nimmo, 2000; Nimmo and Gaidos, 2002; Han and Showman, 2008) is a popular model proposed for double ridge formation. In this model movement along a crack is caused by diurnal tides and generates heat within Europa's ice shell. The generated heat warms the surrounding ice to buoyantly uplift the crust by ~100 m (Nimmo and Gaidos, 2002). The heat generated by the strike slip motion could also create some degree of melting, leading to subsidence near the center of the ridge and forming the double ridge morphology. Ridge heights obtained by this model are ~100 m, of the same order as, but somewhat less than the tallest ridges observed on Europa. It is also unclear to what extend the ridges would relax as the heat that generates flank uplift diffuses away. At this point, it is unclear how the shear heating model produces complex ridges without destroying previous generations of ridges that overlap and anastomose.

Dombard et al. (2013) suggest that intruding water, specifically sills, must be involved in the formation of ridges on Europa in order to explain the flexure and flanking troughs that can be associated with ridges. This model could potentially operate in conjunction with other proposed mechanism, such as shear heating. However, the flexure and fractures are not observed at all ridges on Europa, so the extent to which this applies to all ridge formation is unclear.

2.5 Model description

2.5.1 Model setup

Our model evaluates the surface deformation and stresses that result from the expansion of a crystallizing water body within an elastic ice shell. It is also attempts to estimate the volume of water required in order to match observations of ridges on Europa. While we have postulated that cracks may be a conduit by which water could move into or through the ice shell, crack generation is ignored in this model in order to gain an understanding of the most fundamental behavior of this model. We focus instead on the elastic deformation of the ice shell around a crystallizing water body without complicating factors that would, for example, change the shape of water body or create zones of weakness in the shell. These effects will be explored in future models that build on the ones presented here.

The elastic response of ice to crystallizing water within the ice shell is modeled using the commercially available finite element software, Abaqus™. Finite element methods make it possible to prescribe a complex geometry to model domains such as the water body and determine its response to imposed stresses and conditions (Kavanagh and Clough, 1971). The model is a 2-D cross-sectional view of the ice shell and intrusion (Figure 2.3) deforming under plane strain assumptions. A 2-D model was selected for its simplicity in understanding the fundamental processes related to a crystallizing intrusion in an ice shell. Also, the length of the intrusion in the third dimension is so great that along-strike gradients are expected to be negligible, motivating the plane strain assumption (Turcotte and Schubert, 2002).

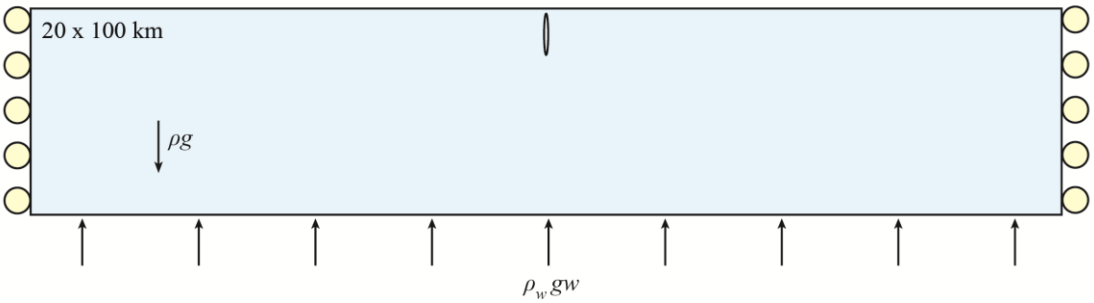

Figure 2.3. Model geometry. The 2-D finite element model represents a 20 km thick and 100 km wide vertical section through the ice shell. Roller boundary conditions on the side of the model allow only vertical movement. Gravity is imposed on the entire model. A water body is represented by a pressurized void (Fig. 4) located in the horizontal center of the ice shell, and whose depth and aspect ratio are varied. An elastic foundation is applied to the base of the ice shell, representing the restoring force an underlying global ocean.

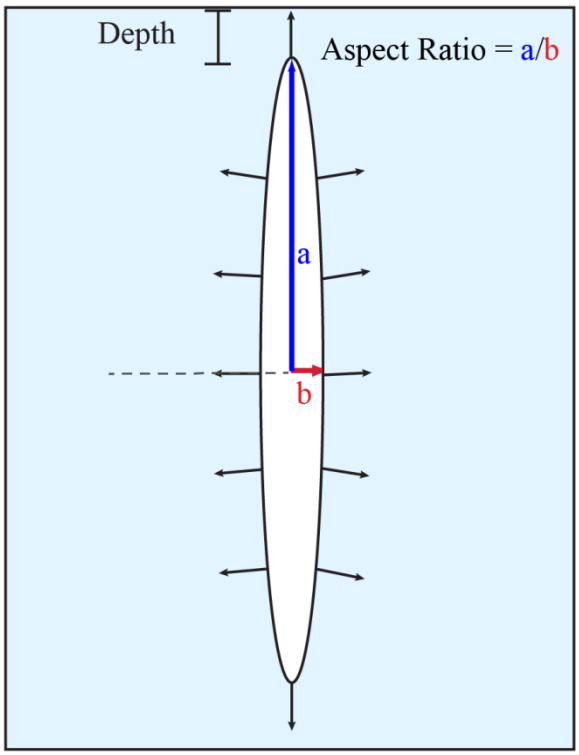

Figure 2.4. Model geometry near the water body. A fixed overpressure was applied to the edge of the intrusion (black arrows). Depth was measured from the surface of the ice shell to the top of the intrusion. The aspect ratio of the intrusion is defined as the vertical axis, a, over the horizontal axis, b. The initial volume of the intrusion is set to $\pi ab \sim 0.225$ km^2.

The model considers an ice shell 100 km across and 20 km thick for all results except for a parametric study in which ice shell thickness was varied. The width of the ice shell was selected after several test runs to minimize the impact of any side boundary conditions on the deformation observed above the intrusion.

Stress free, rolling-type boundary conditions are imposed on the lateral sides of the model to prevent extension of the ice shell, as this behavior would not be expected on a one-plate planet object like Europa. The values used for Young's modulus E, Poisson's ratio, m and ice density ρ_w are included in Table 2.1. Gravity is imposed on the entire model as a body force. The top surface is stress free but an elastic foundation is applied to the base of the model to simulate the restoring force associated with the global ocean beneath the shell so that the shell is isostatically supported. The restoring stress of the elastic foundation is calculated by

$$\sigma_{yy} = \rho_w g w, \qquad \text{Eqn. 2.1}$$

where σ_{yy} is the stress applied to the bottom of the shell, ρ_w is the density of the liquid water, g is the Europan gravity, and w is the deflection of the bottom edge of the model.

The water intrusion is represented by an elliptical void with major axes with aspect ratio *a/b* following the convention that *a* is the semi-axis in the vertical direction and *b* the semi-axis in the horizontal direction. Fig. 4 illustrates these definitions in the case of a dike-like intrusion, where $a > b$. The aspect ratio is varied between 10 and 0.1 in order to evaluate the role of the 2-D intrusion geometry in the deformation of the ice. An aspect ratio larger than 1 corresponds to a dike-like

Symbol	Definition	Value
E [a]	Young's modulus	0.9 GPa
ρ_i [b]	density of ice	930kg m^{-3}
ρ_w [b]	density of water	1000 kg m^{-3}
ν [b]	poisson's ratio	0.325

[a] Source is (Collins et al., 2010)

[b] Source is (Petrenko and Whitworth, 1999)

Table 2.1. Mechanical properties and values used in the model.

intrusion and an aspect ratio less than 1 indicates a sill-like intrusion. The intrusion is a circle when the aspect ratio is 1.

In all our models, the initial cross-sectional area of the intrusion is fixed to πab ~0.225 km^2. The intrusion is centered horizontally within the ice shell. The depth and the aspect ratio a/b of the intrusion are varied systematically in the model. While our model presupposes the existence of a crack as a conduit for water to move in and through the shell, our model geometry does not actually include the presence of a crack, assuming that the crack healed everywhere except where the water body is defined, as the presence of liquid water may prevent the crack healing.

2.5.2 Crystallization

Because the density of ice is less than that of (liquid) water, crystallization would increase the volume of the water body, originally V, by

$$\frac{\Delta V}{V} = \frac{-\Delta\rho}{\rho} \qquad \text{Eqn. 2.2}$$

where $\Delta\rho = \Delta\rho_w - \Delta\rho_i$ is the change of density upon crystallization.

In a solid material, volume change is related to a change of pressure ΔP through the bulk modulus K according to

$$K = \Delta P \frac{\rho}{\Delta\rho} = -\Delta P \frac{V}{\Delta V}, \qquad \text{Eqn. 2.3}$$

The bulk modulus likely changes upon crystallization. If we use a value characteristic of water, K = 2.2x10^9 Pa, we estimate that the maximum pressure generated by crystallization is about 150 MPa. The actual pressure will likely be less as ice probably undergoes brittle failure and water may be extruded to the surface. Repeated episodes of crystallization and replenishment of the water body would have

the effect of increasing overpressure. Our reference models use ΔP = 100 MPa but we consider ΔP ranging from 50 MPa to 500 MPa.

In this model, we capture the effect of crystallization by imposing a uniform overpressure around the edge of the water body. Overpressure is expected to be uniform if the interior of the intrusion is liquid, clearly a simplification of this model. This approach allows the water body to change shape as the ice shell around it generates a heterogeneous stress field in response to the water body overpressure. The final area of the water body, A_f, is estimated from the convex hull around the nodes that define the boundary of the water body. The liquid water area corresponding to the final ice body is given by

$$A_w = A_f \frac{\rho_i}{\rho_w} \qquad \text{Eqn. 2.4}$$

The actual overpressure corresponding to crystallization of the intrusion is the one for which $A_w = \pi ab$ ~0.225 km^2. However, we will see that generating realistic ridge morphologies requires higher overpressure, which can only be generated if water is added to the system, that is, if our model represents the integrated effect of several episodes of water body emplacement and crystallization. Preliminary work on details of this process, its energetics, and the conditions for which repeated intrusions are possible, has been conducted by Melosh and Turtle (2004).

2.5.3 Deformation around crystallization and intruding water

Our model focuses on the deformation associated with the crystallization of a water intrusion within an ice shell. In order to simulate the expansion caused by the crystallization of the water intrusion, an overpressure was imposed on the shell-intrusion boundary.

The response of an elastic material to a stress tensor σ is given by

$$\varepsilon_{ij} = \frac{1}{E}[(1+\nu)\sigma_{ij} - \nu\sigma_{kk}\delta_{ij}], \quad \text{Eqn. 2.5}$$

where ε is the strain tensor, E is the Young's modulus, ν is the Poisson's ratio, and δ is the Kronecker operator. In plane strain ε_{zz}, ε_{xz}, and ε_{yz} are zero and the relationship between the stresses can be simplified to

$$\begin{cases} \sigma_{zz} = \nu(\sigma_{xx} + \sigma_{yy}) \\ \sigma_{xz} = \sigma_{yz} = 0 \end{cases}. \quad \text{Eqn. 2.6}$$

In the finite element method, the equations describing momentum conservation are expressed as their weak form and integrated over elements that each cover a small fraction, or element, of the ice shell. The result is a stiffness matrix relating displacement on a set of points, or nodes, that are used to define the elements, and the forces applied on these same nodes. This system of equations is solved so that self-consistent displacement and stress fields are defined over the ice shell. These equations are not solved over the water body, which only generates an overpressure along its boundary with the ice shell, not a full, spatially variable stress field.

The finite element mesh is dominated by quadrilateral elements and is refined near the intrusion (Figure 2.5). Directly above and below the intrusion, nodes are spaced only 2 m apart. Such a fine mesh is necessary to accurately capture the deformation field directly above the intrusion and to precisely measure the trough widths in double ridges. At the farthest edges the mesh is seeded only every 3200 m in order to reduce computational time. As the region near the intrusion is the area of interest, a coarser mesh at the edges is acceptable. A finer mesh at the far edges did

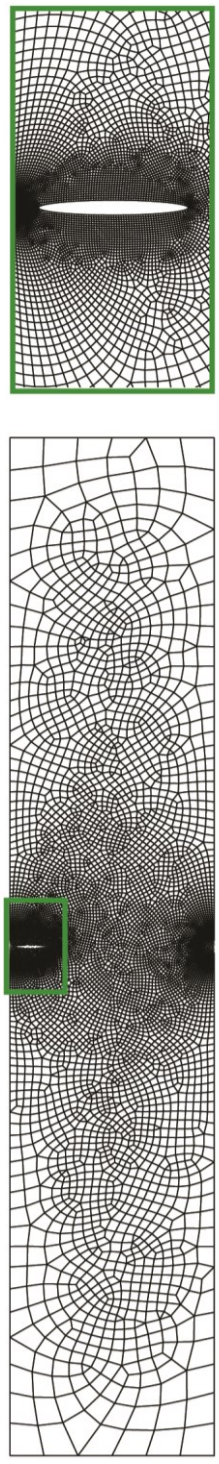

Figure 2.5. Example finite element mesh created in Abaqus™ for an intrusion aspect ratio of 10 and depth 2 km. The mesh is defined as ‘‘quad-dominated’’ with seeds along the boundary of the model. Seed spacing varies horizontally from 2 to 3200 m from the center to the edge of the model and at 2 m along the intrusion.

not have any significant impact on the general appearance of the ridge, nor did it impact the deformation observed near the intrusion.

Gravity is important in our model because of the isostatic restoring force present at the base of the shell. For consistency, we impose gravity as a body force throughout the shell. However, as we do not solve the momentum equations in the water body, it acts as a massless void inside the shell, which generates a deformation field when gravity is imposed. The ice shell must ‘‘sink’’ into the ocean when gravity is imposed until hydrostatic equilibrium is achieved. These effects are an artifact of the model setup that defines geometrical shapes in the absence of gravity. Because the equations of elasticity are linear, they obey of the principle of superposition of solutions. Therefore, we isolate the effect of over-pressurization of the water body upon crystallization by removing from the displacement field obtained with both overpressure and gravity the deformation field obtained by gravity alone. Although complex, this strategy is necessary to capture accurately the interaction between overpressure and the density contrasts present at the surface and along the base of the ice shell.

In practice, we run the model in two steps. In step 1, only gravity is imposed. In step 2, both the gravity and overpressure of the intrusion are imposed. At each step we record the displacement values for each node. We isolate the effect of pressurization by removing the values obtained at step 1 from the displacements obtained at step 2.

2.6 Results

Model results are presented in two principal manners. One is the distribution of stress in the ice shell (Figure 2.6) from which we can understand the mechanics of model deformation, and the other profiles of displacement at the surface of the ice shell (Figure 2.7), which are directly compared to the morphology of ridges observed on Europa. Pressurization of the water body compresses the ice surrounding it, resulting in a topographic high immediately above the intrusion if the intrusion is in the upper half of the model. If the intrusion is in the lower part of the model, a broad depression appears at the surface while an inverted ridge develops at the base of the model. This situation does not correspond to any observation of tectonic features on Europa. Below, we present in turn the effects of the initial aspect ratio of the intrusion, its depth, its overpressure, and finally the thickness of the ice shell on the morphology and the size of ridges generated above crystallizing water bodies.

2.6.1 General results

The region of the shell in contact with the intrusion is put under compression as the intrusion pressure increases. Figure 2.6 shows the pattern of stress around the intrusion, which determines the surface deformation. Stress is concentrated in four lobes on the ends of the intrusion that have the smallest radius of curvature. Stress is generally higher in the relatively thin layer of ice immediately above the intrusion. In our reference models, where water overpressure is 100 MPa, stress is sufficiently high at these points to induce plastic failure. However, our models only consider the elastic behavior of ice. The effects of plasticity are left to a future study. The gray regions in

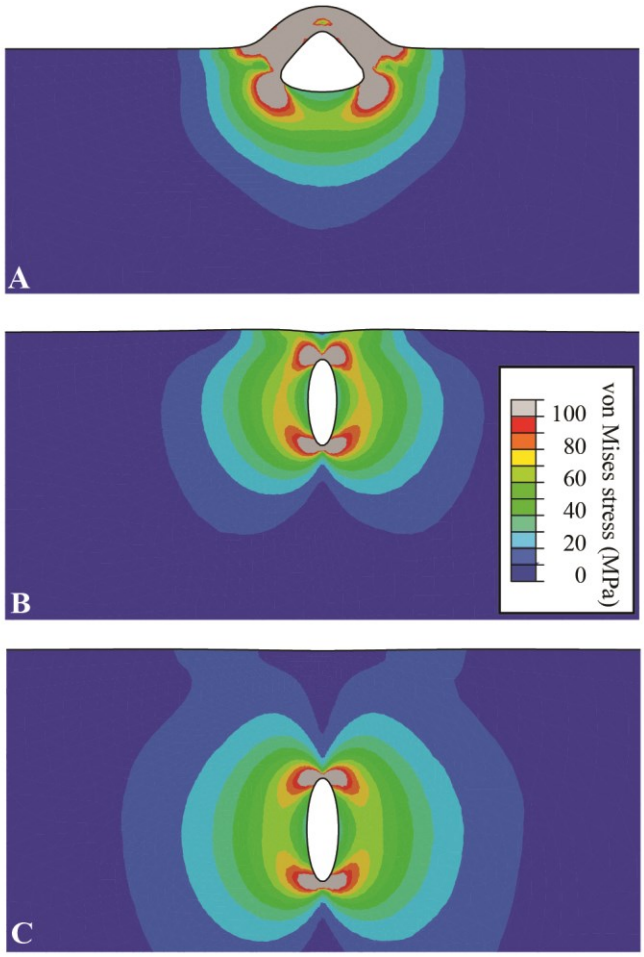

Figure 2.6. Von Mises stresses around a pressurized intrusion of aspect ratio 0.1 (A) or 10 (B and C) and depth 500 (A and B) or 2000 m (C). The deformation is enhanced to facilitate visualization. Regions highlighted in gray have a von Mises stress larger than 100 MPa and may indicate where failure takes place, although failure is not included in these models.

Figure 2.6 indicate areas where failure would be anticipated in a plastic material.

The geometry of the water body exerts a first-order control on the distribution of stress within the shell. The regions of stress enhancement generated above a sill-like intrusion focus into a single point at the surface, creating a broad ridge as the surface is bent upward (Figure 2.6a). In contrast, for a dike-like intrusion (Figure 2.6b) the zones of high stress concentration diverge near the surface. A similar split in the stress enhancement region has been observed in other models of interaction between a crack and a free surface, whether the crack is pressurized or passive (Pollard and Holzhausen, 1979; Mastin and Pollard, 1988; Schouten et al., 2008; Mitchell et al., 2011). The surface is uplifted in two ridges where the stress along the surface is at a maximum. The separation between these two regions of stress enhancement increases as the depth of the intrusion increases (Figure 2.6c).

2.6.2 Effect of the aspect ratio of the water body

Varying the aspect ratio of the water body reveals the impact of the 2-D geometry of the intruding water body on the surface deformation in the ice shell. A change in the aspect ratio changes the surface deformation from a single ridge to a double ridge. A dike-like intrusion creates a double ridge while a sill-like intrusion generates a single ridge.

Figure 2.7 illustrates the variability of surface topography obtained in our models. Profiles are shown without vertical exaggeration (Figure 2.7A and B) and with a 10:1 vertical exaggeration (Figure 2.7C and D) in order to better observe the produced morphologies. Only the central part of the models is shown in Figure 2.7A and B. In all these models, the water body overpressure is 100 MPa.

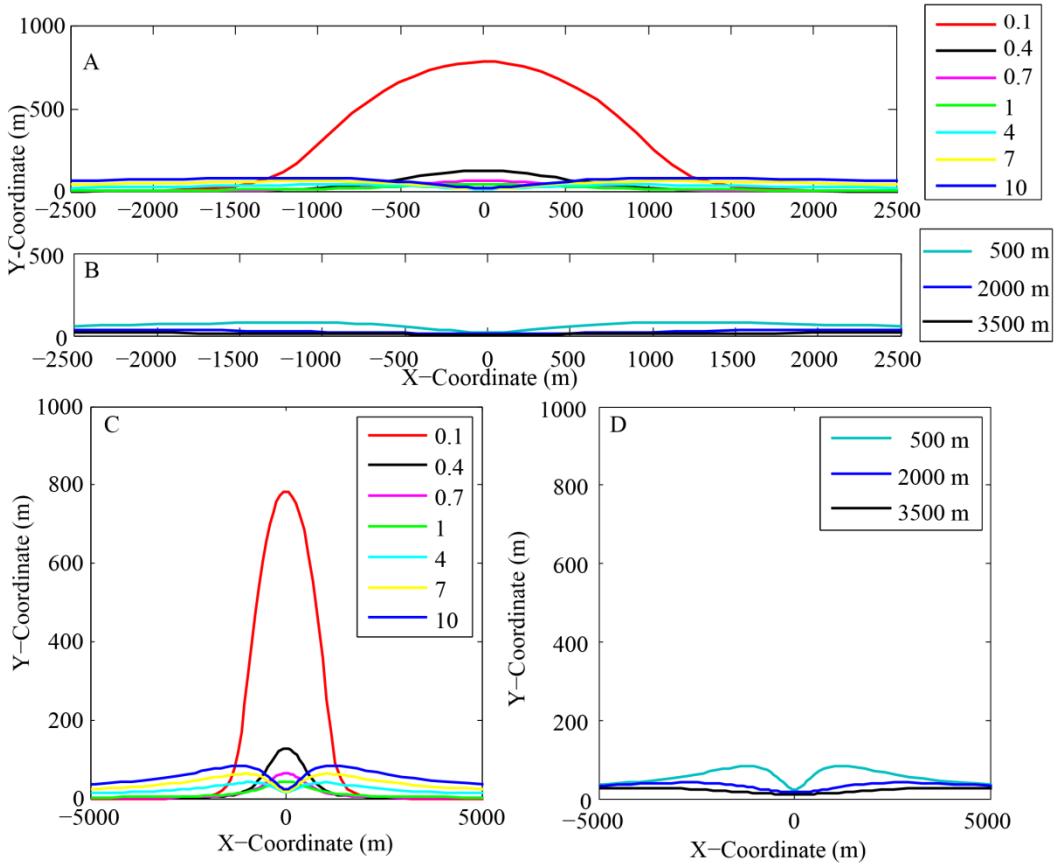

Figure 2.7. Surface displacement profile for (A) intrusions at 500 m depth and various aspect ratios or (B) intrusion with an aspect ratio of 10 and various depths. (A and B) Do not have vertical exaggeration. Panels (C and D) show the central portion of the same displacement profiles as (A and B) but with 10x vertical exaggeration.

Figure 2.7A and C shows how topography varies with the aspect ratio of the water body. The depth of the intrusion is fixed to 500 m in this model series. A single ridge is formed when the aspect ratio is between 0.1 and 1. The lower the aspect ratio of the ridge, the higher the ridge, probably because the width of the water body becomes similar to the flexural wavelength of the layer of ice above the intrusion. The highest ridge obtained in this model series is 784 m when the aspect ratio is 0.1, the lowest aspect ratio considered here. Aspect ratios above 1 produce a double ridge at the surface. Ridge height increase with aspect ratio and reaches 105 m at the highest aspect ratio considered, 10. The higher ridge at extreme aspect ratios is likely due to the increase in stress concentration intensity when the radius of curvature decreases.

The double ridge morphology obtained for dike-like water bodies (aspect ratio larger than 1) is qualitatively similar to double ridges on Europa. The width of the trough defined as the space between the two ridges is also influenced by the aspect ratio. As the aspect ratio increases the trough width increases (Figure 2.8), probably because the average depth of the water body increases with the aspect ratio. With a pressure of 100 MPa and at a depth of 500 m, the maximum trough width obtained was in excess of 2000 m.

2.6.3 Effect of the depth of the water body

As the depth of the water body increases, the amplitude of stress concentration at the surface decreases and, if the aspect ratio is larger than 1, the separation between these zones of stress concentration increases. Figure 2.7B and D shows that this is reflected in the amplitude and width of the ridges that develop at the surface.

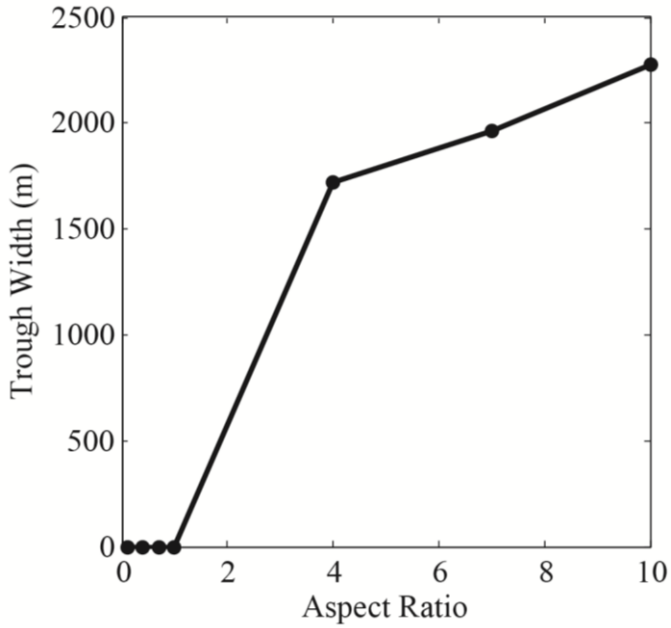

Figure 2.8. Trough width as a function of intrusion aspect ratio. The trough width increases with intrusion depth. The depth of the intrusion is fixed to 500 m and overpressure to 100 MPa.

Considering only a water body with aspect ratio of 10 and 100 MPa overpressure, the peaks of the double ridges become both more subdued and farther apart as the depth of the water body increases, tracking the location and intensity of the zones of stress concentration at the surface.

The ridge height increases with decreasing depth if the inclusion is in the upper half of the shell (Figure 2.9). Then, in the bottom half of the shell, the inclusion generates a broad depression at the surface with a ridge morphology at the base of the ice shell. The increase in height shown in Figure 2.9 observed after 10 km depth is due to a broad upwelling in response of the ice shell to the inverted ridge at the base, not the creation of a ridge at the surface. The single ridge, associated with a sill-like intrusion, however, continues to decrease in height after 10 km depth. The maximum height is obtained for the smallest depth considered in these models, 500 m. In that case, the double ridge is 105 m high and the single ridge 800 m tall.

The initial area of the intrusion remains the same for each model but because we impose an overpressure on the water body, the change in the volume of the intrusion and thus the final size of the body is a result of the model (Eq. (4)). The depth of the intrusion also impacts the amount of water intruded into the ice shell at a given pressure (Figure 2.10) due to the over burden pressure. The amount of material (represented by the area in our 2-D model) intruded into the shell decreases from 6.4x 10^5 m^2 at the shallowest depth run (500 m) to 5.6x 10^5 m^2 at 15 km depth, assuming an aspect ratio of 10. This represents the increased compliance of the ice shell to deeper stress sources. Once the intrusion is deeper than 15 km, the area of the intrusion begins to increase as a negative ridge develops at the base of the ice shell.

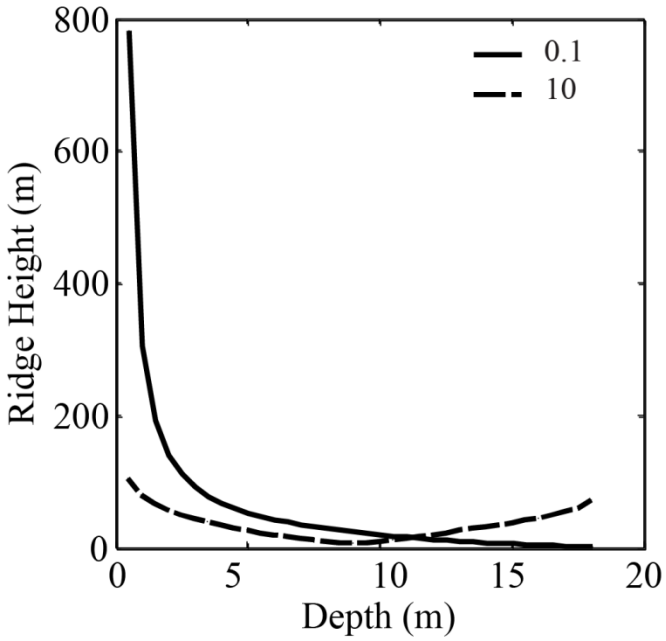

Figure 2.9. Ridge height as a function of intrusion depth for intrusions with an aspect ratio of 10 (dashed) and 0.1 (solid). Ridge height decreases with an increase in depth for intrusions with an aspect ratio of 0.1. Ridge height decrease with an increase in depth until 10 km when the surface deformation changes to a trough morphology at which point the trough depth (plotted as ridge height) begins to increase. Overpressure is fixed at 100 MPa.

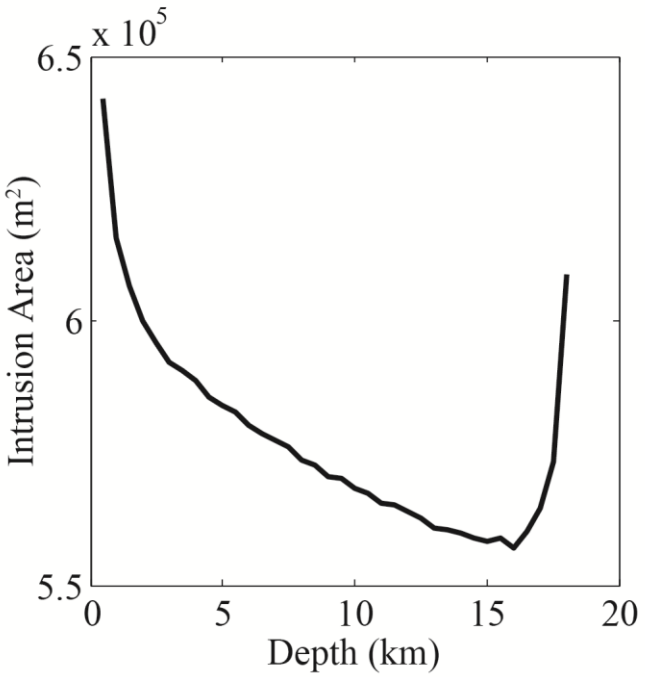

Figure 2.10. Area of intruded material as a function of depth with an aspect ratio of 10 and overpressure of 100 MPa. Intrusion area generally decreases as the intrusion moves to greater depths, and increases as it approaches the base of the shell.

As the depth of a dike-like water body increases, the width of the trough between the two ridges also increases. Figure 2.11 shows the relation between intrusion depth and trough width, defined as the distance between the locations of maximum height on each side of the surface midpoint, assuming an aspect ratio of 10. Once the intrusion becomes deeper than 10 km, the trough width becomes equal to the length of the shell, meaning the highest points are at the edges of our ice shell. Ridge height is still calculated from the lowest point, the center of the trough, to the highest point, the edges of the shell in this case. This behavior is due to a buckling of the ice shell and will be discussed in more detail later.

2.6.4 Overpressure

As our model is purely elastic, deformation should be proportional to stress. Therefore, the topography of the ridge should be directly proportional to the water body overpressure. This is indeed the case, as shown in Figure 2.12. The model behaves linearly with respect to the overpressure of the intrusion, which is only poorly constrained. Horizontal displacements are close to zero. Therefore, changing the applied overpressure will affect ridge height but not trough width.

The final intrusion area and the overpressure are also positively correlated. Over the range of overpressure considered (50–500 MPa), intrusion area varies from 0.43 km^2 to 2 km^2, assuming an initial aspect ratio of 10 and an intrusion depth of 500 m (Figure 2.13). The initial cross-sectional area of the water body was ~0.225 km^2. The increase in intrusion volume may be related to additional water influx (repeated intrusions) or a dramatic change in the density of the intrusion, maybe due to gas exsolution.

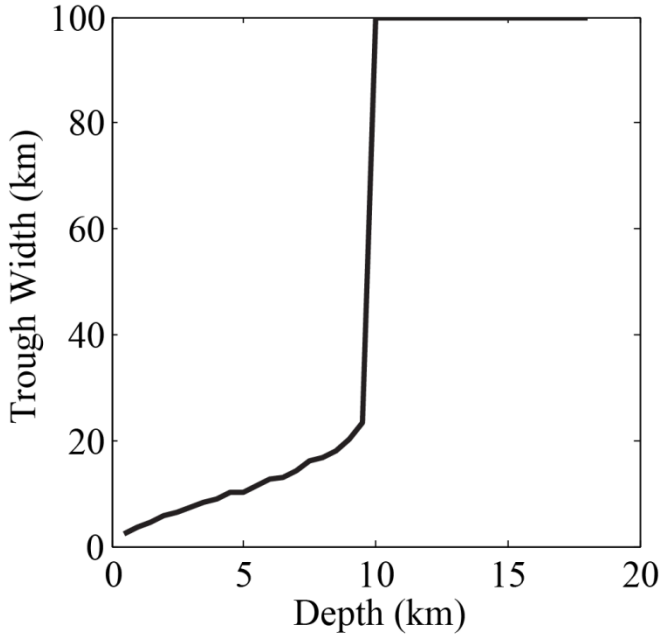

Figure 2.11. Trough width for double ridges formed above an intrusion with aspect ratio $a/b = 10$ as a function of intrusion depth. Trough width is defined as the distance between the nodes on either side of the surface midpoint where vertical displacement is maximum. Trough width increases with depth, and at 10 km the transition from a ridge to a trough surface morphology can be seen.

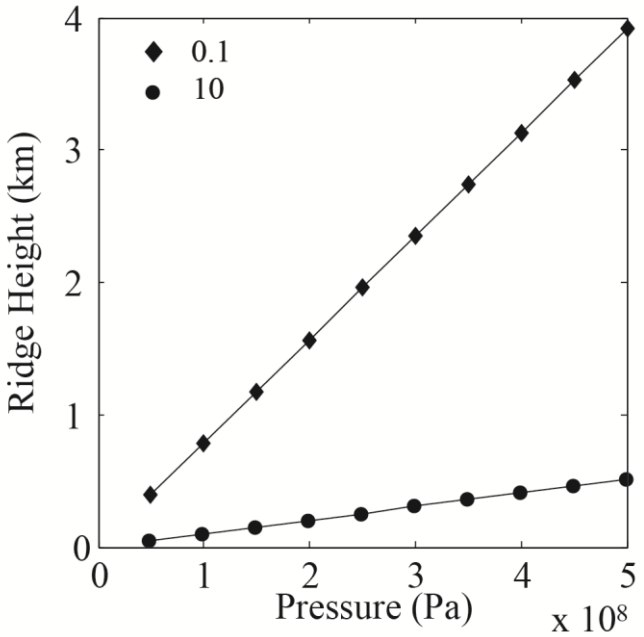

Figure 2.12. Ridge height as a function of pressure for an intrusion with an aspect ratio of 10 (circles) and 0.1 (diamonds) and a depth of 500 m. As expected for an elastic model, ridge height has a linear relationship to pressure for both intrusion geometries.

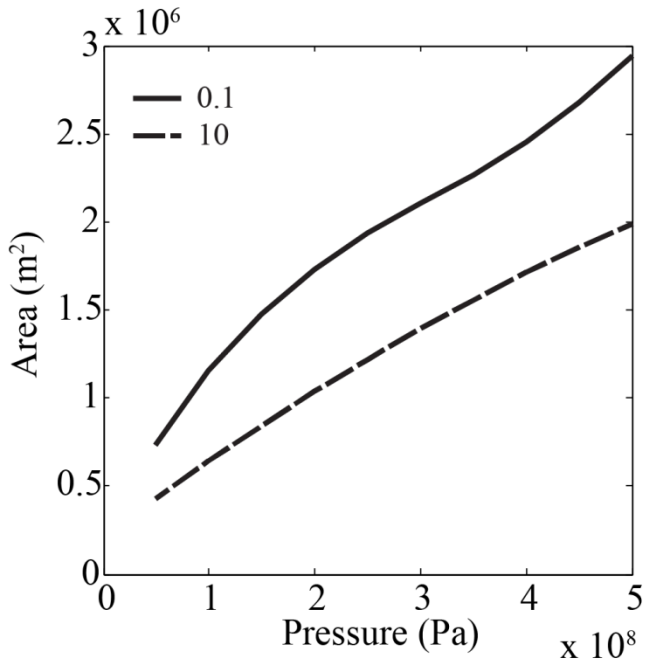

Figure 2.13. Area of material intruded as a function of pressure for an intrusion with an aspect ratio of 10 (dashed) and 0.1 (solid) and a depth of 500 m.

2.6.5 Ice shell thickness

Our reference models all consider a 20 km thick ice shell. As they are more compliant, thinner ice shells should produce larger ridges than thicker ice shells, everything else being equal. Figure 2.14 shows this effect for the case of a dike-like water body (aspect ratio 10). Ridge height decreases as ice thickness increases. However, a similar trend is not observed for sill-like water bodies (Figure 2.14B), for which ridge height remains nearly constant. This indicates that the single ridge morphology is due to flexure of the ice layer above the intrusion, which depends on intrusion depth, not on ice shell thickness. By contrast, the deformation associated with a double ridge is distributed over the entire ice shell. A thinner ice shell also means that the sides of the double ridges are slightly steeper (Figure 2.14A). However, this effect may be compensated by the lesser overpressure that can be supported in the water body in a more compliant thin ice shell.

2.7 Discussion

Water within the ice shell has been proposed based on the surface morphology of Conamara chaos (e.g. Sotin et al., 2002; Schmidt et al., 2011). Intruding water may utilize pre-existing cracks as regions of low resistance, or the phase change to ice may

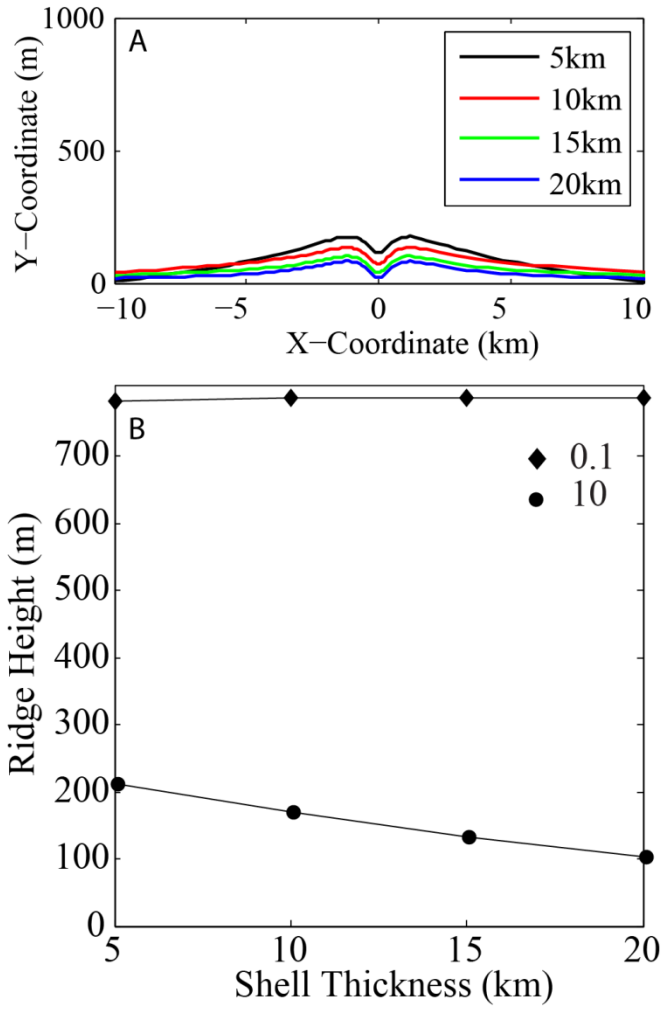

Figure 2.14. Effect of ice shell thickness on surface deformation. (A) Profiles for an intrusion with an aspect ratio of 10, depth of 500 m, and an overpressure of 100 MPa with no vertical exaggeration. (B) Ridge height as a function of ice shell thickness. A negative correlation between the ice shell thickness and ridge height can be observed for intrusions with an aspect ratio of 10, however intrusions with an aspect ratio of 0.1 seem fairly insensitive to the change.

propagate a crack within the ice shell. Both could explain the along strike changes from cracks to ridges.

Dombard et al. (2013) suggest that sills must be involved in the formation of ridges in order to match the observations of lithospheric flexure and flanking fractures. This model did not consider dike-like intrusions in detail as the intrusion and crystallization of material would be expected to generate compressive stresses inconsistent with flanking fractures. Flanking fractures are not observed on all ridges on Europa, raising the question of the ubiquity of underlying sills in association with Europan ridges. We do not consider the results of Dombard et al. (2013) to be inconstant with our model; however it may provide an additional layer of complexity to be considered in future models.

The morphology of a double ridge, a trough flanked by two raised edifices, is produced in our model by the 2-dimensional expansion of a dike-like water body. Water bodies that are sill-like to circular in cross-section produced a single ridge with no central trough. The reason for the different responses is that the stresses acting on different sides of the intrusion induce different types of surface deformation. Stress applied to the top of the intrusions uplifts the surface directly above the intrusion (Figure 2.15). As the layer of ice above the intrusion is relatively thin, the uplift is essentially a flexural response. By contrast, stresses applied to the side of intrusion compress horizontally the surrounding crust. Thanks to the Poisson effect, that compressed region expands vertically, forming a ridge on each side of the intrusion (Figure 2.15). Stress on the bottom of the intrusion can also produce surface uplift but

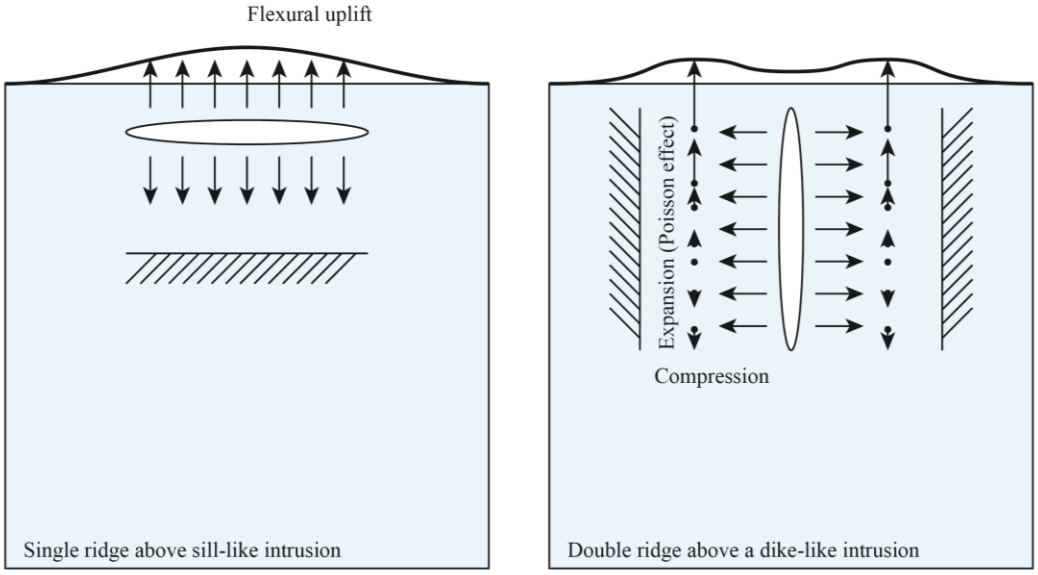

Figure 2.15. Schematic diagram explaining the relationship between intrusion aspect ratio and surface ridge morphology. For a sill-like intrusion (left), the dominant force is exerted on the horizontal sides of the intrusion and causes flexural uplift of the thin region of ice above the intrusion. For a dike-like intrusion, on the other hand, the dominant force is exerted on the vertical sides of the intrusion. The ice adjacent to the intrusion is compressed horizontally and expends vertically (Poisson effect), forming two ridges, one on either side of the intrusion.

only as an isostatic response from displaced ocean water. The surface expression of this uplift is diffused over a broad region.

The aspect ratio of the intrusion controls the relative importance of flexural uplift and sideways compression. The total force available for uplift can be evaluated as bP whereas vertical expansion along the side of the intrusion is given by the integral of the vertical strain and is approximately avP/E. In a dike-like intrusion, uplift is limited to the narrow upper edge of the intrusion whereas expansion accumulates on the long vertical edge of the intrusion. Therefore, the surface deformation is dominated by the latter and a double ridge develops (Figure 2.15A). The opposite is true for a sill-like intrusion (Figure 2.15B). This effect also contributes to the impact of the aspect ratio on the height of the ridge. As an intrusion becomes more sill-like (lower aspect ratio) the vertical uplift is enhanced. As the intrusion becomes more dike-like (a higher aspect ratio) the deformation on the sides of intrusion becomes concentrated further on the sides and increases the ridge height. However, the height of a single ridge is more quickly enhanced and reaches a greater height with the change in aspect ratio than with a double ridge. The height of a dike-like ridge is sensitive to ice shell thickness (Figure 2.14) because the region being compressed encompassed the entire shell whereas in the case of a sill-like water body, it is limited to the region between the intrusion and the surface.

The depth of the intrusion impacts both the height of the ridge and the trough width (i.e. interior ridge spacing). A shallower intrusion creates a taller ridge and a narrower trough. At depths greater than 10 km in a 20 km thick ice shell, a change in deflection of the ice shell is observed. It is unlikely that such a wide and gently

sloping feature would be observed on Europa (Prockter and Pappalardo, 2000). The sudden jump in trough width (Fig. 11) is due to the downward deflection of the entire ice shell. The depth also impacts the amount of material intruded at a given pressure. The deeper the intrusion then the smaller the final area. Deeper than 15 km, the intrusion area increases as the pressure applied is able to overcome the underlying restoring force of the global ocean and expand downwards.

This has some interesting implications for along-strike transitions in ridge morphology. The transition from single to double ridges could indicate a change in the underlying intrusion geometry, from a sill-like intrusion to a dike-like intrusion. It is not possible for this change to arise due to a change in intrusion depth or ice shell thickness. Changes in trough width and height could indicate other more subtle changes to the intrusion geometry. The surface expression of a dike-like water body may even disappear along-strike if the body becomes deeper than the halfway depth of the ice shell.

The predominance of double ridges on Europa implies that most of the underlying water bodies have a dike-like geometry. Sills on Earth develop along stratigraphic horizons or along a neutral buoyancy level. Moreover, sills may adopt a circular rather than linear planform. Shallow impurities on Europa have been proposed to explain the formation of chaos (e.g. Sotin et al., 2002; Schmidt et al., 2011) by preferential melting at the location of heterogeneities. Sill-like structures and, in these models, chaos terrain both require a stratigraphic horizon, so perhaps there is a correlation between single ridges and chaos features. This idea can be partially tested by conducting a spatial analysis of the correlation between single

ridges and chaos and related terrains. However the change from a dike to a sill is not commonly observed and the tensional cracks observed on Europa would be more consistent with vertical failure, thus providing a pre-existing path for water to intrude into the ice.

Both overpressure and ice shell thickness affect ridge height but do not affect trough width. Most ridges on Europa have a trough width less than 1 km (Coulter, 2009). In order to obtain a trough width consistent with these observations the intrusion must be less than 2 km from the surface of the ice shell. This requires that the ice shell is less than 20 km thick for the intrusion to obtain a shallower neutral buoyancy level, unless an additional source of overpressure forces water to rise above its neutral buoyancy level. An increase in the size of the water body, or a reduction in water density, maybe due to gas exsolution, would not only help the intrusion reach shallow depths, it would also facilitate the generation of the required overpressure. It is also possible that the crystallizing water has its origins from within the ice shell; however any proposed process would have to also explain the pre-existing cracks commonly observed to be associated with ridges on Europa.

The amplitude of the surface deformation also has non-unique solutions. The ridge heights are impacted by aspect ratio, depth, ice shell thickness and pressure. The positive correlation between ridge height and trough width as noted by Coulter et al. (2009) indicates that the depth of the intrusion cannot be the only factor to impact the ridge height. Our model would suggest that we would expect to see a negative correlation. In the context of our models, the observations would imply that deeper ridges (wider troughs) are also associated with larger overpressurization or higher

aspect ratio (large amplitude). The variation of only one of these parameters would not result in the positive correlation observed.

The ridge heights obtained with our model span a wide range, some of which would not be physically reasonable on Europa. The excessively high amplitude obtained in some models is due to the arbitrary overpressure used here and also to the elastic rheology used in our model. While using an elastic rheology provides a means for understanding the fundamental processes involved in the deformation of ice around an intrusion, it does not allow for strain localization or cracking. The large stresses that develop in our models (Fig 2. 6) would lead to plastic deformation in ice at Europan conditions. If plastic deformation were included in our model, it would be expected to reduce the height of the ridges, given its nonlinear relationship between stress and strain. This means that the volume of water that is required to obtain ridge heights consistent with the observed ridge heights is likely the lower bounds on what would be required.

Figure 2.6 highlights in gray the regions where cracking of the ice shell would be expected. Looking at the 500 m sill model, it is clear that the ice shell would not be able to support such stresses and that cracking would be anticipated to dominate. We can however use the locations where cracking would be expected to predict where cracks are most likely to occur on ridges. Narrow cracks observed on Europa (Kattenhorn, 2002) may indicate the presence of a single ridge above a linear sill-like intrusion with topography too subtle to be detected in SSI images. A dike like intrusion would be expected to develop cracks on the flanks of the ridges, when it was shallow enough. Deeper intrusions, however, may not have visible cracks at the

surface. If cracking did reach the surface of the ice it could provide a pathway for impurity enriched material to reach the surface or disturb overlying ice, providing a potential explanation for the albedo changes observed near some ridges, as discussed in Section 2.

In order to match the ridge heights observed for double ridges we would need approximately 1.5 km^2 of water intruded into the ice shell, based on Figs. 12 and 13. This amount of material would not have to be intruded in a single event, as the deformation fields of repeated events would be superposed as long as the model remains elastic. Cracks can provide a zone of weakness within the ice shell that allows material to be intruded at the same location without requiring the initiation of a new crack.

If water intrusions are involved in ridge formation we would expect that water within the ice shell would be pervasive. The volume contained in each intrusion increases upon pressurization to form the ridge. Therefore there needs to be mechanism either to continuously pump water in the shell or to dramatically reduce the density of the water inside the intrusion. The latter may correspond to exsolution of volatiles contained in the water. This process would be analog to gas exsolution in magma that produces explosive eruptions and may form pyroclastic plumes as are observed on Enceladus (Porco et al., 2006; Hurford et al., 2007a, 2007b) and Europa (Roth et al., 2014). Interestingly, the sources of the plumes of Enceladus have been located in the trough of features that resemble, albeit imperfectly, double ridges (Porco et al., 2006). Cryomagmatic flows may develop in the waning stages of such eruptions. The flat, occasionally hummocky floor observed in the trough of some

complex ridges may be evidence for such cryomagmatic activity. Alternatively, the large increase in intrusion volume required in some cases may reflect repeated influx of water from the internal ocean of Europa. In that case, maintaining a mass balance with the global ocean requires a mechanism to recycle ice into the ocean, possibly by melting the base of the shell. In that case, Europa would feature a version of vertical tectonics with basal melting and advection of water into intrusion that are expressed at the surface as double ridges.

2.8 Conclusion

Evaluating the presence and location of water within the ice shell is of key importance to determine the astrobiological potential and to understand the geologic processes that occur on icy bodies. If ridge formation on Europa is related to the crystallizing of a water body then water within the ice shell would be expected to be pervasive.

The unique physical properties of ice create an equally unique set of possible geologic processes. In a confined location, crystallization causes stresses in the surrounding ice whose pattern is influenced by the aspect ratio of the intrusion. Evaluating the strain and surface deformation from these stresses provides insight into the possible formation mechanism for ridges on Europa. The geometry of the intrusion, represented in our model as the aspect ratio, is a controlling factor in the surface morphology above a crystallizing water intrusion. A sill-like intrusion creates a single ridge, while a dike-like intrusion creates the double ridge morphology. The difference in the surface deformation can be explained by the stress pattern created

within the ice shell. A single ridge has one lobe that reaches the surface a single point, while double ridges have two lobes that are separated by a low stress region between them. Double ridge heights reach 100 m, shorter than many of the double ridges observed on Europa, with 100 MPa of overpressure, intrusion depth of 500 m, and intrusion aspect ratio of 10. If ridges are formed by intrusive water bodies then their size requires a large increase in the intrusion volume, which would imply either that cryovolcanic processes are important in ridge formation or that the ice shell undergoes a sort of vertical tectonic activity dominated by mass exchange between the ice shell and the internal ocean.

Chapter 3 : Stress Field Above an Ice Cauldron on Europa: application to the formation of Thera Macula

3.1 Abstract

Chaos and Macula are geological features on Europa where the pre-existing surface material has been broken into discrete blocks surrounded by matrix material. Schmidt et al. (2011) proposed that Maculae and Chaos are analogues to terrestrial ice cauldrons: depression at the surface of glaciers that from in response to melting in the glacier's interior. On Europa, if a melt lens forms in the ice shell above an ascending warm ice diapir, briny water would erupt along cracks formed during melting, and crystallization of the melt lens would uplift the surface. This model requires the propagation of cracks vertically from the melt lens to the surface to allow extraction of brine from the subsurface water body and explain the appearance of Thera Macula.

Using an axisymmetric finite element model, I model the stresses induced by melting of a lens within Europa's ice shell and its subsequent crystallization. I evaluate the pattern of yielding during this melt-freeze cycle, examine the orientation and location of failure and compare surface deformation with observations of Thera Macula. The model is able to match some of the observed features of Thera Macula, such as a circumferential ridge, an initial draw-down of the overlying surface and surficial radiating cracks, but does not predict the propagation of fluid filled cracks up from the melt lens.

3.2 Introduction

Thermal plumes within Europa's ice shell have long been discussed as a mechanism for formation of chaos on Europa (e.g. Pappalardo et al., 1998; Head and Pappalardo, 1999; Collins et al., 2000; Sotin et al., 2002; Schenk and Pappalardo, 2004). Chaos on Europa is characterized by ice disruption. Pre-existing blocks of material appear to have been broken up, rotated and are separated by hummocky (Spaun et al., 1998; Greenberg et al., 1999), impurity enriched, matrix (Prieto-Ballesteros and Kargel, 2005). Pre-existing ice may have been broken by rising plumes or warm diapirs inside the ice shell, which would have also transported impurities to the surface, forming the matrix (e.g. Collins et al., 2000). Alternative melt-through models of chaos formation (Greenberg et al., 1999) may also require a locally enhanced heat input (O'Brien et al., 2002)

Recently Schmidt et al. (2011) proposed that Thera Macula (Figure 3.1) represents chaos in the process of forming above a melt lens with ~20,000-60,000 km^3 of liquid water. Thera Macula is a roughly 60 km by 120 km oval shaped region. Its southern half contains chaos whereas its northern half is less disrupted. Both northernmost and southernmost ends of the Macula sit as much as 800 m above the surrounding terrain. However, the boundary between the northern and southern regions rests almost 800 m below the surrounding plains. Also at the boundary, blocks containing pre-existing terrain have been broken and are now surrounded by matrix material. A narrow circumferential depression runs around a majority of both the northern and southern regions of Thera Macula. Cracks and faults are clearly visible along this depression. An 800 m high ridge at the southern boundary of the

macula appears to be the site of brine injection in the preexisting ice shell based on the positive relief of the ridge and associated ice coloration (Schmidt et al., 2011). Some features in the uplifted northern regions appear to have radial cracks associated with them. However, no definitive evidence for large scale radial cracking is identified (Figure 3.1c).

It is important to note that although topographic images created using photoclinometry (Figure 3.1) provide valuable information, errors tend to accumulate along profile tracks, introducing uncontrolled and unknown longer-wavelength undulations (Schmidt et al., 2011). While the relative heights of short-wavelength features are reliable, the consideration of shadows and potential errors is needed when interpreting across long distances, such as the entire expanse of Thera Macula.

Schmidt et al. (2011) proposed that a rising ice diapir can explain the features observed at Thera Macula and chaos. They postulated that an ascending diapir may stall inside the ice shell but that the heat radiated by the diapir would melt an overlying volume of impurity-laden ice, causing the surface to flex downward in response to the decrease in volume upon melting. In their view, the stress related to the flexure of the ice would cause tensile fractures in the ice and allow transport of brine to the surface. The edges of the melt lens would then flow inward as the pressure at the center of the lens is reduced. The hydrostatic pressure and stresses caused by the collapse of the overlying ice shell as a volume of ice melts would seal the liquid water in place, preventing outward flow. The impurity-rich water would crystallize and form the matrix between blocks of pre-existing plain materials. Crystallization of the entire lens would then create a dome above the melt lens as the

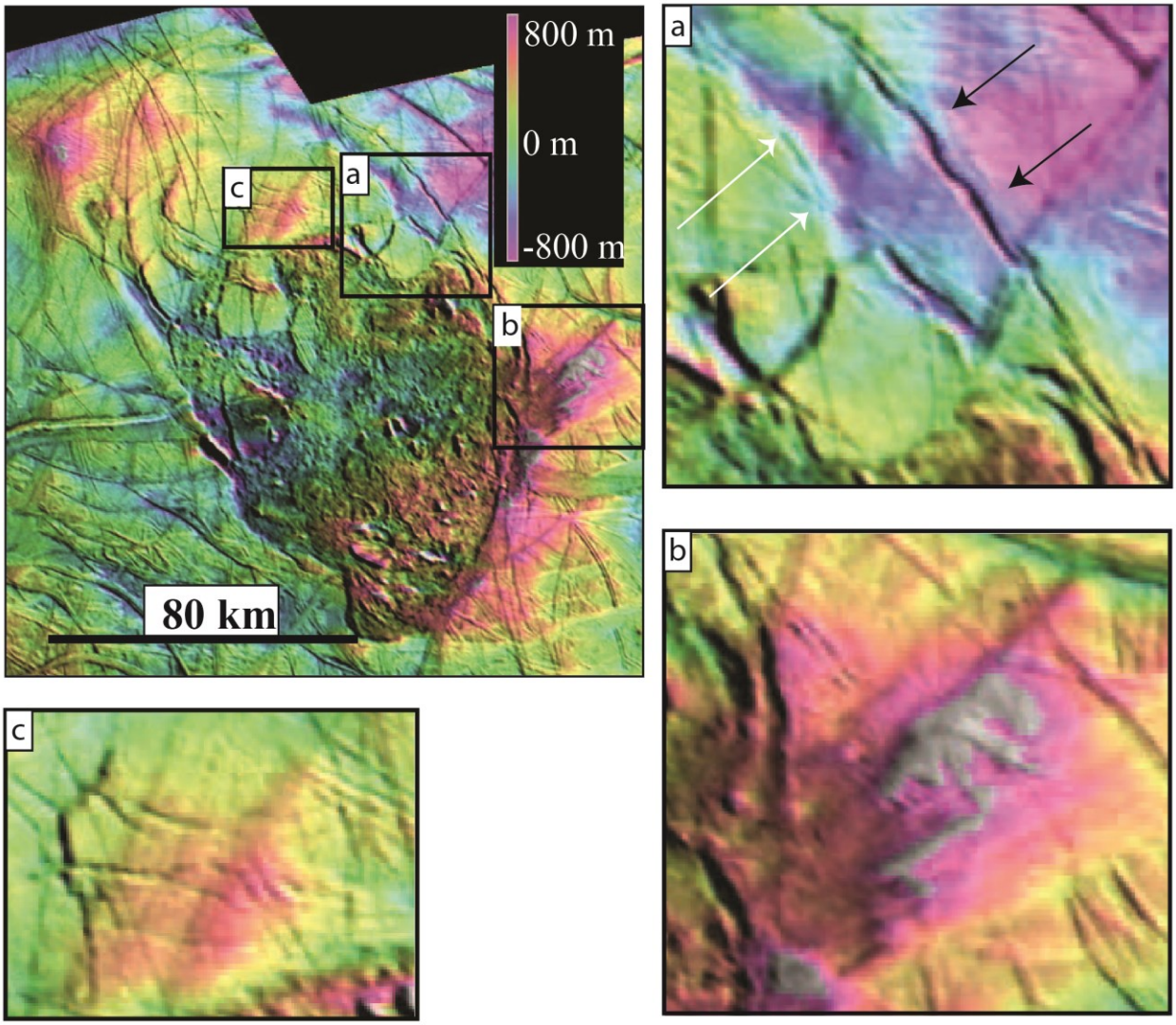

Figure 3.1. Digital elevation models of Thera Macula created using photoclinometry, shaded following the images collected by Galileo's Solid State Imaging camera (Schmidt et al., 2011). The macula consists of a southern chaotic region and a semi-circular northern region with a total relief of approximately 1.6 km. Broken blocks containing pre-existing terrain are surrounded by matrix. A circumferential depression (a) runs around a majority of both the northern and southern regions of Thera Macula. At the southern boundary of the chaotic region there is also a ridge-like linear feature (b) that sits more than 800 m above the surrounding terrain and appears to intersect a nearly circumferential crack that bounds Thera Macula. (c) An uplifted feature that exhibits (arguably) radial fractures.

volume of water in the lens is prevented from flowing back towards the original edges of the melt lens.

Schmidt et al. (2011) draw this model in part from analogies with ice cauldrons that form in terrestrial glaciers as a consequence of melting induced by subglacial volcanic eruptions (e.g. Gudmundsson et al., 2004). However, these depressions result in part from the drawdown of liquid water in Jökuklhaups (Björnsson, 2002). There is no evidence for upward transport of liquid water from the melt lens to the surface, a key feature of the Schmidt et al. (2011) model. Therefore, Europan ice cauldrons are best regarded as a closed system. Furthermore, the pressure increase in the melt lens upon crystallization would either melt back recently crystallized ice, or force new cracks at the edge of the lens due to stress concentration. Therefore, it is unclear what, if any, permanent topography would result from ice melting and subsequent crystallization.

I use an axisymmetric, elastic-plastic finite element model to model the stresses and deformation field induced by melting of a lens within Europa's ice shell and its subsequent crystallization. As plasticity is history-dependent, the melt-freeze cycle is not reversible and results in permanent tectonic and topographic signatures. My model does not consider, due to software limitations, the flow of water inwards during the melting of the lens. However, I will discuss the likely impacts of such a mechanism in section 3.5. I report the orientation and location of failure and associated topography and compare them to observations of Thera Macula. In particular, I evaluate the possibility that tensile cracks propagate from the melt lens to

the surface and whether the southern half of Thera Macula, with chaos morphology, corresponds to a late stage of evolution than the northern half.

3.3 Model setup

I consider the elastic-plastic deformation of an ice shell under loads corresponding to the ascent of a warm ice diapir and the melting and subsequent crystallization of a lens-shaped region in the ice shell. The model is solved using the commercially available software finite element software, Abaqus™.

Figure 3.2 shows the model geometry. Although Thera Macula is elongated in the NW-SE direction, I set up an axisymmetric model for simplicity. The melt lens is placed at a depth of 2 km, as deduced by Schmidt et al. (2011) based on the shape of ice blocks. Its radius is 40 km, matching the approximate radius of Thera Macula. The lens thickness is set to 6 km, based on the Schmidt et al. (2011) water volume estimates. The plume rests 1.5 km beneath the melt lens, a total of 9.5 km below the surface, and has a radius of 60 km. A range of 20 to 60 km radius for the plume was tested and had minimal impact on the resulting deformation and yielding patterns. The ice shell is 15 km thick and 100 km across to be consistent with the assumptions of Schmidt et al. (2011) and to minimize the impact of boundary conditions on model results. The model is meshed with axisymmetric quadratic elements with reduced interpolation. Nodes are uniformly placed every 500 m along the edges of each model part.

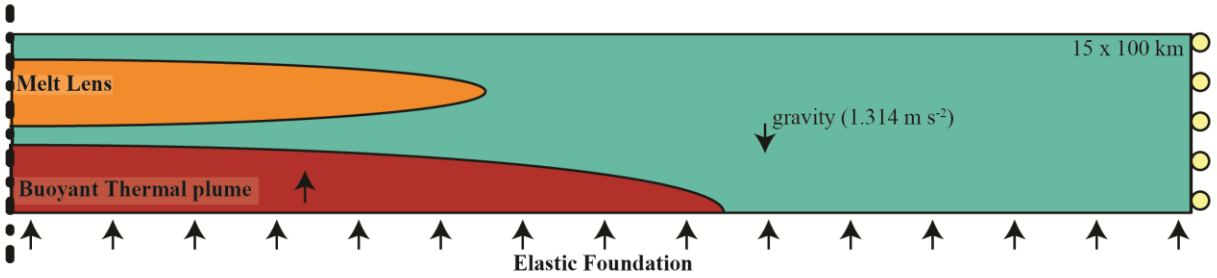

Figure 3.2. Model setup. The model is axisymmetric with a predefined initial geometry. The ice shell is 15 km deep and 100 km across. The melt lens is at a depth of 2 km with a 40 km horizontal radius and 3 km vertical radius. The plume rests 1.5 km beneath the deepest point of the melt lens and has a radius of 60 km. Gravity is imposed on the entire model, and an elastic foundation is applied to the base of the ice shell, representing the restoring forces of an underlying global ocean. A rolling side is applied to enable the entire ice shell to sink to a state of isostatic equilibrium with the global ocean and prevent extension of the ice shell.

Gravity (1.314 m s^{-2}) is imposed on the entire model, and an elastic foundation is applied to the base of the ice shell, representing the restoring forces of an underlying global ocean (e.g., Johnston and Montési, 2014). A rolling side is applied to enable the entire ice shell to sink to a state of isostatic equilibrium with the global ocean, and prevent extension of the ice shell.

The simulation is conducted in four stages: initiation, diapir emplacement, melting, and crystallization. Stresses and yielding history are propagated between these steps. In my model, ice has a density of, ρ_i = 930 kg m^{-3} (Petrenko and Whitworth, 1999) and obeys a non-associated elastic-plastic rheology with Mohr-Coulomb failure criterion, 30 kPa yield stress, dilation angle of 0˚, and a friction angle of 30˚. A Young's modulus of 0.9 GPa is used for the ice on Enceladus based on the abundance of fractures (Collins et al., 2010). A higher young's modulus would be more consistent with an unfractured ice sheet. The Poisson ratio is 0.3 (Collins et al., 2010).

All the density changes in this model are implemented using the thermal expansion capacities of Abaqus™. Therefore, mass is conserved during model evolution. Density changes are implemented as a change of intrinsic volume, which can be accommodated by actual expansion of the region that changes density and/or accumulation of elastic stresses inside and outside the expanding region. Note that I do not solve for the heat equation in my model. Instead, the density changes are implemented using an imposed change in a dummy variable (the solidity index) used solely to parameterize density. This approach was benchmarked against standard problems of expansion of a cavity in an elastic medium.

The first stage (initiation) sets up the initial configuration. The entire model is assumed to be solid ice. Gravity and a hydrostatic prestress $\sigma_h = \rho_i g z$, where z is depth, are imposed simultaneously. The prestress allows the ice shell to reach isostatic equilibrium without adding strain and differential stresses caused by compression. Essentially, I assume that the ice has relaxed to a state of hydrostatic equilibrium before the diapir arrives.

The second stage (diapir emplacement) represents the arrival of the thermal diapir, which is implemented as a predefined area with a reduced density of 915 kg/m^3 corresponding to warm ice. Note that I do not solve for heat transfer in this model. However my implementation should result in the maximum possible surface deformation above the diapir. For simplicity, the rheology of ice in the plume is identical to the rest of the ice shell.

The third stage (melting) represents the period of melting in the predefined melt lens. I introduce a solidity index, s that changes from 1 in solid ice to 0 in liquid water. As s decreases, the density of ice increases from $\rho_i = 930$ kg m^{-3} to $\rho_w = 1000$ kg m^{-3} and the material in the predefined melt lens domain obtains progressively more liquid-like properties, although it is still technically modeled as a solid. The bulk modulus, K, Young's modulus, E, and Poisson's ratio, ν, change with "solidity" according to Eqn. 3.1 to 3.3.

Eqn. 3.1 $$\nu = \nu_w - (\nu_w - \nu_i)s$$

Eqn. 3.2 $$K = K_w - (K_w - K_i)s$$

Eqn. 3.3 $$E = 3K(1-2\nu)$$

The bulk modulus for ice, K_i, is calculated using Eqn. 3.3 for solid ice properties (E_i = 0.9 GPa, ν_i = 0.33, as discussed earlier). The liquid is nearly incompressible, with K_w = 2.2 GPa and ν_w = 0.499 which leads to a reduction of Young's Modulus to 13.16 MPa. As a result, the "liquid" melt lens supports very little shear stress. The lens in my model is considered liquid when the solidity index reaches $5x10^{-3}$. I cannot reduce the solidity further in my model due to software limitations of Abaqus™.

The elastic-plastic rheology selected is time independent and I do not model thermal evolution in detail. Therefore, progress in the melting stage is tracked solely by the value of the solidity index, which is decreased progressively from 1 to $5x10^{-3}$, the lowest value technically achievable. Abaqus™ automatically adjusts the increment of solidity index at each step of the calculation following numerical stability arguments.

In the fourth stage (crystallization), the plume cools, returning to neutral buoyancy and the melt lens crystallizes, returning to the initial ice material properties. Here again, progress is measured by the value of the solidity index, *s*, which increases progressively from 0 to 1. The density of the diapir ice concurrently increases to ρ_i = 930 kg m^{-3}. As plastic strain is not recoverable, a residual topography develops in the model, which can then be compared with the observed topography of Thera Macula (Figure 3.1).

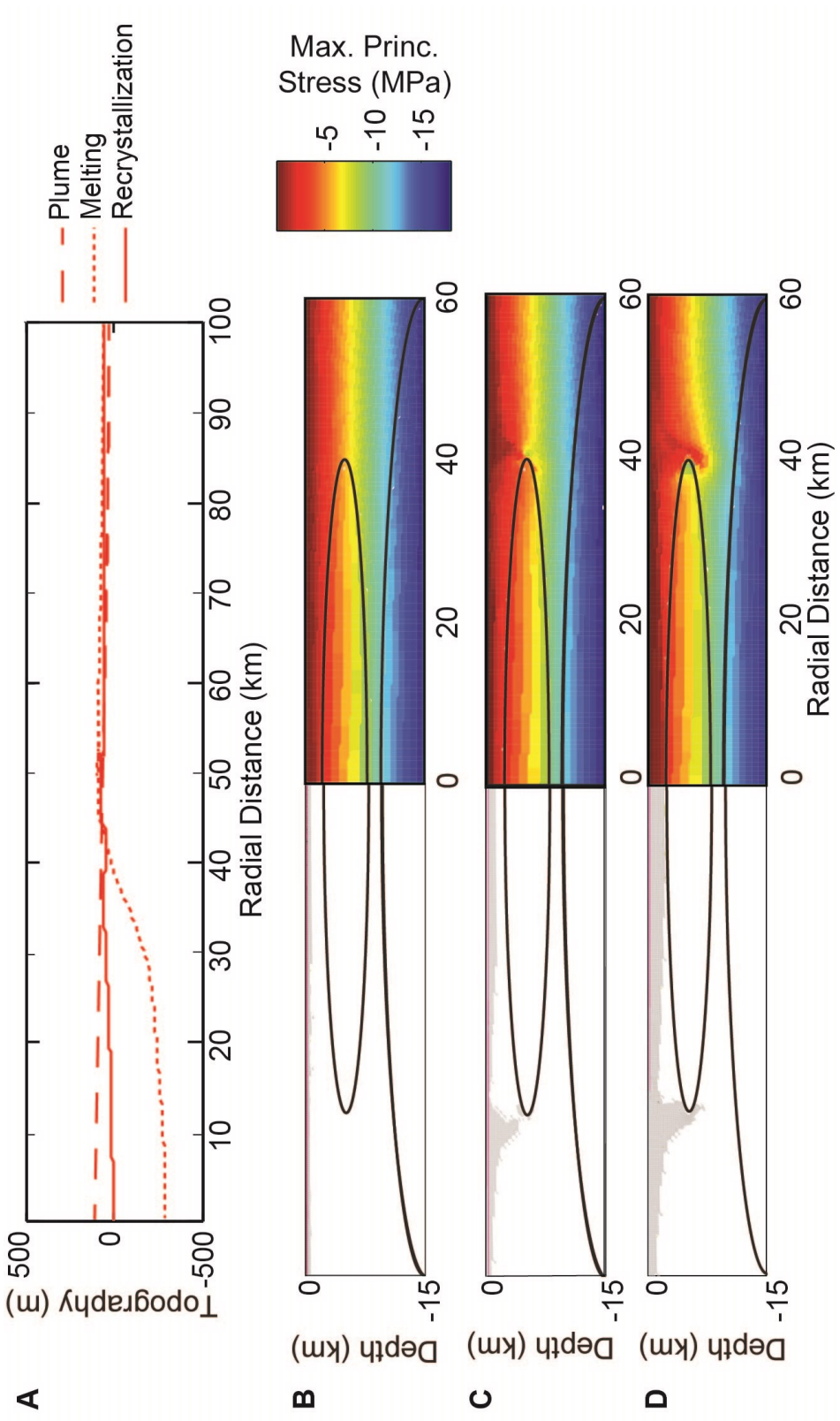
A
B
C
D
Topography (m)
500
0
-500
Plume
Melting
Recrystallization
10
20
30
40
50
60
70
80
90
100
Radial Distance (km)
Max. Princ.
Stress (MPa)
-5
-10
-15
Depth (km)
0
-15
0
20
40
60
Radial Distance (km)

Figure 3.3. A) Topographic profile of the surface ice shell at the end of each stage. B-D) Left side: failure (grey), tensile yielding (pink) and right side: maximum principal stress (colors) and the end of the B) plume, C) melting, and D) crystallization stages. Shallow yielding and upwarping of the surface is predicted at the end of the plume stage. Melting in the melt lens is associated with downwarping of the surface, and yielding near the edge of the lens. Crystallization of the lens results in a broader zone of yielding and returns the topography almost to its original value. Tensile yielding is predicted only in the upper most meters of the ice shell.

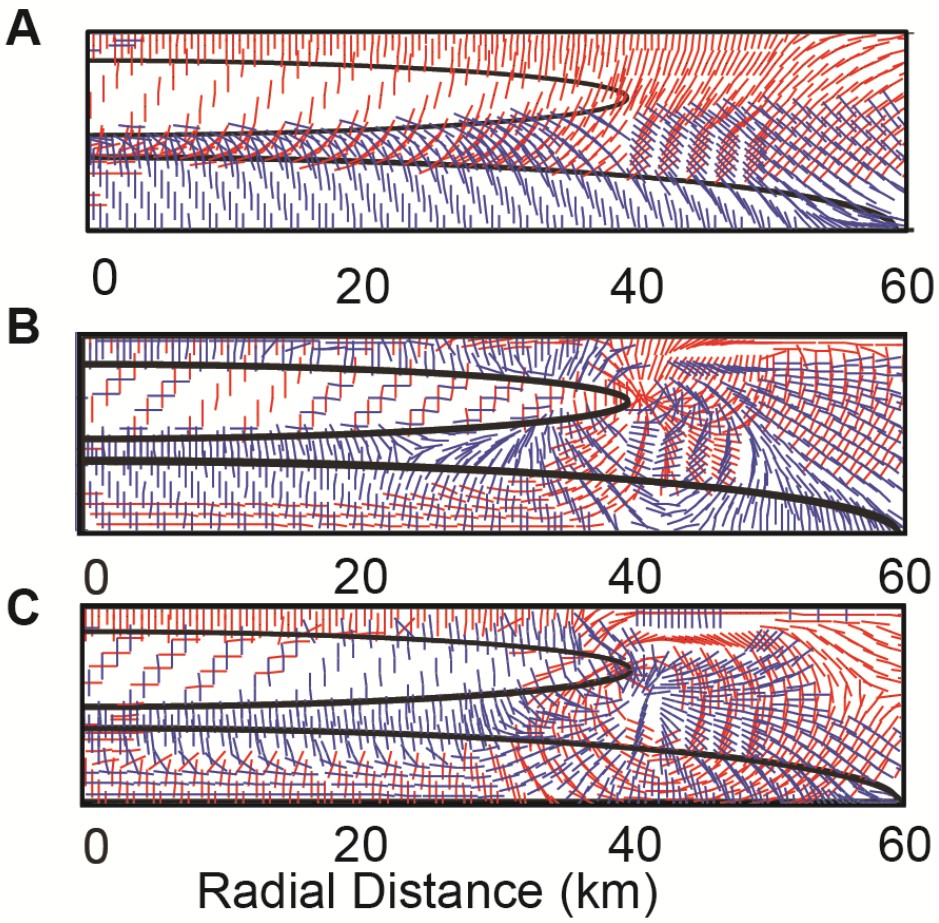

Figure 3.4. Orientation of the maximum (blue) and minimum (red) principal stresses at the A) plume, B) melting and C) crystallization stages. Radial failure is predicted during the plume stage (A). Additional circumferential yielding (beyond the edge of the lens) is predicted during melting (B) and tectonic inversion in the circumferential yielding zone is predicted during the crystallization stage (C).

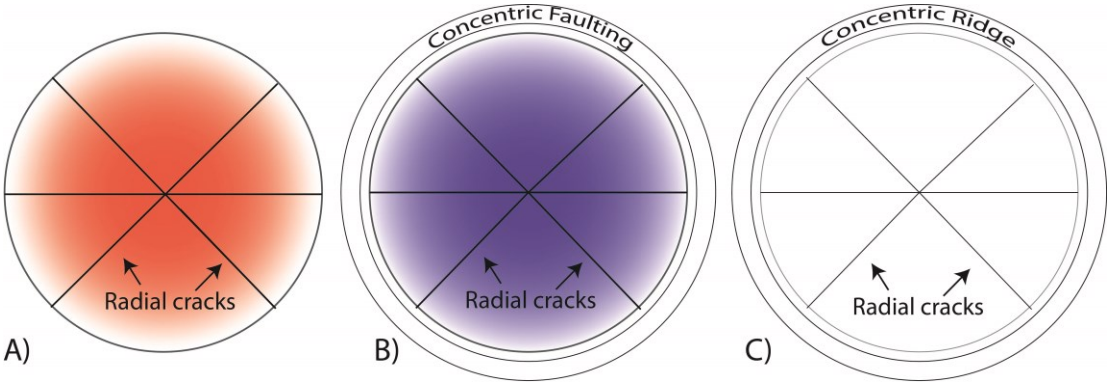

Figure 3.5. Map view diagram of predicted surface deformation. Red shading indicates high standing topography and blue shading low-standing topography. A) After the plume arrives, slight doming of the feature is predicted with formation of shallow radial cracks. B) After melting of the lens is complete, the ice above the lens is flexed downward into a bowl shape and a circumferential graben begins to form. C) Once the lens has crystallized there is minimal topographic relief associated with the feature, however, the circumferential ridge and the radial cracks remain.

3.4 Results

Imposing gravity in the initiation stage generates noise on the order of a few MPa, concentrated at the plume-ice shell and lens-ice shell boundaries This noise, which is related to the non-uniform grid across parts in my model, should not impact the results as the criterion for yielding at that depth is two orders of magnitude higher than the noise amplitude. Indeed, no yielding or deformation is observed as the surface of my models. However, this initial noise provides nucleation sites for plastic shear bands or faults. The ice shell settles into hydrostatic equilibrium with the global ocean with no deformation of the surface of the ice shell.

Figure 3.3 shows the surface topography of the features, with a vertical exaggeration of 20 (Figure 3.3A), and the stresses and yielding after each stage of the model. The amplitude of the maximum principal stress is shown on the right of each panel (Figure 3.3B-D). Yielding is shown on the left with grey highlighting regions of shear yielding where the Mohr-Coulomb criterion is verified, i.e., where faulting is expected, and pink indicating where the maximum principal stress is positive, i.e., where tensile failure, expressed geological as the development of cracks, is expected. The orientation of the maximum (blue) and minimum (red) principal stresses are plotted in Figure 3.4 for each model stage. When no directional symbol is plotted the maximum principal stress is perpendicular to the figure (hoop stress).

The arrival of the buoyant thermal plume (Figure 3.3) causes the surface of the ice shell to bow upward slightly, creating a dome tens of meters high and approximately 40 km across. Shear yielding from this flexure occurs within the top several meters (Figure 3.3B). Tensile stresses, which can create mode 1 cracks, are

present only at the uppermost surface of the ice shell and do not extend into the ice shell. In that region, the hoop stress is the maximum principal stress. As cracks propagate perpendicular to the direction of maximum principal stress I predict at this stage initiation of shallow cracks that propagate only tens of meters into the ice and radiate away from the diapir.

As the ice above the diapir melts and creates a lens, the density decreases and the material properties of the ice change (as described in the methods section). This change in density draws down the overlying surface, resulting in a bowl-shaped depression approximately 300 m deep and 45 km across (Figure 3.3A). As in the previous step, tensile stresses in the ice shell are only observed at the uppermost surface and do not propagate to the melt lens (Figure 3.3C). Tensile stresses are located in the melt lens, but because the lens is fluid, the stresses may not create tensile cracks but cause cavitation and/or gas exsolution instead. Shear yielding propagates from the surface down towards the melt lens in this simulation stage, forming an interconnected region of plastic failure near the edge of the melt lens. The maximum principal stress is horizontal in this region so failure is expected to generate normal faults inside the ice shell and circumferential cracks at the surface. I predict that a graben outlining the melt lens will form at this stage, accompanied by shallow circumferential cracks.

The yielding region does not reach the melt lens at this step. However, it does approach it. In addition, the stresses becomes positive just a few meters below the surface, preventing cracking in the interior of the ice shell. Therefore, there is no evidence of a connected pathway utilizing normal faults or cracks between the melt

lens and the surface. This result is robust against variations of model geometry and material parameter. It indicates instead that the volume decrease in the melt lens pulls on the lens walls inward forming a stress field consistent with spallation cracks, but insufficient to overcome the overburden lithostatic stress.

The cooling of the diapir removes its buoyancy and the crystallization of the melt lens changes the material properties of the lens back to ice (solidity index s=1). This change in stresses causes inversion (reverse faulting) in the region of yielding described above, resulting in a circumferential ridge outlining the freezing melt lens. A slight uplift, of only a few meters is observed near the edges of the circumferential graben (Figure 3.3D). Yielding associated with the ridge reaches the edge of the melt lens and may form a connected pathway for fluids to reach the surface. Yielding above the melt lens extends further into the ice shell than at previous simulation stages and approaches the top of the melt lens, without reaching it. As the hoop stress is the maximum principal stress, I expect radial normal faults to form at this stage (Figure 3.4). However, all but the uppermost surface of the ice shell is in a compressive state, prohibiting the formation of any crack.

At the end of the simulation, the surface features radial cracks from the diapir uplift stage, a circumferential graben and a slight topographic anomaly from the melting/freezing cycle (Figure 3.3A).

3.5 Discussion

Figure 3.5 is a cartoon summarizing the surface features expected after A) the arrival of the buoyant thermal plume B) the melting of the lens C) the cooling and

crystallization of the melt lens. In my model the arrival of a thermal plume creates a slight dome only tens of meters high. The radius of the dome is directly related to the radius of the plume. Shallow radial cracks are predicted to propagate from the center of the dome outward. While some features within Thera Macula have radial cracks, no large scale radial cracks are observed. There is a possibility that radial cracks did form, but were overwritten by later surface deformation possibly during the final melt lens crystallization stage.

As the plume radiates heat, causing melting of impurity-rich ice the volume of the lens decreases and draws down the overlying ice creating a bowl-shaped depression at the surface. My model predicts the deepest point of the depression to be 300 m, which is less than the deepest point observed on Thera Macula (800 m) or the depression needed to compensate the change of ice density (~500 m). Partial compensation is due to elastic stresses in the essentially intact ice shell above the melt lens. Therefore, the melt lens must be thicker than the dimensions estimated from topography at the end of the melt-freeze cycle assuming isostasy (e.g. Schmidt et al., 2011). The formation of the depression is accompanied by the formation of circumferential normal faults and cracks, albeit without significant topographic signature (Fig. 3.3A). Bounding circumferential cracks are observed around Thera Macula (Fig. 3.1a). In the southern region, these cracks appear to intersect a ridge-like linear feature (Fig. 3.1b). While it has been suggested that this feature formed from fluid injection into a crack, my model shows that neither crack nor normal faults connect to the melt lens (Fig. 3.3C), making fluid transport unlikely. The orientation of the maximum principal stress in the region of yielding nearest the edge of the melt

lens suggests that the failure would spall the edge of the lens without providing a pathway for water to move into the ice shell. An additional mechanism or source of overpressure on the order of at least a few MPa, would be required to allow the fluid to infiltrate the yielding region and reach the surface.

As the melt lens cools and crystallizes, the circumferential fault inverts to form a circumferential ridge, which is observed around the southern region of Thera Macula. In my model the ridge only appears after the melt lens has crystallized, suggesting that the southern region would have already completed or is in the final stages of completing the melt-freeze cycle proposed. The low topography of the center suggests that it may have yet to crystallize (it resides in the melt stage). The northern edge of the Southern Chaotic Region of Thera Macula shows the initial break up of surface but minimal topographic anomalies. This seems to suggest that melting either has not occurred in the north or is just initiating. Notably there are a few ridge-like features bounding the northern edge of Thera Macula (Figure 3.1c). They are not circumferential to the macula and so would be expected to be formed by other processes. The results from plume-induced melting-freeze cycle modeled here, would seem to suggest that the southern region of Thera Macula is in later stages of cooling than the northern region. However, if the lens were cools asymmetrically, the stress state predicted would be different and it is not evident that a bounding ridge would be anticipated.

One of the key steps in the Schmidt et al. (2011) model is the formation of fluid-filled cracks from the melt lens up into the ice shell. These cracks lead to the creation of polygonal blocks, as well as the formation of hummocky matrix material

between the blocks. My model indicates that cracks would not propagate from the melt lens up, but rather from the surface down and that only the very surface of the ice shell would experience tensile stresses. Unlike crevasses that form moulins in terrestrial ice sheets (Weertman, 1971; Krawczynski et al., 2009), the surface cracks are not water-filled and therefore cannot become gravitationally unstable and propagate downward towards the melt lens. A change in the size and geometry of the melt lens cannot resolve this difficulty. It is possible that radial reverse faults formed in the crystallization stage (Fig. 3.3D) would cut blocks of preexisting terrains to form chaos, but I observe no evidence of a preferential azimuth of chaos block margins.

Buoyancy forces do not contribute to the upward migration of water from the melt lens, as water is denser than ice and the cracks would have to cross a region around the melt lens where the ice is under compression. Tidal forces may be able to overpressurize pre-existing water-filled cracks at depth in the ice (Rudolph and Manga, 2009). Although the 100 kPa generated by tidal forces is not enough to entirely cancel the compressive stresses above the melt lens, it does make fluid injection easier if the reservoir were in some way pressurized. The total additional over pressurization would have to exceed 1 MPa to crack into the overlying ice. It is possible that a background tensile stress is present due to the over pressurization of the global ocean (Rudolph and Manga, 2009) and that the thinning of part of the ice shell able to support elastic stresses would enhance pre-existing stresses (Michaut and Manga, 2014) . If present, tensile stresses could further facilitate the cracking of the ice shell above the melt lens. However, brittle failure would immediately relieve the

stress. In a ductile regime the ice would not be expected to fail but would instead flow in response to tensile stresses.

My finite element model of the melting and crystallization of ice related to a thermal plume is able to model the formation of a circumferential graben and a depression with an elevation 300 m below the background. The lowest elevation in my model is obtained once the whole volume of water is melted. A volume of water greater than 60,000 km^3 is needed to match the -800 m of topography observed at Thera Macula.

A circumferential ridge is not observed until the melt lens begins to recrystallize. When the lens cools in my model, the surface elevation returns to near zero, although short-wavelength residual topography is observed as elastic-plastic failure is not reversible. If the melt lens were to flow inward and were prohibited from flowing back out, a domal uplift would be expected. Flow at the edge of the melt lens may be prohibited if that region crystallizes first due to the enhanced heat loss where the lens is thinnest. However, heat redistribution within the fluid-filled lens and preferential cracking of the newly crystallized region when the pressure of the lens increases as it crystallizes (Johnston and Montési, 2014) would limit the efficiency of this restriction and the associated doming.

The northern region of Thera Macula has a surface elevation near that of the background and has a pronounced circumferential graben. According to my model, the central region is most recently active and possibly earlier in the formation process than the southern terrain. If a diapir were the driving mechanism of formation of Thera Macula, I would expect to see changes in the appearance of the northern region

of Thera Macula in data from a future mission and it is the most likely to have liquid water present.

3.6 Future Modeling and Directions

Fluid flow is not included in this model; however it could have an important impact on the results presented. While the material properties of the melt lens were changed to be consistent with a fluid, the material was still partially governed by its prescribed shape. Allowing for fluid flow may allow the fluid to flow towards the center of the lens. However, it is unclear if it could then be prevented from flowing out as it crystallizes. Allowing the inward flow of material in the lens in future models would further elucidate the mechanics possible with the proposed model. If the water were to become hydraulically sealed in the center it may allow for an additional source of tensile stresses above the melt lens. However, if the treatment of the lens as a fluid were rigorous in a model, it would need to allow for liquid water to drain through the ice shell, due to density contrasts. Such a model has the potential to determine if it is even possible to retain a large volume of water within an ice shell.

Although the current model predicts the location and orientation of cracks and yielding within the ice shell, it does not allow for the propagation of a cracks once initiated. Cracks have the ability to relieve stresses within the ice shell and modify the stress field. Including crack propagation, such as through the inclusion of extended finite element method (XFEM), can provide additional constraints on the ability of a melt lens to generate the geologic appearance observed at Thera Macula. It would be of particular interest to determine if the propagation of cracks through the ice above the melt lens, or outer most edge is preferred. If cracks can propagate a significant

distance through the overlying ice, it is possible that with additional tensile stresses, such as those from a hydraulically sealed lens, then a feature similar to chaos could form . However, if crack propagation is preferred at the edge of the lens, then it would be difficult to maintain a hydraulically sealed melt lens, and the formation of Chaos through this process would be unlikely.

Chapter 4 : The Impact of a Pressurized Regional Sea on Stresses on Enceladus

4.1 Abstract

Enceladus is a geologically active icy satellite of Saturn that erupts jets of water-rich material from several fracture sets, known as Tiger Stripes , at its South Pole. The south polar region has an anomalously high heat flux and youthful appearance. The topographic depression at the south polar region suggests that a regional ocean is localized beneath the South Pole, although it has also been proposed that Enceladus currently features a global ocean that decouples the ice shell from the rigid silicate-rich interior. However, due to the limited heat sources identified on Enceladus maintaining a global or regional ocean is challenging. Constraining the extent or existence of an ocean would provide insight into the evolutionary history and the current geological state of Enceladus. We develop an axisymmetric elastic model with a pressurized water reservoir at the base of the ice shell beneath the South Pole that represent a regional ocean as it cools and crystallizes. We compare the stresses from a model with the ice shell bonded to the rocky interior with an ice shell on riding on a frictionless surface. We also evaluate a range of ocean size (lateral extent and thickness), and cryosphere (the layer comprised of the ocean and ice shell) thickness. We find that the basal boundary conditions have important implications for the stresses in the ice shell, as well as the style of faulting predicted at the surface. Yielding at the surface is more likely when the cryosphere is thin (40 km) and the ocean is large.

A model with a 35 km thick ocean with a curvature of 160 km in a 40 km thick cryosphere predicts yielding at the South Pole and mid latitudes. The South Pole is expected to feature tensile radial cracks and is surrounded by a separate region of reverse faulting in a compressive stress regime at mid latitudes, consistent with geological observations on Enceladus. While the orientation of the Tiger Stripes at the South Pole is not predicted, the contribution of stress from a pressurized water reservoir may be important to consider when evaluating the possibility of yielding in the South Polar Terrain of Enceladus. If a bonded base is applied then no further yielding is predicted. However, a roller base results in tensile circumferential normal yielding at the north pole. If the South Polar Ocean is limited in extent, its pressurization would likely favor intrusion of water along the base of the ice shell, leading to at least partial decoupling between the ice shell and the rocky interior of the satellite.

4.2 Introduction

4.2.1 Enceladus

Enceladus is an icy satellite of Saturn, imaged by the Voyager and Cassini missions. Data from these missions reveal that Enceladus likely has a rocky interior as well as an overlying cryosphere between ~ 30 and 100 km thick (Barr and McKinnon, 2007; Schubert et al., 2007). During two of Cassini's encounters with Enceladus in 2005 the UltraViolet Imaging Spectrograph (UVIS) observed jets of water emanating from the southern hemisphere (Hansen et al., 2006; Porco et al., 2006). The observations of jets along with measurements of a high heat flux suggest that a reservoir of liquid water is present beneath the South Pole.

The precise size and location of this water body is still highly debated. A global ocean was initially proposed as the source of the water within Enceladus' jets by analogy with the Galilean satellites of Jupiter, particularly Europa (Ross and Schubert, 1989; Nimmo et al., 2007; Schubert et al., 2007). Additionally, the fracture pattern in the South Polar Terrain (SPT) is consistent with a temporally varying global stress field arising from nonsynchronous rotation of the ice shell above a global liquid ocean (Patthoff and Kattenhorn, 2011). However, Collins and Goodman (2007) proposed the existence of a regional sea as a means to explain the heat flow and depression of the South Pole relative to the rest of Enceladus.

Maintaining a global or regional ocean on Enceladus is thermally difficult. The heat flux from the SPT is larger than what is available from orbital dynamics (Meyer and Wisdom, 2007). Any ocean currently present in Enceladus is likely loosing heat. Roberts and Nimmo (2008) showed that a 40 km thick ocean would crystallize in ~30 Ma. The existence of an ocean on Enceladus today indicates a dynamic thermal history. The possibility of a sizeable reservoir of water and the observation of ongoing geologic activity makes Enceladus an exciting and important planetary body to study.

4.2.2 South Polar Terrain

The most geological distinctive feature of the SPT on Enceladus is a series of sub-parallel, linear fractures called Tiger Stripes often interpreted as tensile cracks ~500 m deep (e.g. Spitale and Porco, 2007). The jets currently erupting icy materials into space originate at the Tiger Stripes (Spitale and Porco, 2007; Porco et al., 2014). The Tiger Stripes are surrounded by and cut across many other fractures at the surface

(Figure 4.1) The outermost edge of the SPT is bonded by a circumferential deformation belt, the Southern Curvilinear Terrain (SCT), commonly interpreted to be a compressional feature (e.g. Porco et al., 2006).

The stress needed to explain the tectonic deformation and activity of the SPT and surrounding region is typically attributed to tidal activity (e.g. Patthoff and Kattenhorn, 2011). It has also recently been proposed that the fracture patterns at the SPT are consistent with a large convective cell beneath the South Pole (Crow-Willard and Pappalardo, 2015). Here, we evaluate the alternative possibility that the stress responsible for tectonic activity is related to the crystallization of a regional sea underneath the SPT.

4.2.3 Water Reservoir on Enceladus

Both a global ocean (Ross and Schubert, 1989; Nimmo et al., 2007; Schubert et al., 2007) and a regional sea (e.g. Tobie et al., 2008) have been proposed to exist beneath the ice shell of Enceladus to explain enhanced heat flux of the SPT (Spitale and Porco, 2007), the origin of jets, and topography (Collins and Goodman, 2007).

Sustaining liquid water on a planetary body with a rocky composition and a radius of only 252 km is problematic. The latent heat from planetary accretion and decay of radiogenic elements do not provide enough heat to maintain liquid water in Enceladus over the age of the Solar System (Squyres et al., 1983). Moreover, the parameters and tidal quality factor needed to maintain liquid water in Enceladus are inconsistent with the lack of evidence for liquid water on Mimas (Squyres et al., 1983). It has been proposed that the presence of liquid water on Enceladus could be episodic (Porco et al., 2006; Tobie et al., 2008; O'Neill and Nimmo, 2010). If this is

true then Enceladus may experience cycles of melting and recrystallization of water rather than having sustained a liquid ocean throughout its existence. The high heat flux at the STP implies that the ocean is likely loosing heat and crystallizing at present. Identifying ways of detecting and characterizing the state and extent of subsurface water in Enceladus would clarify the thermal history of the satellite.

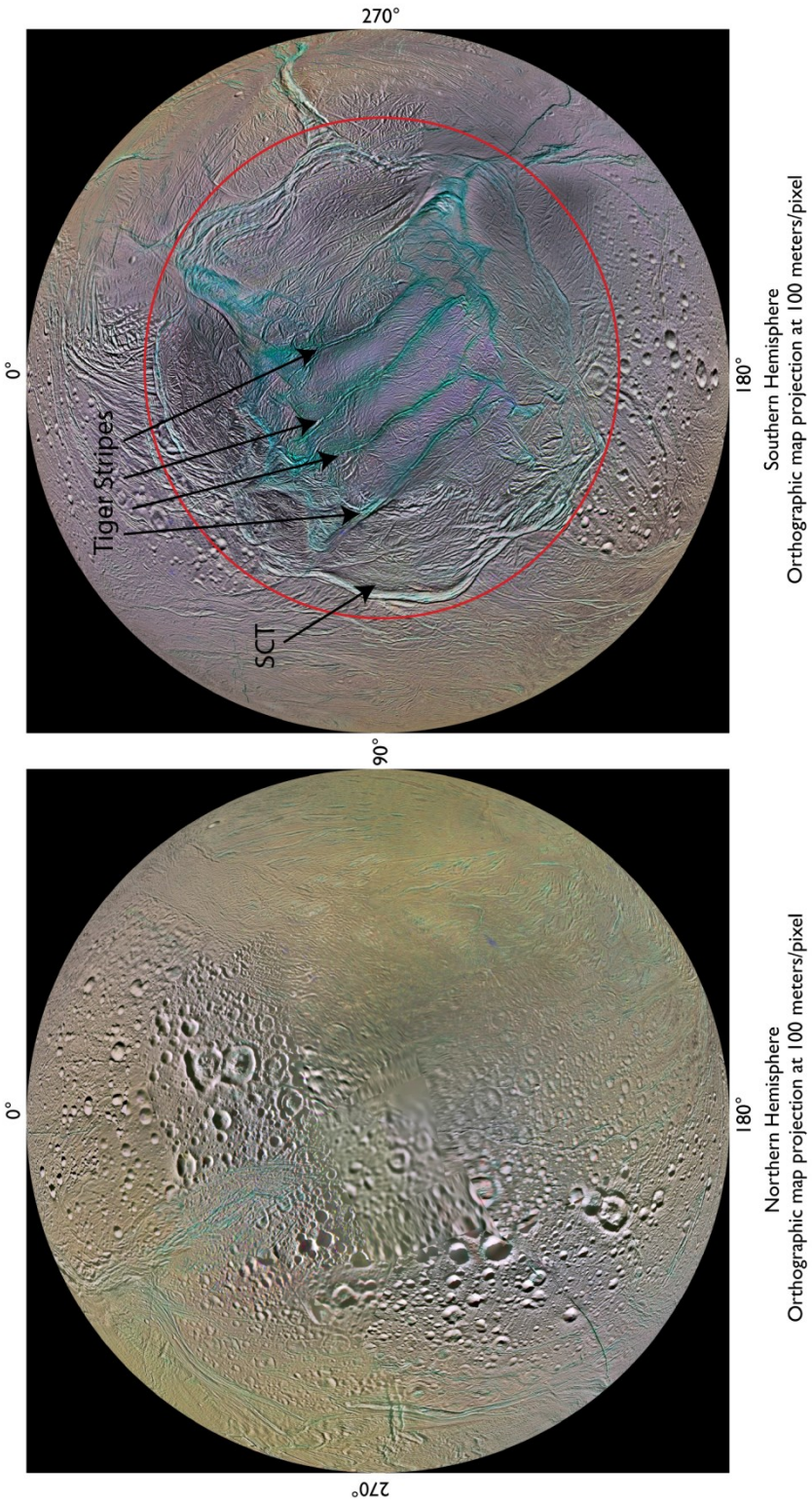

Figure 4.1. Enhanced 3-color map of Enceladus, courtesy of NASA/LPI/Paul Schenk (PIA 18435). The Tiger Stripes are the parallel lines blue cracks at the South Pole. The compressional band around the SPT is indicated by the arrow labeled SCT. The red circle is ~60° from the South Pole.

The presence of either a global ocean or a regional sea has important implications for the creation, focusing (Tobie et al., 2008) and orientation of tidal stresses as well as the deformation of the ice shell. A regional sea beneath the South Pole on Enceladus can be either positively pressurized (such as by crystallization) or negatively pressurized (if actively melting) relative to the hydrostatic pressure state. A present day, a positively pressurized water reservoir is most consistent with the observations of ongoing eruption of water from jets appear to originate from the Tiger Stripes (Porco et al., 2014) and high heat flux at the SPT. I present here a model that evaluates the stresses that could arise from the pressurization of a regional sea in order to better constrain the possible geologic setting of present day Enceladus.

4.3 Model Description

4.3.1 Model Setup

We consider the effects of a pressurized regional sea on the stresses within the overlying ice shell on Enceladus to gain a better understanding of the deformation that would result from such an interaction. The model was constructed using the finite element software COMSOL Multiphysics™.

Because of the location of the sea at one of the poles of Enceladus, the model follows an axisymmetric geometry and calculates the stresses within the entire ice shell (Figure 4.2). The radius of Enceladus is held constant at 252 km for all models. However, the size of the regional sea, the thickness of the cryosphere, T, and basal boundary conditions were varied (Table 4.1).

The ocean is assumed to fill a spherical indentation at the base of the ice shell, centered at the South Pole (Figure 4.3). The geometry of the sphere that limits the ocean is defined by two parameters, the ocean curvature, *C*, and the ocean thickness, *D* defined as the maximum height of the ocean above the inner silicate-rich core of the satellite. Per definition, this thickness is achieved at the South Pole (Figure 4.3). Ocean curvature was varied from a minimum of 50 km to the radius of the rocking interior (212 km for a 40 km cryosphere and 172 km for a 80 km cryosphere). Ocean depth was varied between 5 and 35 km for all models with a cryosphere thickness of 40 km. For models with a cryosphere thickness equal to 80 km, the range was between 5 and 75 km.

The lateral extent of the ocean at the base of the cryosphere is a function of both ocean thickness and curvature. Because of this it can be more informative to discuss the extent of the ocean in terms of ocean angle, *A* (Eqn. 4.1).

$$A = \cos^{-1}((R_i{}^2 - C^2 + y_c{}^2)/(2y_c R_i))\frac{180}{\pi}, \qquad \text{Eqn. 4.1}$$

where R_i is the radius of the rocky interior, y_c is the center of the ocean circle calculated by

$$y_c = R_i + D - C. \qquad \text{Eqn. 4.2}$$

If the ocean angle is 90°, then the edge of the ocean is at the equator. We did not consider oceans that extend beyond the equator.

The model geometry is meshed using triangular meshing elements auto-generated by COMSOL Multiphysics™ using a physics-based meshing algorithm and pre-defined extra-fine element size (~10 km). The mesh for a 40 km cryosphere and a

regional ocean with a curvature of 100 km and ocean thickness of 35 km is shown in Figure 4.4.

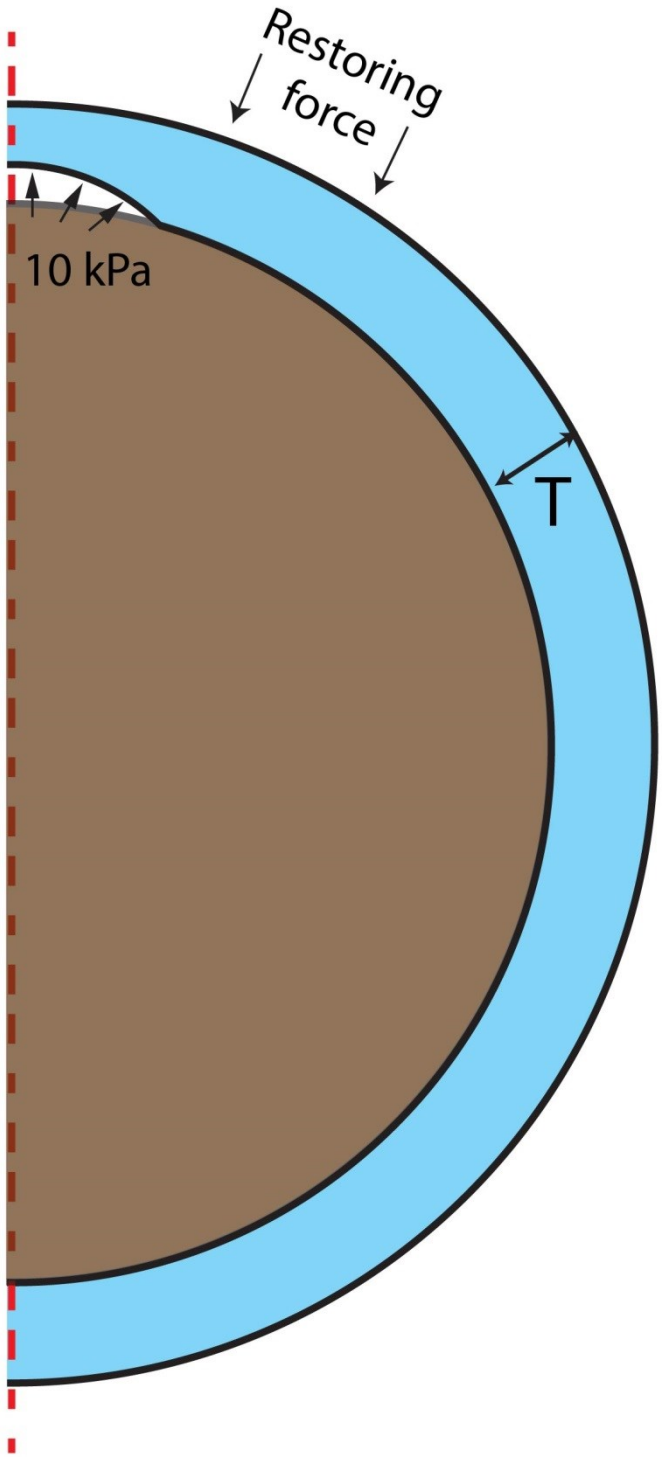

Figure 4.2. Model setup. Red dashed line is axis of symmetry. The South Pole, where the ocean is located, is a the top of this model.10 kPa of overpressure is applied to ocean interface. A buoyant restoring force is applied to the surface. *T* is cryosphere thickness (either 40 or 80 km).

Cryosphere Thickness, *T*	Basal Boundary Conditions	Ocean Thickness, *D*	Ocean Curvature, *C*
40 km	Roller	5 - 35 km	50 - 210 km
	Bonded	5 - 35 km	50 - 210 km
80 km	Roller	5 - 75 km	50 - 170 km
	Bonded	5 - 75 km	50 - 170 km

Table 4.1. General model categories and model parameters considered.

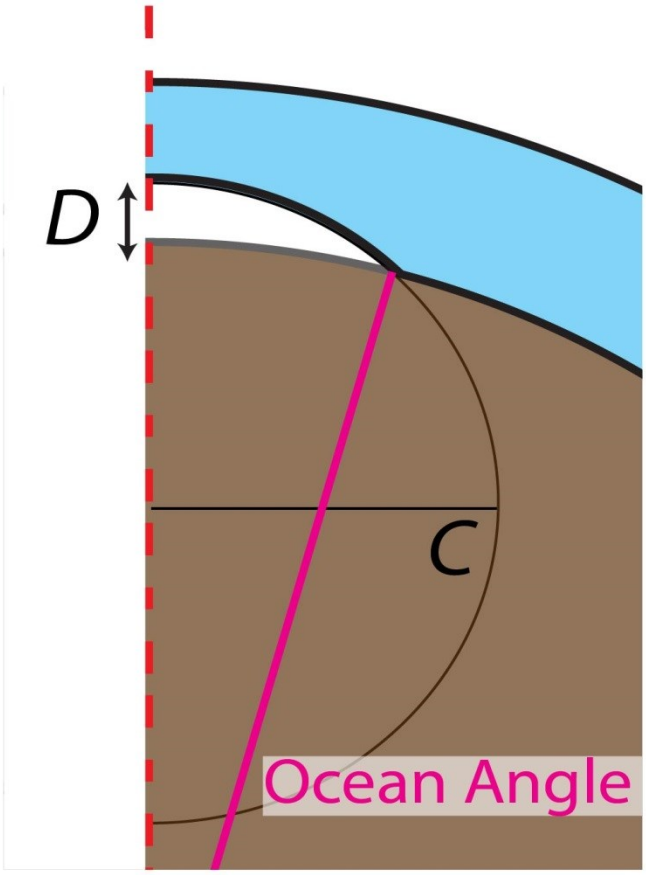

Figure 4.3. Definitions of ocean geometry. The red line is the axis of symmetry, *D* is the thickness of the ocean, and *C* is the radius of the ocean. The range in parameters considered is show in Table 4.1. The ocean angle is indicated by the pink like connecting the center or the rocky interior with the outer most edge of the ocean.

We only solve for the elastic deformation of the ice shell. While plastic deformation is expected when stresses exceed the strength of the ice, as observed in places in our model, we are attempting to illuminate the fundamental behavior of the response of an ice shell to a pressurized underlying water reservoir. Additionally, the precise strength and post-failure behavior of ice at the low temperatures observed on Enceladus are poorly constrained at present. The intensity of stress and therefore failure also depends on the pressurization of the sea, which is at present unconstrained. Therefore, adding a more complex rheology would not necessarily add realism to the model and carries with it the risk of obscuring the relations between the parameters considered.

We elected to use the an elastic ice rheology based on pure water ice on Earth (Petrenko and Whitworth, 1999). We considered the behavior of ice with a Young's modulus, *E*, of 9 GPa, and a Poisson's ratio, ν, of 0.3 (Table 4.2). The deformation of an elastic material in response to stress is a linear relationship defined by Eqn. 4.3.

$$\varepsilon_{ij} = \frac{1}{E}[(1+\nu)\sigma_{ij} - \nu\sigma_{kk}\delta_{ij}], \qquad \text{Eqn. 4.3}$$

where ε is the strain tensor and δ is the Kronecker operator.

As the rocky interior is more rigid than the ice shell, it is assumed not to deform at all in our models. The interaction between the ice shell and rocky mantle was represented by the boundary condition at the base of the cryosphere. Since little is known about the nature of the interface, two different boundary conditions were considered. The first is the case of a bonded surface interface where no movement is allowed, imposing the boundary condition of zero displacement (u=0) at the base of the ice shell. In order to consider the case where there is a layer that facilitates the

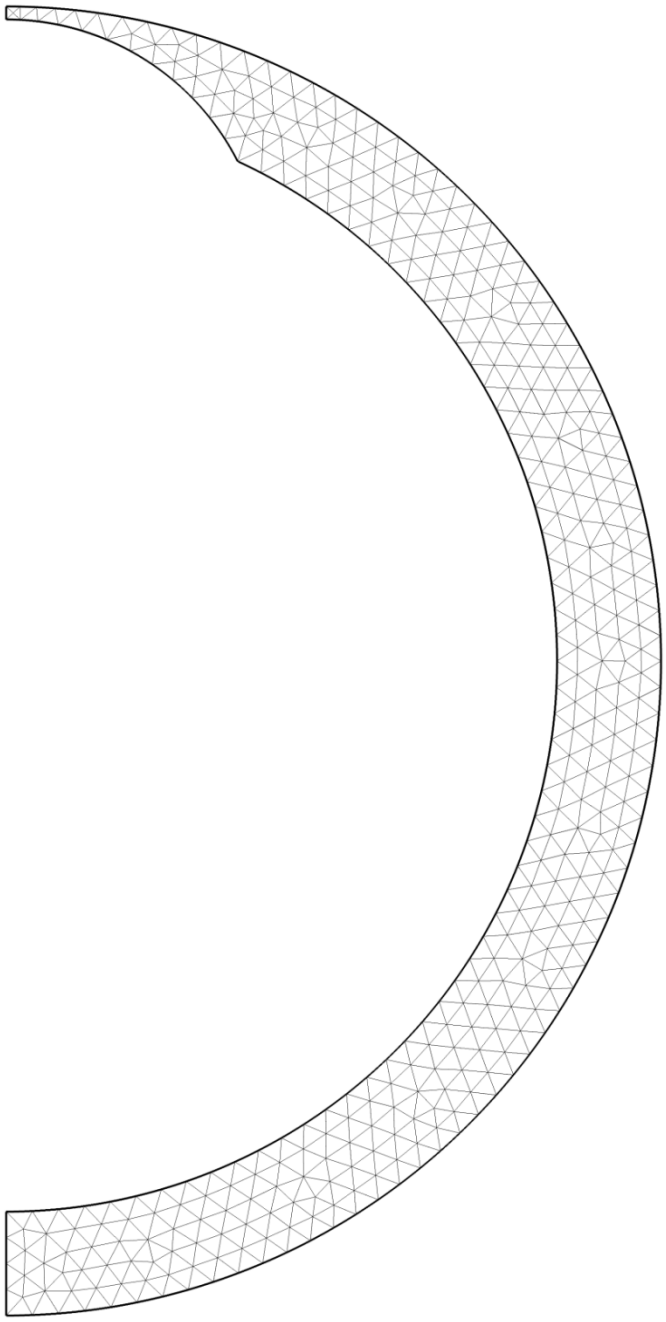

Figure 4.4. Example mesh for a model with a 40 km cryosphere and a regional ocean with a curvature of 100 km and ocean thickness of 35 km.

movement of the ice shell, such as water or till, we consider a roller boundary, which prohibits motion normal, *n*, to the surface of the boundary, but allows tangential movement (Eqn. 4.4), with no shear stress along the interface.

$$n \cdot u = 0 \qquad \text{Eqn. 4.4}$$

A buoyancy restoring force, *F*, is imposed at the surface of the planet (Eqn. 4.5) to account for density contrast related to the uplift of the ice at surface.

$$F = \rho g\left(u_x \sin\theta + u_y \cos\theta\right) \qquad \text{Eqn. 4.5}$$

$$\theta = \cos^{-1}(y/d\,d) \quad , \qquad \text{Eqn. 4.6}$$

where ρ is the density of ice, 930 kg m^{-2} (Petrenko and Whitworth, 1999), g is the gravitational acceleration on Enceladus, 0.113 m s^{-2}, u_x is the displacement in the x-direction, and u_y is displacement in the y-direction, and θ is the colatitude, defined in Eqn. 4.6 , where y is the y-coordinate, and d is the distance from core.

A constant pressure of 10 kPa is applied to the boundary between the regional sea and the overlying ice. The use of an elastic rheology (Eqn. 4.3) means that the magnitude of the stress and strain scales linearly with the magnitude of the overpressure applied. This pressure is consistent with the pressure predicted from the crystallization of water on Enceladus (Manga and Wang, 2007). However, our model is not attempting to constrain the magnitude of the over-pressurization possible in a south polar ocean on Enceladus.

Symbol	Definition	Value
E	Young's modulus	9 GPa
ρ	density of ice	930 kg m^{-3}
ν	poisson's ratio	0.3

Table 4.2. Ice shell rheological parameters used in models. (Petrenko and Whitworth, 1999)

4.4 Results

For the consideration of the model results, we separate the models into four categories based on the properties of the cryosphere and its base: 40 and 80 km cryospheres with roller boundaries, and 40 and 80 km cryospheres with bonded boundaries (Table 4.1). Each model category contains models with different ocean curvature *C* and depth *D*. We will occasionally refer to a specific model using the nomenclature of the cryosphere thickness, boundary condition, ocean thickness, and ocean curvature (i.e. 40R5D50C means a 40 km cryosphere with a roller boundary and a 5 km thick ocean, an ocean curvature of 50 km). The extent of the ocean at the base of the cryosphere is given by the ocean angle (Eqn. 4.1)

The model results focus on the von Mises stresses (shear stresses), and the maximum principal stresses acting on the surface and base of the ice shell. A positive stress indicates tension in our models. The stresses acting on a boundary are separated into vertical, shear, longitudinal and latitudinal stresses to inform us about the orientation of failure anticipated on the specified surface. The shear stresses at the surface are near zero for the model, in agreement with the free surface boundary condition. Any non-zero shear stress is due to noise and is always less than 2 kPa (usually less than 0.5 kPa). The principal stresses, used to identify tensile failure (crack formation), are most important at the surface. The von Mises stresses provide information about the overall stress state with of the ice both at a surface and internally and are used to identify shear failure (faulting). As will be discussed in section 4.2, the stresses reported do not include the overburden pressure in the ice shell, which may modify the tectonic interpretation of these models. Combining the

principal stress and von Mises stress analyses allows us to predict the type of failure that at the surface of Enceladus and compare it with observations.

Imposing 10 kPa of overpressure in the regional ocean results in two types of yielding: von Mises (>20 kPa von Mises stress) and tensile (>2 kPa principal stress). If a point meets the tensile yielding criteria we always categorize it as tensile failure, which is manifested as an open crack or fissure. However, the tensile yielding criteria is not met but the von Mises criterion is verified, we categorize failure as shear failure, which likely produces a fault.

For the sake of simplicity the location of yielding is divided into three categories: south polar, mid latitude, north polar. South polar yielding is defined as continuous yielding originating at the South Pole. A similar definition is used for the north polar region (using the north pole instead). Mid latitude yielding is defined as a region yielding not originating at either of the poles.

While our models predict both tensile and von Mises yielding, the post-failure behavior, which indicates whether the extent of crack propagation or strain localization, is not modeled in detail. We only note the extent and location of the yielding regions and incorporate this information into our interpretation.

4.4.1 General Results

Tensile yielding at the South Pole is predicted in nearly every model, and is only absent when the ocean is too small relative to the cryosphere. Tensile yielding at the north pole is also predicted in several models when the model has a roller base. This is due to the ocean effectively pushing the rocky interior against the base of the cryosphere at the north pole. Mid latitude yielding is predicted in a subset of models

with a 40 km cryosphere and never in the 80 km cryosphere. It develops as a result of stress concentration at the edge of the ocean. When the base of the cryosphere is bonded to the rocky interior, the mid-latitude yielding is tensile in nature. However, when a roller base is used, von Mises yielding is predicted in the mid-latitude region. Figure 4.5 summarizes the style of yielding observed in our four main model categories and Figure 4.6 illustrates the geometry of the regions of yielding in polar projections.

In every model, the highest magnitude of stress at the surface is directly above the ocean, at the South Pole. Although stress is always a enhanced directly adjacent to the pressurized ocean, the stress magnitude elsewhere in the ice shell depends on the size of the ocean, the thickness of the ice shell, and the basal boundary conditions used. Yielding is more likely to occur in models with a larger ocean and the lateral extent of yielding (failure angle) at the surface is controlled largely by the lateral extent of the ocean (ocean angle).

4.4.2 Effects of Basal Boundary Conditions

The kind of basal boundary conditions considered (bonded and roller) influences the pattern of stresses within the ice shell and yielding at the surface. The most noticeable change is not directly above the ocean, but rather in the northern hemisphere. Figure 4.7 compares the distributions of von Mises stress with a bonded interface boundary (A) and a roller boundary (B) for a 40 km thick cryosphere, a 30 km thick ocean, and an ocean angle of 68˚. In both models, the von Mises stress directly above the ocean at the South Pole exceeds 20 kPa, as indicated by the thin black line. However, when the base of the cryosphere is bonded to the rocky interior

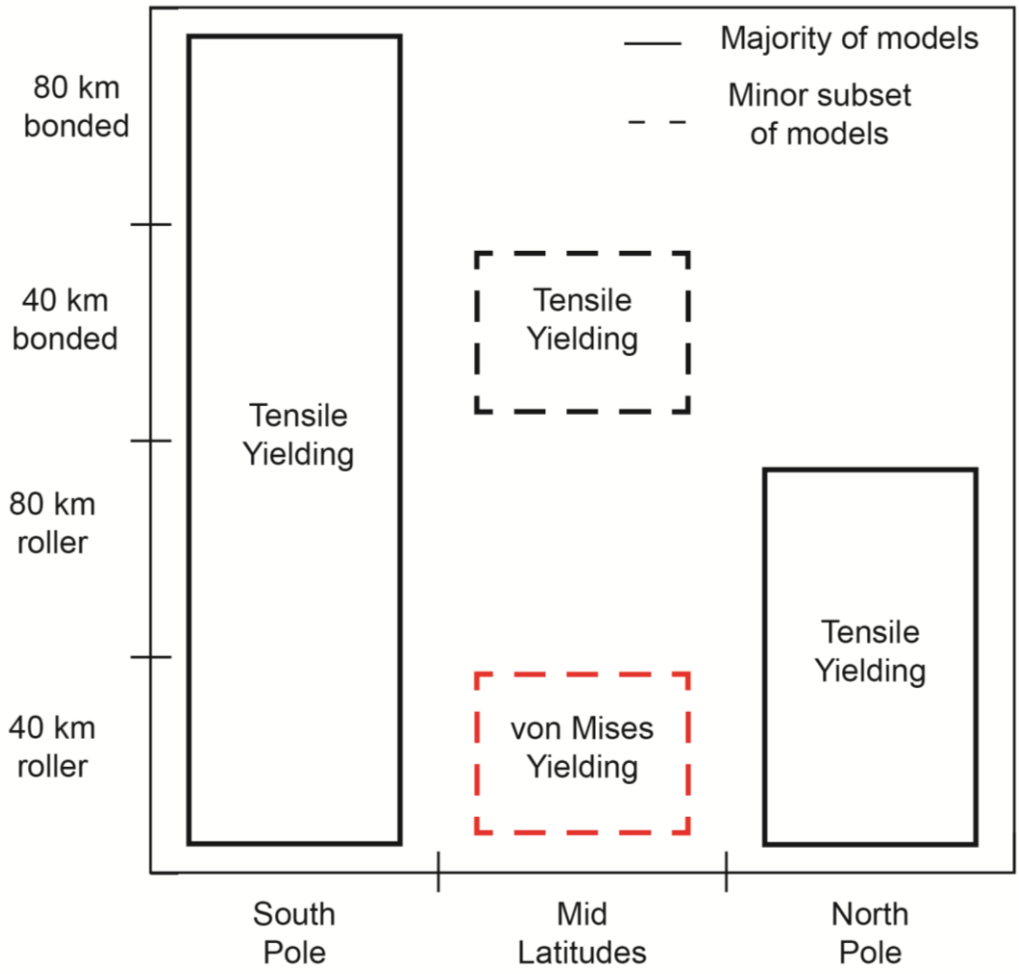

Figure 4.5. Summary of yielding regime predicted in the South Pole, mid-latitude, and north pole for each model category. Red lines indicates von Mises yielding, black indicate tensile yielding. Dotted lines indicate predicted yielding type is reported for a small subset of models for the given category.

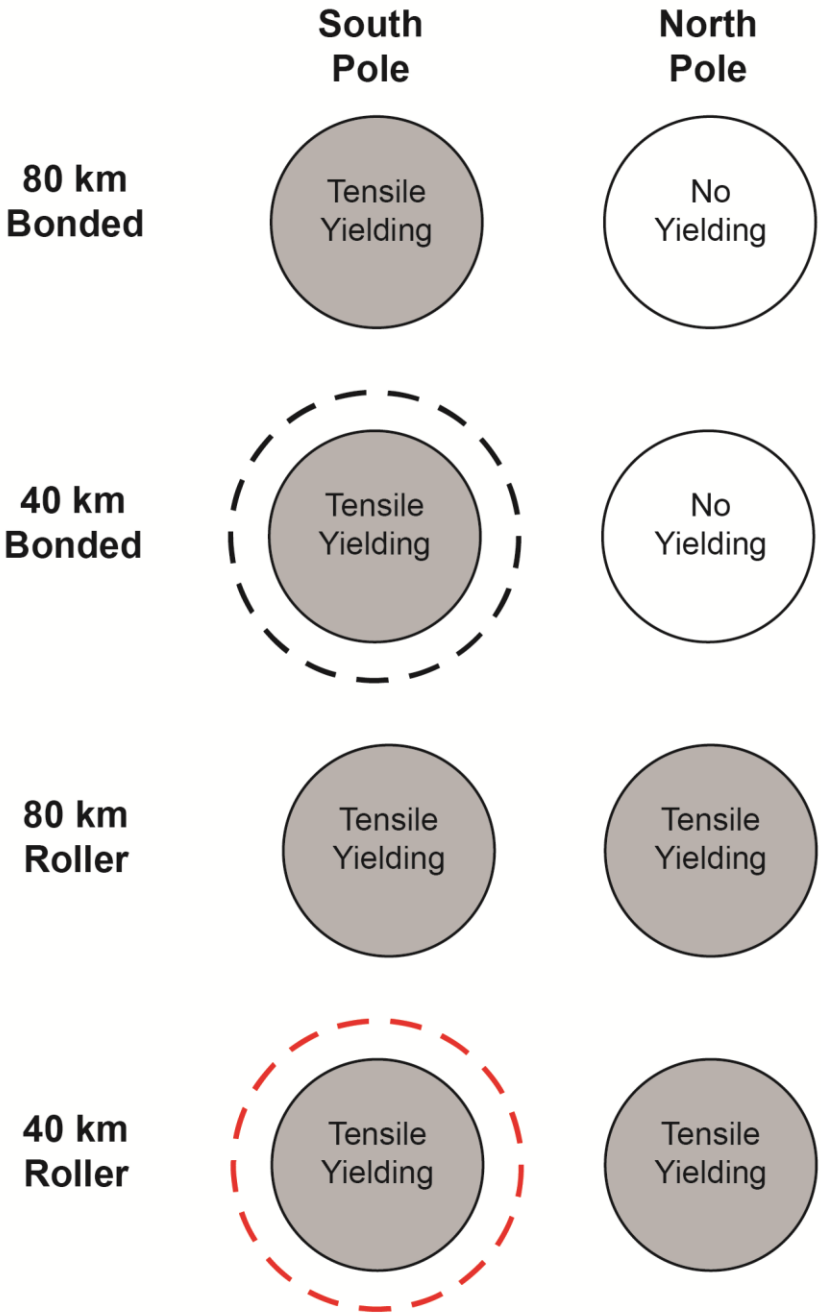

Figure 4.6. Summary of yielding predicted in models in map view of the southern hemisphere on the left and northern hemisphere on the right. Red indicates von Mises yielding, black and grey indicate tensile yielding. Dotted lines indicate predicted yielding type is reported for a small subset of models for the given category. The size of each yielding domain depends on the ocean angle and ice shell thickness.

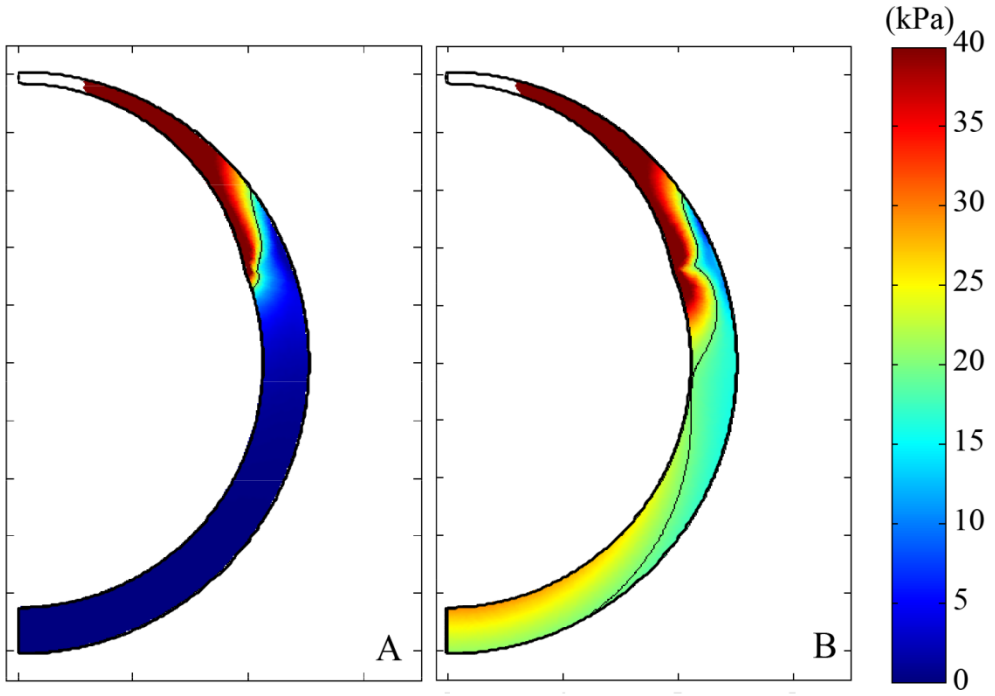

Figure 4.7. Distribution of von Mises stress (in kPa) in a 40 km thick cryosphere and a 30 km thick ocean with an ocean angle of 68˚ for A) an ice shell with a base fixed to the rocky interior and B) an ice shell with a base allowing tangential movement. White indicates stresses above 40 kPa and the black contour outlines shear failure at a von Mises stress of 20 kPa. In the model with a fixed base (A) the von Mises stresses are confined to the southern hemisphere, however, when the base is allowed tangential movement (B) stress is transmitted through the ice shell to induce yielding at the antipodes of the ocean.

(Fig. 4.7A), stress is only enhanced in the region adjacent to the pressurized ocean and approach zero in the northern hemisphere. In contrast, when the base of the cryosphere is allowed tangential motion (Fig. 4.7B), the enhanced stresses are no longer limited to the region immediately adjacent to the ocean. Two lobes of enhanced stress are seen around the outermost edge of the ocean. The magnitude of stress within the ice shell decreases near the equator, but increases again near the north pole. This stress pattern is explained by the ocean overpressure essentially lifting the entire ice shell in the axial direction, or equivalently pushing the rocky interior downward. At the north pole, the shell is forced against the rocky interior, which acts as a rigid indenter. Yielding is predicted in both the north and south polar regions when the cryosphere is allowed to move freely across the rocky interior. When the base of the cryosphere is bonded to the rocky interior, however, the rocky interior shelters the northern hemisphere from the stress generated by ocean pressurization. No yielding is predicted at the north pole.

Figure 4.8 shows the von Mises stress distribution for an 80 km thick cryosphere and a 70 km thick ocean with an ocean angle of 67˚. Again, stress is increased adjacent to the ocean in both the fixed and roller boundary models. Higher stress is observed in the northern hemisphere when the boundary allows for tangential movement but do not reach sufficient amplitude to exceed a yield stress of 20 kPa. Two lobes of enhanced stress are observed around the outermost extent of the ocean, although still of insufficient amplitude for shear failure to affect the surface of the satellite.

-

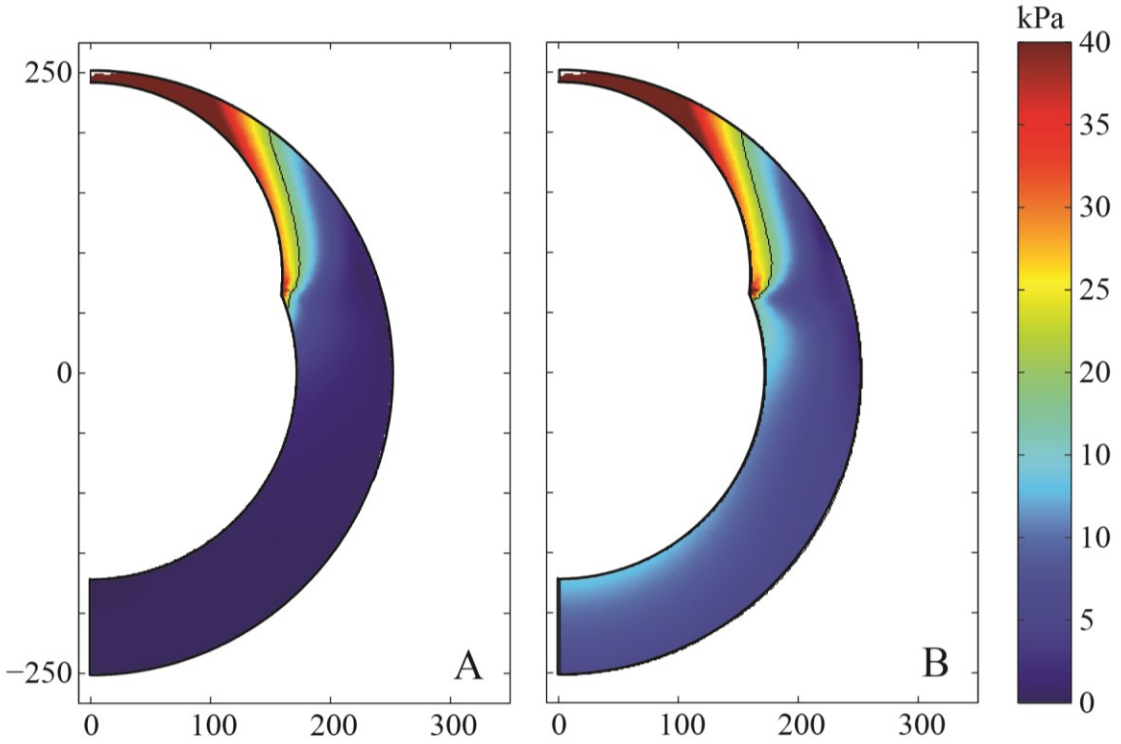

Figure 4.8. Same as Figure 4.7 but for a 80 km thick cryosphere, a 70 km thick ocean, and an ocean angle of 67˚. When the base is fixed (A), the von Mises stresses are confined to the southern hemisphere but when the base is allowed tangential movement (B), stress is transmitted through the ice shell to the antipodes of the ocean. However, yielding in the north pole is not predicted which the thicker ice shell.

Another important implication of the basal boundary condition is that a roller base results in shear failure at mid latitude in a 40 km thick cryosphere. Figure 4.9 shows how the location of yielding at the surface of the satellite (shaded regions) varies with ocean curvature for each ocean thickness. Grey indicates tensile yielding while red indicates von Mises yielding. When the von Mises criterion is verified, the vertical stress is zero and the longitudinal and latitudinal stresses are negative (compression), implying the formation of reverse faults. The vertical stress, which is solely due to buoyancy restoring forces, quickly approaches zero as the distance from the South Pole increases in all models and the predicted topography becomes vanishingly small.

It is important to keep in mind that the stresses reported do not include the overburden stresses. Given an ice density of 930 kg m^{-3} the overburden stress increases by ~10 kPa per 100 m. The maximum surface stress reported by our models is 700 kPa. If that stress was maintained down through the ice shell (which we would not expect), the crack could propagate to 7 km depth.

4.4.3 Effects of cryosphere thickness and ocean geometry

A thicker ice shell reduces the stress in the ice shell for a given ocean size. Figures 4.7 and 4.8 show that even with a larger ocean the stresses in the ice shell are lower for an 80 km cryosphere. The von Mises stress in the models with a 40 km thick cryosphere exceed 40 kPa across much of the South Polar Region, whereas in the model with a 80 km thick cryosphere, stresses only exceed 40 kPa right at the south Pole.

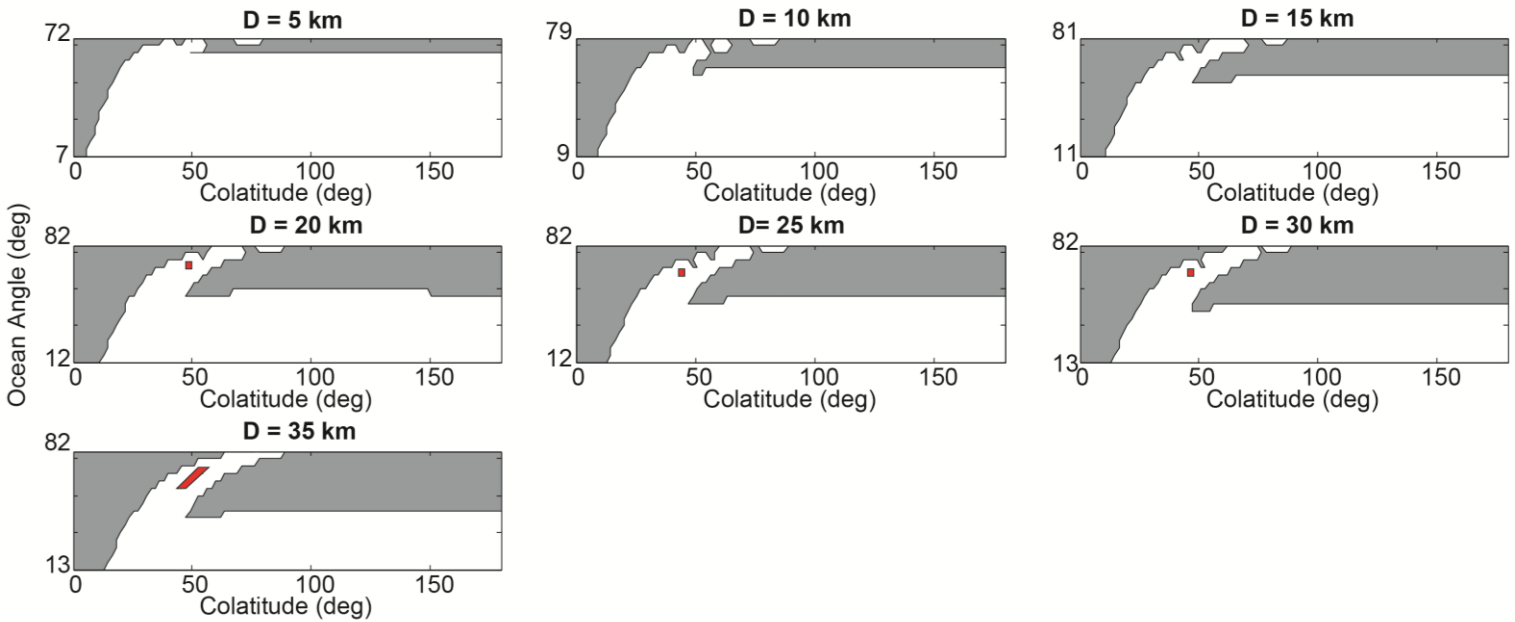
D = 5 km
D = 10 km
D = 15 km
D = 20 km
D= 25 km
D = 30 km
D = 35 km
Ocean Angle (deg)
Colatitude (deg)
72
7
79
9
81
11
82
12
82
12
82
13
82
13
0
50
100
150

Figure 4.9. Location of surface yielding in 40 km thick ice shell with a roller base. Tensile yielding is indicated by shaded grey regions. Von Mises yielding is indicated as red shaded regions. Each plot includes the range of ocean angles compatible with the ocean thickness, *D*. An increase in either ocean angle or ocean thickness increases the extent of surface yielding. These is the only model configartion for which von Mises yield is observed at mid-latitude. Failure is expected at the north pole (colatitude 180°) if the ocean angle is large than ~45°. Failure at the South Pole is predicted in every model.

The lateral extent of yielding also decreases with increasing cryosphere thickness. A 5 km thick ocean with an ocean angle of 72° induces yielding across much of the north pole in an 40 km thick cryosphere (Figure 4.9). However, no yielding is predicted for the same size ocean in an 80 km thick cryosphere (Figure 4.10).

In all models, the lateral extent of yielding increases as the ocean angle increase or ocean thickness increases (Figures 4.9 - 12), regardless of the basal boundary conditions. Comparing between Figures 4.9 and 4.11 or 4.10 and 4.12, it is apparent that a thinner ice shell results in a greater extent of surface yielding. The radial extent of the region with enhanced stresses is determined by the ocean size. The extent of yielding in the South Polar Region is always less than the ocean angle.

4.4.4 Types of Surface Faulting

Thus far, we only differentiated between tensile and von Mises yielding. However, using Anderson's theory of faulting (Anderson, 1905) and the relative magnitude of the surface components of stress (latitudinal, longitudinal and vertical), predictions about the type of faulting can be made. Our model predicts only normal faults at the poles on the surface, that are either concentric (CNF) or radial (RNF) about the pole. When tensile failure is predicted, these state of stress imply concentric or radial fractures. Concentric reverse faulting (CRF) is predicted at mid-latitudes but only for a 40 km thick cryosphere and roller boundary conditions. While other types of faulting are possible (such as strike-slip) the yielding criteria were not met when the stress components were oriented to allow them.

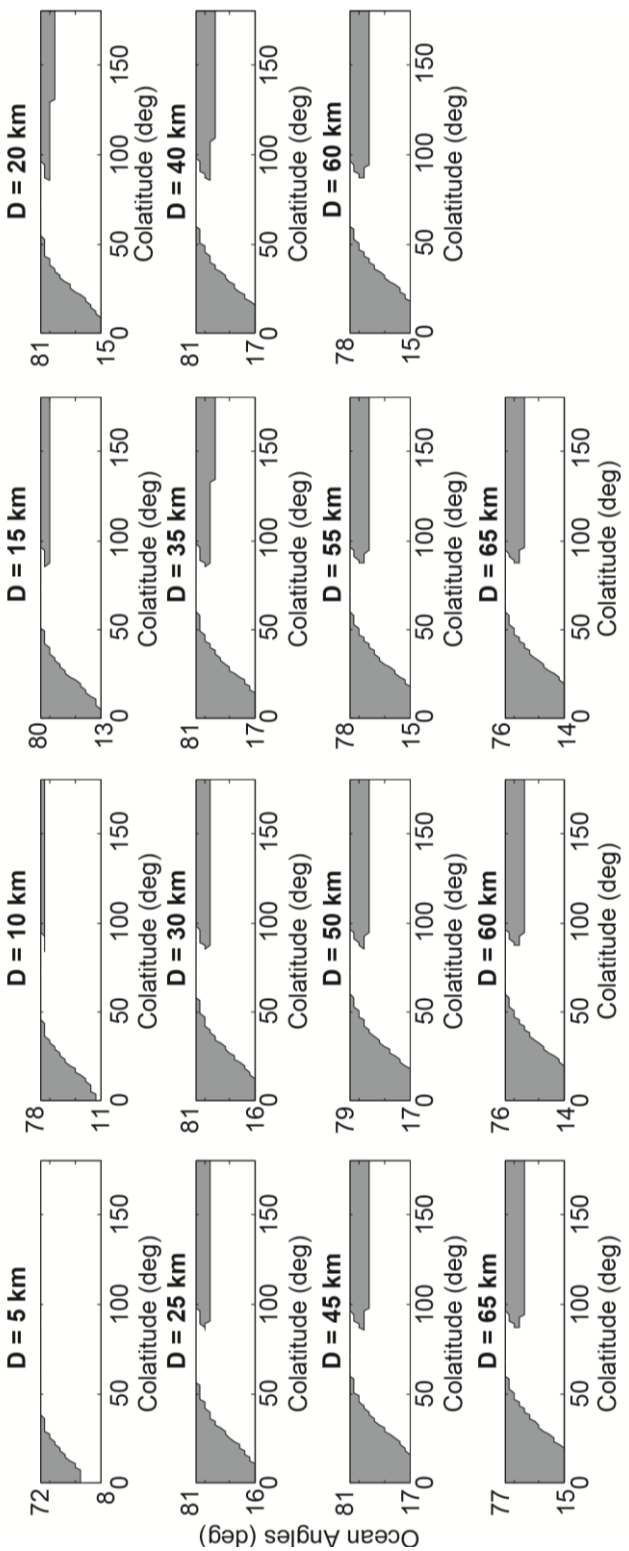

Figure 4.10. Same as figure 4.9 but for a 80 km thick ice shell with a roller base. The conditions under which failure is expected at the north pole (colatitude 180°) are less common than for a 40 km thick ice shell and require an ocean angle larger than ~60°.

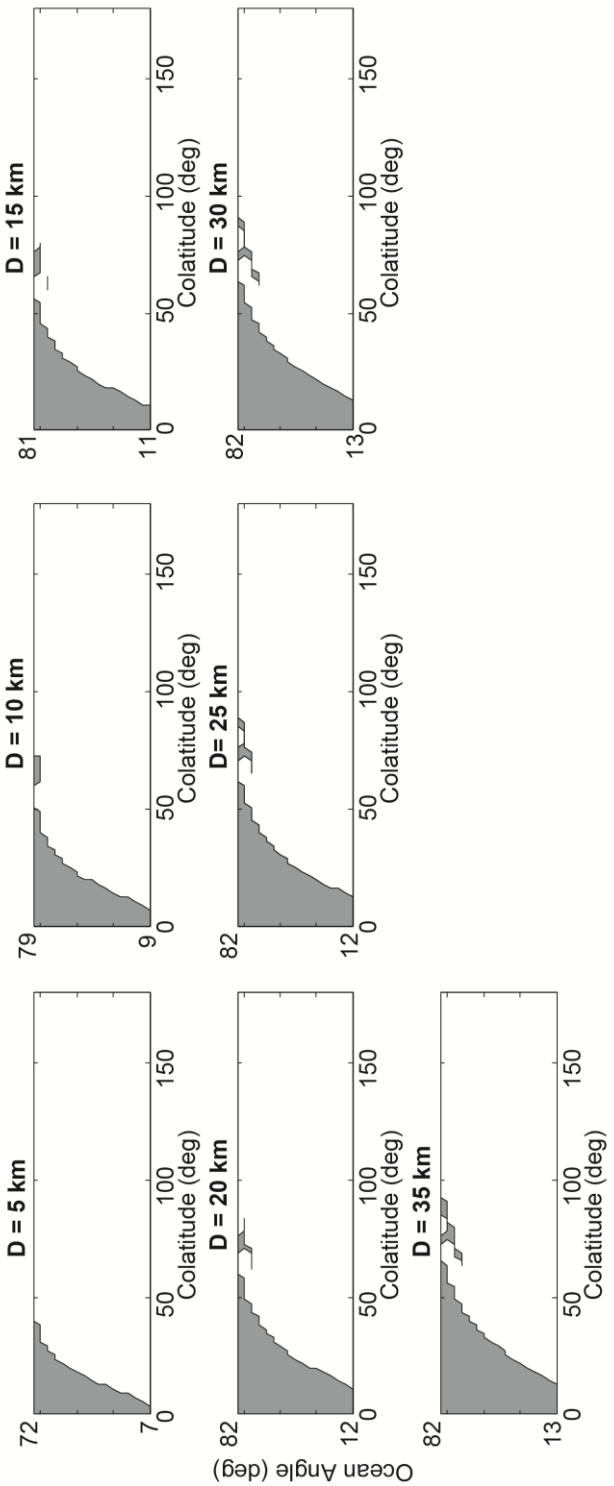

Figure 4.11. Same as figure 4.9 but for a 40 km thick cryosphere with a bonded base. Yielding at the north pole (colatitude 180°) is never observed. Only tensile failure is predicted in the mid-latitude band, and only for the largest oceans (ocean angle larger than ~70°).

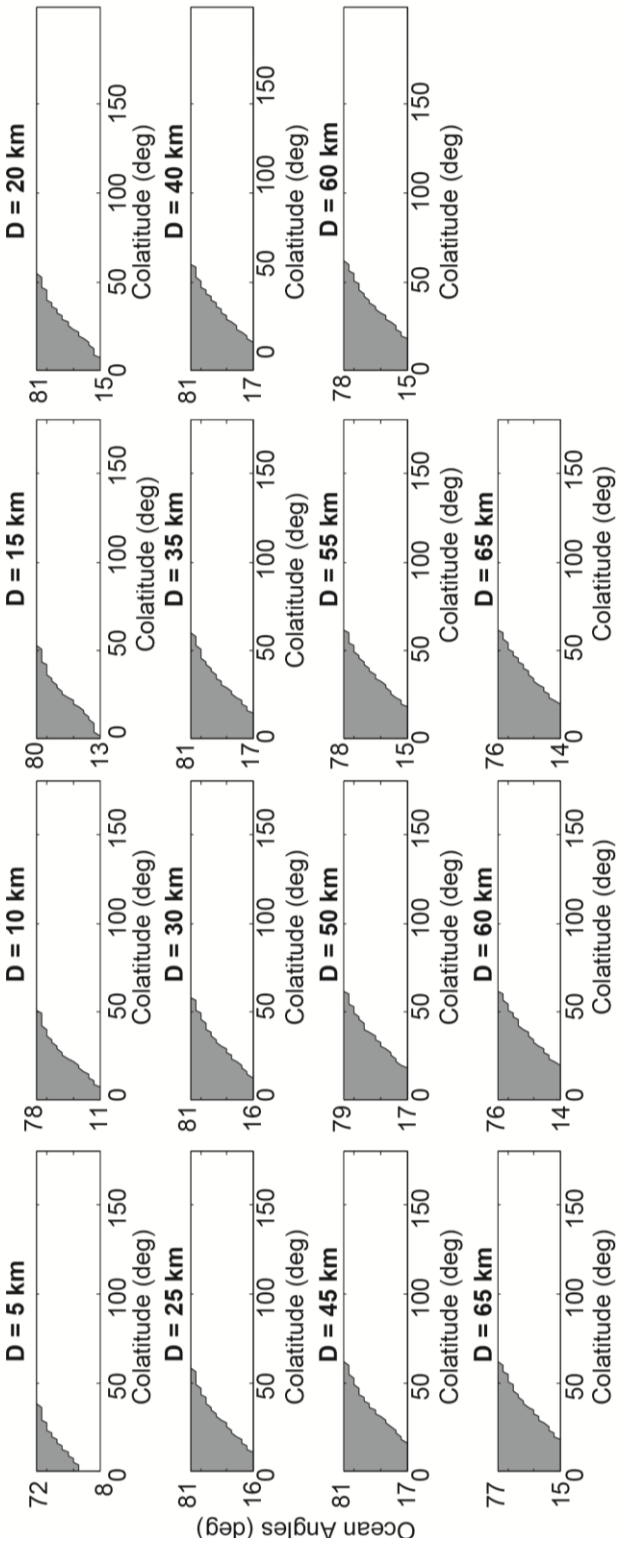

Figure 4.12. Same as figure 4.9 but an 80 km thick cryosphere with a bonded base. Yielding is observed only at the South Pole (colatitude 0°).

We classify the faulting regime observed in our model into ten categories. Representative distribution of stress for each regime are shown in Figure 4.13. Regimes A, C, and E have RNF at the South Pole. In Regimes C and E, that region is surrounded by CNF, which is itself surrounded by a second region of RNF for Regime C. Regimes B and D have CNF at the South Pole, surrounded by a region of RNF for Regime B. Each of these five categories is accompanied by a variant, identify as Ap, Bp, Cp, Dp, or Ep, in which faulting is predicted at the north pole. Faulting at the north pole is always CNF. Only a few models predict faulting at mid-latitude (Figure 4.9-4.12).

Figure 4.14 summarizes the geometrical parameters for which each regime is observed for each model category. The color of the boxes indicate the regime type, with white indicating that no surface failure was reported. Only the models with 80-km thick cryosphere and smallest ocean do not feature failure of any sort. Failure at the north pole is observed only in models with roller boundary conditions and relatively large ocean. Regimes A and Ap are the most commonly observed, showing that the most likely evidence on a pressurized regional ocean on Enceladus is the formation of radial fracture at the South pole.

Models that predict yielding in the mid latitudes are highlighted by a black outline in Figure 4.14,. The mid-latitude yielding for a bonded base is always tensile (Figure 4.15B), whereas the mid-latitude yielding for a roller base is always CRF (Figure 4.15A).

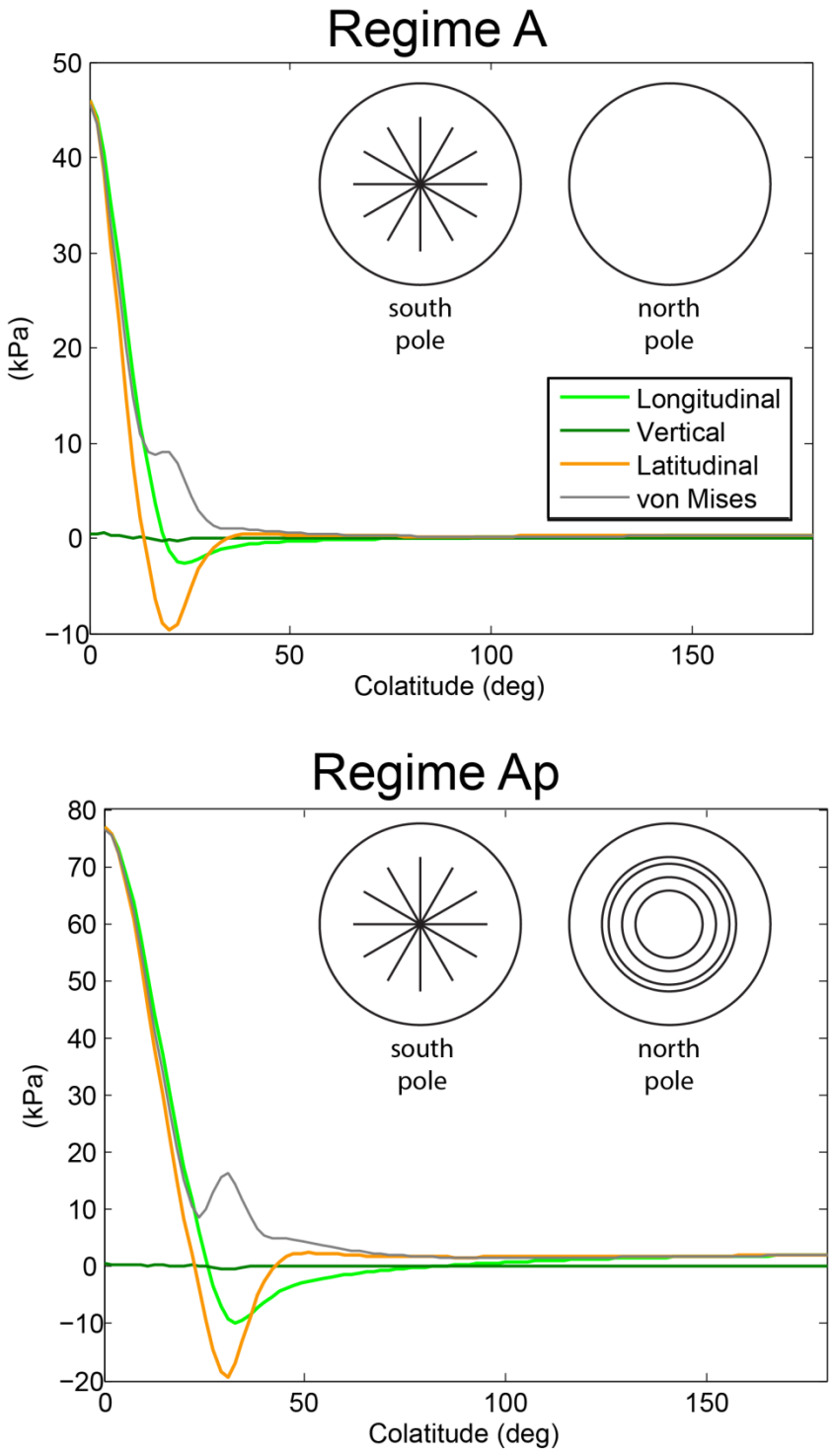

Figure 4.13A. Faulting regime A and Ap. Regime A has RNF at the South Pole, but no yielding in the north (example from 40R25D80C). Regime Ap has RNF in the South Pole, and CNF at the north pole (example from 40R25D130C).

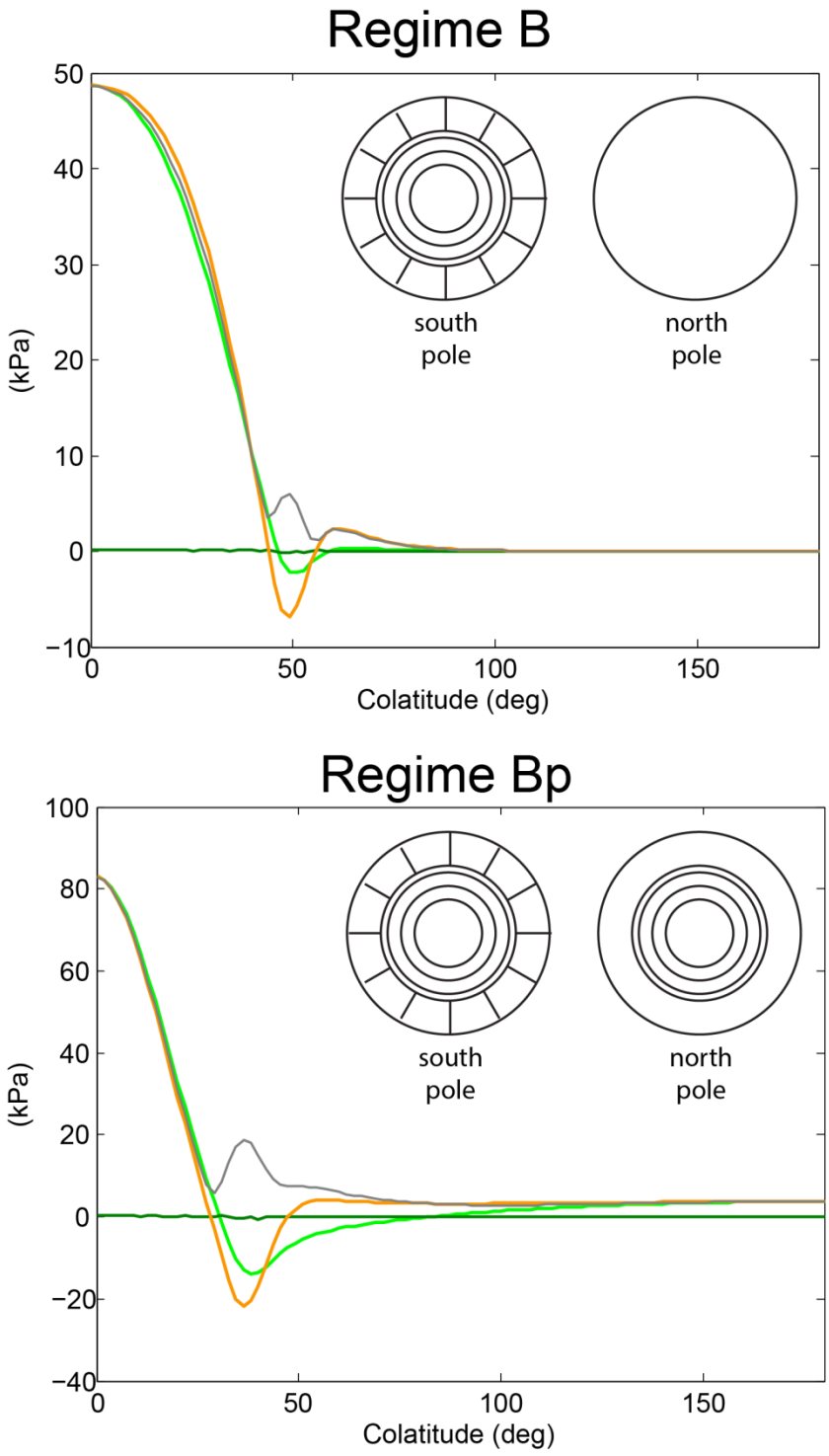

Figure 4.13B. Faulting regimes B and Bp. Regime B has RNF at the South Pole surrounded by CNF and no yielding in the north (example from 40B25D190C). Regime Bp has RNF at the South Pole surrounded by CNF, and CNF at the north pole (example from 40R25D150C).

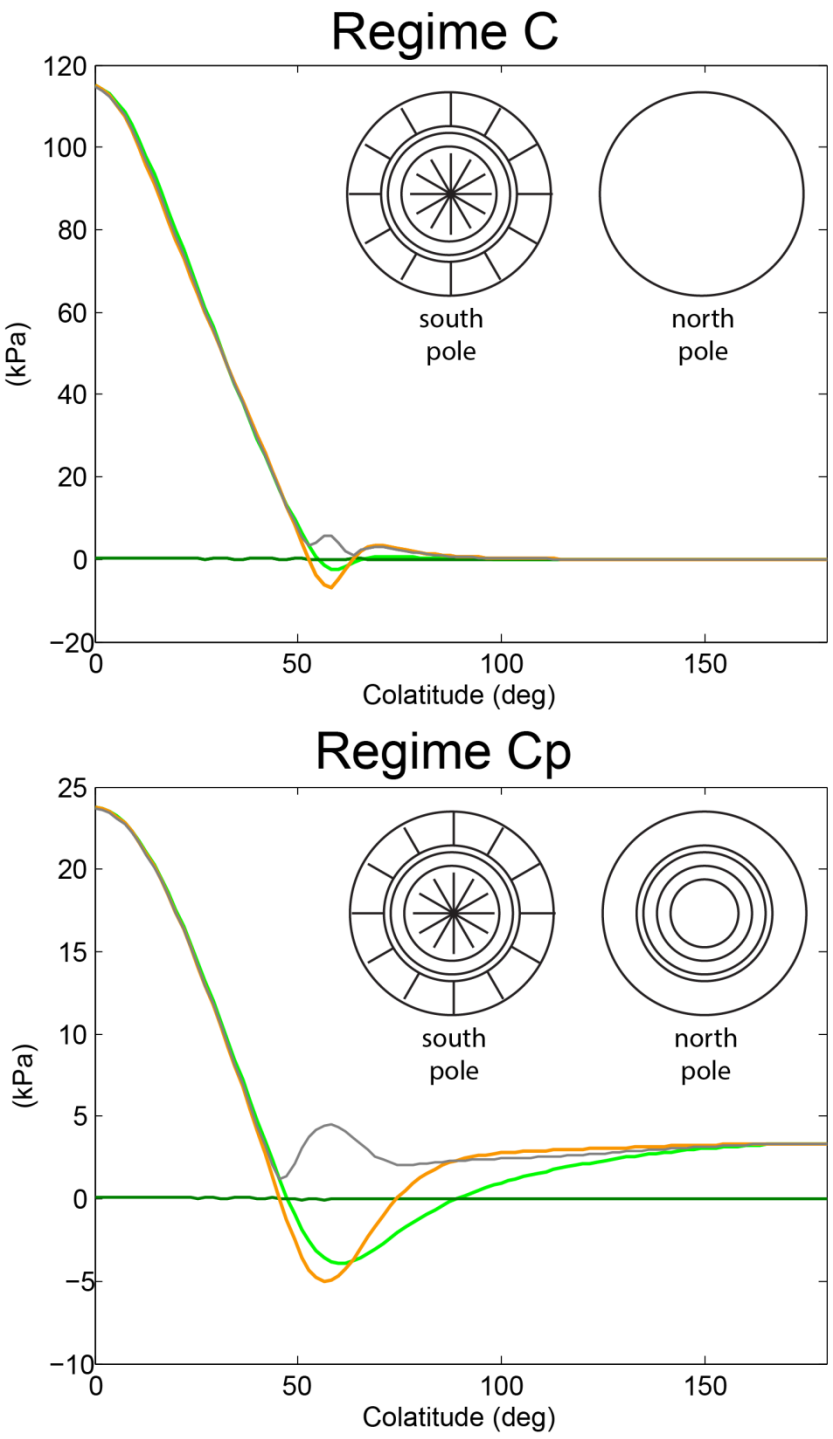

Figure 4.13 C. Faulting regimes C and Cp. Regime C switches between RNF, CNF and back to RNF at the South Pole with no yielding in the north (example from 40B30D130C). Regime Cp has the same pattern in the South Pole but CNF at the north pole (example from 80R40D140C).

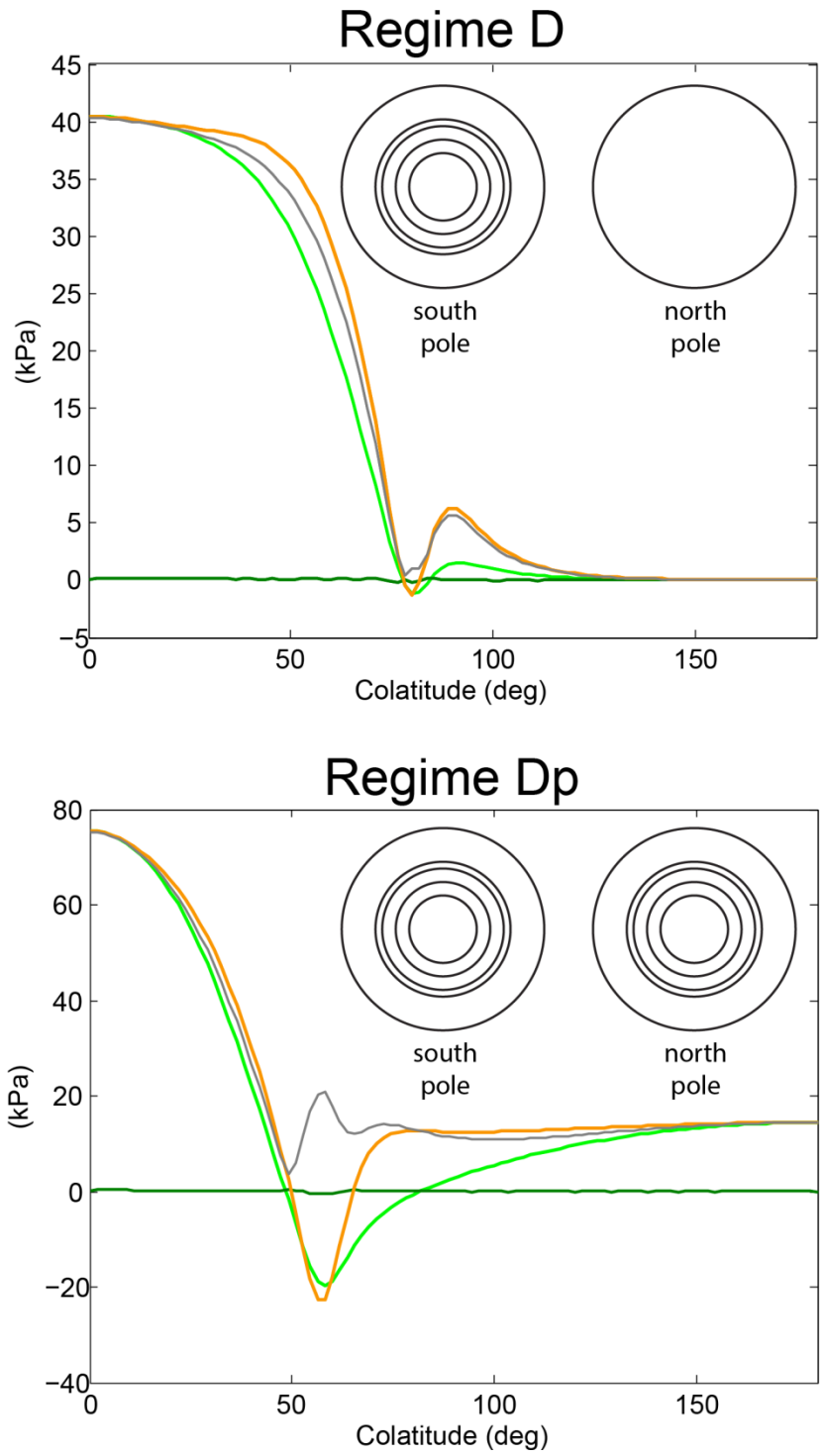

Figure 4.13D. Faulting regimes D and Dp. Regime D has CNF at the South Pole with no yielding in the north (example from 40B15D210C). Regime Dp has CNF at both the south and north poles (example from 40R25D210C).

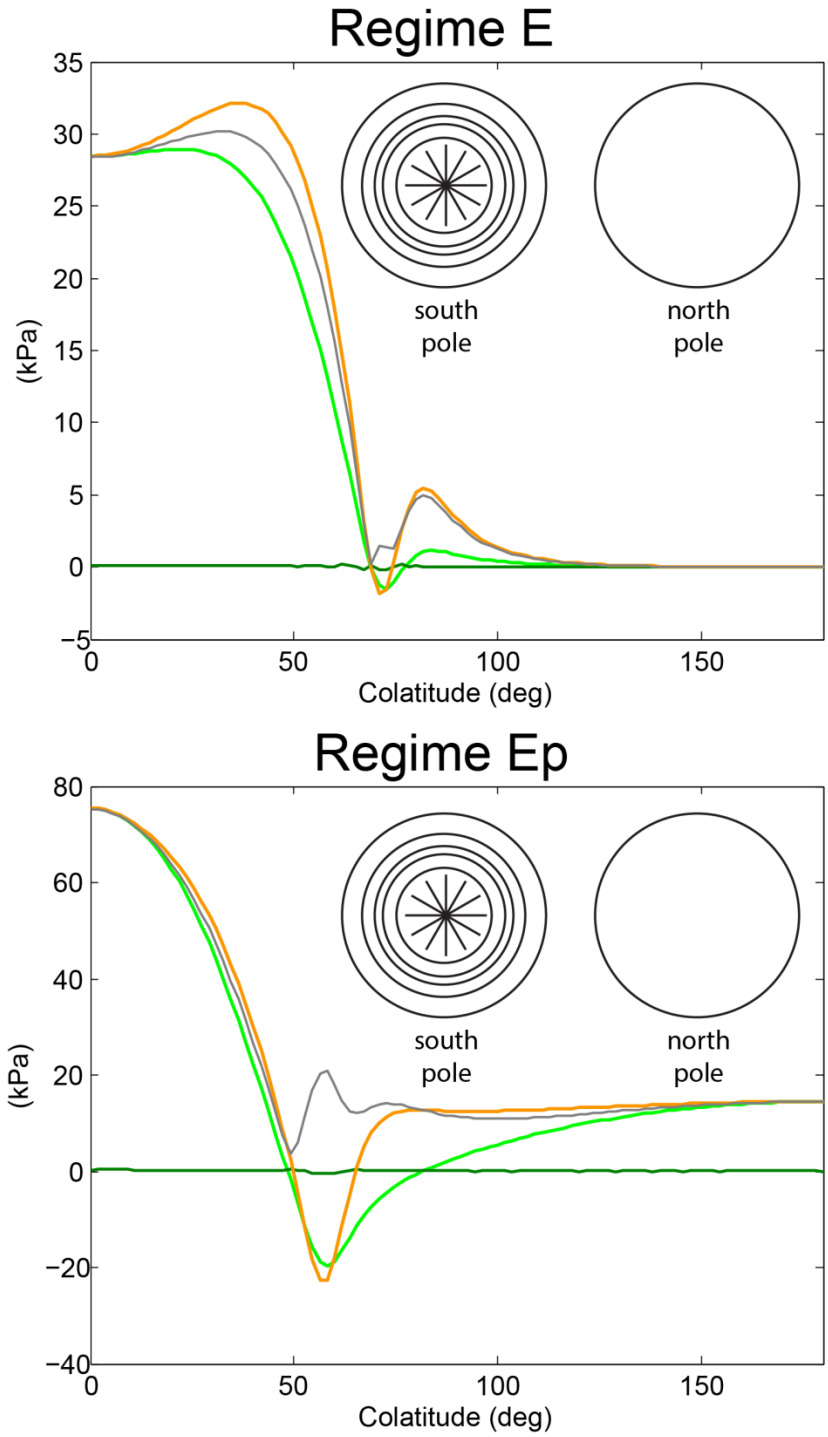

Figure 4.13 E. Faulting regimes E and Ep. Regime E has RNF surrounded by CNF at the South Pole with no yielding in the north (example from 40B5D210C). Regime Ep has the same pattern the south and CNF at the north pole (example from 40R25D190C).

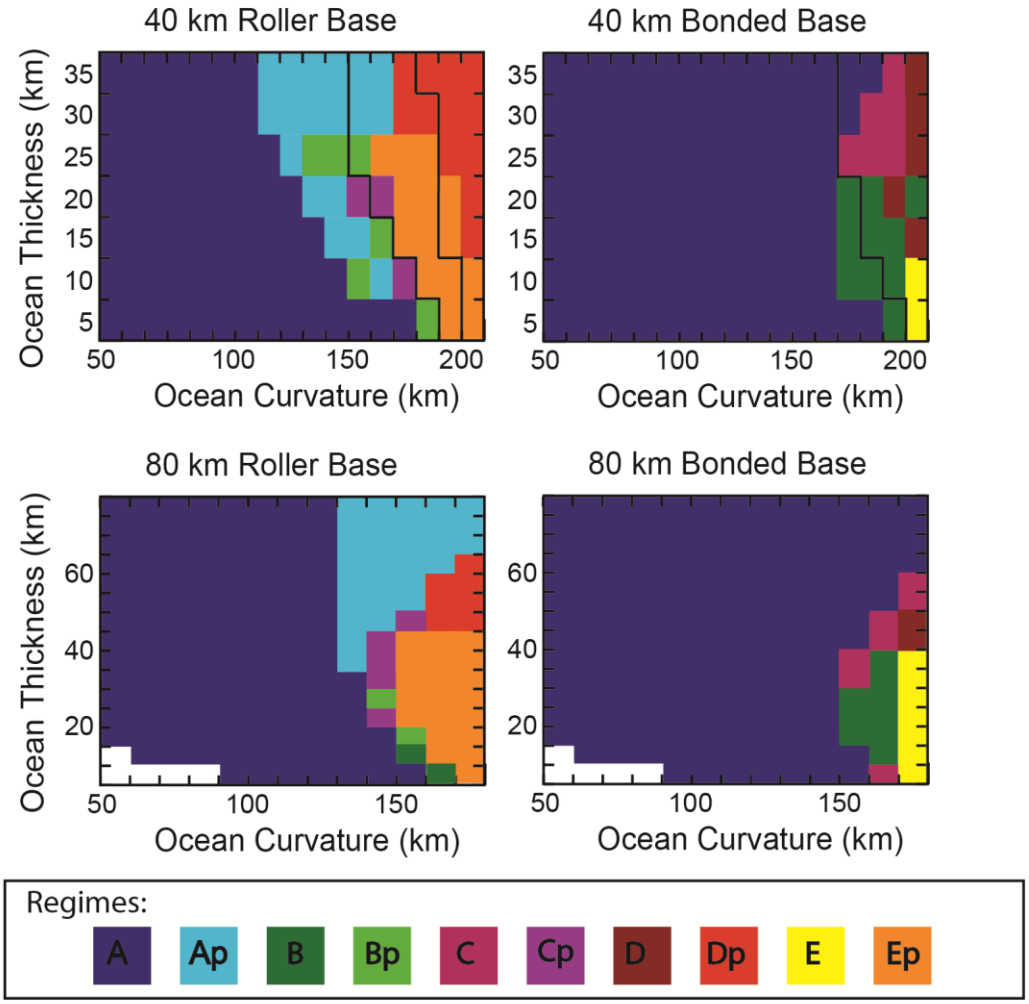

Figure 4.14. Surface faulting regimes predicted for each model according to ocean geometry parameters. White indicates no surface yielding. The black outlines on the 40 km models indicate region with mid latitude yielding. Mid-latitude yielding follows the tensile failure criterion for the bonded base case and the von Mises criterion for a roller base. Regimes A and Ap are the most commonly predicted faulting regimes, regardless of ice shell thickness.

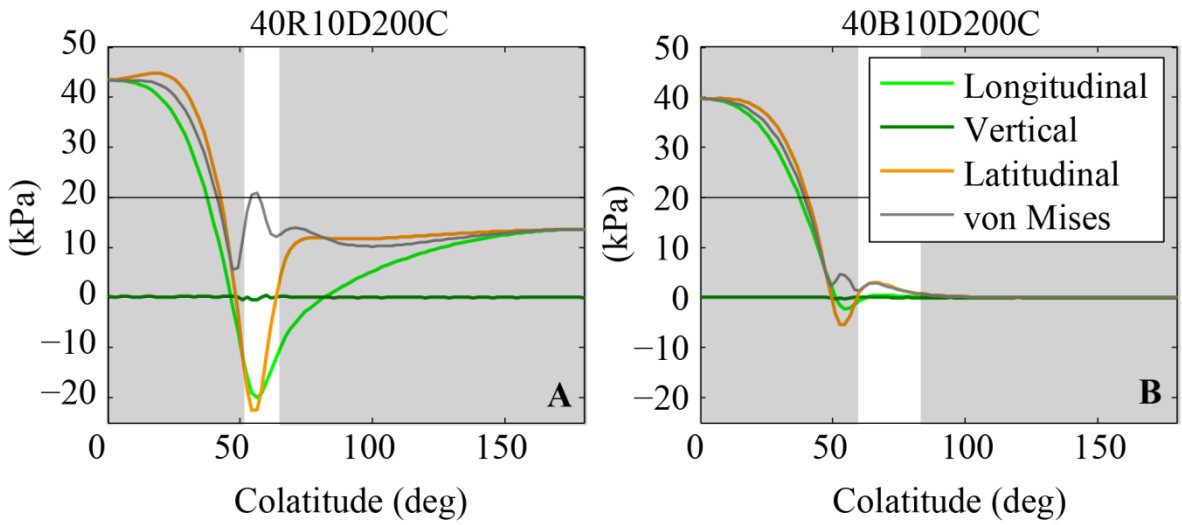

Figure 4.15. Examples of surface stresses in A) 40 km roller base model with mid latitude CRF yielding and B) 40 km bonded base model with mid latitude tensile yielding. The mid-latitude region of yielding for both models is highlighted in white in both plot.

4.4.5 Separation of Bonded Interface

While our models do not allow for movement of the overlying ice shell normal to the rocky interior, we can discuss the conditions that make it possible for fluid to be injected along the base of the ice shell. Injection of fluid would only be expected when the vertical stresses at the base of the ice shell are tensile. Figure 4.16 reports the vertical stresses at the base of the 40 km fixed cryosphere over the entire range of ocean thicknesses and curvature. As a stress singularity is always present at the edge of ocean, we do not report the stress at the node at the interface between the pressurized ocean and ice shell in Figure 4.16. The vertical stress at the node adjacent to the edge node is shown in Figure 4.17. Each colored line indicates a set of models with a different ocean thickness with markers indicating individual model runs. With an increase in ocean thickness the lines shift vertically, indicating an increase in tensile stress. A sinusoidal pattern can be observed in the tensile stresses as the ocean angle increases, with peaks in tensile stresses at ocean angles of ~70-80 degrees.

It is important to note that the vertical stresses reported in figures 4.16 and 4.17 neglect the overburden stress. At the base of a 40 km thick ice shell the overburden stress would be 4.2 MPa, which is sufficient to turn the vertical stresses compressive. However, the formation of tensile cracks depends on the effective stress, σ', related to the total stress σ according to

$$\sigma' = \sigma - P_p \qquad \text{Eqn. 4.5}$$

where P_p is the pore fluid pressure (e.g. Walder and Nur, 1984). Pore fluid pressure reduces the stress that a rock "feels".

There are currently no constraints on the pore pressure at the base of a ice shell of Enceladus or any other icy satellite. However, it is possible for pore fluid pressure in rocks on Earth to reach near-lithostatic levels allowing failure with only minor changes in the stress field (e.g. Thomas et al., 2009). The presence of an adjacent ocean may allow fluid infiltration into the ice, increasing pore pressure and decoupling between the ice shell and the rocky interior of the satellite. If near-lithostatic pore pressure were not present at the base of the ice shell, the likelihood of tensile failure would decrease, as the vertical stress generated by a pressurized ocean are never sufficient to overcome the overburden stresses in our models. If the pore pressure were equal to the overburden stress then initiation and injection of fluid and separation would occur in many of our models.

In our purely elastic models, we cannot model the propagation of this crack, which would also be influenced by other stress sources such as tidal stresses, injection of fluid, and crack tip stress intensity factors. It is interesting to note that several models show a region of vertical compression a few degrees away from the edge of the polar ocean, which would likely impede propagation of basal crack. The region of vertical compression is due to reverberation of stress in the elastic shell and is most prominent at 30° and 100° colatitude for a 40-km thick ice shell (Figure 4.16). The region of compression at 30° disappears and only compressive vertical stresses are seen in models with an ocean angle of > 60° for an 80-km thick ice shell.

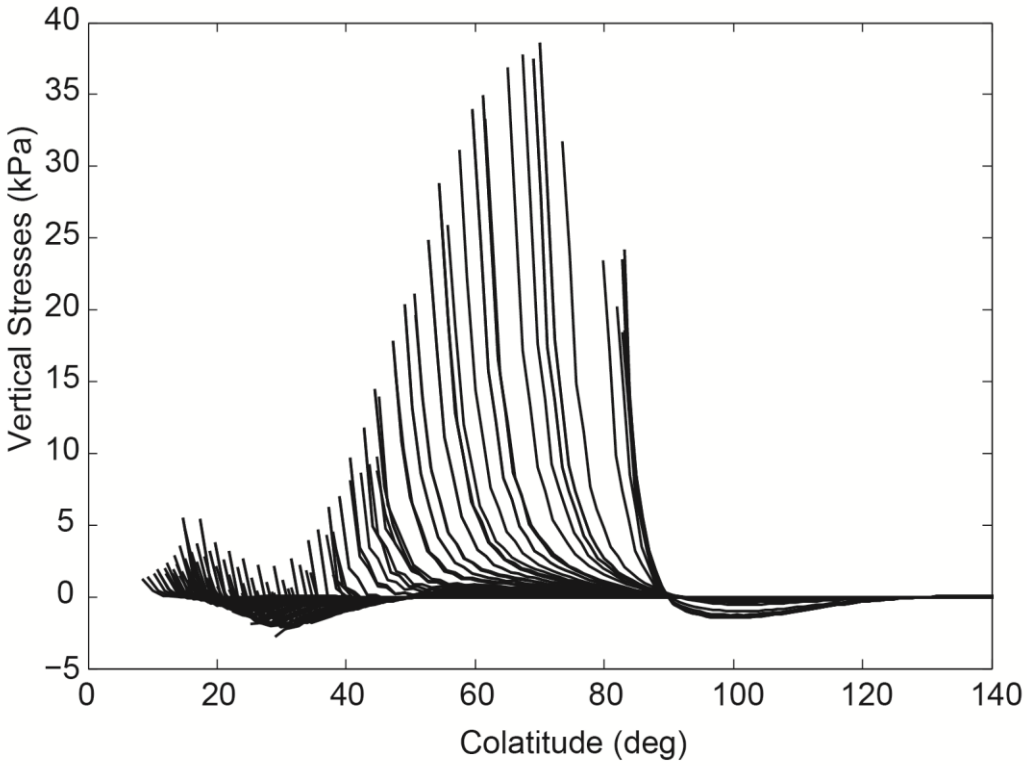

Figure 4.16. Vertical stress at the base of a 40 km ice shell with bonded base for all ocean curvature and thickness. For models with a higher ocean angle, the line starts at higher colatitude. Both tensile and compressive stresses are predicted in the model ensemble, but not every model exhibits both stress states. Models with an ocean angle of 20˚ to 40˚, and again at ~85° show a transition from tensile vertical stresses to compressive stresses at the base. Most models exhibit tension, which is needed for cracks to initiate at the base of the ice shell.

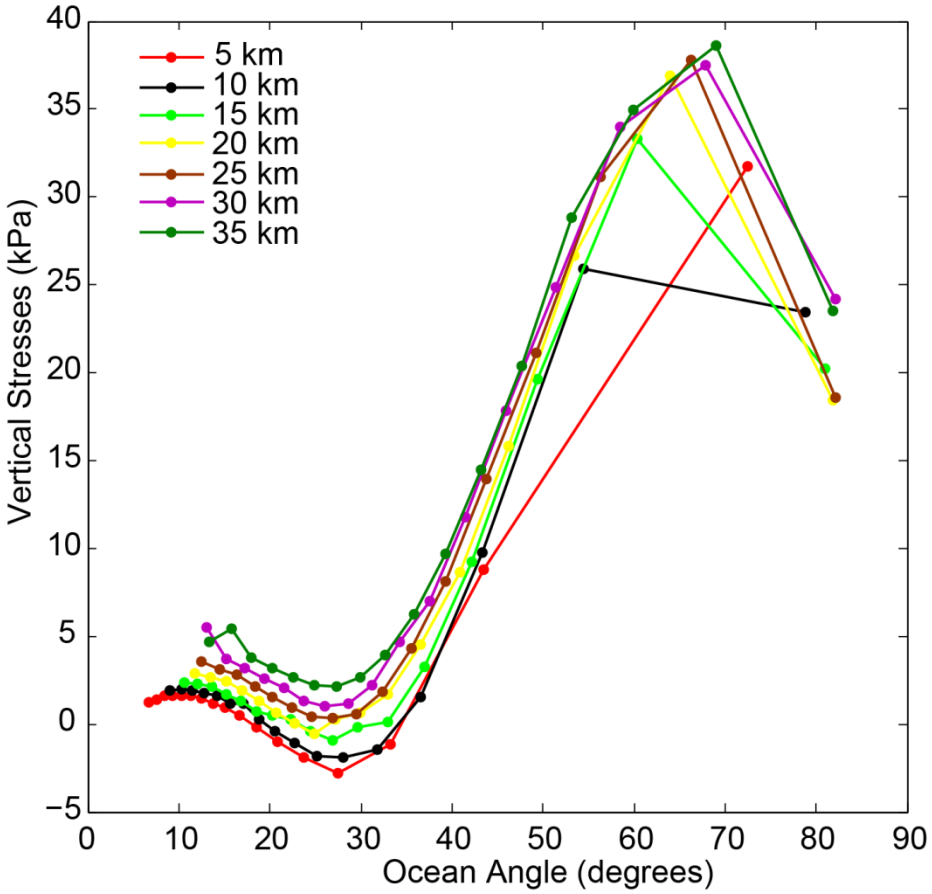

Figure 4.17. Vertical stresses near the edge of the ice shell (1 node in from the edge) vs the ocean angle for a 40-km thick cryosphere and bonded basal conditions. Each colored line indicates a set of models with the ocean thickness indicated in legend. The markers indicate the individual models run. Tension increases as the ocean thickness increases. A sinusoidal pattern can be observed in the tensile stresses as the ocean angle increases. Most models show tensile stresses near the edge of the ice shell, and the magnitude of those stresses increases with a thicker ice shell.

4.5 Discussion

Enceladus could have either a global (Ross and Schubert, 1989; Nimmo et al., 2007; Schubert et al., 2007) or regional (Collins and Goodman, 2007) ocean.. The only models that predicts a stress state consistent with the proposed compressional nature of the SCT is a thinner ice shell (40 km) with decoupled (or at least partially decoupled) ice shell (figure 4.15). The ice shell does not need to be decoupled by a water layer corresponding to a global ocean, as high pore fluid pressure and basal sediments (till) also have the ability to allow tangential movement of the ice shell across the interior of Enceladus. In addition, as shown in section 4.4.3, the stress field for a bonded ice shell can facilitate fluid injection at the base the ice shell (assuming high pressure fluids). However, Figure 4.16 shows that most of the models for a 40-km thick lithosphere bonded to the rocky interior feature a region of compression along the base of the ice shell at about 30° from the South Pole, forming a barrier to crack propagation. A crack propagation model is needed to rigorously determine the distance a fluid filled crack could propagation prohibiting us from making any conclusive evaluation.

None of our models is able to match the orientation of the Tiger Stripes, which violate the axisymmetric assumption of our models. It may well be that the geometry of Tiger Stripes is due to finite propagation of cracks initiated in the stress field predicted in our models, or that Tiger Stripes are influenced by other sources of stress such as nonsynchronous rotation or tidal stresses. If the Tiger Stripes are vertically propagating tensile cracks that reach the subsurface ocean, then the ocean would have to be within a few hundred meters of the surface or have significant pore

fluid pressure present to compensate overburden stresses. It is possible that a non-spherical geometry (as used for the ocean in all our models) could produce additional stresses in a thinner cryosphere. It may also be that the source of water for the jets is a near surface reservoir, isolated within the ice shell. However all models with a sufficiently large ocean predict tensile yielding at the South Pole (Figure 4.14), which would reduce the pressure in an isolated shallow water reservoir.

The cracks in the SPT are neither circumferential nor clearly radial. However, if the yielding at in the SPT were due to finite propagation of cracks initiated by the stresses in our model, the models predicting only radial cracks would be the most common. The models that are consistent with the compressional band, SCT, and radial fractures at the South Pole are those with a roller base, and ocean thickness of 35-40 km and an ocean curvature of 150-160 km.

Roller base models also predict circumferential cracking at the north pole if the ocean curvature, or equivalently the extent of the regional ocean, is large enough. Imaging and mapping efforts of the north pole of Enceladus have been far fewer than that of the South Pole. While no clear pattern of yielding has been documented in any of the current literature it may be that resurfacing by cratering or other process has erased evidence of tectonic activity at the north pole. It also possible that tensile failure at the north pole never occurred, and the ice shell is bound to the interior in the north, too thick, or that the south polar ocean is not large enough. Either way, further evaluation and detailed mapping of failure in the north pole of Enceladus is needed.

The use of an elastic rheology, while useful in gaining insight into the general behavior of a system does not allow for history dependence or strain localization,

both of which are likely important for the current stress state on Enceladus. Our model starts with the pressurization of the ocean. However, it is possible that the cryosphere was initially entirely frozen. The melting of ice to form an ocean would create the opposite state of stress than described here. Surface stresses at the South Pole would be compressive rather than tensile. If the ice failed during melting of the ocean, those faults could potentially provide pre-existing zone of weakness within the ice that could be reactivated once crystallization of the ocean began. History-dependence of failure would prevent the geological record of these early thrust faults to be completely erased, as we show for the melt/freeze cycle of water lenses in the crust of Europa (Chapter 3), although these faults would be difficult to identify due to subsequence surface modification. Additionally, failure of ice relieves stress and has the ability to change the local stress field. Either localization or reactivation have the ability to change the types of faulting predicted in our model. To consider this effect, however, an elastic-plastic or viscous rheological behavior would need to be utilized in the model.

According to our models, geological observations such as the region of thrust faulting that surrounds the SPT seem generally consistent with the existence of a pressurized ocean beneath the South Pole and are most consistent with a 40 km thick cryosphere. However, our models also suggest the existence of some layer decoupling the ice shell (possibly a liquid water layer). If the pressurization of the ocean were due to crystallization, which is consistent with the magnitude of stresses used in our model, it would suggest that Enceladus is currently cooling. This means that the initial source of heat for Enceladus either has decreased or is off. We cannot

differentiate between the source of heating being episodic or simply having been shut off in the geologically recent past.

4.6 Conclusion

Since the observation of water-rich jets on Enceladus, the debate about the potential of Enceladus to support a reservoir of water has been ongoing. Determining the volume of water, as well as its location relative to the ice shell can provide valuable constraints on Enceladus's thermal and evolutionary history.

While the stresses from a pressurized ocean beneath the South Pole on Enceladus are unable to explain the geometry of Tiger Stripes on their own, it could be important to consider them in conjunction with tidal or nonsynchronous rotation stresses. A thinner cryosphere makes surface failure easier or at least more extensive. Given the fractured nature of the surface of Enceladus a thinner cryosphere ice shell is preferred by our models. The size and lateral extent of the ocean have important implications for the stresses generated at the surface. Additionally the basal boundary conditions, either bonded or decoupled, can determine the pattern of stresses in both the south and north pole. An ice shell base bonded to the rocky interior could have fluid injected along all or part of its extent, allowing for at least a partially decoupled ice shell. A partially decoupled ice shell would result in a localized sea beneath the South Pole with a decoupled ice shell extending part way to the north pole. Our model results suggest that the ice shell must be at least partially decoupled in order to predict a circumferential compressional feature (the SCT). However, an ice shell that is entirely decoupled from the rocky interior would predict yielding in the north pole, which has not been currently identified. This may be due to the absence of yielding in

the north pole, or the limited mapping in that region. Further mapping efforts are needed to more definitively determine the basal boundary conditions on Enceladus.

Chapter 5 : Concluding discussion and future work

5.1 Summary

This dissertation focused on the tectonics related to crystallizing water bodies in the shells of icy satellites. Chapter 2 evaluated the size and geometry needed for a crystallizing water body to reproduce the surface appearance of Europan ridges. Chapter 3 evaluated the Chaos formation mechanism proposed by Schmidt et al. (2011) by comparing modeled stresses for melting and crystallization of an ice lens with observations of Thera Macula. Chapter 4 focused on how a crystallizing regional sea beneath the South Pole of Enceladus could impact the stress fields within the ice shell.

5.1.1 Summary of Ridge Formation Model

In a confined location, the stresses generated by the expansion of a crystallizing body of water will deform the surrounding ice. In the model evaluated in Chapter 2, both a double and single ridge can be generated depending on the aspect ratio of the crystallizing intrusion. A sill-like intrusion creates a single ridge, while a dike-like intrusion creates a double ridge. In all models, ceteris paribus, ridge height increases with a decreasing intrusion depth. A large increase (greater than 1.75 km^2) in the cross-sectional intrusion area is required to match the observed height of double ridges on Europa. Because the model assumes that sills or dikes extend infinitely along strike, and because ridges are ubiquitous across Europa's surface, this formation mechanism suggests large volumes of water would have had to be injected

into Europa's ice shell. This implies either that cryomagmatic processes are important in ridge formation or that the ice shell undergoes a sort of vertical tectonic activity dominated by mass exchange between the ice shell and the internal ocean. However, as liquid water is removed from the ocean and injected into the ice shell the overpressure in the ocean would decrease, making further fluid injection more difficult. This suggests that fluid injection and crystallization alone is unable to explain the formation of so many ridges on Europa.

5.1.2 Summary of Macula Formation Model

Schmidt et al. (2011) proposed that the ongoing melting and crystallization of ice related to a thermal plume can explain the characteristics of Thera Macula and that chaos are features that are the final product of this process where the ice has e fully crystallized. In Chapter 3, I developed a model of this process that reproduces some of the characteristics of Thera Macula, such as a circumferential ridge, an initial draw-down of the overlying surface and surficial radiating cracks. Model results are consistent with the interpretation that the central region of Thera Macula is at an earlier formation stage than its southern region. As argued by Schmidt et al. (2011) surface modification immediately following the melting of the lens should be significant and can occur rapidly. If Thera Macula is in the process of forming and further melting of the lens has occurred, a change in its appearance may be observable in future missions to Europa. If a change in Thera Macula were observed it would suggest that Thera Macula is a prime candidate for locating liquid water near the surface.

However the model results are inconsistent with the extrapolation of the thermal plume model to explain the formation of chaos. The predicted compressive stresses above the melt lens would inhibit the formation and propagation of tensile cracks from the melt lens, which are critical to explaining the formation of chaos. This means an alternative explanation for the formation of chaos is needed in order to explain the break-up of the overlying ice.

5.1.3 Summary of Enceladus South Polar Ocean Model

A pressurized south polar ocean will generate stresses within the surrounding ice shell, however the geometry of the ocean and the geology of the ice shell will have an impact on the magnitude and pattern of stresses experienced in the surrounding ice. In Chapter 4 I have modeled a range of ocean sizes (lateral extent and thickness), cryosphere thickness, and basal boundary conditions for the putative south polar ocean on Enceladus. Analysis of the model results provides insight into the conditions that are consistent with present-day observations of the South Polar Terrain (SPT). The observed fractures at the SPT are consistent with a thinner (40 km) cryosphere. The Southern Curvilinear Terrain (SCT), a circumferential reverse faulting band around the south pole, is also consistent with a thin (40 km) cryosphere and can only be reproduced in my models a roller base, suggesting that the ice shell may be underlain by decoupling material such as liquid water. Analysis of the stresses at the base of the ice shell also suggest that the injection of fluid injection at the base is possible if the pore pressure is near lithostatic.

Detailed mapping of the north pole is needed to more fully evaluate which set of model parameters are consistent with the global geologic setting of Enceladus. If extensive tensile cracking were observed at the north pole, it would suggest that the ice shell was or is decoupled from the rocky interior, potentially by liquid water. However, if tensile cracking is not observed at the north pole, it would suggests liquid water is isolated at the South Pole or that the ice shell is quite thick (80 km).

5.2 Synthesis of important parameters

All of the models presented in this dissertation consider tectonic processes that involve the crystallization of a water body within a continuous ice shell. Image analysis of the icy surfaces is key to developing and evaluating these models as it is one of the few sources for information about the physical condition of the ice and the tectonic setting. While each model considered different input parameters, some of these parameters (discussed below) are universally important to the final model results.

5.2.1 Water body depth

Generally the nearer to the surface the water body resides, the greater and more localized the surface deformation. In the case of Europan ridges (Chapter 2), ridge height decreases with increasing water body depth and in the case of a dike-like intrusion the distance between the peaks of the double ridge increases concurrently. Eventually the intrusion reaches a depth (greater than approximately half the thickness of the ice shell) where the surface expression becomes too subtle to be

detected. In Chapter 3, a melt lens nearer to the surface is more likely to have failure propagate through the ice shell and connect with the melt lens. Furthermore, the ice above a shallower intrusion will have less overburden stress reducing the stress that must be overcome to produce tensile cracks. Without evoking additional sources of tensile stress, the melt lens would have to reside meters below the surface in order for tensile cracks to reach it. The results from both the chaos and ridge formation model prefer a shallower intrusion.

The depth of the ocean in Chapter 4 is dependent on the size (thickness) of the ocean. However, a shallower (larger) body of water results in higher surface stresses and a greater lateral extent of surface yielding. Additionally, tensile cracks are more likely to propagate all the way down to the water and provide a potential source for aerial plumes if the overburden stress is reduced by a shallower ocean. The modeled maximum depth of this shallow ocean depends on the magnitude of tensile stresses, which is poorly constrained.

5.2.2 Water body size and geometry

A crystallizing water body will increase in volume by 9% upon complete crystallization. A larger body of crystallizing water will thus result in a correspondingly larger absolute change in water body size, and greater deformation of the surrounding ice. Additionally the lateral extent of surface non-recoverable deformation is largely controlled by the lateral extent of the water body (Chapters 3 and 4). In Chapter 3 the model predicts development of a ridge circumferential about the melt lens. However, the location of the circumferential ridge is not directly above the edge of the melt lens, but beyond the maximum lens extent. This suggests that if

chaos or Macula are formed by this melt-freeze cycle then the lateral extent of the melt lens is always less than the bounding ridge. Such a constraint may be important when estimating the volume of water associated with these features, or when selecting target regions to study in future planetary missions.

On Enceladus, the lateral extent of south polar yielding from a pressurized ocean was usually less than the lateral extent of the global ocean. Unlike estimating the volume of water for a melt lens on Europa, using the lateral extent of yielding on Enceladus could lead to an under estimation of the volume of water beneath the South Pole.

5.2.3 Basal boundary conditions

The basal boundary condition has important implications for the stresses and deformation of the ice shell. It is generally accepted that a global ocean underlies the ice shell on Europa. It is because of the presence of this global ocean that the models of Europa all impose a restoring force at the base of the ice shell. The restoring force is meant to simulate the presence of an ocean, allowing deformation of the base and exerting a buoyant force in response to deformation. In Chapter 2 this basal boundary condition allows for the formation of a ridge at the base of the ice shell and a subtler uplift feature.

The buoyant plume model of chaos formation acts to isolate the base of the ice shell from the stresses exerted by the melt lens. However, preliminary models using a fixed base did show subtle changes in the stresses when a fixed base was used.

The impact of basal boundary conditions is most pronounced when considering the global stresses resulting in a pressurized ocean (Chapter 4). A bonded

ice shell protected the north pole from the stresses resulting from a pressurized ocean, inhibiting failure at the north pole. When the ice shell was decoupled from the rigid interior (roller base) stresses were transmitted to the north pole, allowing tensile failure.

5.2.4 Additional source of stress

All of my models either require or favor additional sources of stress in the ice shell. The ridge formation model of Chapter 2 presupposes the existence of a fluid filled crack within the ice shell. If the model is applied to cycloidal ridges then tidal stresses are needed to explain the trajectory of the crack. Additionally the results suggest that an additional force is needed to inject considerable volumes of water into the crack, suggesting multiple intrusive events may be required.

Chapter 3 indicates that an additional source of tensile stress may be required for fluid filled cracks to propagate between the surface and the melt lens. Buoyancy from an underlying plume was insufficient. It is possible that gas exsolution would provide additional force to crack the overlying ice shell, but there may be other sources not yet considered.

The orientation of tiger stripes on Enceladus requires that we invoke tidal stresses in order to explain the orientation of the tiger stripes. As the magnitude of tidal stresses anticipated (Hurford et al., 2007a) is comparable to the stresses resulting from a pressurized ocean, the results from Chapter 5 would likely be modified by their inclusion.

5.3 Potentially Important parameter/processes not modeled

Each of the models considered here have potential for assessing cryomagmatic processes on icy satellites. The results of my analyses indicate many areas where the models can be improved. Several parameters, considered either as separate models or incorporated into the models presented in this dissertation, could enhance understanding of tectonics arising from crystallization of water bodies.

5.3.1 Crack propagation

Failure and cracking are critical to all of the models presented, making a more rigorous consideration of crack propagation valuable to the evaluation of the models. Cracks modify the local stress field by relieving stress and providing a source for localization of strain. Flanking fractures are observed in association with some ridges (e.g. Dombard et al., 2013). Incorporating crack propagation into the model presented in Chapter 2 would provide an additional constraint that has the possibility of allowing the further refinement of the model results. Additionally, strain localization associated with cracks would most likely change the wavelength (width) of the ridges.

While strain localization was allowed in Chapter 3, through the use of non-associated plasticity, the model is not able to consider the propagation of a pressurized fluid filled crack to more rigorously determine under what conditions water might reach the surface. It is possible that if pore fluid pressure adjacent to the lens were high enough and a tensile crack were initiated that it would modify the adjacent stress state to allow fluid injection. Additionally, a crack propagation model

may allow for determination of the impact of gas exsolution on tensile crack formation.

The importance of evaluating the possible propagation of a fluid filled crack at the base of a bonded ice shell was discussed in Chapter 4 in detail. Additionally cracks near the surface of the ice shell will also provide seeds for strain localization and potentially modify the surface deformation. Models of crack formation on Enceladus due to tidal stresses (Patthoff and Kattenhorn, 2011) have been published, and further refinement of these models is ongoing. However, the addition of stresses from a pressurized ocean has the potential to significantly alter the predicted yielding patterns from the Patthoff and Kattenhorn (2011). models

5.3.2 Path-dependent evolution

The models presented in Chapters 2 and 4 both use an elastic ice rheology, meaning that all strain is recoverable. Now that the fundamental behavior of the system is better understood the addition of a plastic rheology has the potential to further elucidate the formation mechanisms for ridges and the importance of a pressurized global ocean on Enceladus. Using a plastic rheology reduces the amplitude of surface deformation by allowing strain localization.

Multiple intrusive events may be needed in order for a dike-like crystallizing water intrusion to match the height of ridges observed on Europa. However considering multiple intrusive events is not trivial to do in Abaqus™ as it requires that mass be added, which means the system is no longer closed. Preliminary model runs also indicate that having enough intrusive events to obtain the double ridge height of ~200 m may be problematic. However, the development of a model

allowing for multiple intrusion and crystallization cycles could provide constraints on the volume of water needed to form double ridges. It may be that the volume of water required makes a crystallizing water intrusion an unrealistic model for ridge formation.

Considering plastic deformation in the model of Enceladus has the potential to change the reported lateral extent of yielding. Additionally, having a path dependent rheology would enable the consideration of the stresses contributed by the melting of a south polar sea initially. Much like the inversion reported by the model of chaos formation (Chapter 3), a similar process could take place when plastic deformation is considered. Such an addition would allow for the further refinement of the model and may provide additional constraints to the location, size and shape of the ocean.

5.3.3 Refinement of parameters space

The ice rheology used in all models was selected based on the rheological properties of pure water ice on Earth. However, several factors can influence the rheology of the ice such as the temperature, grain size, and the amount and type of impurities. The strength of ice at the low temperatures observed in the outer solar system is generally unconstrained. A detailed analysis of the relative importance of a range of rheological parameters, such as the Young's modulus, yield strength, and density contrasts, could be important to the development of future models. A study that evaluates the full range of possible rheological parameters and evaluates the impact and relative importance of each parameter would be useful in the construction of future models. Such a study is also key to the community's ability to fully evaluate the range in which models can match observations on icy satellites.

5.4 Concluding Remarks

Tectonic activity on Europa and Enceladus has almost certainly included the crystallization of water bodies. Constraining where this process is active and important (and where it is not) enhances our understanding of icy satellites, and cryospheric processes. Icy satellites also offer an opportunity to test our understanding of glacial and ice shelf processes in a different tectonic setting. While I have used glacial processes from earth to inform my models for Europa, I also hope that my models may inform future models of glacial processes.

These models also attempt to constrain the location of water within the ice shell not only to understand icy satellites but also to provide targets for future missions. Based on the results presented in this dissertation, Thera Macula may be one of the best targets to look for near surface water (or partially molten ice) on Europa.

Further modeling studies that consider crack propagation, path dependent evolution, and the full range of rheological parameters for ice are key to further understanding the tectonics of icy satellites.

Appendix A: Example Code used to Generate Chapter 2 Models

```
from part import *
from material import *
from section import *
from assembly import *
from step import *
from interaction import *
from load import *
from mesh import *
#from optimization import *
from job import *
from sketch import *
from visualization import *
from connectorBehavior import *
#from odbNodeElementFunc import odbNodeElement
from math import *
from odbAccess import *
import sys
import pprint

#DEFINE CENTER VARIABLES

#BASE MODEL NAME
MODEL_NAME_START = 'Model-'
#MODEL NAME VARIABLE USED IN PROGRAM
MODEL_NAME = ''
#BASE OUTPUT NAME
OUTPUT_NAME_START = 'Output-'
#OUTPUT NAME USE IN THE PROGRAM
OUTPUT_NAME = ''
#STARTING CENTER Y
CENTER_START = 4500
CENTER_STEP = -500
CENTER_END = 3500

#DEFINE RATIO VARIABLES
RATIO_START = 100
RATIO_END = 101
RATIO_STEP = 10
#Fixed Volume in meters
FIXED_VOLUME = 225000

#Crack Variables
CRACK_START = 10
CRACK_END = 50
CRACK_STEP = 10
CRACKD_START = 500
CRACKD_END = 1000
```

```
48. CRACKD_STEP = 50
49. #DEFINE FUNCTIONS
50. def odbNodeElement(odbPath):
51.     # Open the output database.
52.
53.     odb = openOdb(odbPath + '.odb')
54.     assembly = odb.rootAssembly
55.
56.     # Model data output
57.
58.     #print 'Model data for ODB: ', odbPath
59.
60.     # For each instance in the assembly.c
61.
62.     numNodes = numElements = 0
63.     fhandle = open(odbPath + 'Coord.txt','w+')
64.     for name, instance in assembly.instances.items():
65.         n = len(instance.nodes)
66.         #print 'Number of nodes of instance %s: %d' % (name, n
    )
67.         numNodes = numNodes + n
68.         Ridge = odb.rootAssembly.instances['SHELL-1'].nodes
69.         #print 'Instances'
70.         # For each node of each part instance
71.         # print the node label and the nodal coordinates.
72.         # Three-dimensional parts include X-, Y-, and Z-
    coordinates.
73.         # Two-dimensional parts include X- and Y-
    coordinates.
74.         #git
75.         # if instance.embeddedSpace == THREE_D:
76.         #   fhandle.write('Node     X         Y         Z')
77.         #   for node in instance.nodes:
78.         #       x, y, z = node.coordinates
79.         #       fhandle.write('%4d %6.4f %6.4f %6.4f' % (node.
    label, x,y,z))
80.         # else:
81.         fhandle.write('Node     X         Y\n')
82.         for node in Ridge:
83.             x, y, z = node.coordinates
84.             fhandle.write('%8d %6.10f %6.10f\n' % (node.label,
     x,y))
85.
86.     fhandle.close()
87.
88. def odbNodeDisplacement(OUTPUT_NAME):
89.     odb = openOdb(OUTPUT_NAME + '.odb')
90.     gravitation=odb.steps['GravityStep'].frames[1].fieldOutput
    s['U'].values
```

```
    displacement=odb.steps['IntrusionStep'].frames[1].fieldOutputs['U'].values
    #Obtain subset of nodes for shell only
    #ShDisp=displacement.getSubset(region='SHELL-1')
    #ShGrav=gravitation.getSubset(region='SHELL-1')
    f=open(OUTPUT_NAME + 'Displacement.txt', 'w+')
    g=open(OUTPUT_NAME + 'Gravity.txt', 'w+')
    f.write('Node    X     Y\n')
    for v in displacement:
        f.write(' %d %6.5f %6.5f\n' % (v.nodeLabel, v.data[0], v.data[1]))
        f.close()
        g.write('Node    X     Y\n')
        for v in gravitation:
            g.write(' %d %6.5f %6.5f\n' % (v.nodeLabel, v.data[0], v.data[1]))
        g.close()


    for CENTER_VALUE in range(CENTER_START,CENTER_END,CENTER_STEP):
        for CRACK_VALUE in range (CRACK_START,CRACK_END,CRACK_STEP):
            for CRACK_DEPTH in range(CRACKD_START,CRACKD_END,CRACKD_STEP):
                for RATIO_NOW in range(RATIO_START,RATIO_END,RATIO_STEP):
                    RATIO_CORR = float(RATIO_NOW)/float(10)

                    #AXIS LENGTH in X direction (B)
                    B_LENGTH = sqrt(FIXED_VOLUME/RATIO_CORR)

                    #AXIS LENGTH in Y direction (A)
                    A_LENGTH = float(FIXED_VOLUME/B_LENGTH)

                    #CREATE THE MODEL NAME
                    MODEL_NAME = MODEL_NAME_START + `CRACK_VALUE` + '-' + `CRACK_DEPTH` + '-'+ `CENTER_VALUE` + '-' + `RATIO_NOW`
                    #create model
                    #mdb.models.changeKey(fromName='Model-1', toName=MODEL_NAME)
                    myModel = mdb.Model(name=MODEL_NAME)

                    #CREATE THE OUTPUT_NAME
                    OUTPUT_NAME = OUTPUT_NAME_START + `CRACK_VALUE` + '-' + `CRACK_DEPTH` + '-'+ `CENTER_VALUE` + '-' + `RATIO_NOW`

                    #create model
```

```
126.
127.                         ### PART ###
128.                         myModel.ConstrainedSketch(name='__profil
    e__', sheetSize=200.0)
129.                         myModel.sketches['__profile__'].Line(poi
    nt1=(-50000.0, -10000.0), point2=(50000.0, -10000.0))
130.                         myModel.sketches['__profile__'].Line(poi
    nt1=(50000.0, -10000.0), point2=(50000.0, 10000.0))
131.                         myModel.sketches['__profile__'].Line(poi
    nt1=(50000.0, 10000.0), point2=(CRACK_VALUE, 10000.0))
132.                         myModel.sketches['__profile__'].Line(poi
    nt1=(-CRACK_VALUE, 10000.0), point2=(-50000.0, 10000.0))
133.                         myModel.sketches['__profile__'].Line(poi
    nt1=(-50000.0, 10000.0), point2=(-50000.0, -10000.0))
134.                         #adding the crack
135.                         myModel.sketches['__profile__'].Line(poi
    nt1=(-CRACK_VALUE, 10000.0), point2=(0, 10000.0-
    CRACK_DEPTH))
136.                         myModel.sketches['__profile__'].Line(poi
    nt1=(CRACK_VALUE, 10000.0), point2=(0, 10000.0-CRACK_DEPTH))
137.                         myModel.sketches['__profile__'].EllipseB
    yCenterPerimeter(
138.                             axisPoint1=(B_LENGTH, CENTER_VALUE),
     axisPoint2=(0.0, CENTER_VALUE -
     A_LENGTH), center=(0.0, CENTER_VALUE))
139.                         myModel.Part(dimensionality=TWO_D_PLANAR
    , name='Shell',
140.                             type=DEFORMABLE_BODY)
141.                         myModel.parts['Shell'].BaseShell(sketch=

142.                             myModel.sketches['__profile__'])
143.                         del myModel.sketches['__profile__']
144.
145.                         ### MATERIAL & SECTION ###
146.
147.                         myModel.Material(name='Material-1')
148.                         myModel.materials['Material-
    1'].Density(table=((930.0,
149.                             ), ))
150.                         myModel.materials['Material-
    1'].Elastic(table=((900000000.0,
151.                             0.325), ))
152.                         myModel.HomogeneousSolidSection(material
    ='Material-1', name=
153.                             'Section-1', thickness=None)
154.                         myModel.parts['Shell'].setElementType(el
    emTypes=(ElemType(
155.                             elemCode=CPE4R, elemLibrary=STANDARD
    , secondOrderAccuracy=OFF,
```

```
                            hourglassControl=DEFAULT, distortion
   Control=DEFAULT), ElemType(
                            elemCode=CPE3, elemLibrary=STANDARD)
   ), regions=(
                            myModel.parts['Shell'].faces.getSequ
   enceFromMask(('[#1 ]',
                            ), ), ))
                        myModel.parts['Shell'].SectionAssignment
   (offset=0.0,
                            offsetField='', offsetType=MIDDLE_SU
   RFACE, region=Region(
                            faces=myModel.parts['Shell'].faces.g
   etSequenceFromMask(
                            mask=('[#1 ]', ), )), sectionName='S
   ection-1', thicknessAssignment=
                            FROM_SECTION)

                        ### MESH ###
                        myModel.parts['Shell'].seedEdgeByBias(bi
   asMethod=DOUBLE,
                            constraint=FINER, endEdges=
                            myModel.parts['Shell'].edges.getSequ
   enceFromMask(('[#10 ]',
                            ), ), maxSize=3000.0, minSize=100.0)

                        myModel.parts['Shell'].seedEdgeBySize(co
   nstraint=FINER,
                            deviationFactor=0.1, edges=
                            myModel.parts['Shell'].edges.getSequ
   enceFromMask(('[#10 ]',
                            ), ), size=3000)
                        myModel.parts['Shell'].seedEdgeBySize(co
   nstraint=FINER,
                            deviationFactor=0.1, edges=
                            myModel.parts['Shell'].edges.getSequ
   enceFromMask(('[#1c ]',
                            ), ), size=3000.0)
                        myModel.parts['Shell'].seedEdgeBySize(co
   nstraint=FINER,
                            deviationFactor=0.1, edges=
                            myModel.parts['Shell'].edges.getSequ
   enceFromMask(('[#2 ]',
                            ), ), size=3000.0)
                        myModel.parts['Shell'].seedEdgeByBias(bi
   asMethod=
                            SINGLE, constraint=FINER, end1Edges=

                            myModel.parts['Shell'].edges.getSequ
   enceFromMask(
```

```
                            ('[#80 ]', ), ), maxSize=3000.0, min
    Size=50.0)
                        myModel.parts['Shell'].seedEdgeByBias(bi
    asMethod=
                            SINGLE, constraint=FINER, end1Edges=

                            myModel.parts['Shell'].edges.getSequ
    enceFromMask(
                            ('[#10 ]', ), ), maxSize=5000.0, min
    Size=50.0)
                        myModel.parts['Shell'].seedEdgeByBias(bi
    asMethod=
                            SINGLE, constraint=FINER, end2Edges=

                            myModel.parts['Shell'].edges.getSequ
    enceFromMask(
                            ('[#10 ]', ), ), maxSize=5000.0, min
    Size=50.0)
                        myModel.parts['Shell'].seedEdgeBySize(co
    nstraint=FINER,
                            deviationFactor=0.1, edges=
                            myModel.parts['Shell'].edges.getSequ
    enceFromMask(('[#1 ]',
                            ), ), size=100.0)
                        myModel.parts['Shell'].generateMesh()


                        ### ASSEMBLY ###
                        myModel.rootAssembly.DatumCsysByDefault(
    CARTESIAN)
                        myModel.rootAssembly.Instance(dependent=
    ON, name='Shell-1',
                            part=myModel.parts['Shell'])

                        ### STEP, BC, INTERACTIONS & LOAD ###
                        ShInst=myModel.rootAssembly.instances['S
    hell-1']
                        myModel.StaticStep(name='GravityStep', p
    revious='Initial')
                        myModel.Gravity(comp2=-
    1.314, createStepName='GravityStep',
                            distributionType=UNIFORM, field='',
    name='GravityLoad')
                        myModel.StaticStep(name='IntrusionStep',
     previous='GravityStep')
                        myModel.Pressure(amplitude=UNSET, create
    StepName='IntrusionStep',
                            distributionType=UNIFORM, field='',
    magnitude=1e+8, name='Pressure',
                            region=Region(
```

```
                            side1Edges=myModel.rootAssembly.instances['Shell-1'].edges.getSequenceFromMask(
                            mask=('[#1 ]', ), )))
                        myModel.DisplacementBC(amplitude=UNSET, createStepName='GravityStep',
                            distributionType=UNIFORM, fieldName='', fixed=OFF, localCsys=None, name=
                            'BC-1', region=Region(
                            edges=myModel.rootAssembly.instances['Shell-1'].edges.getSequenceFromMask(
                            mask=('[#a ]', ), )), u1=0.0, u2=UNSET, ur3=0.0)
                        myModel.ElasticFoundation(createStepName='Initial', name='Foundation',
                            stiffness=1314.0, surface=Region(
                            side1Edges=ShInst.edges.getSequenceFromMask(mask=('[#4]', ), )))

                                #myModel.rootAssembly.Set(name='Set-1', nodes=
                        #   myModel.rootAssembly.instances['Shell-
                        1'].nodes.getSequenceFromMask(mask=('[#30000 #ffffffff #1fffff ]', ), ))

                        ### JOB & CALCULATE ###
                        mdb.Job(atTime=None, contactPrint=OFF, description='', echoPrint=OFF,
                            explicitPrecision=SINGLE, getMemoryFromAnalysis=True, historyPrint=OFF,
                            memory=90, memoryUnits=PERCENTAGE, model=MODEL_NAME, modelPrint=OFF, multiprocessingMode=DEFAULT,

                            name=OUTPUT_NAME, nodalOutputPrecision=SINGLE, numCpus=1, queue=None, scratch='', type=
                            ANALYSIS, userSubroutine='', waitHours=0, waitMinutes=0)
                        mdb.jobs[OUTPUT_NAME].submit(consistencyChecking=OFF)
                        mdb.jobs[OUTPUT_NAME].waitForCompletion()
                        #myModel.FieldOutputRequest(createStepName='Step-1', frequency=
                        #   LAST_INCREMENT, name='F-Output-2', rebar=EXCLUDE, region=
                        #   myModel.rootAssembly.sets['Set-1'], sectionPoints=DEFAULT,
                        #   variables=('COORD', ))

                        ### OUTPUT ###
```

```
244.                        odbNodeElement(OUTPUT_NAME)
245.                        odbNodeDisplacement(OUTPUT_NAME)
```

Appendix B: Benchmarking Thermal Expansion in Abaqus™

Abaqus™ has the ability to simulate the expansion and contraction of an object following a temperature change while conserving mass. This capacity can be adapted for our purpose by defining a phase change variable θ and a linear expansion coefficient α. These variables play a role analogue to temperature and the thermal expansion coefficient in thermoelastic materials. The response of a thermoelastic material to stress and a temperature change follows Eqn. A.1

$$\varepsilon_{ij} = \frac{-\nu}{E}\sigma_{kk}\delta_{ij} + \frac{1+\nu}{E}\sigma_{ij} + \alpha\theta\delta_{ij}, \qquad \text{(Eqn. A.1)}$$

where ε is the strain tensor, ν is the Poisson's ratio, *E* is the Young's Modulus, and σ is the stress tensor. This equation differs from standard elasticity by its last terms, which represents the intrinsic density change. In our application, the expansion coefficient α is defined in terms the uncompressed density

$$\alpha = \frac{\rho_w - \rho_i}{3\rho_w}, \qquad \text{(Eqn. A.2)}$$

where ρ_w and ρ_I are the density of water and ice respectively.

Figure A.1 shows the setup of a benchmark test and Figure A.2, the results. Here, I consider a square sheet of thermoelastic material under plane strain. The linear expansion coefficient (α) used is 0.001 and the phase change indicator (θ) progresses from 0 to 1. The Young's Modulus is fixed at 10^9 Pa. The base and the sides all have free slip (rollers) conditions, so that the material can only expand in the

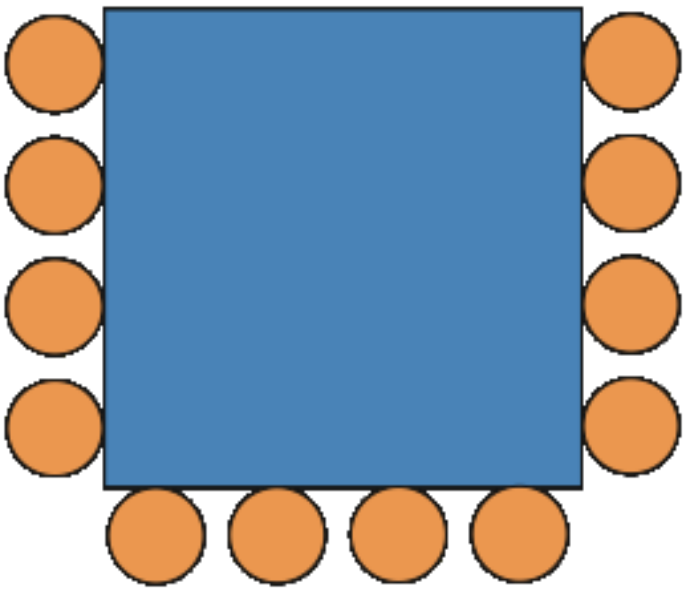

Figure A.1. Setup of the benchmark test for a thermoelastic benchmark. Box is 1 m by 1 m. The top surface is a free surface, all other sides have a rolling boundary condition

y-direction. The top is stress free. Under these conditions, Eqn. A.1 admits the following solution:

$$\begin{aligned} \varepsilon_{yy} &= \alpha\theta\frac{1+\nu}{1-\nu} \\ \varepsilon_{xx} &= 0 \\ \sigma_{yy} &= 0 \\ \sigma_{xx} &= -\frac{\alpha\theta E}{1-\nu} \end{aligned} \qquad \text{(Eqn. A.3)}$$

In the first benchmark (Figure 8A), Poisson's ratio is ν=0.3. According to Eqn. A.3, the strain should be ~1.8571×10^{-3}. As the sides of the model are defined as 1 m, the displacement should increase linearly with y to a maximum of ~1.8571×10^{-3} m. Interestingly the volume change is greater than the intrinsic volume change by a factor $(1+\nu)/(1-\nu)$. The material tries to expend in every direction but is constrained laterally in the horizontal directions *x* and *z*. That compression induces further expansion of the material in the direction where it is unconstrained, the *y* direction. This manifestation of the Poisson effect vanishes when ν=0. Figure A.2B shows that in case, the volume change and maximum displacement is indeed 10^{-3}m.

Equation A.2 is appropriate for an elastic material. However the intrusion is initially a liquid and would, therefore, not have an elastic response. Setting the Poisson ratio to 0 works only for the specific geometry of the benchmark in Figure A.1 and A.2. The Young's modulus can be set to a large number, approaching infinity, into order to minimize the elastic strains but at the cost of extremely high stresses: the material is rigid. Setting the Young's modulus to 0 removes residual elastic stresses, but also implies that the material is extremely compressible unless

ν=1/2. To approximate the behavior of water it is necessary to adjust both *E* and ν to have very small Young's modulus and ν near 1/2.

It is easier to describe the fluid-like behavior in terms of shear modulus, *G*, and bulk modulus, *K*, which are related to E and ν according to:

$$G = \frac{E}{2(1+\nu)}$$
$$K = \frac{E}{3(1-2\upsilon)} \qquad \text{(Eqn. A.4)}$$

A fluid will not support stress if *G*=0 but it will remain compressible if *K* is finite. For water, *K*=2.2 GPa. For convenience, I define defined the solidity ratio

$$s = \frac{G}{K} \qquad \text{(Eqn. A.5)}$$

For a given *K*, Young's modulus and Poisson ratio are given by

$$E = \frac{9Ks}{3+s}$$
$$\upsilon = \frac{(3/2)-s}{3+s}. \qquad \text{(Eqn. A.6)}$$

As *s* approaches zero the Poisson's ratio approaches ½ and the shear modulus approaches 0, while the bulk modulus, per construction, remains as a predefined value, matching the ideal behavior of a liquid. By defining the elastic properties of the intrusion according to Eqns. A.4 and A.6, and progressively decreasing the solidity ratio, I am able to model the transition of an object from mostly solid to mostly liquid (or vice versa) conserving mass.

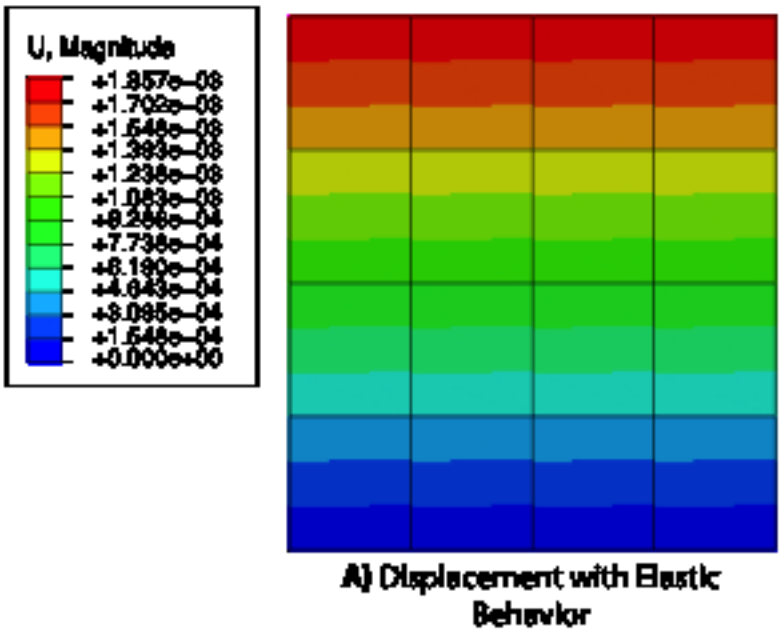

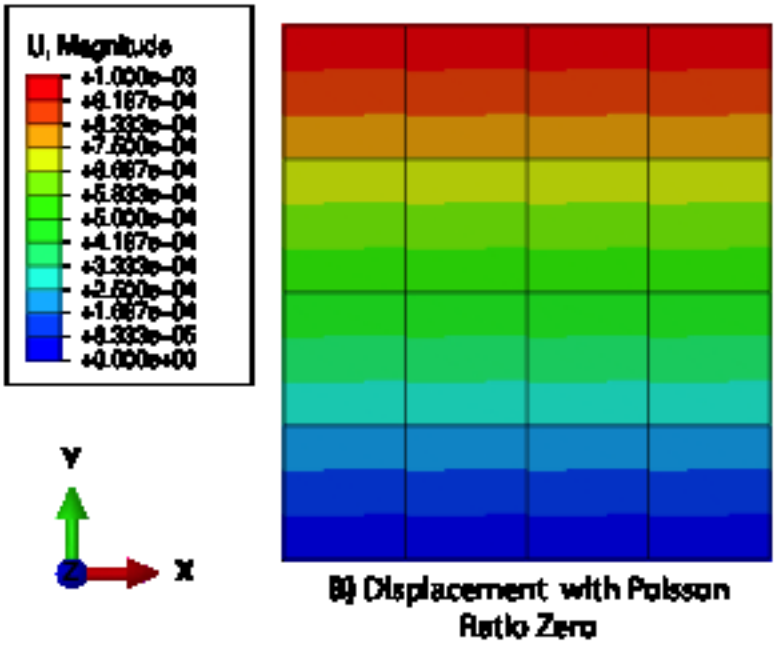

Figure A.2. The displacement associated with a 10^{-3} relative volume change. **A** includes the elastic response of the material and has a Poisson's ratio of 0.3 and Young's modulus of 10^{9}. **B** does not include the elastic response of the material. Only the Poisson's ratio was changed (to zero). The greater displacement in **A** relative to **B** is expected as it included elastic strain as well as thermal and **B** included only thermal.

Appendix C: Surface Stresses from Chapter 5 Models

C.1. Surface stresses in 40 km cryosphere with roller base for D = 5 km , C shown above each plot.

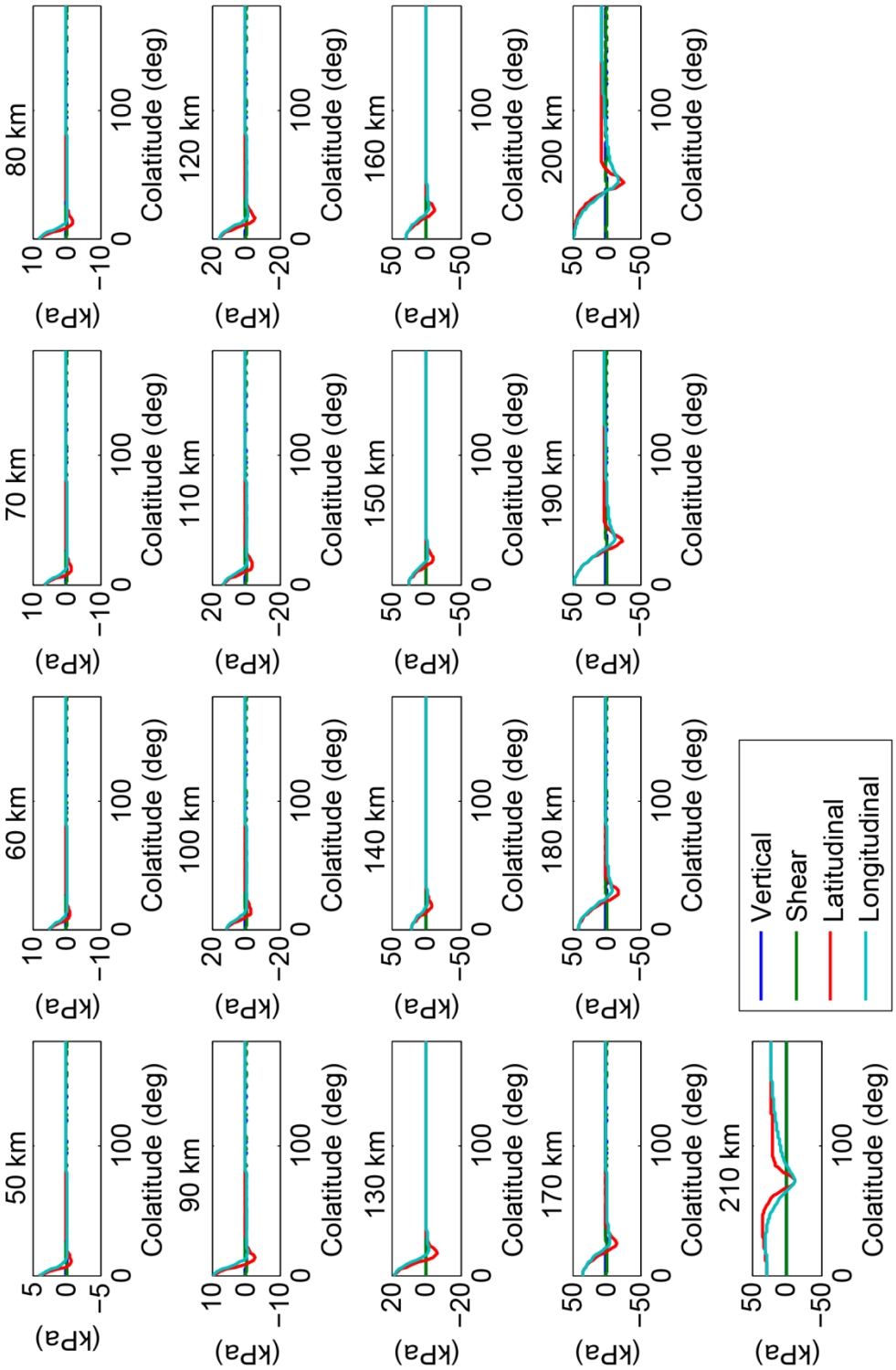

C.2. Surface stresses in 40 km cryosphere with roller base for D = 10 km , C shown above each plot.

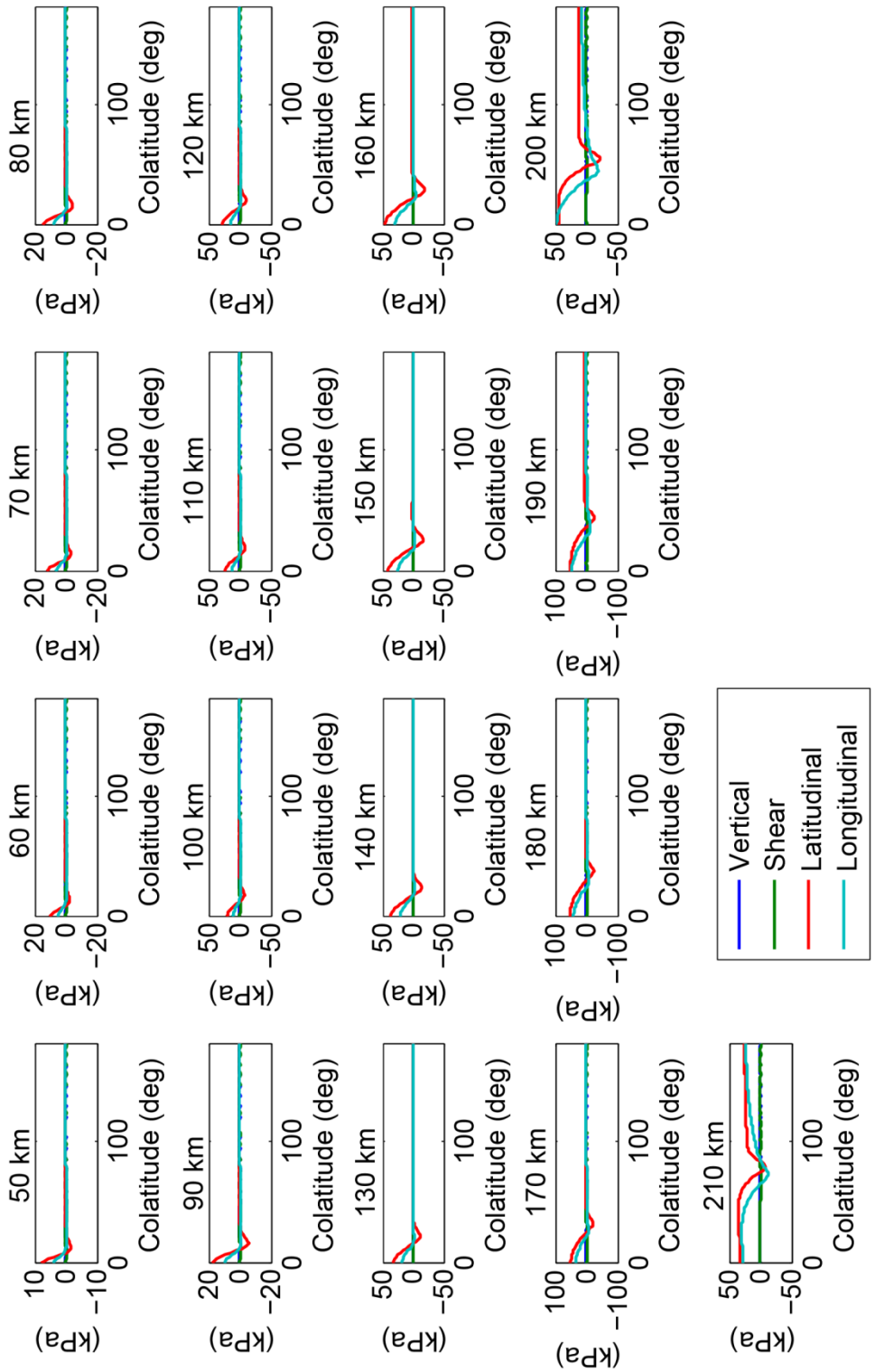

C.3. Surface stresses in 40 km cryosphere with roller base for D = 15 km , C shown above each plot.

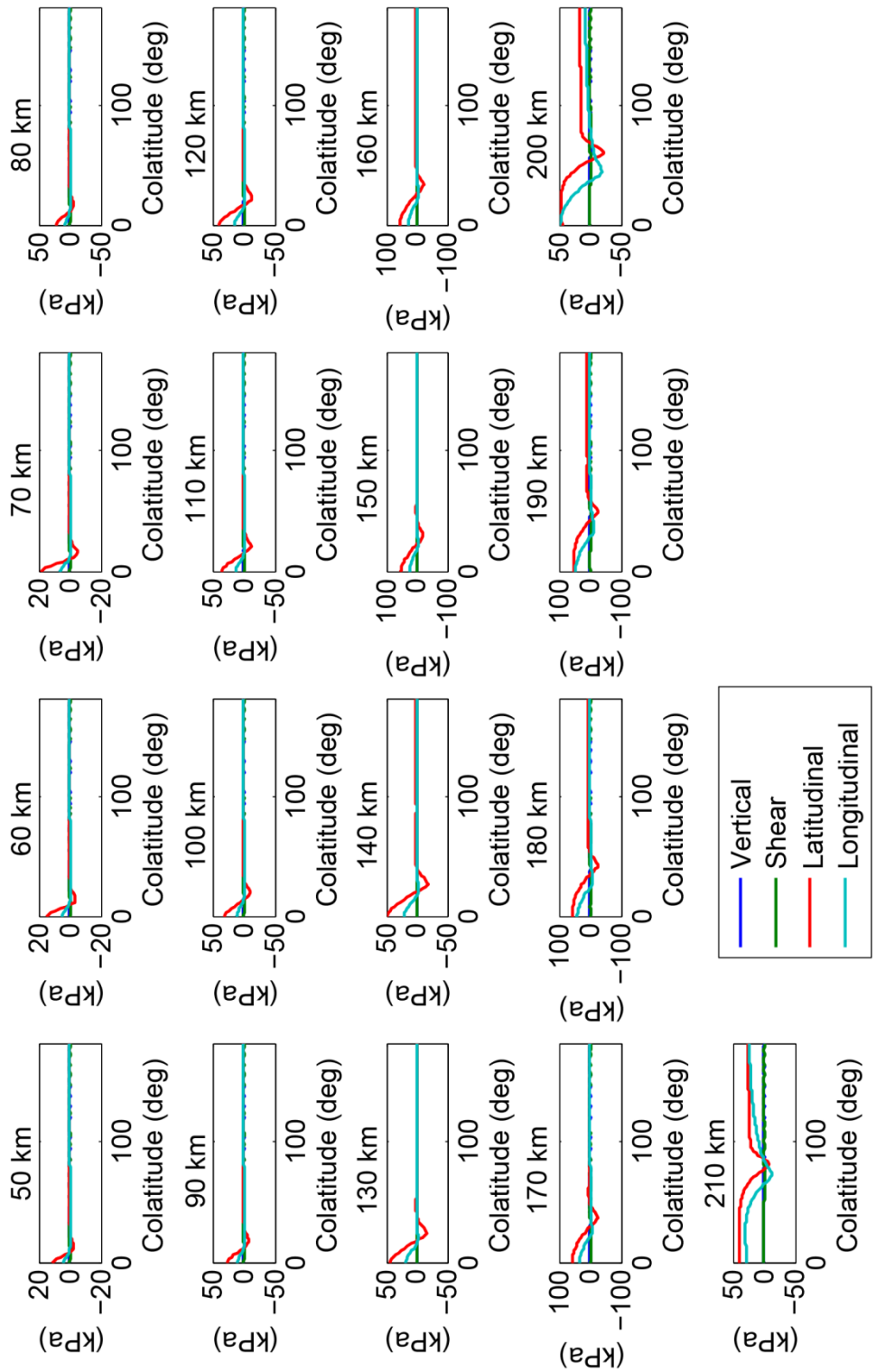

C.4. Surface stresses in 40 km cryosphere with roller base for D = 20 km , C shown above each plot.

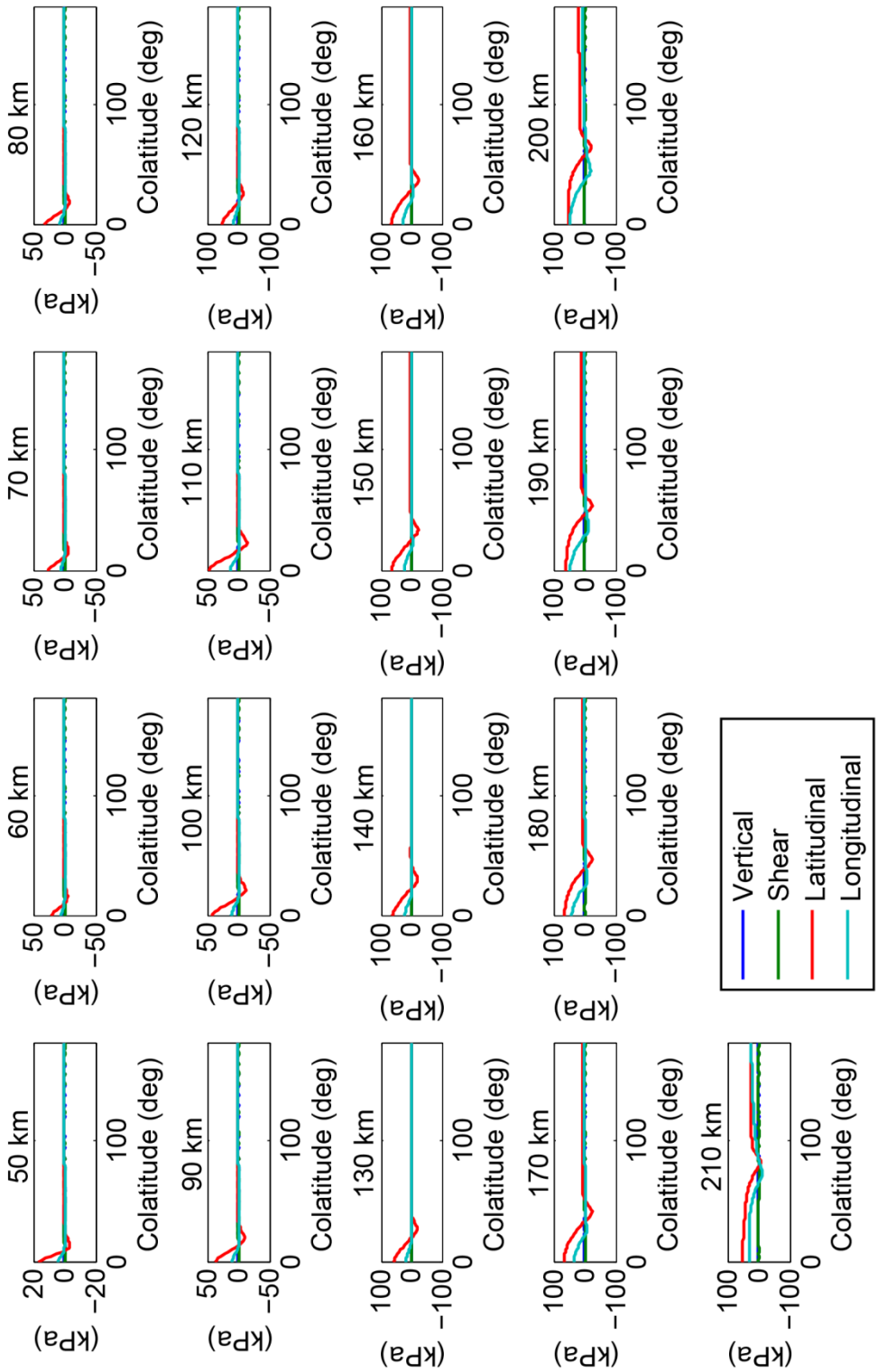

C.5. Surface stresses in 40 km cryosphere with roller base for D = 25 km, C shown above each plot.

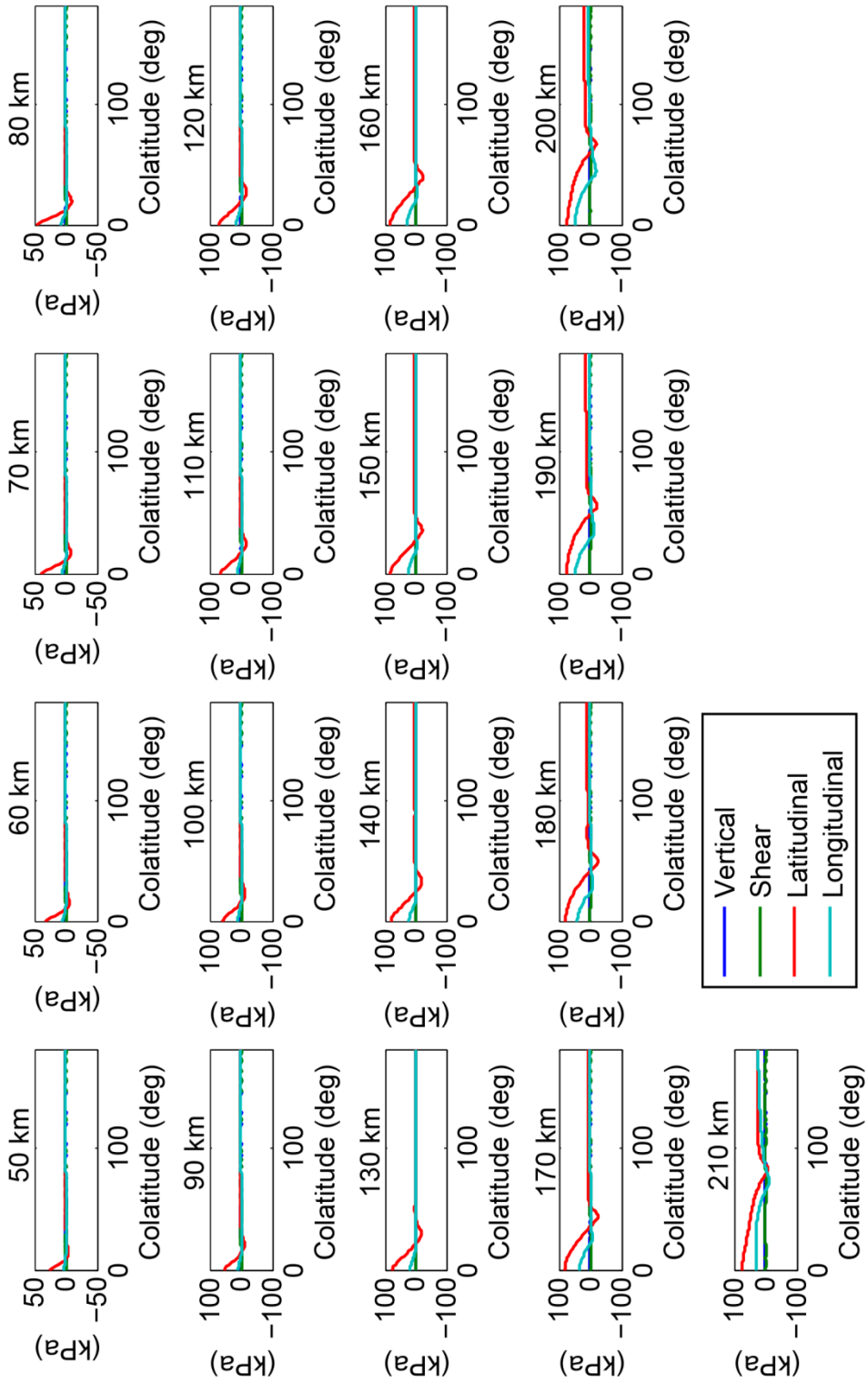

C.6. Surface stresses in 40 km cryosphere with roller base for D = 30 km, C shown above each plot.

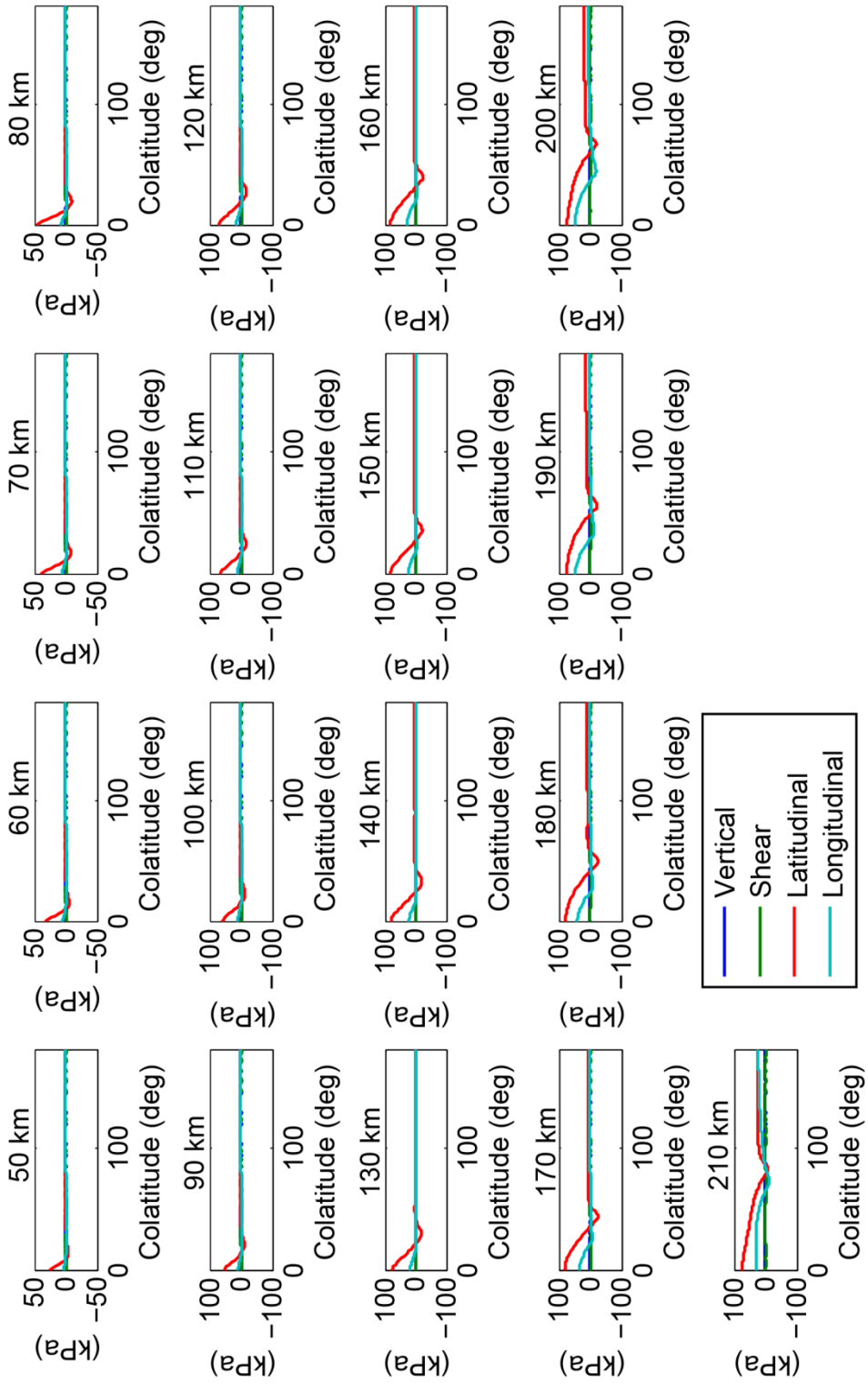

C.7. Surface stresses in 40 km cryosphere with roller base for D = 35 km, C shown above each plot.

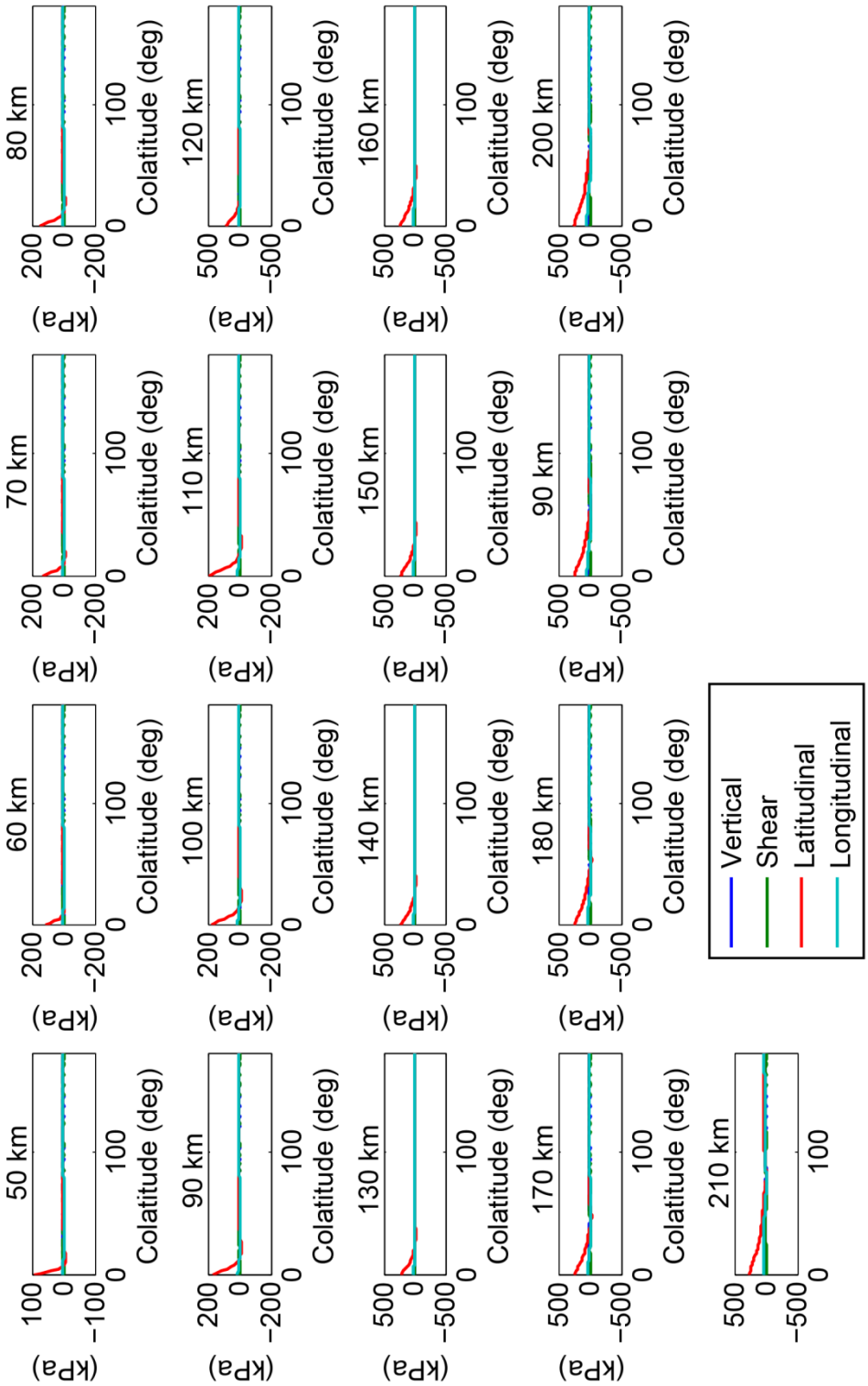

C.8. Surface stresses in 40 km cryosphere with bonded base for D = 5 km, C shown above each plot.

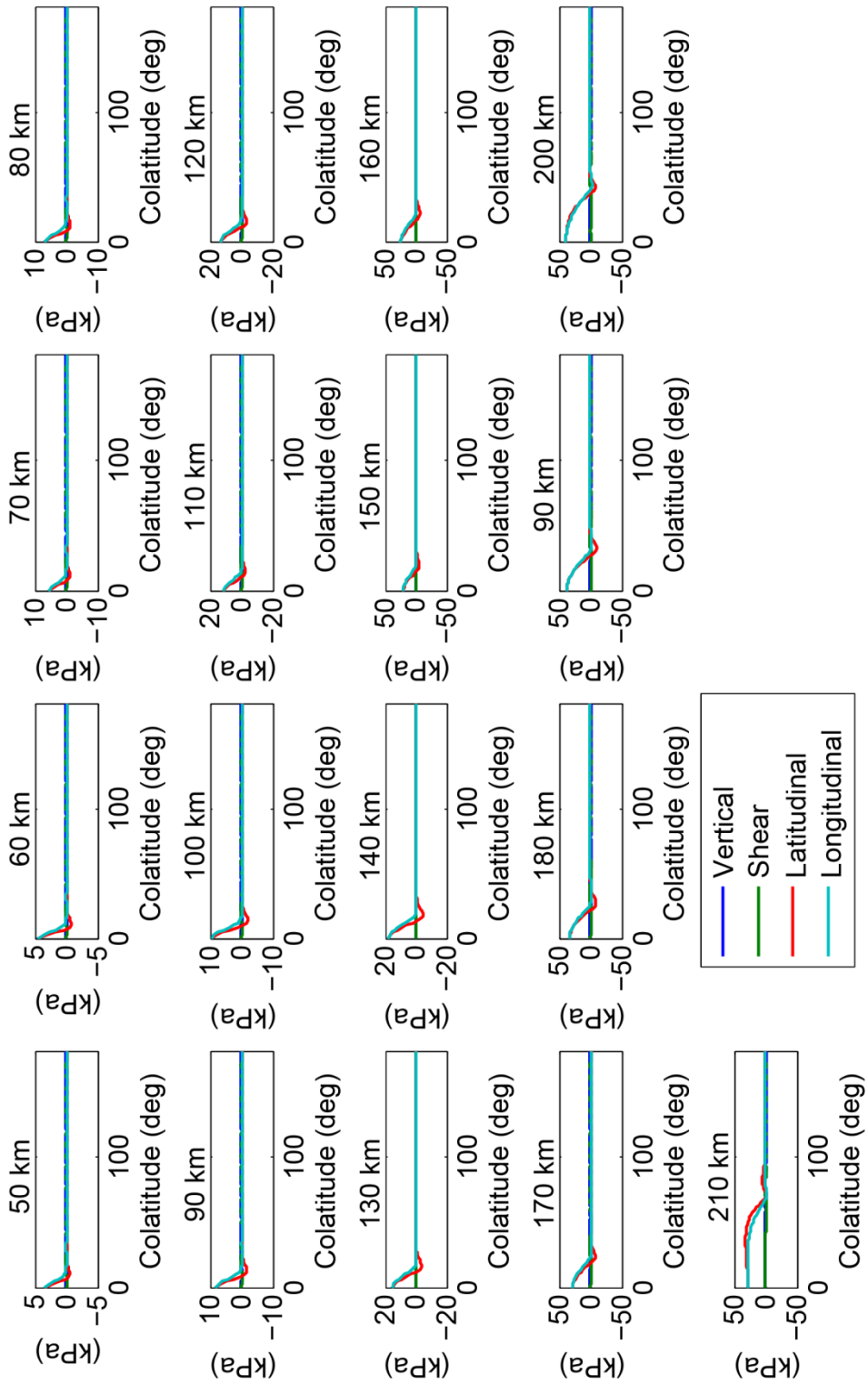

C.9. Surface stresses in 40 km cryosphere with bonded base for D = 10 km, C shown above each plot.

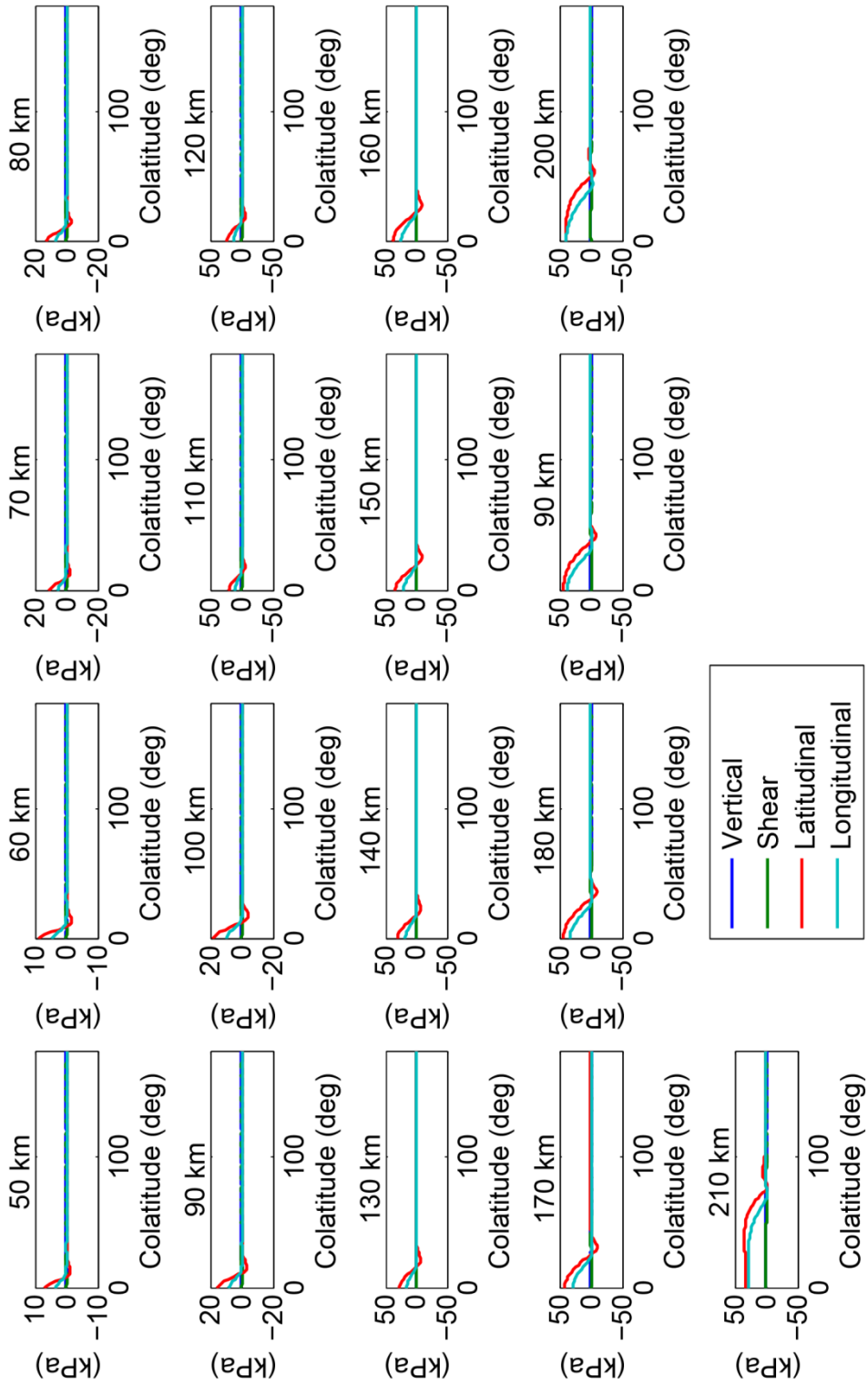

C.10. Surface stresses in 40 km cryosphere with bonded base for D = 15 km, C shown above each plot.

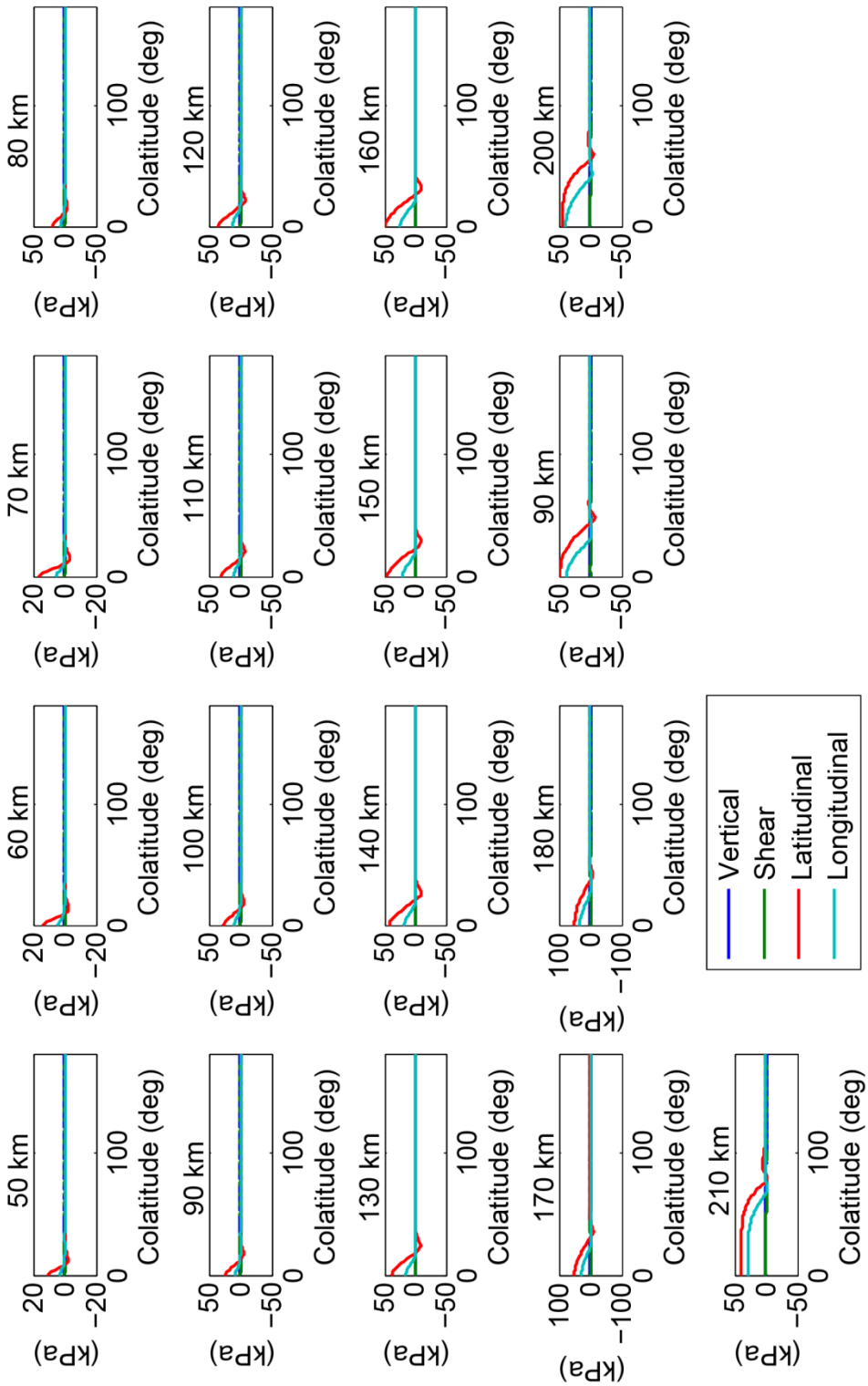

C.11. Surface stresses in 40 km cryosphere with bonded base for D = 20 km, C shown above each plot.

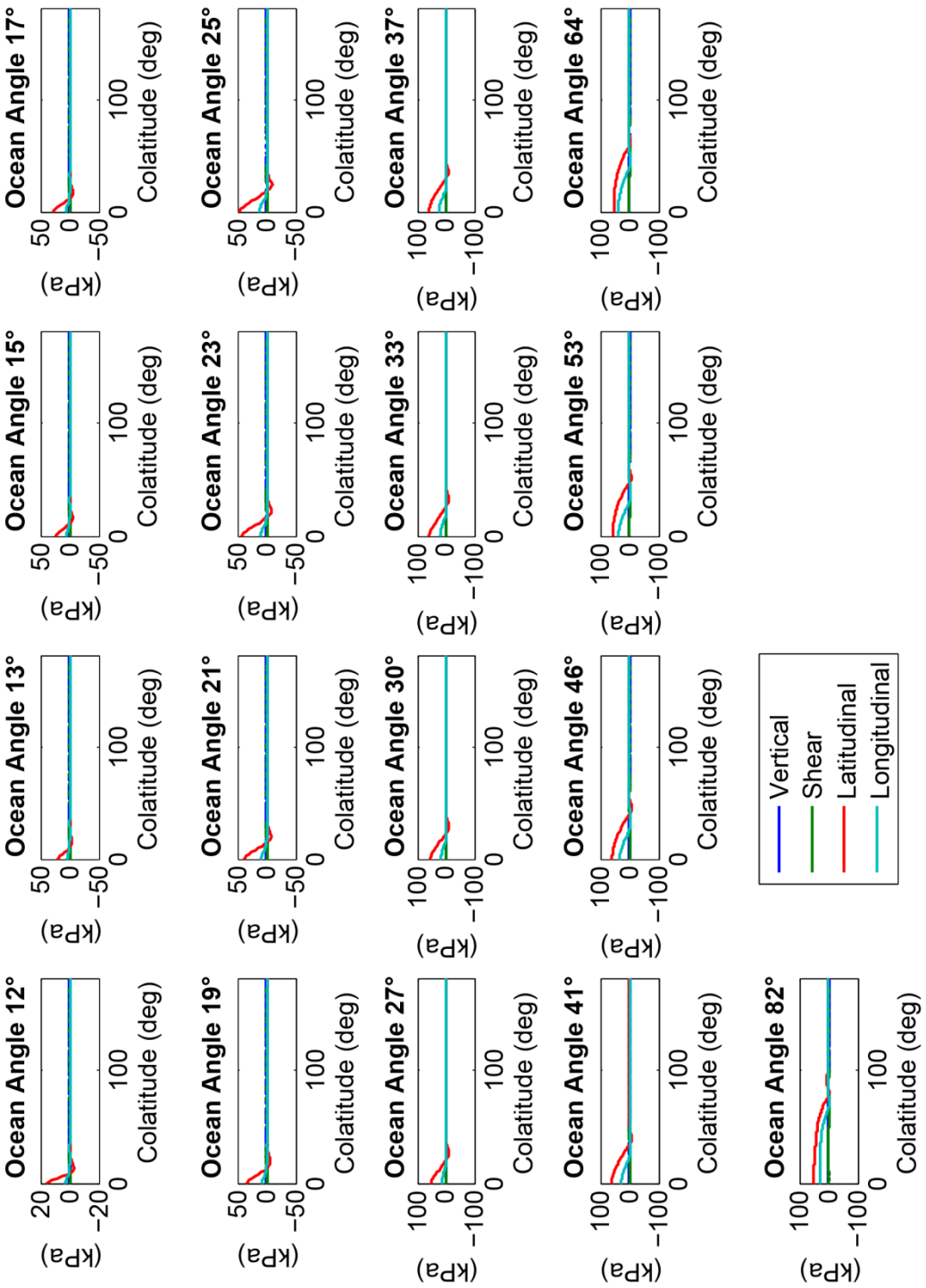

C.12. Surface stresses in 40 km cryosphere with bonded base for D = 25 km, C shown above each plot.

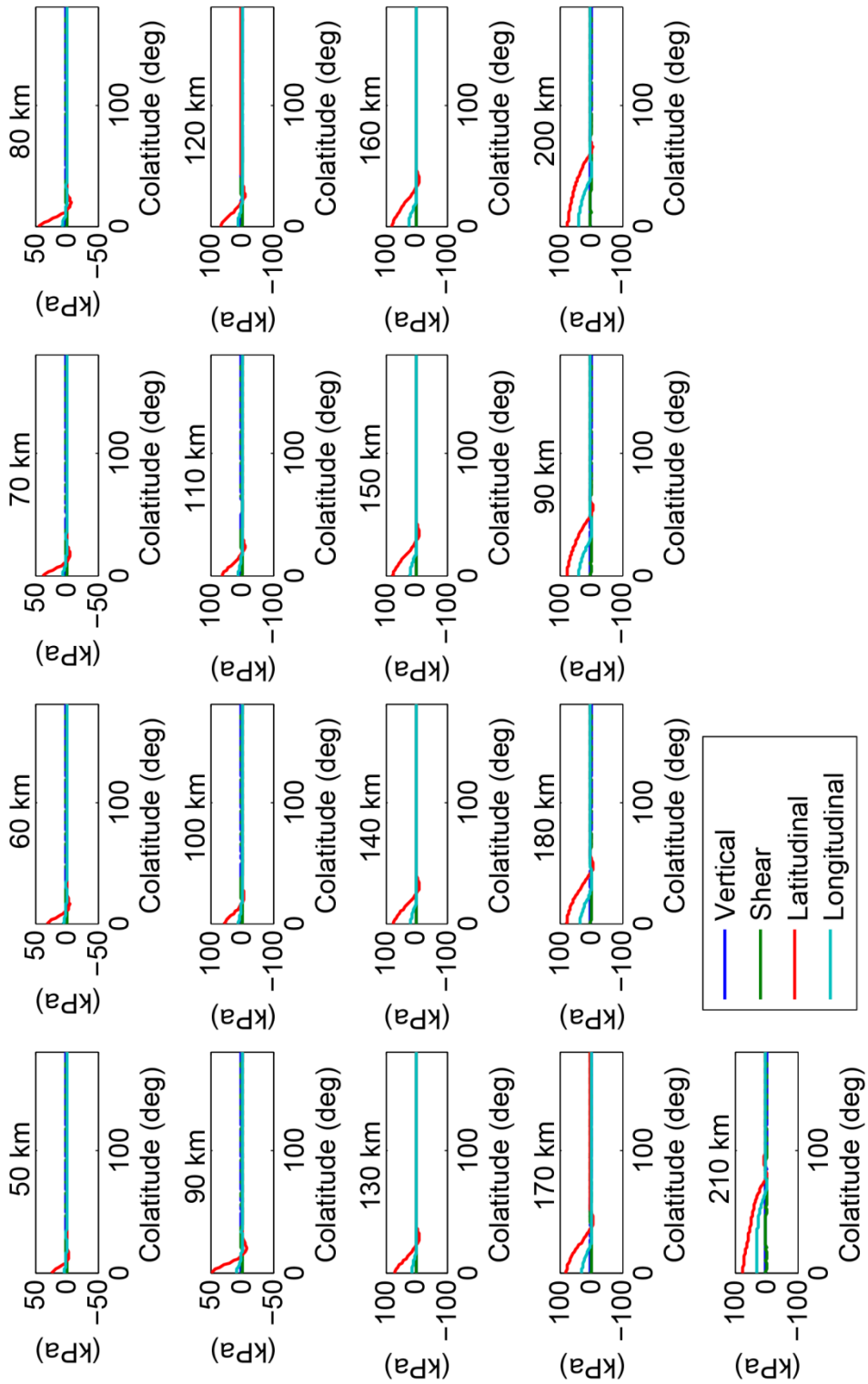

C.13. Surface stresses in 40 km cryosphere with bonded base for D = 30 km, C shown above each plot.

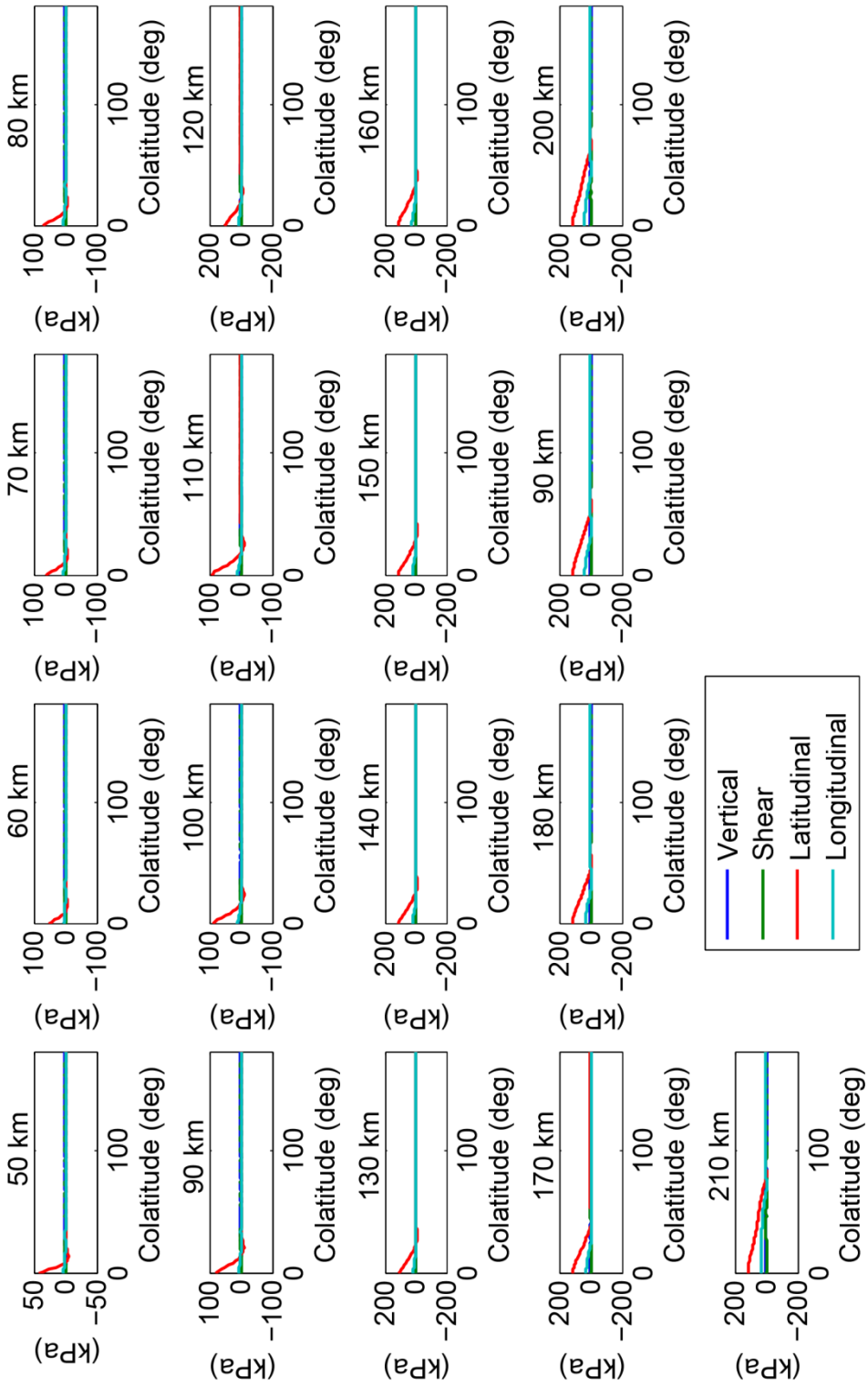

C.14. Surface stresses in 40 km cryosphere with bonded base for D = 35 km, C shown above each plot.

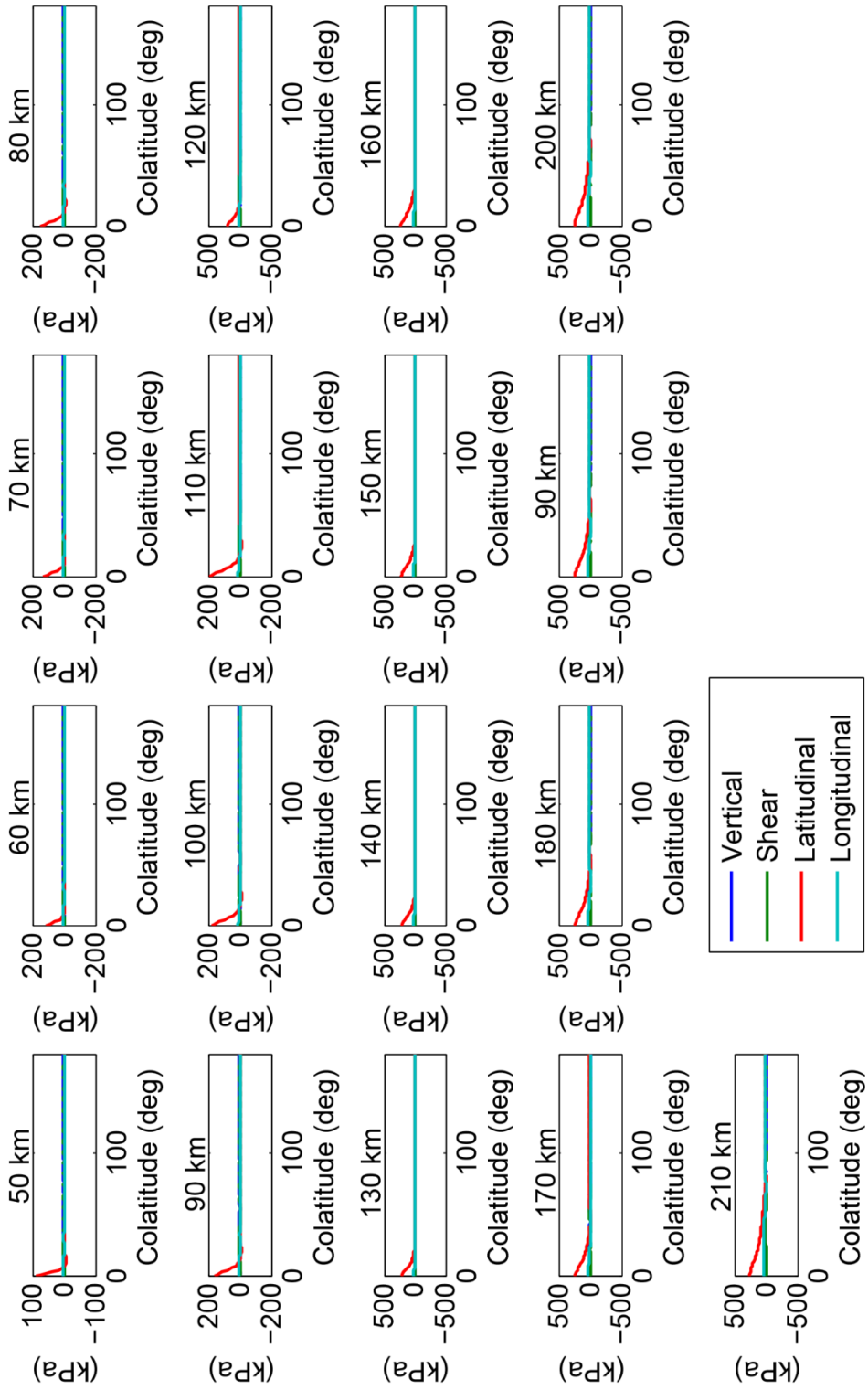

C.15. Surface stresses in 80 km cryosphere with bonded base for D = 5 km, C shown above each plot.

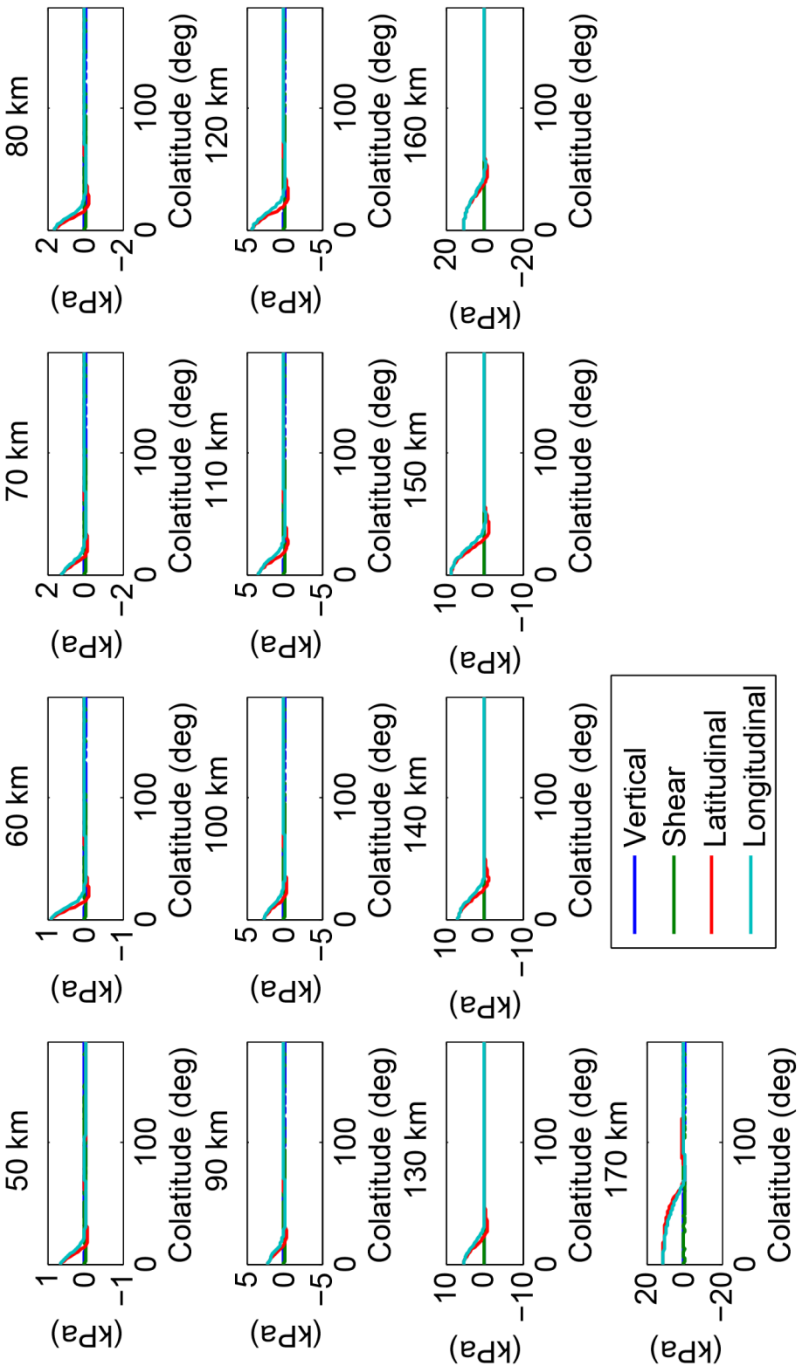

C.16. Surface stresses in 80 km cryosphere with bonded base for D = 10 km, C shown above each plot.

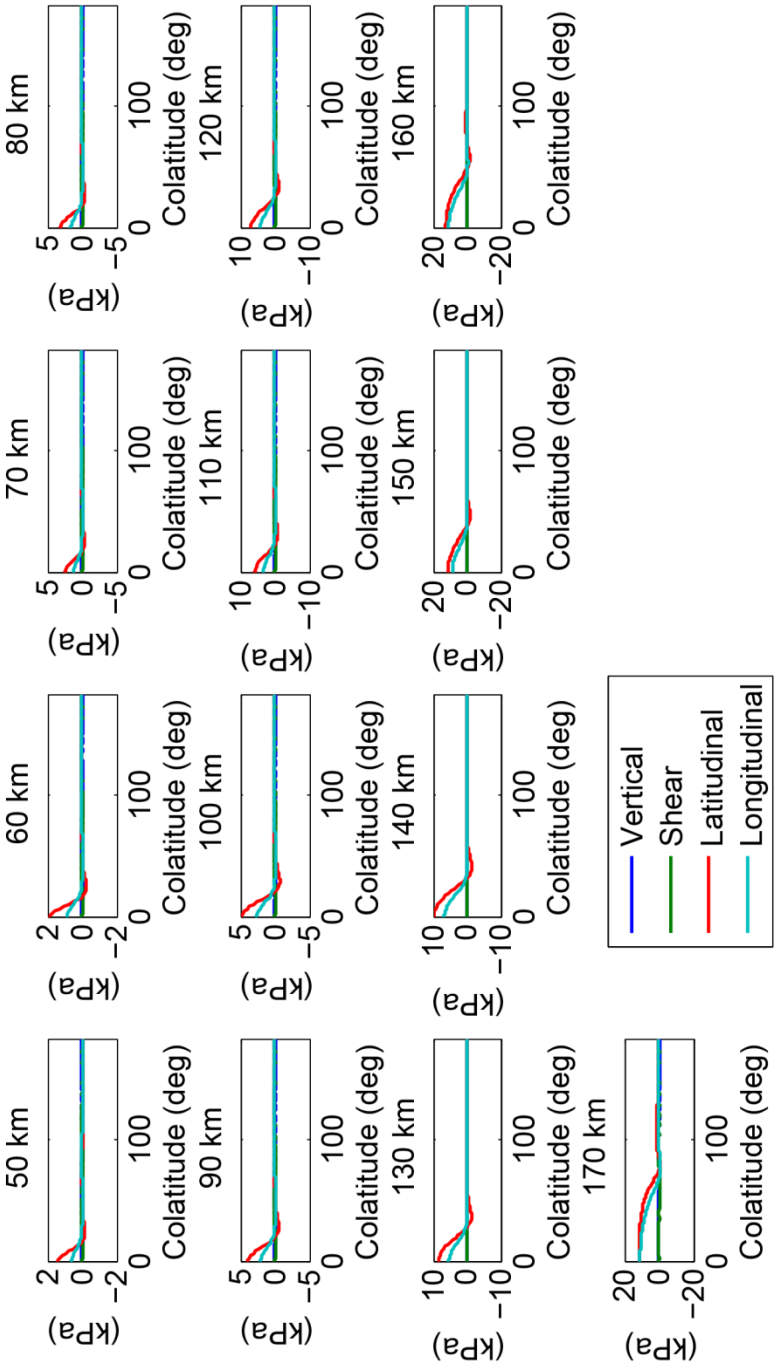

C.17. Surface stresses in 80 km cryosphere with bonded base for D = 15 km, C shown above each plot.

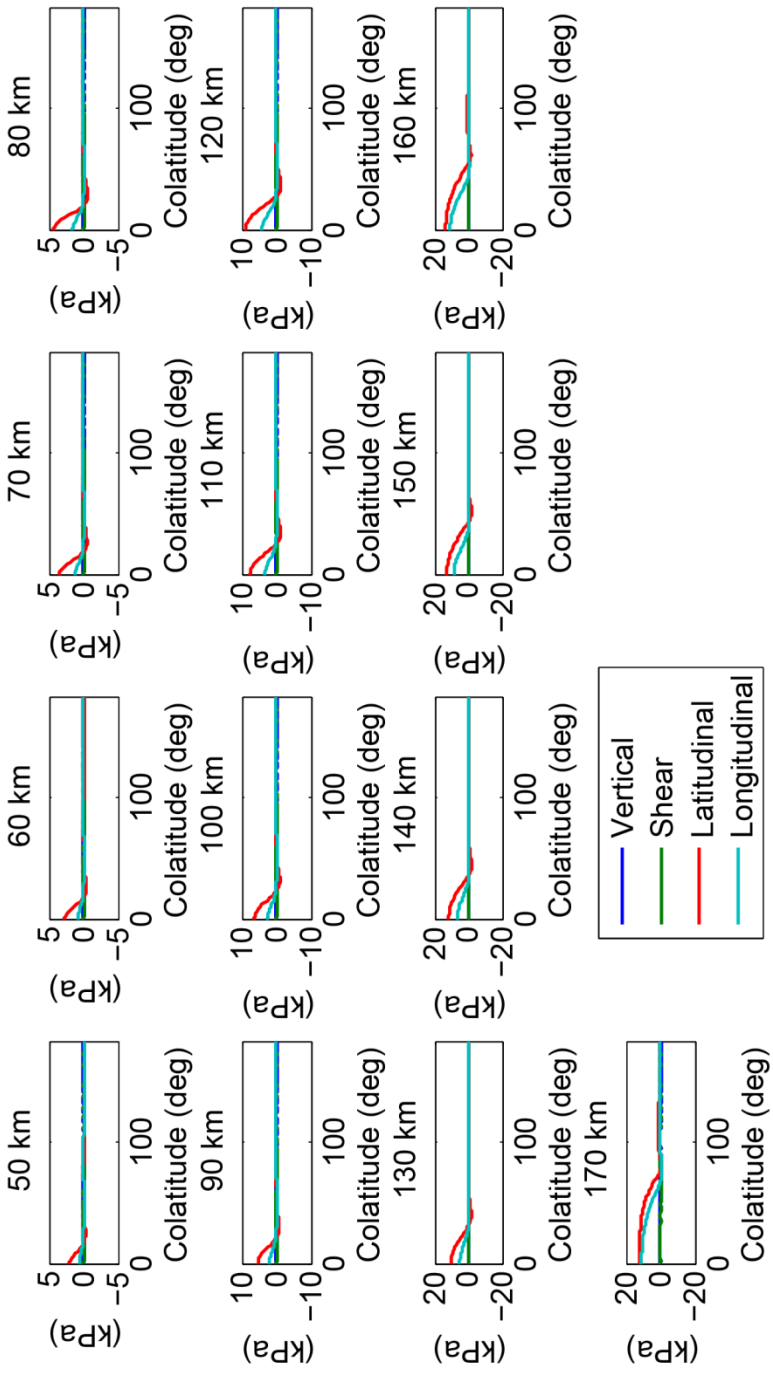

C.18. Surface stresses in 80 km cryosphere with bonded base for D = 20 km, C shown above each plot.

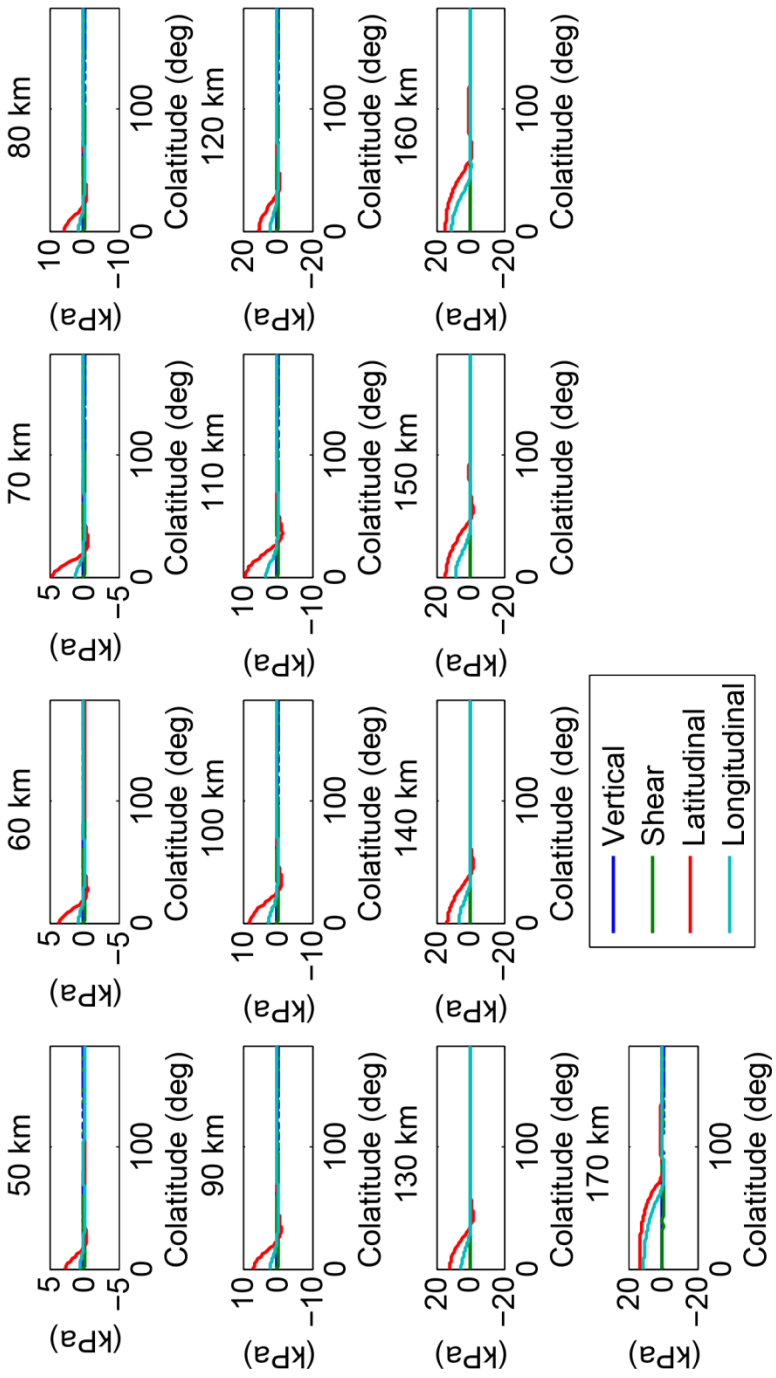

C.19. Surface stresses in 80 km cryosphere with bonded base for D = 25 km, C shown above each plot.

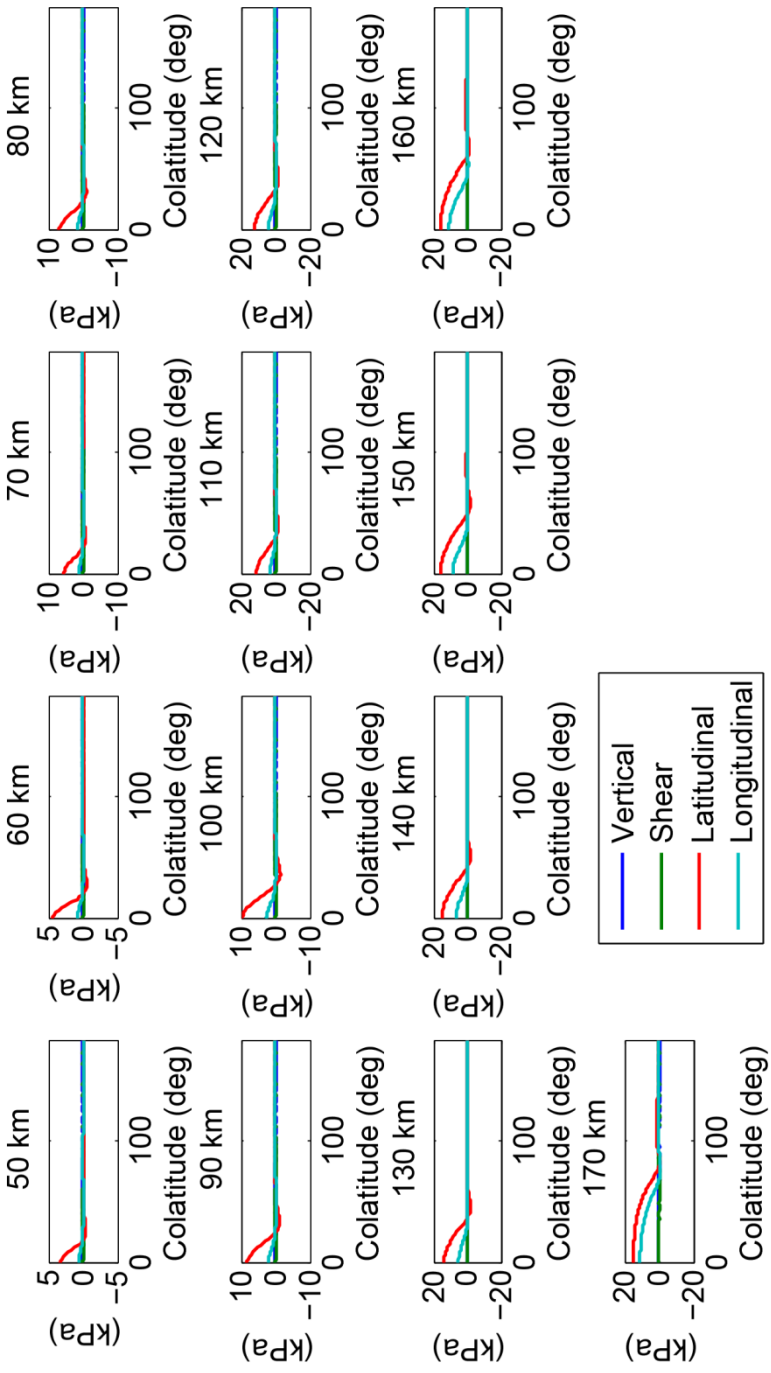

C.20. Surface stresses in 80 km cryosphere with bonded base for D = 30 km, C shown above each plot.

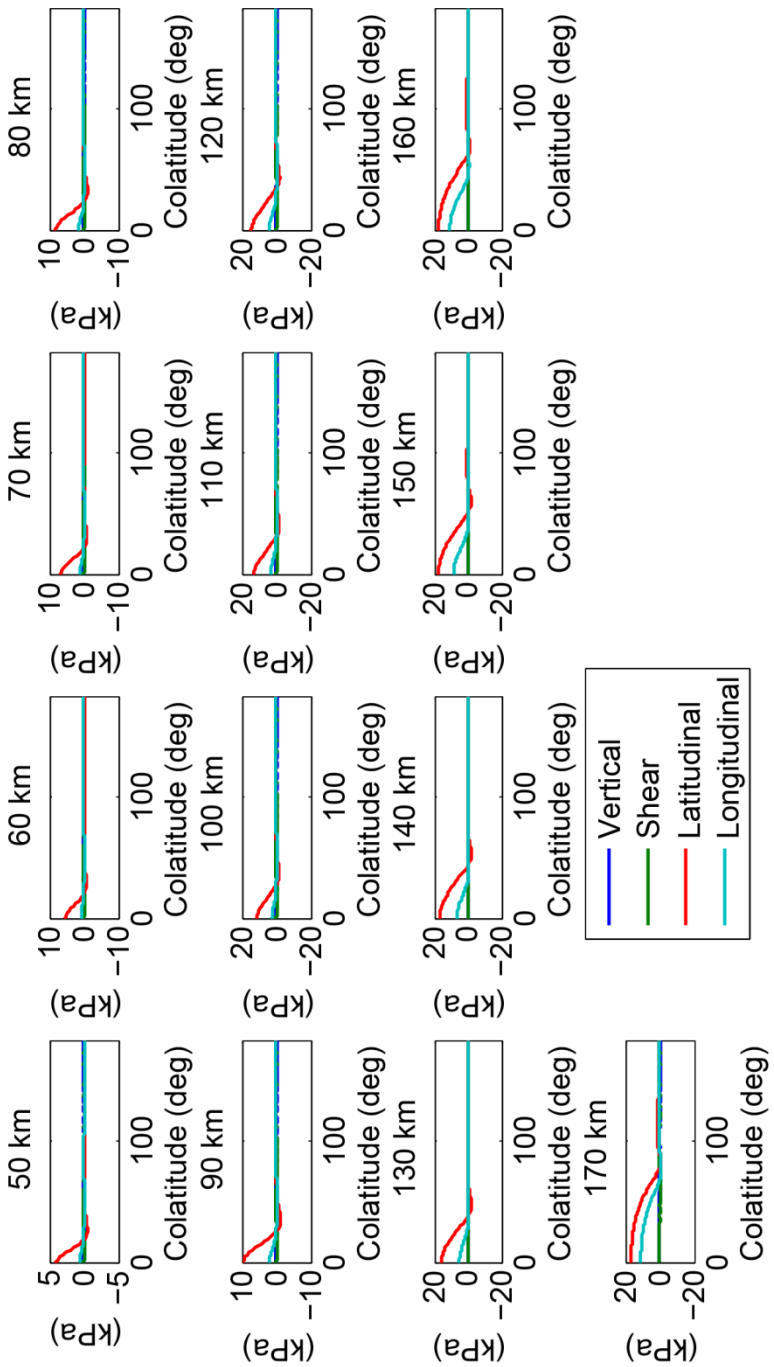

C.21. Surface stresses in 80 km cryosphere with bonded base for D = 35 km, C shown above each plot.

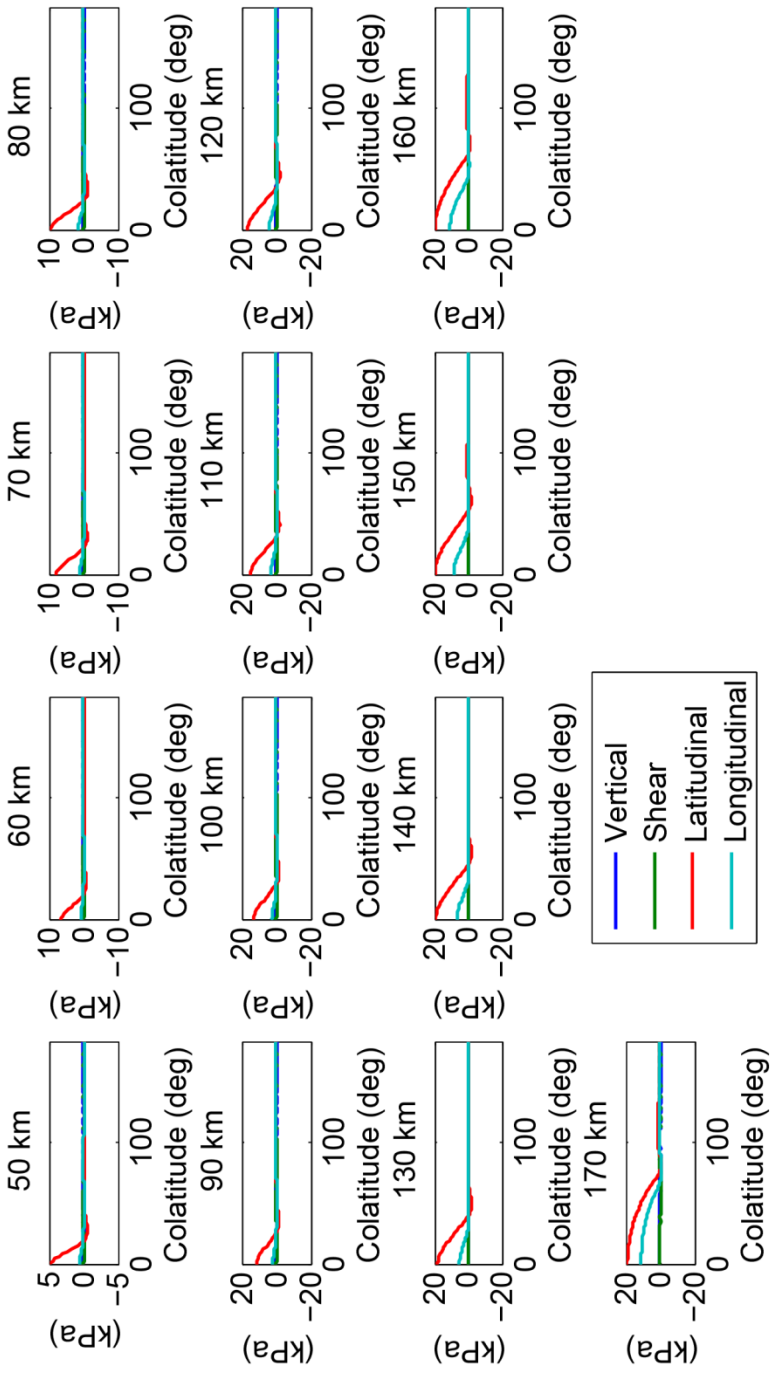

C.22. Surface stresses in 80 km cryosphere with bonded base for D = 40 km, C shown above each plot.

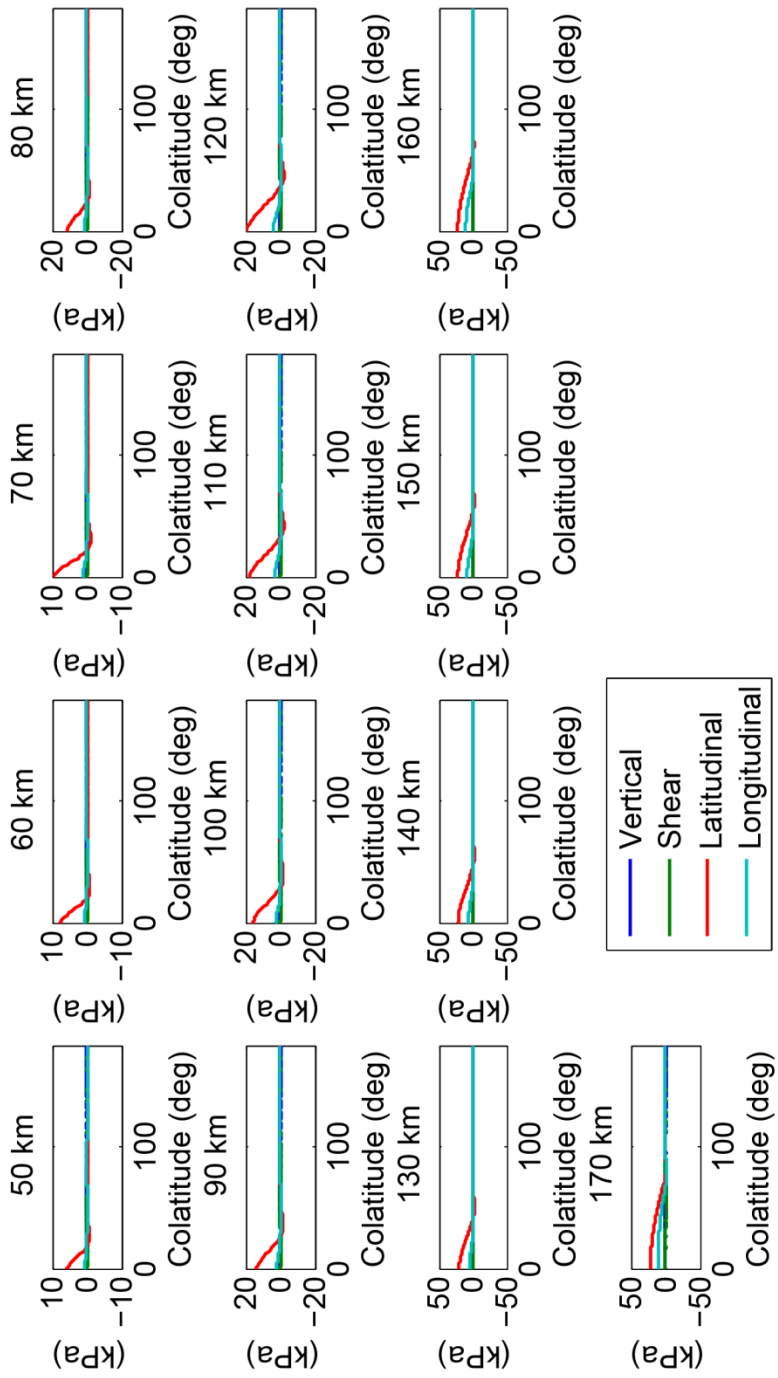

C.23. Surface stresses in 80 km cryosphere with bonded base for D = 45 km, C shown above each plot.

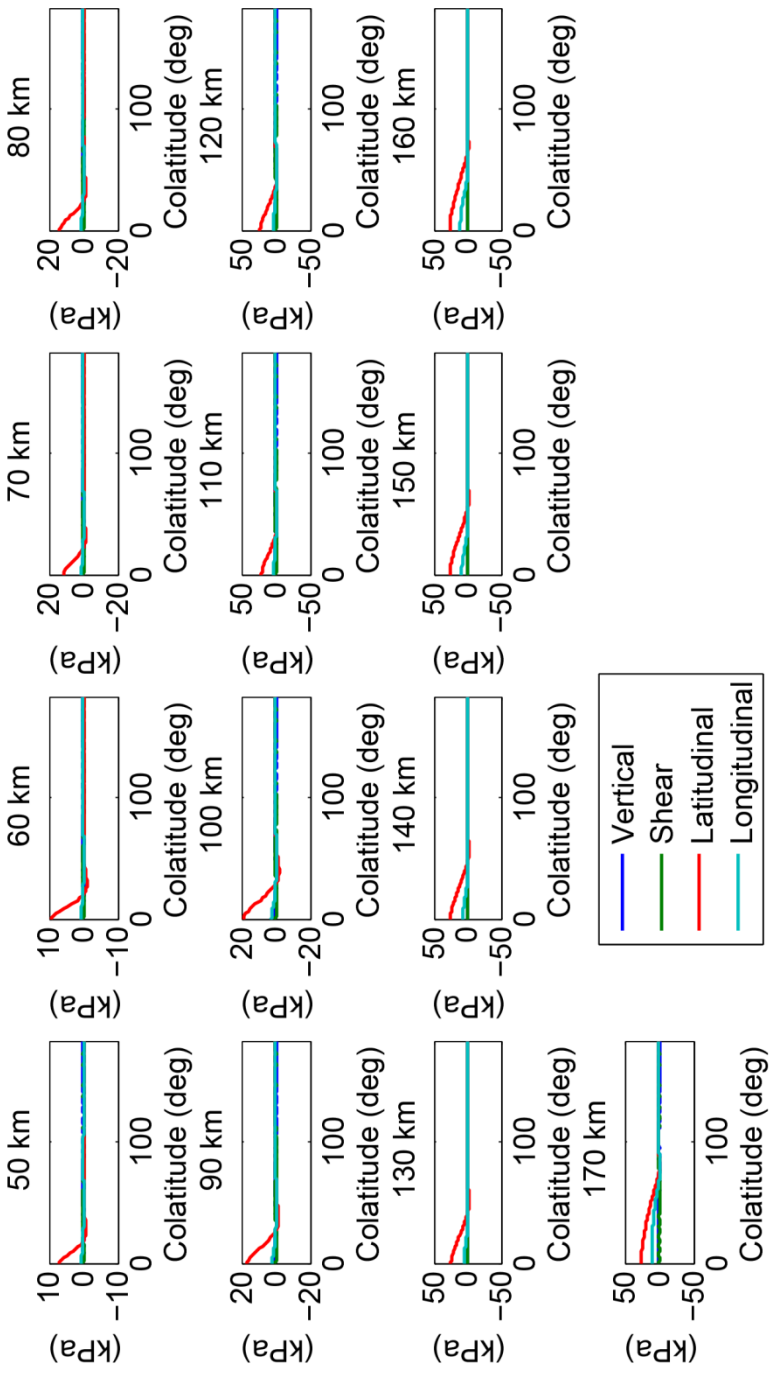

C.24. Surface stresses in 80 km cryosphere with bonded base for D = 50 km, C shown above each plot.

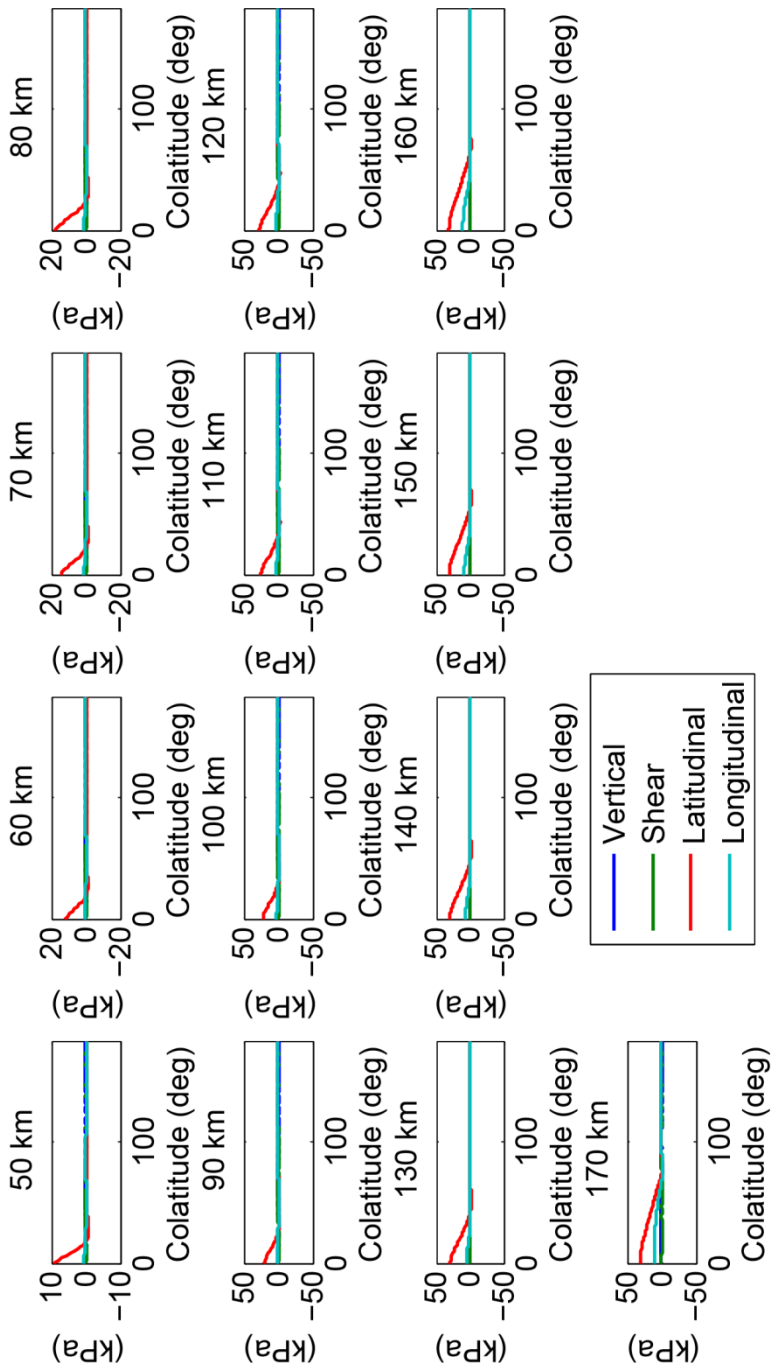

C.25. Surface stresses in 80 km cryosphere with bonded base for D = 55 km, C shown above each plot.

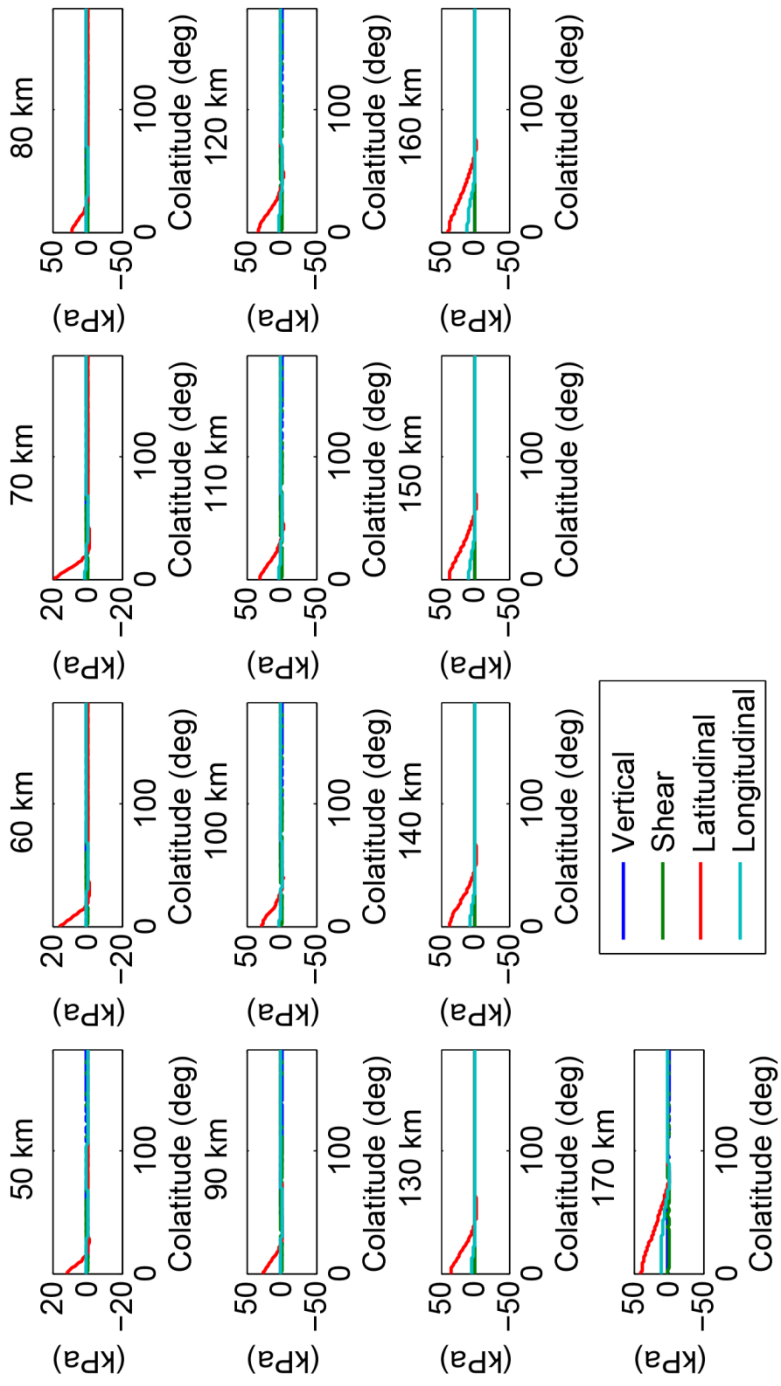

C.26. Surface stresses in 80 km cryosphere with bonded base for D = 60 km, C shown above each plot.

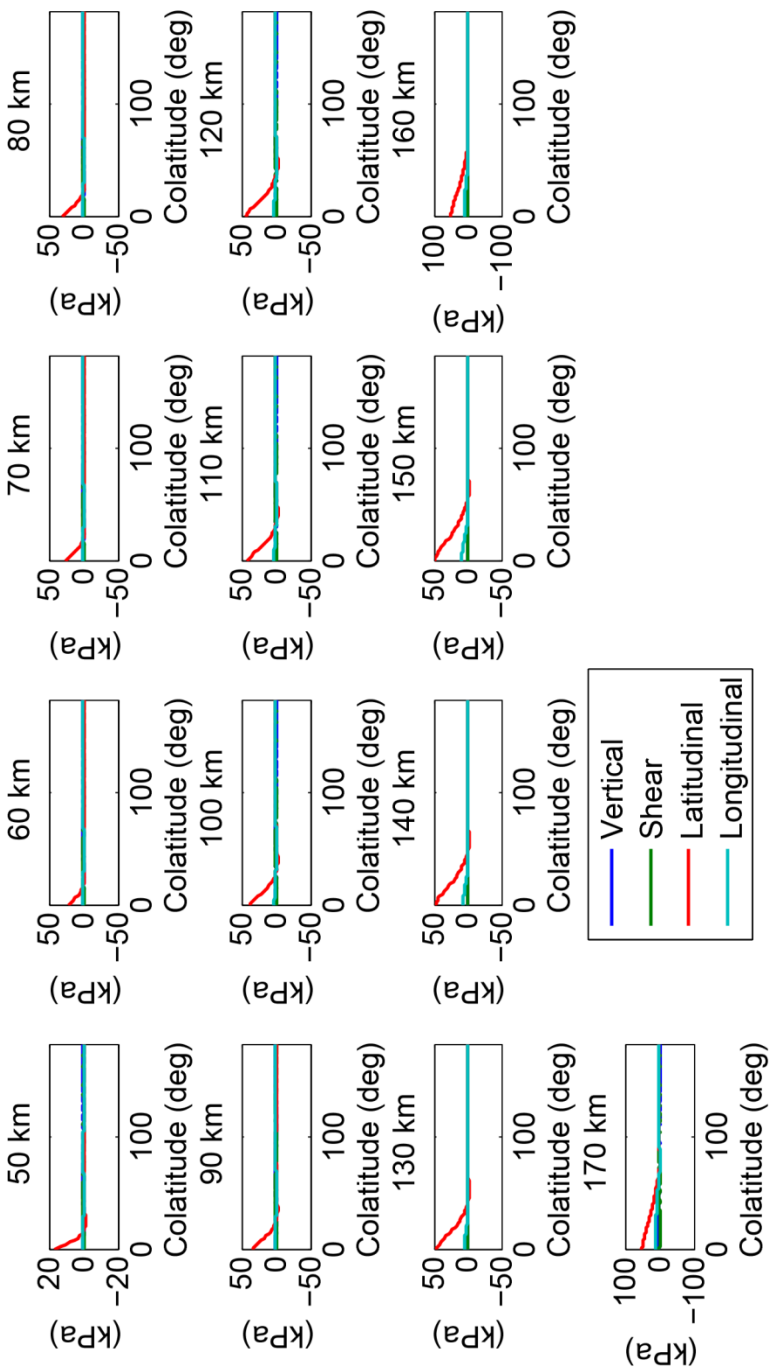

C.27. Surface stresses in 80 km cryosphere with bonded base for D = 65 km, C shown above each plot.

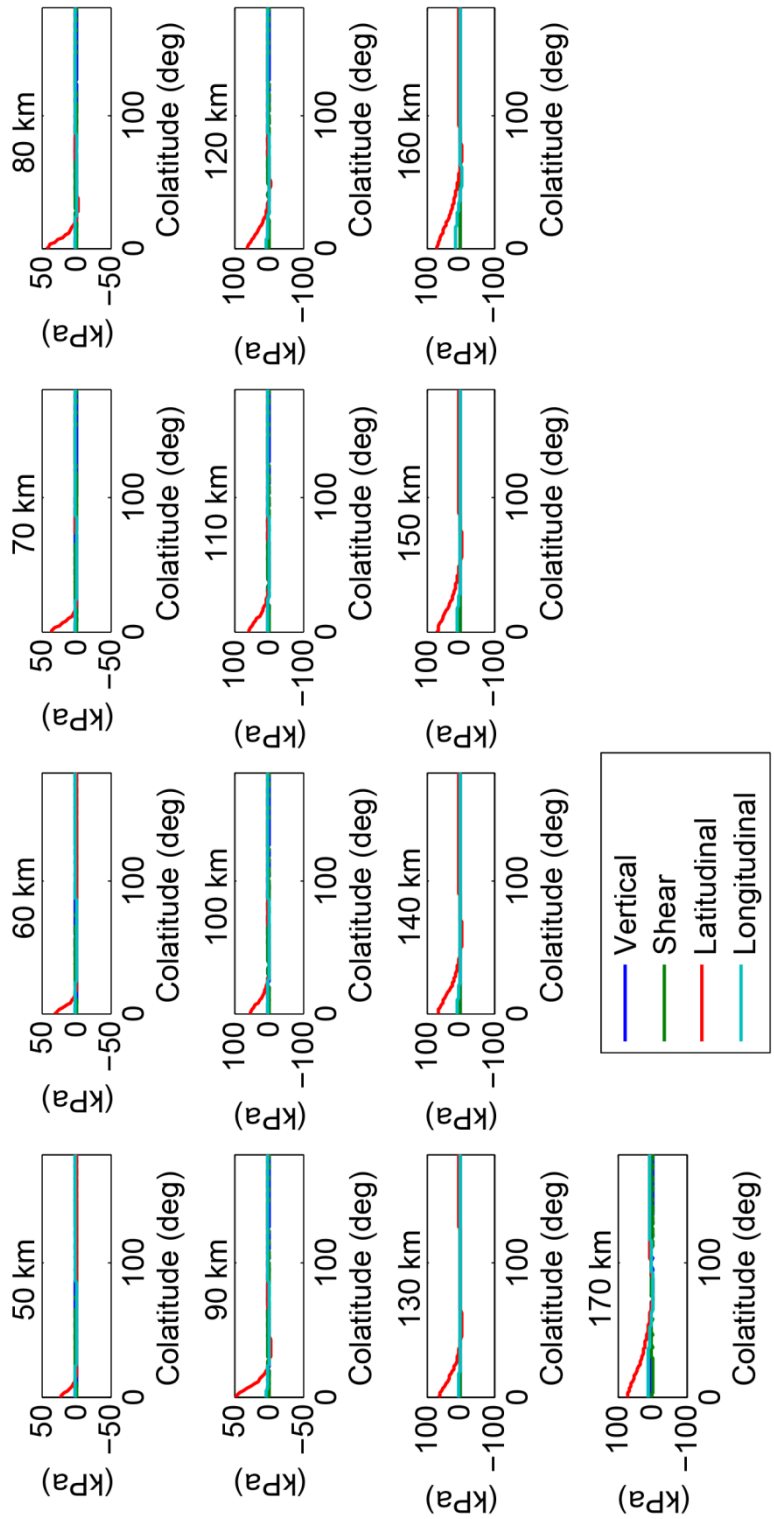

C.28. Surface stresses in 80 km cryosphere with bonded base for D = 70 km, C shown above each plot.

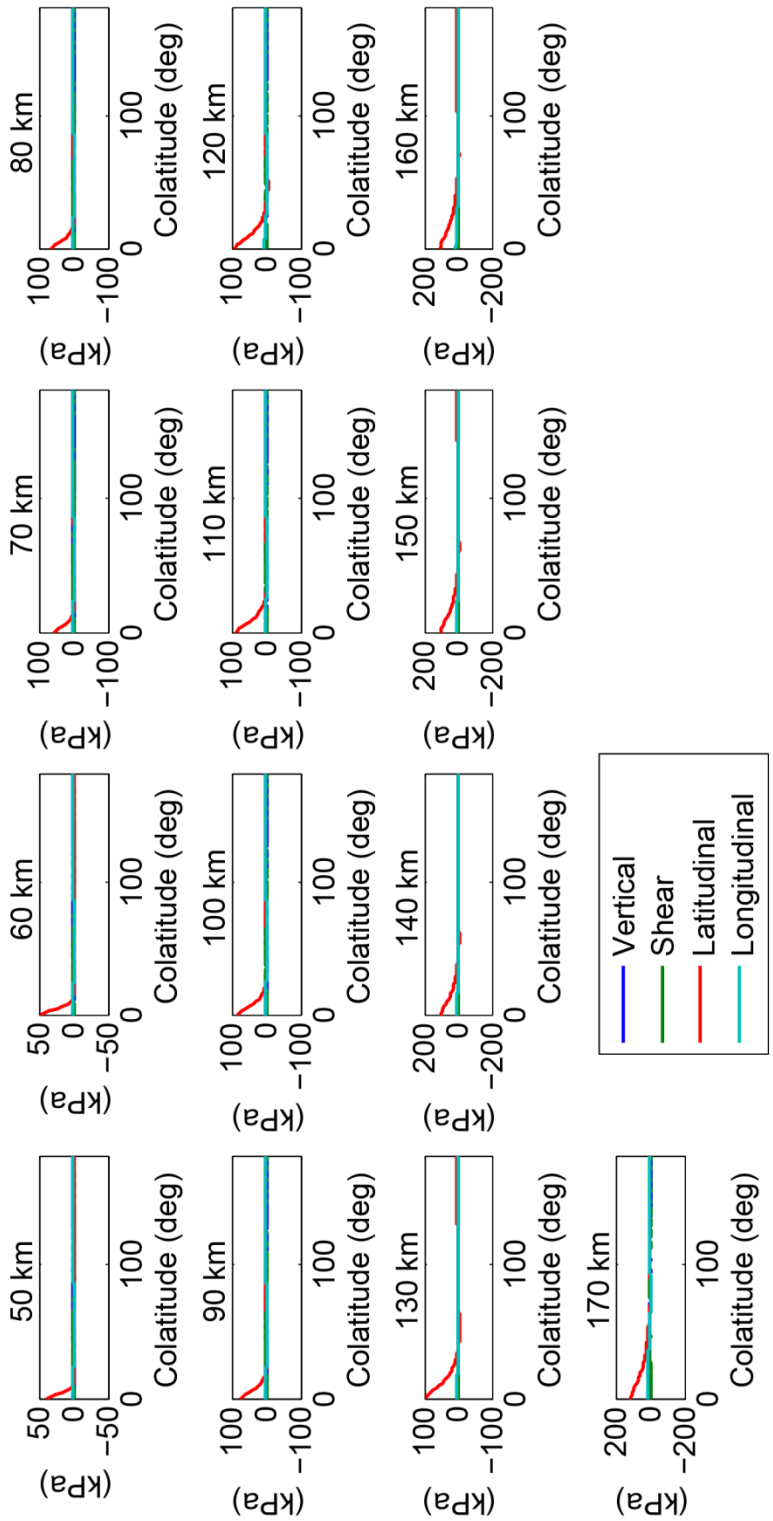

C.29. Surface stresses in 80 km cryosphere with bonded base for D = 75 km, C shown above each plot.

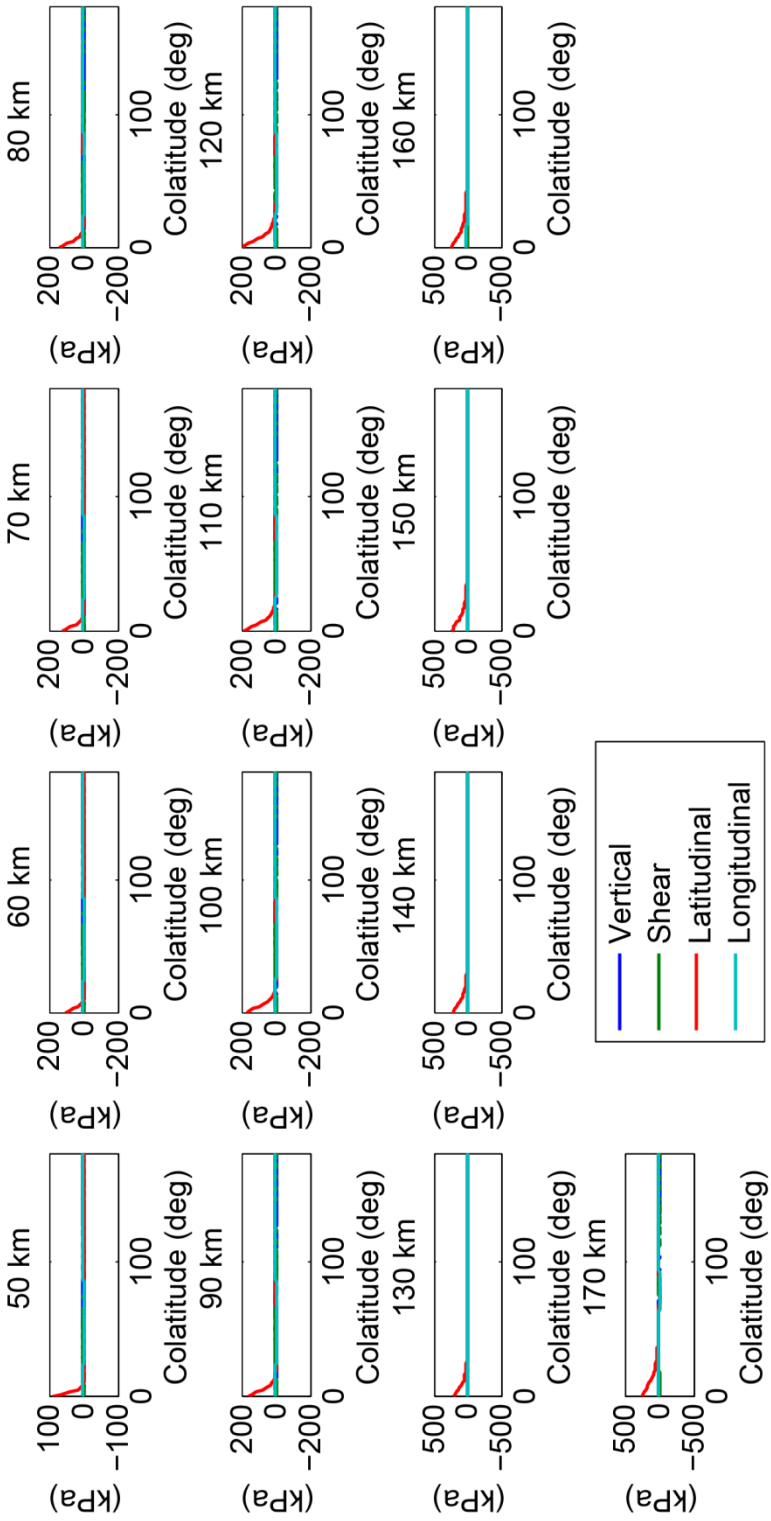

C.30. Surface stresses in 80 km cryosphere with roller base for D = 5 km, C shown above each plot.

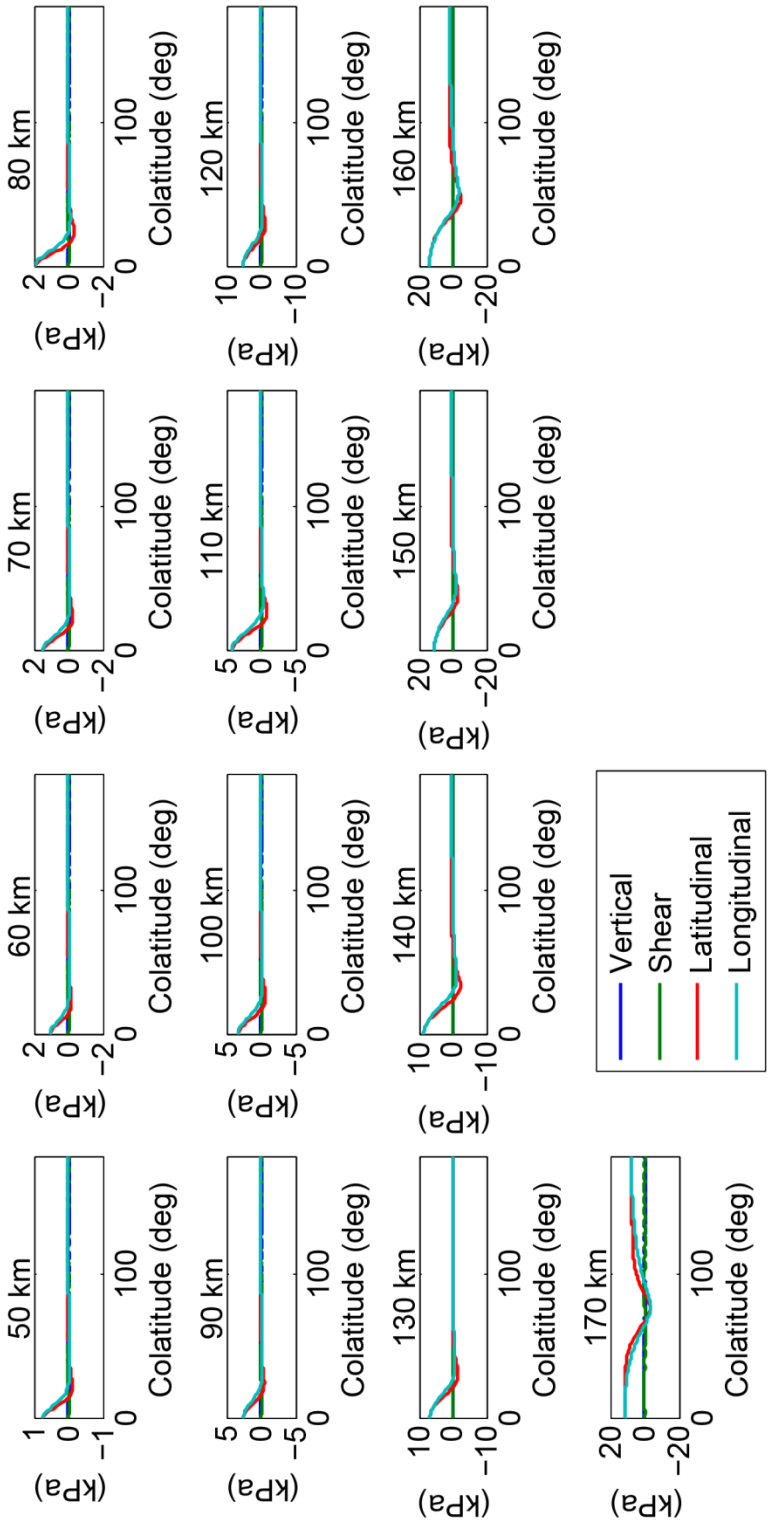

C.31. Surface stresses in 80 km cryosphere with roller base for D = 10 km, C shown above each plot.

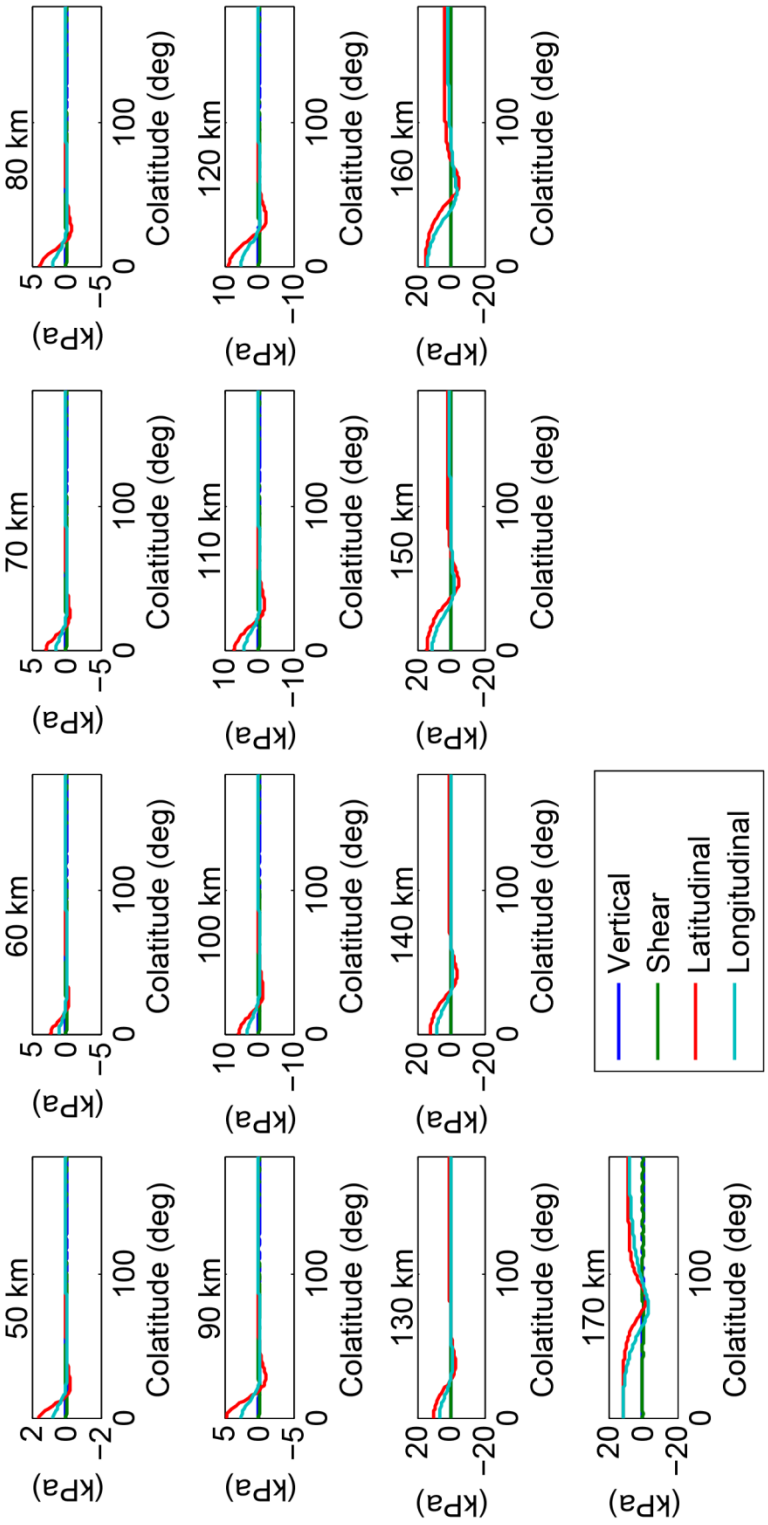

C.32. Surface stresses in 80 km cryosphere with roller base for D = 15 km, C shown above each plot.

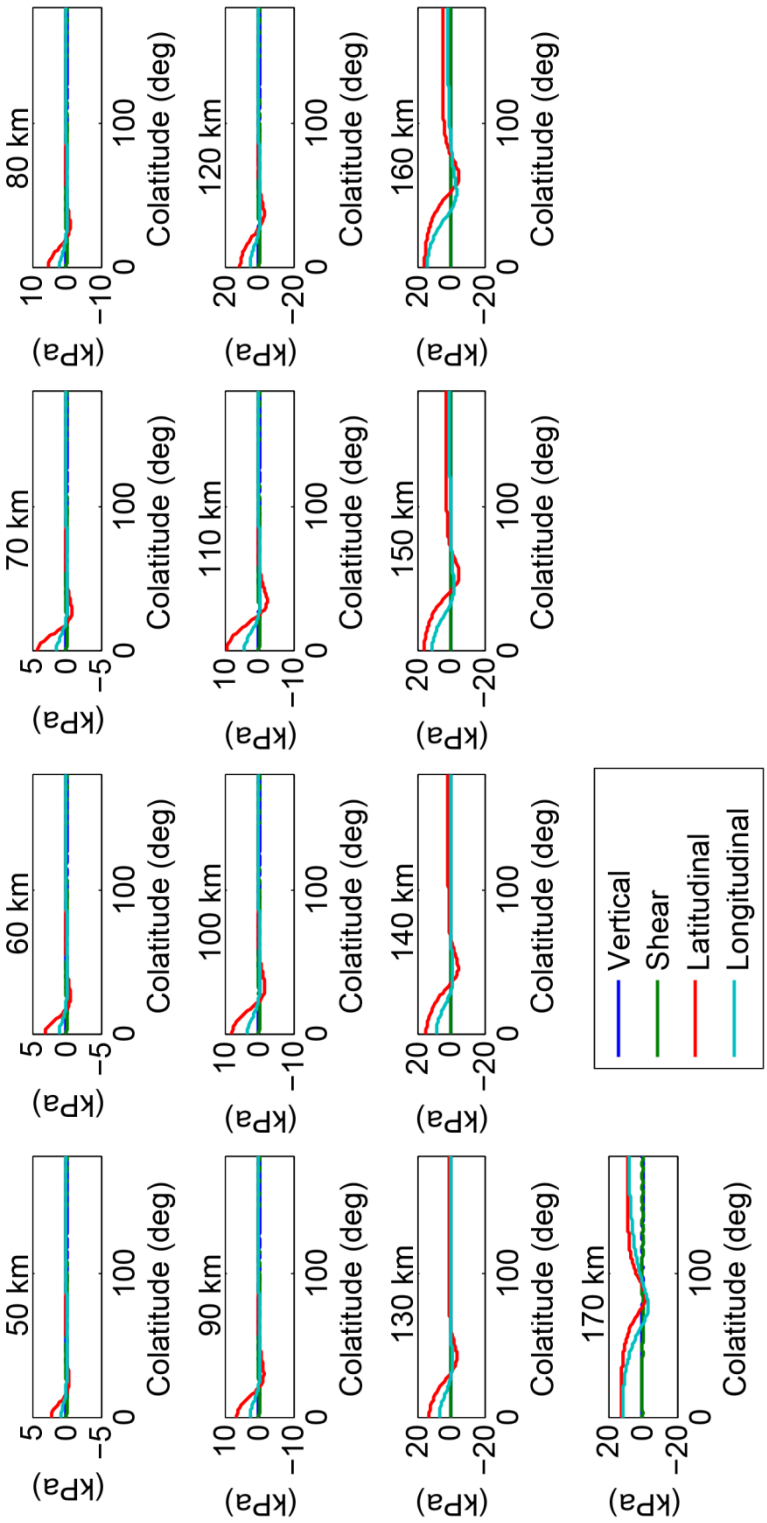

C.33. Surface stresses in 80 km cryosphere with roller base for D = 20 km, C shown above each plot.

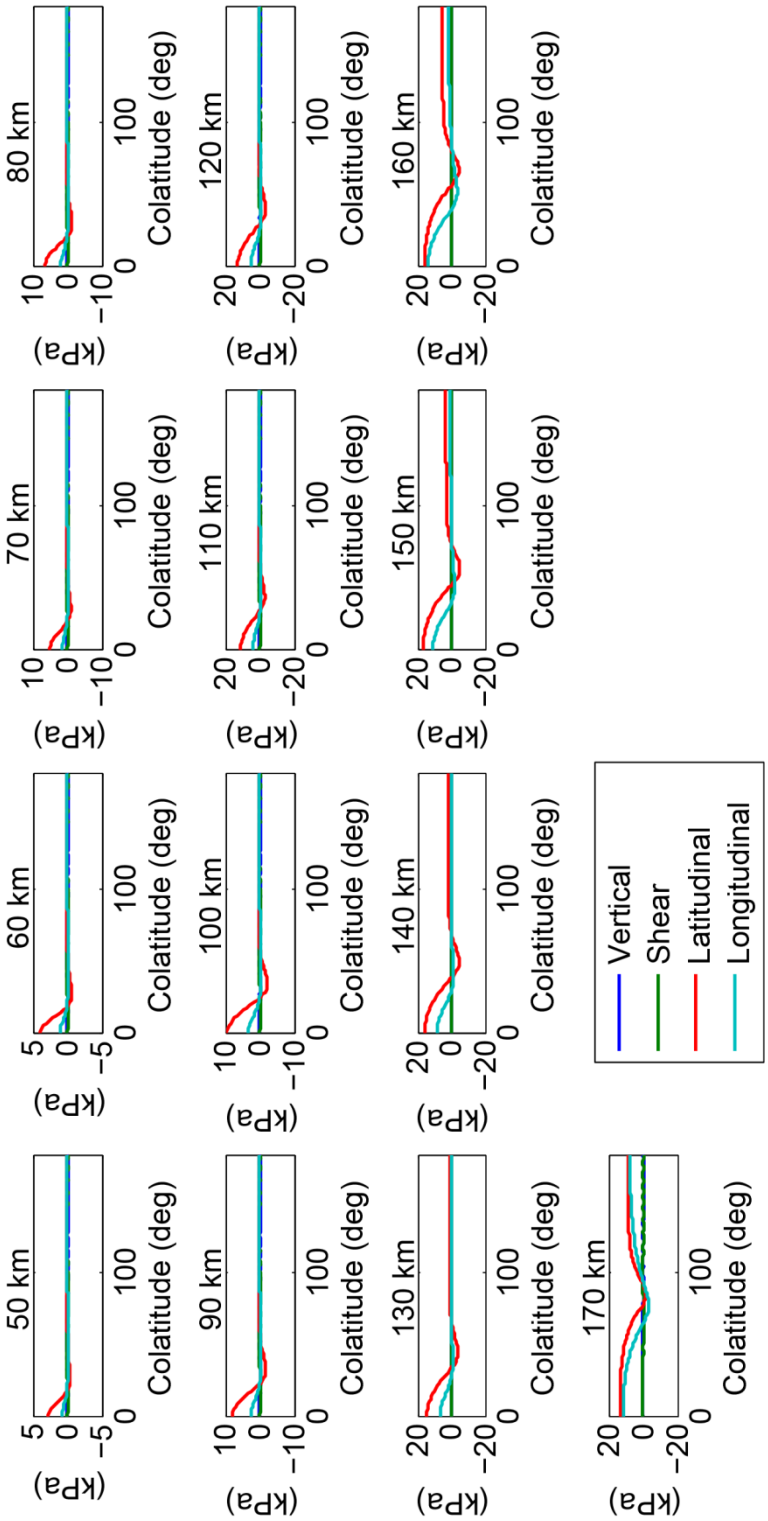

C.34. Surface stresses in 80 km cryosphere with roller base for D = 25 km, C shown above each plot.

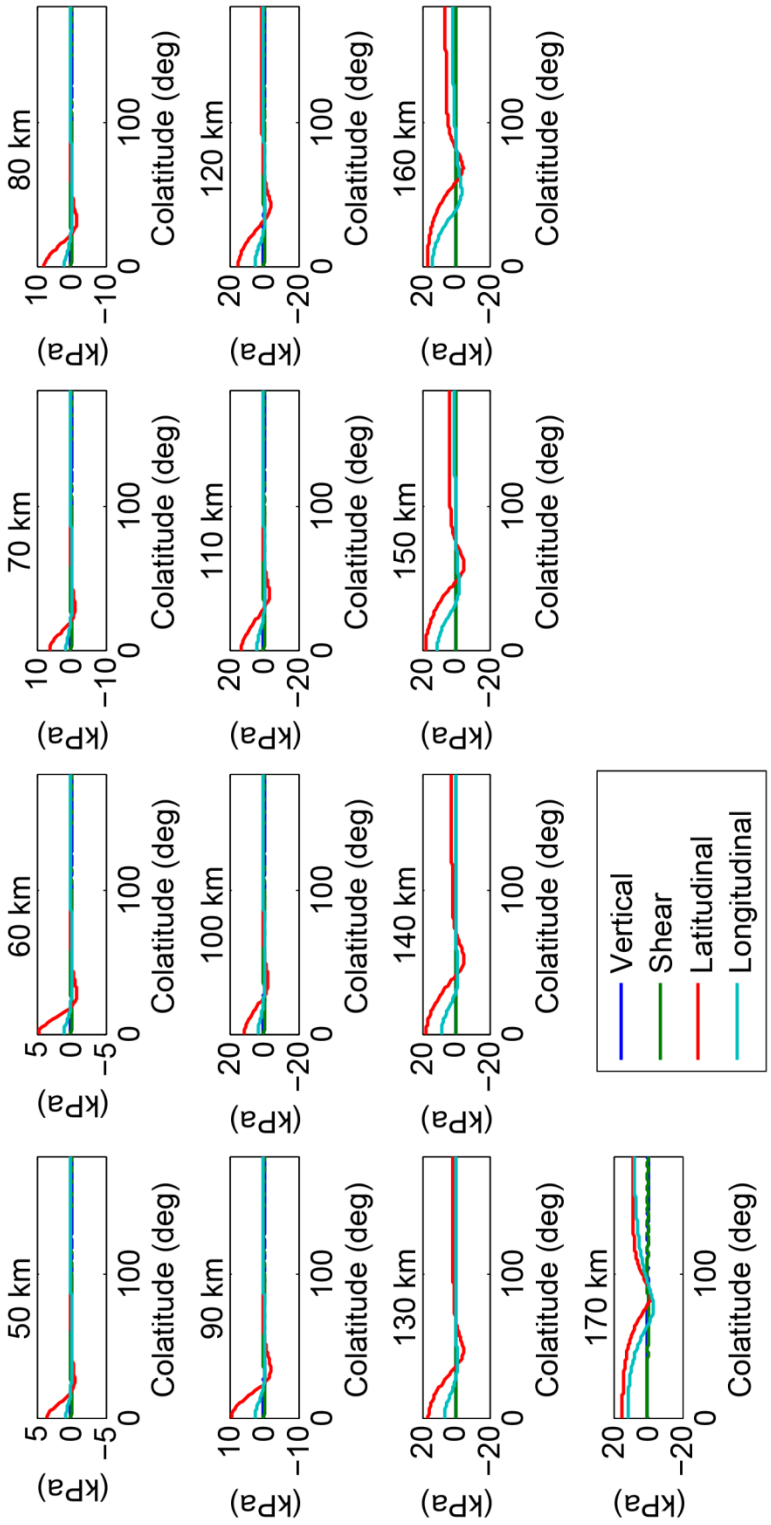

C.35. Surface stresses in 80 km cryosphere with roller base for D = 30 km, C shown above each plot.

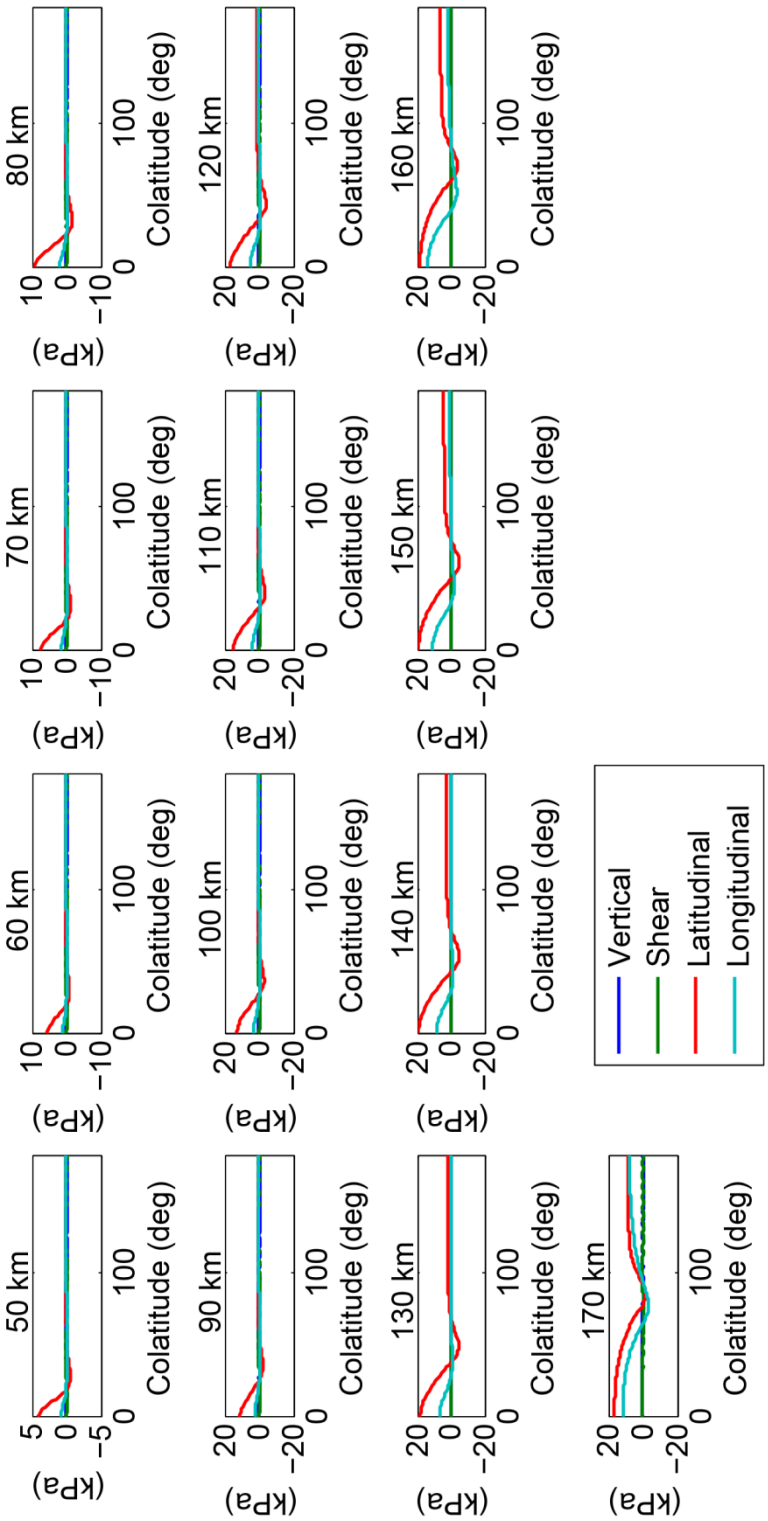

C.36. Surface stresses in 80 km cryosphere with roller base for D = 35 km, C shown above each plot.

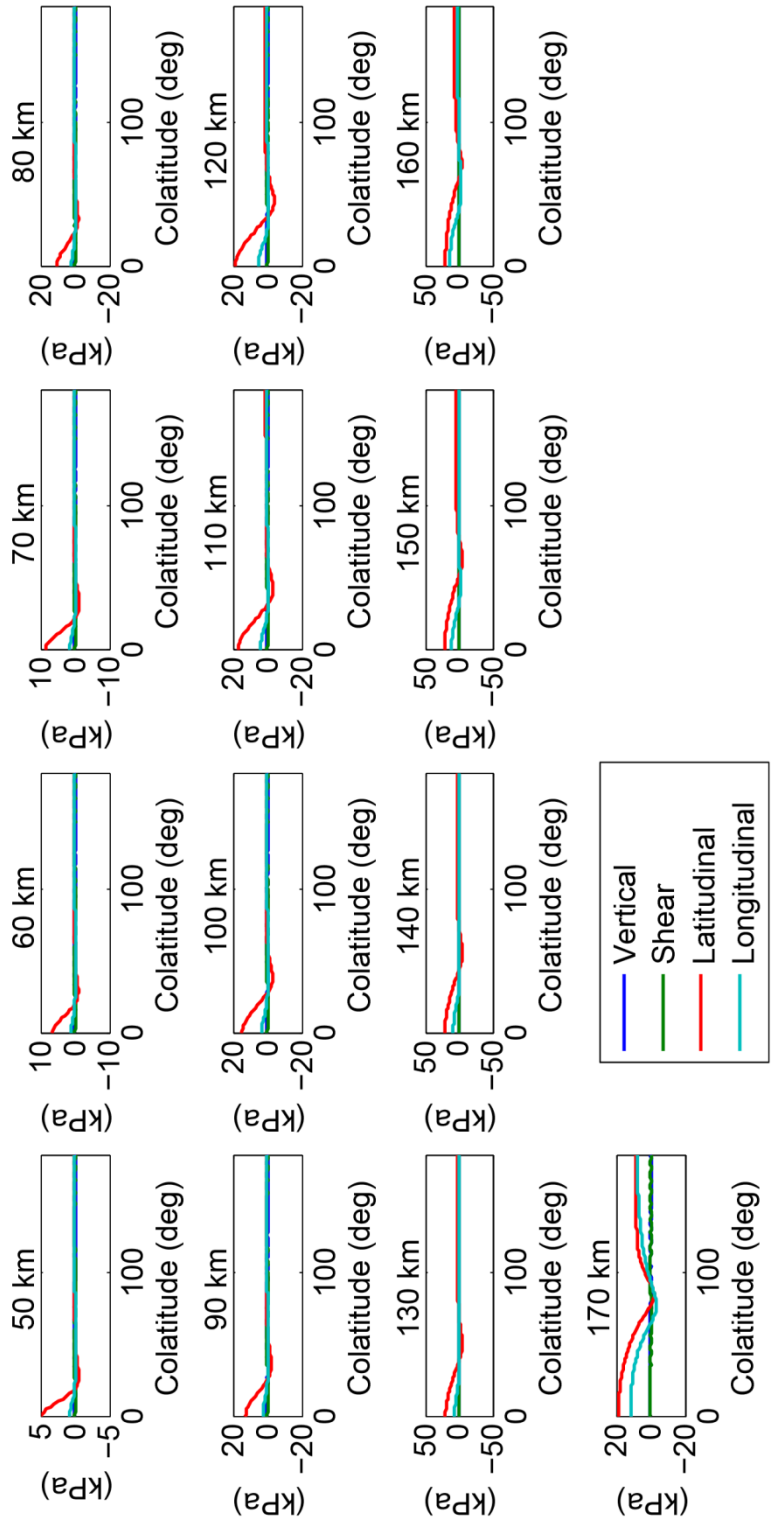

C.37. Surface stresses in 80 km cryosphere with roller base for D = 40 km, C shown above each plot.

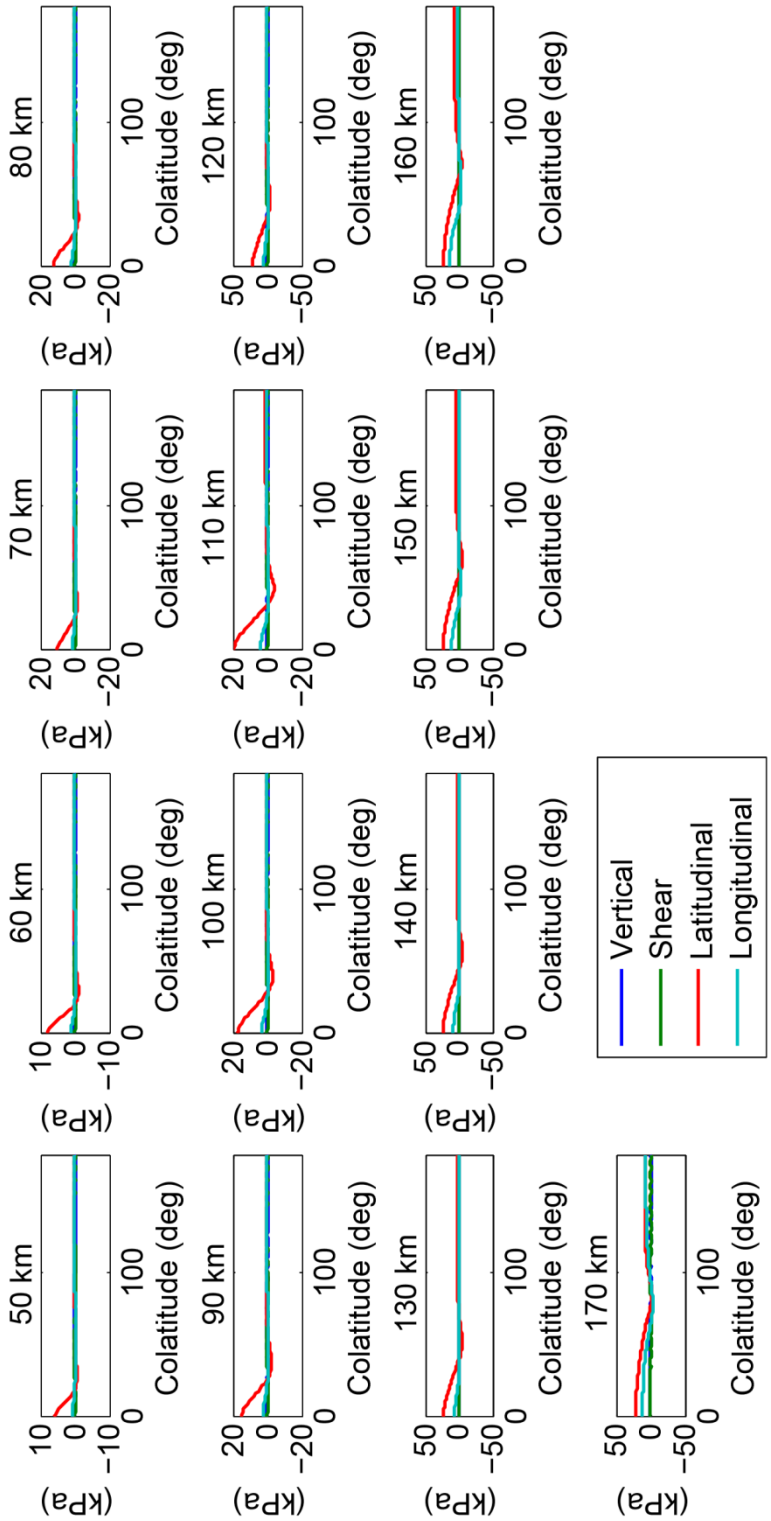

C.38. Surface stresses in 80 km cryosphere with roller base for D = 45 km, C shown above each plot.

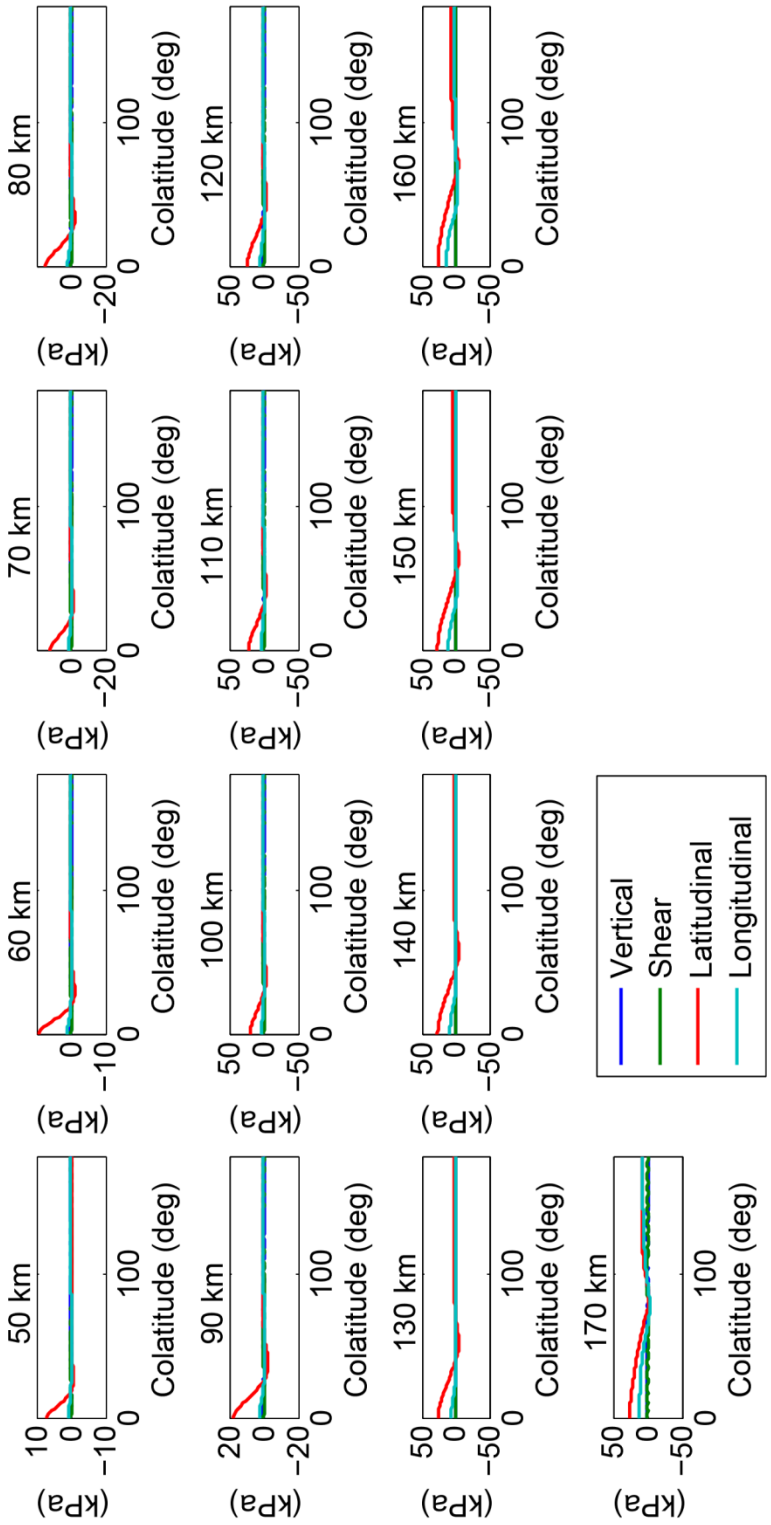

C.39. Surface stresses in 80 km cryosphere with roller base for D = 50 km, C shown above each plot.

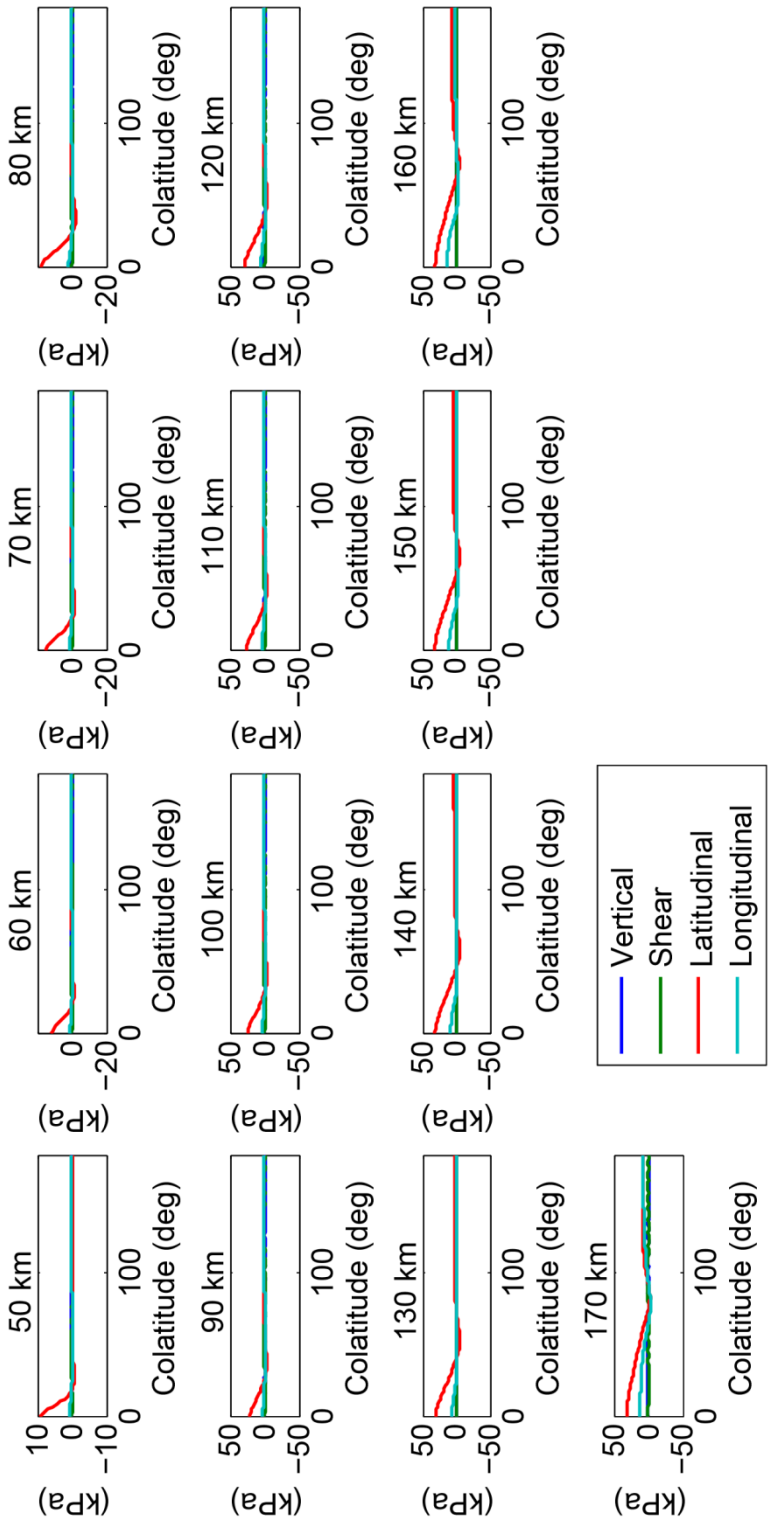

C.40. Surface stresses in 80 km cryosphere with roller base for D = 55 km, C shown above each plot.

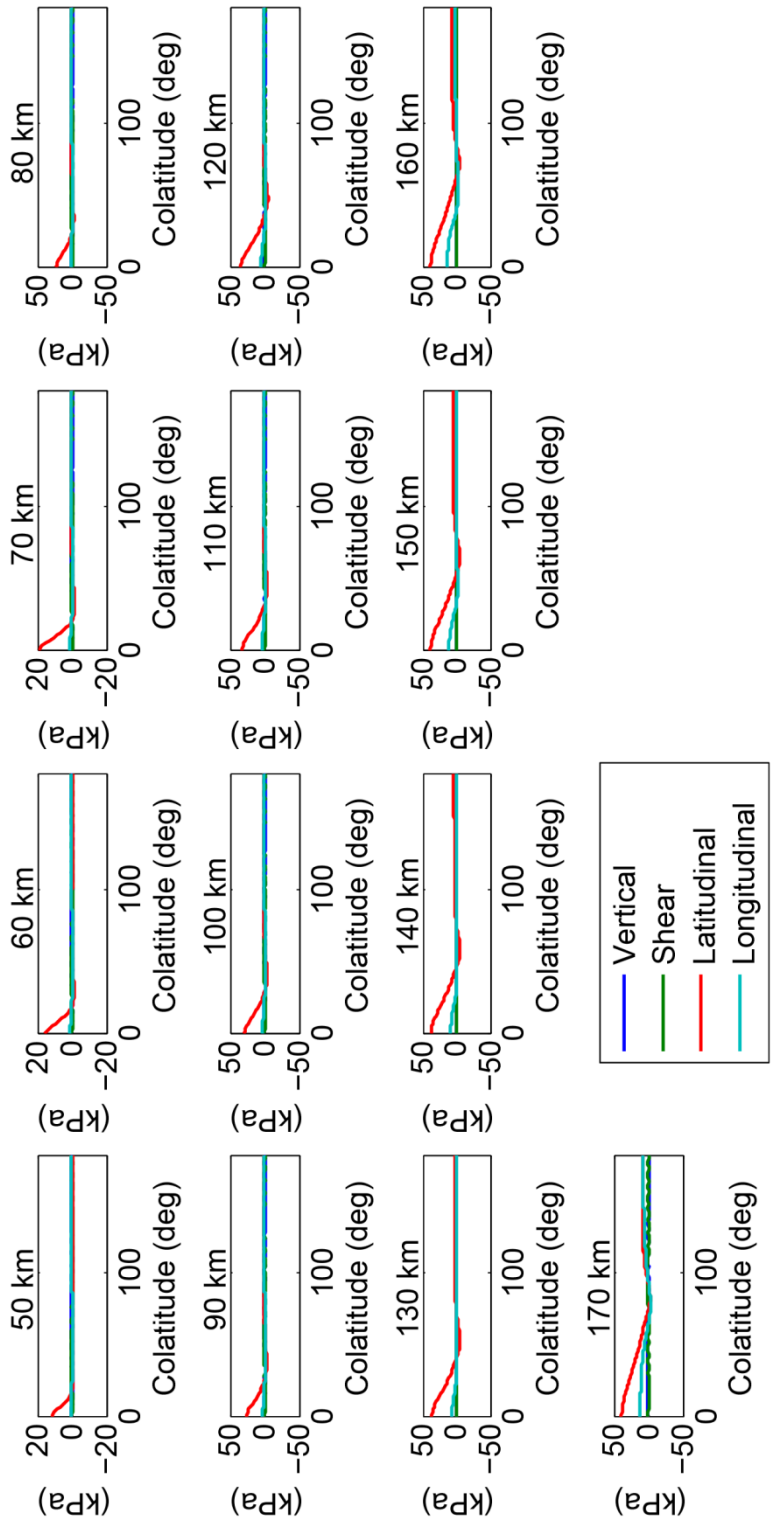

C.41. Surface stresses in 80 km cryosphere with roller base for D = 60 km, C shown above each plot.

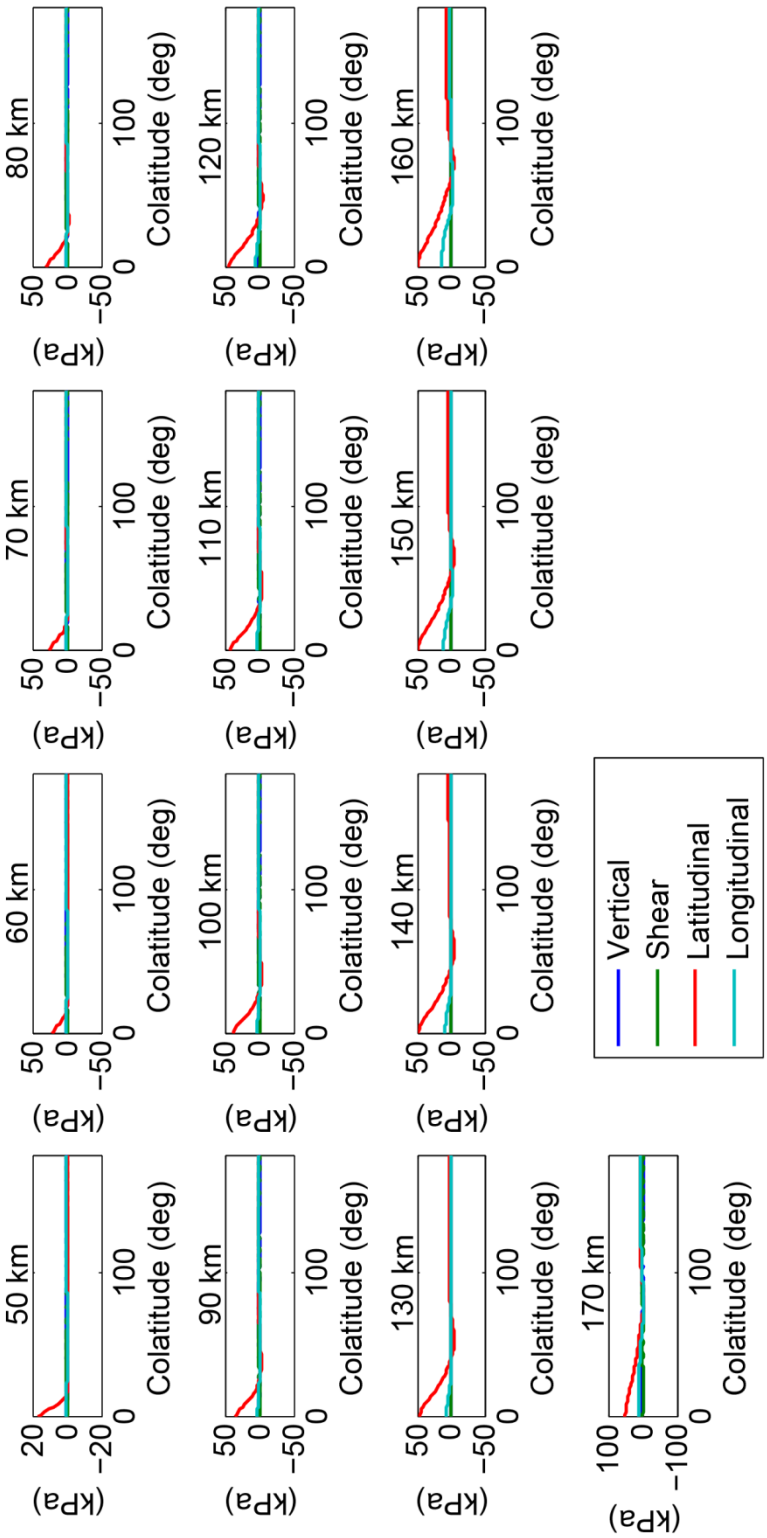

C.42. Surface stresses in 80 km cryosphere with roller base for D = 65 km, C shown above each plot.

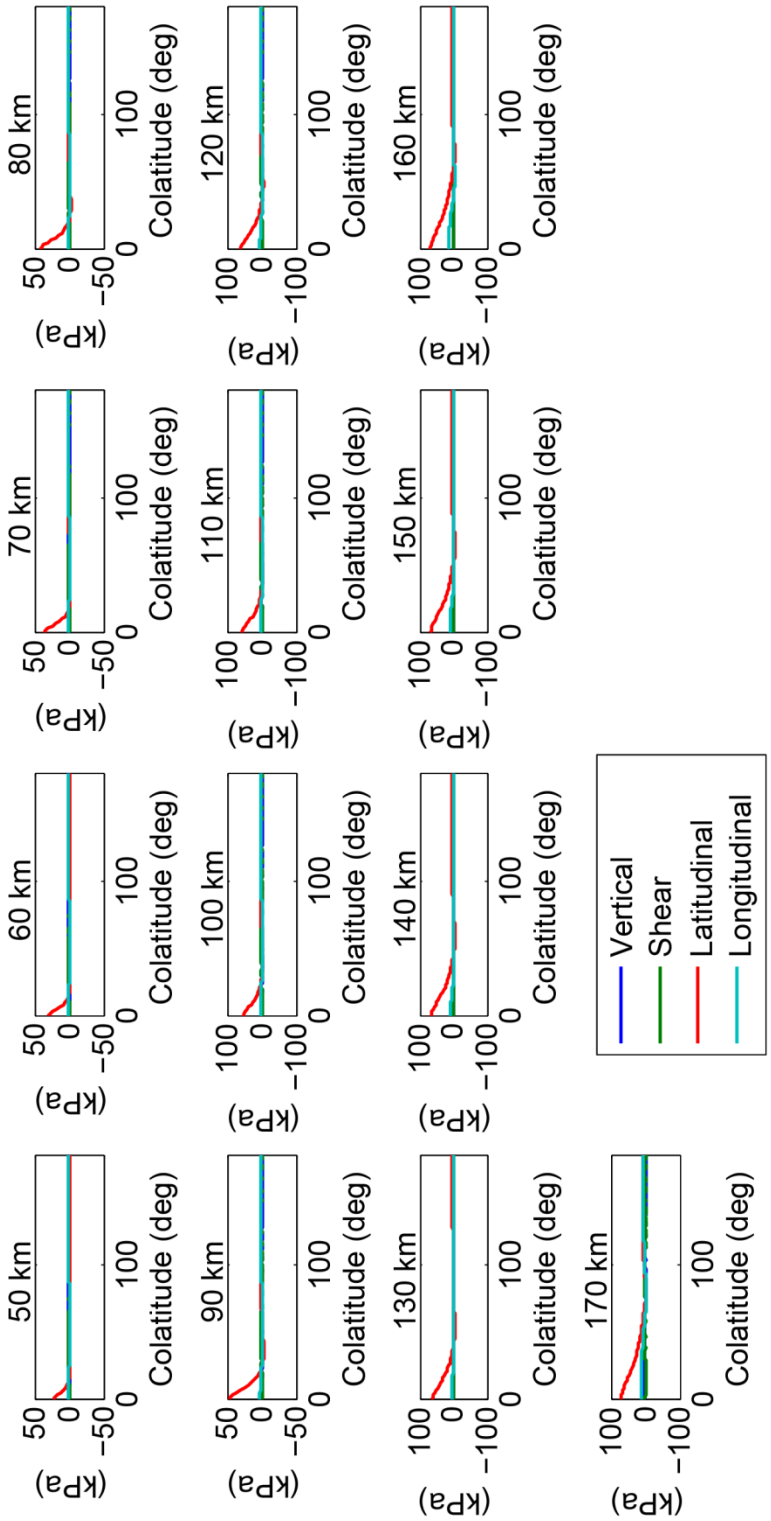

C.41. Surface stresses in 80 km cryosphere with roller base for D = 70 km, C shown above each plot.

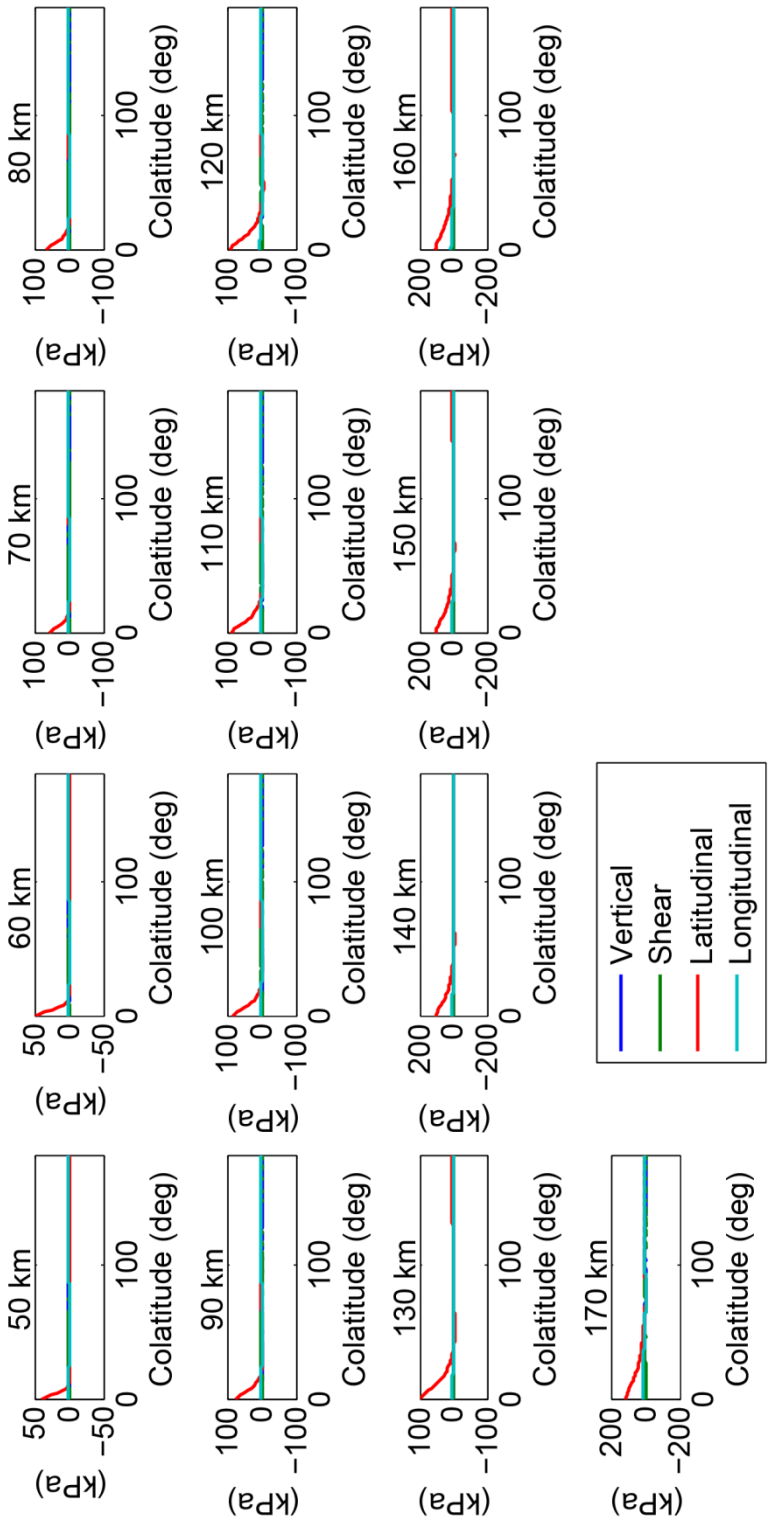

C.42. Surface stresses in 80 km cryosphere with roller base for D = 75 km, C shown above each plot.

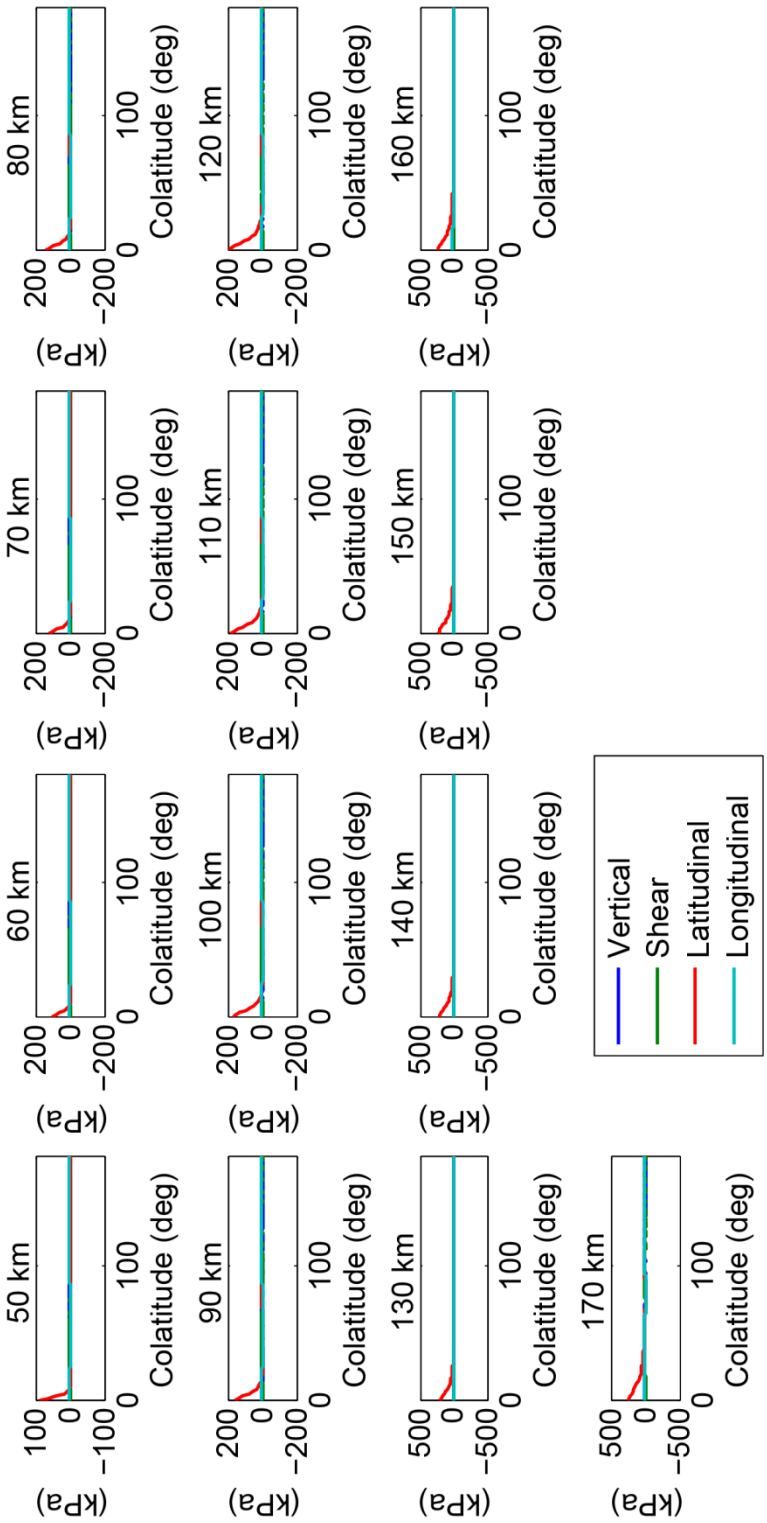

Reference

Anderson, E.M., 1905. The dynamics of faulting. Trans. Edinburgh Geol. Soc. 387–402. doi:10.1144/transed.8.3.387

Anderson, J.D., Schubert, G., Jacobson, R.A., Lau, E.L., Moore, W.B., Sjogren, W.L., 1998. Europa's Differentiated Internal Structure: Inferences from Four Galileo Encounters. Science (80-.). 281, 2019–2022. doi:10.1126/science.281.5385.2019

Barr, A.C., McKinnon, W.B., 2007. Convection in Enceladus' ice shell: Conditions for initiation. Geophys. Res. Lett. 34, n/a–n/a. doi:10.1029/2006GL028799

Björnsson, H., 2002. Subglacial lakes and Jökuklhaups in Iceland. Glob. Planet. Change 35, 255–271.

Buratti, B.J., 1988. Enceladus: Implications of its unusual photometric properties. Icarus 75, 113–126. doi:10.1016/0019-1035(88)90130-3

Carlson, R.W., Anderson, M.S., Johnson, R.E., Smythe, W.D., Hendrix, A.R., Barth, C.A., Soderblom, L.A., Hansen, G.B., McCord, T.B., Dalton, J.B., Clark, R.N., Shirley, J.H., Ocampo, A., Matson, D.L., 1999. Hydrogen peroxide on the surface of Europa. Science (80-.). 283, 2062–2064.

Cassen, P., Reynolds, R., 1979. Is there liquid water on Europa? Geophys. Res. Lett. 6, 731–734.

Chyba, C.F., Phillips, C.B., 2002. Europa as an Abode of Life. Orig. Life Evol. Biosph. 32, 47–68.

Collins, G., Nimmo, F., 2009. Chaotic terrain on Europa, in: Europa, The University of Arizona Space …. University of Arizona Press,, Tucson, pp. 259–281.

Collins, G.C., Goodman, J.C., 2007. Enceladus' south polar sea. Icarus 189, 72–82. doi:10.1016/j.icarus.2007.01.010

Collins, G.C., Head III, J.W., Pappalardo, R.T., Spaun, N., 2000. Evaluation of models for the formation of chaotic terrain on Europa. J. Geophys. Res. 105, 1709–1716. doi:10.1029/1999JE001143

Collins, G.C., McKinnon, W.B., Moore, J.M., Nimmo, F., Pappalardo, R.T., Prockter, L.M., Schenk, P.M., 2010. Tectonics of the outer planet satellites, in: Plantary Tectonics. pp. 264–350.

Coulter, C., 2009. Topographic Profile Analysis and Morphologic Characterization of Europa's Double Ridges, in: Lunar and Planetary Lunar and Planetary Science XL. p. #1960.

Crow-Willard, E.N., Pappalardo, R.T., 2015. Structural mapping of Enceladus and implications for formation of tectonized regions. J. Geophys. Res. Planets n/a–n/a. doi:10.1002/2015JE004818

Dombard, A.J., Patterson, G.W., Lederer, A.P., Prockter, L.M., 2013. Flanking fractures and the formation of double ridges on Europa. Icarus 223, 74–81. doi:10.1016/j.icarus.2012.11.021

Fagents, S. a., 2003. Considerations for effusive cryovolcanism on Europa: The post-Galileo perspective. J. Geophys. Res. 108. doi:10.1029/2003JE002128

Figueredo, P.H., Greeley, R., 2004. Resurfacing history of Europa from pole-to-pole geological mapping. Icarus 167, 287–312. doi:10.1016/j.icarus.2003.09.016

Gaidos, E.J., Nimmo, F., 2000. Tectonics and water on Europa. Nature 405, 637. doi:10.1038/35015170

Greeley, R., Figueredo, P.H., Williams, D.A., Chuang, F.C., Klemaszewski, J.E., Kadel, S.D., Prockter, L.M., Pappalardo, R.T., Head III, J.W., Collins, G.C., Spaun, N.A., Sullivan, R.J., Moore, J.M., Senske, D.A., Tufts, B.R., Johnson, T. V, Belton, M.J.S., Tanaka, K.L., 2000. Geologic mapping of Europa. J. Geophys. Res. 105, 22559–22578.

Greeley, R., Sullivan, R., Klemaszewski, J., Homan, K., Head III, J.W., Pappalardo, R.T., Veverka, J., Clark, B.E., Johnson, T. V, Klaasen, K.P., Belton, M., Moore, J., Asphaug, E., Carr, M.H., Chapman, C.R., Pilcher, C.B., Geissler, P.E., Greenberg, R., Tufts, R., 1998. Europa : Initial Galileo Geological Observations. Icarus 135, 4–24.

Greenberg, R., Geissler, P.E., Hoppa, G. V, Tufts, B.R., Durda, D.D., Pappalardo, R., Head, J.W., Greeley, R., Sullivan, R., Carr, M.H., 1998. Tectonic Processes on Europa: Tidal Stresses, Mechanical Response, and Visible Features. Icarus 135, 64–78. doi:10.1006/icar.1998.5986

Greenberg, R., Hoppa, G., Tufts, B., Geissler, P., 1999. Chaos on Europa. Icarus 141, 263–286. doi:10.1006/icar.1999.6187

Gudmundsson, M.T., Sigmundsson, F., Björnsson, H., Högnadóttir, T., 2004. The 1996 eruption at Gjálp, Vatnajökull ice cap, Iceland: efficiency of heat transfer, ice deformation and subglacial water pressure. Bull. Volcanol. 66, 46–65. doi:10.1007/s00445-003-0295-9

Han, L., Showman, A.P., 2008. Implications of shear heating and fracture zones for ridge formation on Europa. Geophys. Res. Lett. 35, 6–10. doi:10.1029/2007GL031957

Hansen, C., Esposito, L., Stewart, A., Colwell, J., Hendrix, A., Pryor, W., Shemansky, D., West, R., 2006. Enceladus' Water Vapor Plume. Science (80-.). 311, 1422–1426. doi:DOI:10.1126/science.1121254

Hansen, G.B., McCord, T.B., 2004. Amorphous and crystalline ice on the Galilean satellites: A balance between thermal and radiolytic processes. J. Geophys. Res. 109, 1–19. doi:10.1029/2003JE002149

Head, J., Pappalardo, R., 1999. Brine mobilization during lithospheric heating on Europa: Implications for formation of chaos terrain, lenticula texture, and color variations. J. Geophys. Res. 104, 27143–27155. doi:10.1029/1999JE001062

Head, J.W., Pappalardo, R.T., Sullivan, R., 1999. Europa: Morphological characteristics of ridges and triple bands from Galileo data (E4 and E6) and assessment of a linear diapirism model. J. Geophys. Res. 104, 24223–24236.

Hiraoka, K., Arakawa, M., Setoh, M., Nakamura, A.M., 2008. Measurements of target compressive and tensile strength for application to impact cratering on ice-silicate mixtures. J. Geophys. Res. 113, 1–7. doi:10.1029/2007JE002926

Hobbs, P. V., 1974. Ice Physics. Clarendon Press, Oxford.

Hoppa, G. V, Tufts, B.R., Greenberg, R., Geissler, P.E., 1999. Formation of cycloidal features on Europa. Science (80-.). 285, 1899–1902.

Hurford, T.A., Helfenstein, P., Hoppa, G. V, Greenberg, R., Bills, B.G., 2007a. Eruptions arising from tidally controlled periodic openings of rifts on Enceladus. Nature 447, 292–294. doi:10.1038/nature05821

Hurford, T.A., Sarid, A., Greenberg, R., 2007b. Cycloidal cracks on Europa: Improved modeling and non-synchronous rotation implications. Icarus 186, 218–233. doi:10.1016/j.icarus.2006.08.026

Johnson, T. V, Yeates, C.M., Young, R., 1992. Space science reviews volume on Galileo Mission overview. Space Sci. Rev. 60, 3–21.

Johnston, S.A., Montési, L.G.J., 2014. Formation of ridges on Europa above crystallizing water bodies inside the ice shell. Icarus 237, 190–201. doi:10.1016/j.icarus.2014.04.026

Kadel, S., Fagents, S., Greeley, R., Galileo SSI Team, 1998. Trough-bounding ridge pairs on Europa- Considerations for an endogenic model of formation. Lunar Planet. Sci. XXIX.

Kargel, J., Pozio, S., 1996. The volcanic and tectonic history of Enceladus. Icarus 385–404. doi:10.1006/icar.1996.0026

Kargel, J.S., Kaye, J.Z., Head III, J.W., Marion, G.M., Sassen, R., Crowley, J.K., Prieto-Ballesteros, O., Grant, S.A., Hogenboom, D.L., 2000. Europa's Crust and Ocean: Origin, Composition, and the Prospects for Life. Icarus 148, 226–265. doi:10.1006/icar.2000.6471

Kattenhorn, S., 2002. Nonsynchronous Rotation Evidence and Fracture History in the Bright Plains Region, Europa. Icarus 157, 490–506. doi:10.1006/icar.2002.6825

Kattenhorn, S.A., Hurford, T.A., 2007. Tectonics of Europa, in: Watters, T.R., Schultz, R.A. (Eds.), Planetary Tectonics. Cambridge University Press, Cambridge, pp. 199–236.

Kavanagh, K.T., Clough, R.W., 1971. Finite Element Applicatons in the Characterization of Elastic Solids. Int. J. Solids Struct. 7, 11–23.

Kivelson, M.G., Khurana, K.K., Joy, S., Russell, C.T., Southwood, D.J., Walker, R.J., Polanskey, C., 1997. Europa's Magnetic Signature: Report from Galileo's Pass on 19 December 1996. Science (80-.). 276, 1239–1241. doi:10.1126/science.276.5316.1239

Kivelson, M.G., Khurana, K.K., Russell, C.T., Volwerk, M., Walker, R.J., Zimmer, C., 2000. Galileo Magnetometer Measurements: A Stronger Case for a Subsurface Ocean at Europa. Science (80-.). 289, 1340–1343. doi:10.1126/science.289.5483.1340

Kohlhase, C.E., Penzo, P.A., 1977. Voyager mission description. Space Sci. Rev. 21, 77–101. doi:10.1007/BF00200846

Krawczynski, M.J., Behn, M.D., Das, S.B., Joughin, I., 2009. Constraints on the lake volume required for hydro-fracture through ice sheets. Geophys. Res. Lett. 36, L10501. doi:10.1029/2008GL036765

Kusunoki, K., 1955. Observations on the horizontal and vertical distribution of chlorinity of sea ice. J. Oceanogr. Soc. Japan 11, 179–183.

Lake, R.A., Lewis, E.L., 1970. Salt rejection by sea ice during growth. J. Geophys. Res. 75, 583–597. doi:10.1029/JC075i003p00583

Lee, S., Pappalardo, R.T., Makris, N., 2005. Mechanics of tidally driven fractures in Europa's ice shell. Int. J. Sol. Syst. Stud. 177, 367–379. doi:10.1016/j.icarus.2005.07.003

Leto, G., Palumbo, M.E., Strazzulla, G., 1996. Structural characteristic of irradiated and unirradiated ices. Nucl. Instruments Methods Phys. Res. Sect. B Beam Interact. with Mater. Atoms 116, 49–52. doi:10.1016/0168-583X(96)00009-2

Manga, M., Wang, C.-Y., 2007. Pressurized oceans and the eruption of liquid water on Europa and Enceladus. Geophys. Res. Lett. 34, L07202. doi:10.1029/2007GL029297

Mastin, L., Pollard, D., 1988. Surface deformation and shallow dike intrusion processes at Inyo Craters, Long Valley, California. J. Geophys. Res. 93, 13221–13235.

Matson, D.L., Spilker, L.J., Lebreton, J.-P., 2002. The Cassini/Huygens mission to the Saturnian system. Space Sci. Rev. 1–58.

McCord, T.B., Hansen, G.B., Fanale, F.P., Carlson, R.W., Matson, D.L., Johnson, T. V, Smythe, W.D., Crowley, J.K., Martin, P.D., Ocampo, A., Hibbitts, C.A., Granahan, J.C., the NIMS Team, 1998. Salts on Europa's Surface Detected by Galileo's Near Infrared Mapping Spectrometer. Science (80-.). 280, 1242–1245. doi:10.1126/science.280.5367.1242

McCord, T.B., Hansen, G.B., Matson, D.L., Johnson, T. V, Crowley, J.K., Fanale, F.P., Carlson, R.W., Smythe, W.D., Martin, P.D., Hibbitts, C.A., Granahan, J.C., Ocampo, A., 1999. Hydrated salt minerals on Europa's surface from the Galileo near-infrared mapping spectrometer (NIMS) investigation. J. Geophys. Res. 104, 11,827–11851.

Melosh, H.J., Turtle, E.P., 2004. Ridges on Europa: Origin by incremental ice-wedging, in: Lunar and Planetary Institute Science Conference Abstracts. p. 2029.

Meyer, J., Wisdom, J., 2007. Tidal heating in Enceladus. Icarus 188, 535–539. doi:10.1016/j.icarus.2007.03.001

Michaut, C., Manga, M., 2014. Domes , pits , and small chaos on Europa produced by water sills. J. Geophys. Res. Planets 119. doi:10.1002/2013JE004558

Mitchell, G.A., Montési, L.G.J., Zhu, W., Smith, D.K., Schouten, H., 2011. Transient rifting north of the Galápagos Triple Junction. Earth Planet. Sci. Lett. 307 (3-4), 461–469. doi:10.1016/j.epsl.2011.05.027

National Aeronautics and Space Administration, 2003. Galileo End of Mission.

Nimmo, F., Gaidos, E.J., 2002. Strike-slip motion and double ridge formation on Europa. J. Geophys. Res. 107, 1–8. doi:10.1029/2000JE001476

Nimmo, F., Spencer, J.R., Pappalardo, R.T., Mullen, M.E., 2007. Shear heating as the origin of the plumes and heat flux on Enceladus. Nature 447, 289–91. doi:10.1038/nature05783

O'Brien, D., Geissler, P., Greenberg, R., 2002. A Melt-through Model for Chaos Formation on Europa. Icarus 156, 152–161. doi:10.1006/icar.2001.6777

O'Neill, C., Nimmo, F., 2010. The role of episodic overturn in generating the surface geology and heat flow on Enceladus. Nat. Geosci. 3, 88–91. doi:10.1038/ngeo731

Pappalardo, R.T., Head III, J.W., Greeley, R., Sullivan, R.J., 1998. Geological evidence for solid-state convection in Europa's ice shell. Nature 391, 365–368. doi:doi:10.1038/34862

Patthoff, D.A., Kattenhorn, S., 2011. A fracture history on Enceladus provides evidence for a global ocean. Geophys. Res. Lett. 38. doi:10.1029/2011GL048387

Petrenko, V.F., Whitworth, R.W., 1999. Physics of Ice. Oxford University Press, Oxford, UK.

Pollard, D., Holzhausen, G., 1979. On the mechanical interaction between a fluid-filled fracture and the Earth's surface. Tectonophysics 27–57.

Porco, C., DiNino, D., Nimmo, F., 2014. How the Geysers, Tidal Stresses, and Thermal Emission Across the South Polar Terrain of Enceladus Are Related. Astron. J. 148. doi:10.1088/0004-6256/148/3/45

Porco, C.C., Helfenstein, P., Thomas, P.C., Ingersoll, A.P., Wisdom, J., West, R., Neukum, G., Denk, T., Wagner, R., Roatsch, T., Kieffer, S., Turtle, E., McEwen, A., Johnson, T. V, Rathbun, J., Veverka, J., Wilson, D., Perry, J., Spitale, J., Brahic, A., Burns, J.A., Delgenio, A.D., Dones, L., Murray, C.D., Squyres, S., 2006. Cassini observes the active south pole of Enceladus. Science (80-.). 311, 1393–401. doi:10.1126/science.1123013

Prieto-Ballesteros, O., Kargel, J.S., 2005. Thermal state and complex geology of a heterogeneous salty crust of Jupiter's satellite, Europa. Icarus 173, 212–221. doi:10.1016/j.icarus.2004.07.019

Prieto-Ballesteros, O., Kargel, J.S., Fernández-Sampedro, M., Selsis, F., Martínez, E.S., Hogenboom, D.L., 2005. Evaluation of the possible presence of clathrate

hydrates in Europa's icy shell or seafloor. Icarus 177, 491–505. doi:10.1016/j.icarus.2005.02.021

Prockter, L.M., Pappalardo, R.T., 2000. Folds on Europa: Implications for Crustal Cycling and Accommodation of Extension. Science (80-.). 289, 941–943. doi:10.1126/science.289.5481.941

Reynolds, R.T., McKay, C.P., Kasting, J.F., 1987. Europa, tidally heated oceans, and habitable zones around giant planets. Adv. Space Res. 7, 125–32.

Reynolds, R.T., Squyres, W., Colburn, D.S., McKay, C.P., 1983. On the habitability of Europa. Icarus 56, 246–254. doi:10.1016/0019-1035(83)90037-4

Rhoden, A.R., Militzer, B., Huff, E.M., Hurford, T. a., Manga, M., Richards, M. a., 2010. Constraints on Europa's rotational dynamics from modeling of tidally-driven fractures. Icarus 210, 770–784. doi:10.1016/j.icarus.2010.07.018

Rhoden, A.R., Wurman, G., Huff, E.M., Manga, M., Hurford, T. a., 2012. Shell tectonics: A mechanical model for strike-slip displacement on Europa. Icarus 218, 297–307. doi:10.1016/j.icarus.2011.12.015

Roberts, J.H., Nimmo, F., 2008. Tidal heating and the long-term stability of a subsurface ocean on Enceladus. Icarus 194, 675–689. doi:10.1016/j.icarus.2007.11.010

Ross, M., Schubert, G., 1989. Viscoelastic models of tidal heating in Enceladus. Icarus 101, 90–101.

Roth, L., Saur, J., Retherford, K.D., Strobel, D.F., Feldman, P.D., McGrath, M.A., Nimmo, F., 2014. Transient water vapor at Europa's south pole. Science 343, 171–4. doi:10.1126/science.1247051

Rudolph, M.L., Manga, M., 2009. Fracture penetration in planetary ice shells. Icarus 199, 536–541. doi:10.1016/j.icarus.2008.10.010

Schenk, P.M., Pappalardo, R.T., 2004. Topographic variations in chaos on Europa: Implications for diapiric formation. Geophys. Res. Lett. 31, L16703. doi:10.1029/2004GL019978

Schilling, N., Neubauer, F.M., Saur, J., 2007. Time-varying interaction of Europa with the jovian magnetosphere: Constraints on the conductivity of Europa's subsurface ocean. Icarus 192, 41–55. doi:10.1016/j.icarus.2007.06.024

Schilling, N., Neubauer, F.M., Saur, J., 2008. Influence of the internally induced magnetic field on the plasma interaction of Europa. J. Geophys. Res. 113, 1–12. doi:10.1029/2007JA012842

Schmidt, B.E., Blankenship, D.D., Patterson, G.W., Schenk, P.M., 2011. Active formation of "chaos terrain" over shallow subsurface water on Europa. Nature 479, 502–505. doi:10.1038/nature10608

Schouten, H., Smith, D.K., Montési, L., Zhu, W., Klein, E.M., 2008. Cracking of the lithosphere north of the galapagos triple junction. Geology 36, 330–342. doi:10.1130/G24431A.1

Schubert, G., Anderson, J.D., Travis, B.J., Palguta, J., 2007. Enceladus: Present internal structure and differentiation by early and long-term radiogenic heating. Icarus 188, 345–355. doi:10.1016/j.icarus.2006.12.012

Schulson, E.M., Duval, P., 2009. Creep and Fracture of Ice. Cambridge University Press.

Smith, B.A., Soderblom, L.A., Beebe, R., Bliss, D., Boyce, J.M., Brahic, A., Briggs, G.A., Brown, R.H., Collins, S.A., Cook, A.F., Croft, S.K., Cuzzi, J.N., Danielson, G.E., Davies, M.E., Dowling, T.E., Godfrey, D., Hansen, C.J., Harris, C., Hunt, G.E., Ingersoll, A.P., Johnson, T. V, Krauss, R.J., Masursky, H., Morrison, D., Owen, T., Plescia, J.B., Pollack, J.B., Porco, C.C., Rages, K., Sagan, C., Shoemaker, E.M., Sromovsky, L.A., Stoker, C., Strom, R.G., Suomi, V.E., Synnott, S.P., Terrile, R.J., Thomas, P., Thompson, W.R., Veverka, J., 1986. Voyager 2 in the uranian system: imaging science results. Science (80-.). 233, 43–64. doi:10.1126/science.233.4759.43

Sohl, F., Choukroun, M., Kargel, J.S., Kimura, J., Pappalardo, R.T., Vance, S., Zolotov, M.Y., 2010. Subsurface Water Oceans on Icy Satellites: Chemical Composition and Exchange Processes. Space Sci. Rev. 153, 485–510. doi:10.1007/s11214-010-9646-y

Sotin, C., Head III, J.W., Tobie, G., 2002. Europa : Tidal heating of upwelling thermal plumes and the origin of lenticulae and chaos melting. Geophys. Res. Lett. 29, 74–1–74–4. doi:10.1029/2001GL013844

Spaun, N., Head, J., Collins, G.C., Prockter, L., Pappalardo, R.T., 1998. Conamara Chaos region, Europa: Reconstruction of mobile polygonal ice blocks. Geophys. Res. Lett. 25, 4277–4280. doi:10.1029/1998GL900176

Spencer, J.R., Pearl, J.C., Segura, M., Flasar, F.M., Mamoutkine, A., Romani, P., Buratti, B.J., Hendrix, a R., Spilker, L.J., Lopes, R.M.C., 2006. Cassini encounters Enceladus: background and the discovery of a south polar hot spot. Science (80-.). 311, 1401–5. doi:10.1126/science.1121661

Spitale, J.N., Porco, C.C., 2007. Association of the jets of Enceladus with the warmest regions on its south-polar fractures. Nature 449, 695–7. doi:10.1038/nature06217

Squyres, S.W., Reynolds, R.T., Cassen, P.M., Peale, S.J., 1983. The evolution of Enceladus. Icarus 53, 319–331. doi:10.1016/0019-1035(83)90152-5

Thomas, A.M., Nadeau, R.M., Bürgmann, R., 2009. Tremor-tide correlations and near-lithostatic pore pressure on the deep San Andreas fault. Nature 462, 1048–51. doi:10.1038/nature08654

Thordarson, T., Self, S., 1993. The Laki (Skaftár Fires) and Grímsvötn eruptions in 1783–1785. Bull. Volcanol. 55, 233–263.

Tobie, G., Cadek, O., Sotin, C., 2008. Solid tidal friction above a liquid water reservoir as the origin of the south pole hotspot on Enceladus. Icarus 196, 642–652. doi:10.1016/j.icarus.2008.03.008

Turcotte, D., Schubert, G., 2002. (2002). Geodynamics. Cambridge University Press., 2nd ed. Cambridge University Press.

Verbiscer, A.J., French, R.G., McGhee, C. a., 2005. The opposition surge of Enceladus: HST observations 338–1022 nm. Icarus 173, 66–83. doi:10.1016/j.icarus.2004.05.001

Walder, J., Nur, A., 1984. Porosity reduction and crustal pore pressure development. J. Geophys. Res. Solid Earth … 89, 11539–11548.

Weertman, J., 1971. Theory of water-filled crevasses in glaciers applied to vertical magma transport beneath oceanic ridges. J. Geophys. Res. 76, 1171–1183. doi:10.1029/JB076i005p01171

Zahnle, K.J., Schenk, P., Levison, H., Dones, L., 2003. Cratering rates in the outer Solar System. Icarus 163, 263–289. doi:10.1016/S0019-1035(03)00048-4